
Effective Field Theories and Electromagnetic Properties of Light Nuclei

Effektive Feldtheorien und elektromagnetische Eigenschaften leichter Kerne
Vom Fachbereich Physik der Technischen Universität Darmstadt
zur Erlangung des Grades eines Doktors der Naturwissenschaften (Dr. rer. nat.)
genehmigte Dissertation von Jonas Braun [REDACTED]
Darmstadt 2019 – D 17



TECHNISCHE
UNIVERSITÄT
DARMSTADT

Institut für Kernphysik
Fachbereich Physik

Effective Field Theories and Electromagnetic Properties of Light Nuclei
Effektive Feldtheorien und elektromagnetische Eigenschaften leichter Kerne

Genehmigte Dissertation von Jonas Braun [REDACTED]

1. Gutachten: Prof. Dr. Hans-Werner Hammer
2. Gutachten: Prof. Dr. Robert Roth

Tag der Einreichung: 12.02.2019

Tag der Prüfung: 24.04.2019

Darmstadt 2019 – D 17

Bitte zitieren Sie dieses Dokument als:

URN: urn:nbn:de:tuda-tuprints-86820

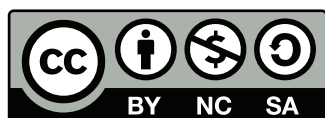
URL: <http://tuprints.ulb.tu-darmstadt.de/id/eprint/8682>

Dieses Dokument wird bereitgestellt von tuprints,

E-Publishing-Service der TU Darmstadt

<http://tuprints.ulb.tu-darmstadt.de>

tuprints@ulb.tu-darmstadt.de



Die Veröffentlichung steht unter folgender Creative Commons Lizenz:

Namensnennung – Nicht kommerziell – Share Alike 4.0 International

<http://creativecommons.org/licenses/by-nc-sa/4.0>

Erklärung gemäß §9 Promotionsordnung

Hiermit versichere ich, dass ich die vorliegende Dissertation selbstständig angefertigt und keine anderen als die angegebenen Quellen und Hilfsmittel verwendet habe. Alle wörtlichen und paraphrasierten Zitate wurden angemessen kenntlich gemacht. Die Arbeit hat bisher noch nicht zu Prüfungszwecken gedient.

Darmstadt, den 12. Februar 2019

(Jonas Braun)



Abstract

Electromagnetic properties and nuclear reactions in light nuclei are investigated in different low-energy ranges applying effective field theories. In particular, two topics with distinct degrees of freedom are considered: one-neutron halo nuclei in the Halo effective field theory (Halo EFT) and threshold neutral pion photoproduction employing chiral effective field theory (χ EFT).

In Halo EFT, the relevant degrees of freedom are the shallowly bound halo neutron and the tightly bound core nucleus. We extend the Halo EFT approach to shallow D -wave bound states, where the strong interaction between the core and the halo neutron is parametrized by contact interactions. We develop a power-counting scenario for arbitrary partial wave bound states and discuss its implications for universality. Furthermore, the results for electromagnetic form factors, electromagnetic transitions, and neutron capture reactions in weakly-bound D -wave states are presented of which we derive several universal correlations between electric observables. We apply our results to the two carbon isotopes ^{15}C and ^{17}C , that both have shallow bound states with a neutron in a D -wave relative to the core. Together with *ab initio* results from the no-core shell model (NCSM) and experimental data for the neutron separation energies, we obtain predictions for several electric observables in ^{15}C at leading order (LO), i.e. the quadrupole and hexadecupole moments and radii as well as E1 neutron capture cross sections, using the experimentally measured E2 transition strength in ^{15}C . The effects of next-to-leading order corrections for our results are also addressed. We find that additional counterterms, which are required for the absorption of divergences, become more dominant in higher partial wave bound states, especially in the magnetic sector. Hence, we discuss the consequences for universality in such weakly-bound states.

Threshold neutral pion photoproduction off light nuclei is investigated in chiral perturbation theory (ChPT) at LO in the chiral expansion. We calculate the expectation value of the pion production operator with nuclear wave functions obtained by the NCSM and apply a density matrix approach for the evaluation of the appropriate pion production amplitudes. At LO, one-nucleon and two-nucleon effects contribute to the amplitude. We compare our results for ^2H , ^3H , and ^3He with the literature and find that we agree on both the one-nucleon contribution and the two-nucleon contribution, with the latter dominating at this order. The total amplitude is furthermore compared to experimental data of ^2H which reveals that the experimental result is about 11% larger than our prediction. Moreover, we predict the threshold neutral pion photoproduction amplitude for ^6Li in ChPT for the first time.

Parts of this work have been published in:

- [1] *Electric properties of one-neutron halo nuclei in Halo EFT*,
J. Braun and H. W. Hammer,
Few-Body Systems, 58(2), 94 (2017), arXiv: 1612.07689 [nucl-th].
- [2] *Universal correlations in shallow D -wave systems*,
J. Braun, R. Roth, and H. W. Hammer,
arXiv: 1803.02169 [nucl-th] (2018).
- [3] *Halo structure of ^{17}C*
J. Braun, H. W. Hammer, and L. Platter,
Eur. Phys. J. A54(11), 196 (2018), arXiv: 1806.01112 [nucl-th].



Kurzfassung

Elektromagnetische Eigenschaften und Kernreaktionen in leichten Kernen werden mithilfe von effektiven Feldtheorien in verschiedenen Niedrigenergiebereichen untersucht. In diesem Zusammenhang werden zwei Theorien mit unterschiedlichen Freiheitsgraden betrachtet: Ein-Neutron-Halokerne in Halo effektiver Feldtheorie (Halo-EFT) und Neutrale-Pion-Photoproduktion an der Schwelle unter Verwendung der chiralen effektiven Feldtheorie.

In der Halo-EFT sind die relevanten Freiheitsgrade das schwach gebundene Haloneutron und der verbleibende, stark gebundene Atomkern. Der Halo-EFT-Ansatz wird auf schwach gebundene D -Wellen-Zustände erweitert, bei denen die starke Wechselwirkung zwischen dem Kern und dem Haloneutron durch Kontaktwechselwirkungen parametrisiert wird. Ein Power-Counting-Szenario für beliebige Partialwellen-Zustände wird entwickelt und dessen Auswirkungen auf die Universalität werden diskutiert. Darüber hinaus werden die Ergebnisse für elektromagnetische Formfaktoren, elektromagnetische Übergänge sowie Neutroneneinfang in schwach gebundenen D -Wellen-Zuständen präsentiert, aus denen mehrere universelle Korrelationen zwischen elektrischen Observablen abgeleitet werden. Unsere Ergebnisse werden auf die beiden Kohlenstoffisotope ^{15}C und ^{17}C angewendet. Beide Isotope weisen schwach gebundene Zustände mit einem Neutron auf, das sich in einer D -Welle relativ zum Kern befindet. Zusammen mit *ab initio* Ergebnissen aus dem No-Core-Shell-Model (NCSM) und experimentellen Daten für die Neutronen-Separations-Energien werden, mithilfe des experimentell gemessenen E2-Übergangs in ^{15}C , Vorhersagen für mehrere elektrische Observablen für ^{15}C in führender Ordnung gemacht. Dabei werden Vorhersagen für die Quadrupol- und Hexadecupol-Momente und deren Radien sowie für E1-Neutroneneinfang-Wirkungsquerschnitte getroffen. Des Weiteren werden die Beiträge der nächst führenden Ordnung für unsere Ergebnisse besprochen. Zusätzliche Gegenterme, die zur Absorption von Divergenzen erforderlich sind, werden für höhere Partialwellen-Zustände, insbesondere für magnetische Observablen, immer wichtiger. Die Folgen, die daraus für die Universalität in solchen schwach gebundenen Zuständen entstehen, werden diskutiert.

Die Neutrale-Pion-Photoproduktion an der Schwelle wird im Rahmen der chiralen Störungstheorie an leichten Kernen in führender Ordnung der chiralen Entwicklung untersucht. Um die Pion-Produktionsamplituden zu berechnen, wird der Erwartungswert zwischen der Kern-Wellenfunktion, die mithilfe des NCSM bestimmt wird, und den Pion-Produktionsoperatoren gebildet. Des Weiteren wird ein Dichtematrix-Ansatz für die Auswertung verwendet. In führender Ordnung tragen Ein-Nukleon-Effekte und Zwei-Nukleonen-Effekte zur Pion-Produktion bei. Die erhaltenen Ergebnisse für ^2H , ^3H und ^3He werden mit Literaturwerten verglichen. Sowohl der Ein-Nukleon-Beitrag als auch der Zwei-Nukleonen-Beitrag, der in dieser Ordnung dominiert, stimmen mit den Literaturwerten überein. Darüber hinaus wird die Gesamtamplitude mit den experimentellen Werten der Pion-Produktion an ^2H verglichen. Der experimentelle Wert liegt etwa 11% über unserer Vorhersage. Außerdem wird erstmals die Amplitude der Pion-Photoproduktion an der Schwelle für ^6Li in chiraler Störungstheorie berechnet.

Teile dieser Arbeit wurden bereits veröffentlicht in:

[1] *Electric properties of one-neutron halo nuclei in Halo EFT*,

J. Braun and H. W. Hammer, *Few-Body Systems*, 58(2), 94 (2017), arXiv: 1612.07689 [nucl-th].

[2] *Universal correlations in shallow D-wave systems*,

J. Braun, R. Roth, and H. W. Hammer, arXiv: 1803.02169 [nucl-th] (2018).

[3] *Halo structure of ^{17}C*

J. Braun, H. W. Hammer, and L. Platter, *Eur. Phys. J. A*54(11), 196 (2018), arXiv: 1806.01112 [nucl-th].



Contents

1. Introduction	1
2. Effective Field Theories	5
2.1. Chiral Effective Field Theory	6
2.1.1. Chiral Symmetry	6
2.1.2. Chiral Perturbation Theory	7
2.2. Halo Effective Field Theory	11
2.2.1. Pionless Effective Field Theories	11
2.2.2. Halo Nuclei	13
3. No-Core Shell Model	17
3.1. Importance-Truncation Scheme	18
3.2. Center-of-Mass Motion	20
4. Halo EFT Results	21
4.1. Carbon-15 and Carbon-17	21
4.2. Effective Lagrangian	22
4.3. Dimer Propagators	24
4.3.1. <i>S</i> -Wave Propagator	25
4.3.2. <i>D</i> -Wave Propagator	25
4.4. Power-Counting Scheme	28
4.5. Higher Partial Waves	30
4.6. Electromagnetic Interactions	32
4.7. Electromagnetic Form Factors	33
4.7.1. Electric Form Factors	33
4.7.2. Magnetic Moments	39
4.8. Electromagnetic Transitions	41
4.8.1. <i>E2</i> Transitions	41
4.8.2. <i>M1</i> Transitions	45
4.9. Neutron Capture	48
4.9.1. <i>E1</i> Neutron Capture	49
4.9.2. <i>M1</i> Neutron Capture	53
4.10. Results for Carbon-15 and Carbon-17	57
4.10.1. <i>S</i> -Wave Charge Radius	58
4.10.2. <i>D</i> -Wave <i>E2</i> Transition and Form Factors	59
4.10.3. Neutron Capture	65
4.11. Conclusion	68
5. Pion Photoproduction	71
5.1. Pion Photoproduction at Threshold	71
5.2. Neutral and Charged Pion Photoproduction	73
5.3. Density Matrix Approach	75
5.4. Plane Wave to Harmonic-Oscillator Basis Transformation	77

5.5. One-Nucleon Results	80
5.5.1. Magnetic Moment Benchmark	80
5.5.2. One-Nucleon Contribution to the Neutral Pion Photoproduction	82
5.5.3. Charged Pion Photoproduction	86
5.6. Two-Nucleon Results	87
5.6.1. Intrinsic Kinetic Energy Benchmark	88
5.6.2. Two-Nucleon Contribution to the Neutral Pion Photoproduction	89
5.7. Results of the Neutral Pion Photoproduction at Threshold	95
5.8. Conclusion	96
6. Conclusion and Outlook	99
A. Halo EFT Calculations	101
A.1. Self Energy of the D -Wave Propagator	101
A.2. Minimal Substitution in the D -Wave Interaction	102
A.3. $B(E2)$ Transition from the S -to- D -Wave State	104
A.3.1. First Loop Diagram	104
A.3.2. Second Loop Diagram	107
A.3.3. A_0 Diagram	108
A.4. Electric Form Factors	110
A.4.1. Direct Photon Coupling	110
A.4.2. Loop Diagram	111
B. P-Wave State in Beryllium-11	115
Bibliography	121

1 Introduction

A major standing goal in nuclear theory is the fundamental description of static properties and nuclear reactions of nuclei all over the nuclear chart. This bears the challenge that the strong interaction, described by Quantum Chromodynamics (QCD), is non-perturbative at low energies. This energy regime, however, is relevant for the description of the interaction between two or more nucleons inside the nucleus [4]. To overcome this problem, one applies chiral effective field theory (χ EFT), which establishes a direct connection to QCD and leads to a systematic description of the nuclear force in chiral perturbation theory (ChPT). In ChPT, the relevant degrees of freedom are pions and nucleons instead of quarks and gluons as in QCD.

In principle, the derived interactions can be employed in *ab initio* methods that solve the nuclear many-body problem, e.g., the no-core shell model [5], coupled cluster theory [6] or in-medium similarity renormalization group [7]. However, the *ab initio* methods have difficulties in describing exotic nuclei such as halo nuclei since they are limited by the computational complexity of the nuclear many-body problem. These exotic nuclei are important for the understanding of nuclear structure and demonstrate the occurrence of new degrees of freedom away from the valley of stability [8, 9].

The emergence of halo states near the drip lines was first observed by *Tanihata et al.* [10, 11], who measured the nuclear radii of neutron-rich nuclei in the light *p*-shell region and found for ^{11}Li and ^6He a remarkably large value. *Hansen and Jonson* [12] related the large matter radius of ^{11}Li to the small two-neutron separation energy of about 378 keV [13] and concluded that ^{11}Li is surrounded by a two-neutron halo which extends to several times the nuclear radius. The halo structure can be explained by quantum mechanics since the weakly-bound halo nucleons can tunnel out of the effective potential of the core to the classically forbidden region. The deuteron is the lightest neutron halo nucleus [14], consisting of one halo neutron and a proton core, with a binding energy of about 2.22 MeV [15]. Similarly, neutron halo structures occur in heavier neutron-rich nuclei near the drip line such as ^{11}Be or ^{19}C [9]. Because of the Coulomb barrier, which confines the protons to a small region around the core, neutron halos are more common than proton halo nuclei near the proton drip line such as ^8B or ^{17}Ne [9].

In this thesis, two different topics are investigated: the electromagnetic properties of one-neutron halo nuclei and the threshold neutral pion photoproduction off light nuclei. For the description of one-neutron halo nuclei, we apply the Halo effective field theory (Halo EFT), which is motivated by the new degrees of freedom, the tightly bound core and the weakly-bound halo neutron, close to the neutron drip line [16, 17]. In Halo EFT, the separation of scales between the small neutron separation energy of the halo nucleus and the large excitation energy of the core nucleus is exploited to derive a systematic expansion of low-energy observables in powers of the small over the large energy scale. Thus, predictions made in Halo EFT can be improved systematically through the calculation of additional orders in the low-energy expansion. In this energy regime, the long-range part of the nucleon-nucleon force from χ EFT due to one-pion exchange cannot be resolved so that pions are no longer explicit degrees of freedom in Halo EFT. The interaction between the core and halo neutron is parametrized by contact

interactions tuned to reproduce a few low-energy observables. Halo EFT can be regarded as a complementary approach to *ab initio* methods. It provides insights into universal correlations of such shallowly bound systems while it also requires experimental or theoretical input for numerical predictions.

In recent decades, meson photoproduction off nuclei has been used as a probe for gaining further insights into nuclear structure and for studying the strong interaction in the non-perturbative low-energy regime in order to test ChPT. On the experimental side, the photoproduction of mesons almost completely replaced meson induced reactions such as pion elastic scattering due to the large progress in the measurement of cross sections of electromagnetically induced reactions [18]. The pion production off light nuclei was experimentally investigated, e.g. at Saskatoon [19, 20] for ${}^2\text{H}$, ${}^4\text{He}$ and ${}^{12}\text{C}$ and at MAMI [21, 22] for ${}^7\text{Li}$ and H, respectively. On the theoretical side, the study of photon- and pion-nucleon interactions to quantitatively test ChPT has a long history in hadron physics [23–25]. The threshold neutral pion photoproduction off light nuclei is motivated by the work of *Lenkewitz et al.* [26]. They computed the *S*-wave pion production amplitude at threshold for ${}^3\text{He}$ and demonstrated that ${}^3\text{He}$ can be assumed to be a neutron-like target. Hence, ${}^3\text{He}$ can be used to check the counterintuitive ChPT prediction that the threshold neutral pion photoproduction amplitude off the neutron is larger in magnitude than the amplitude off the proton [23, 27]. In nuclear physics, the *ab initio* approaches aim for the theoretical calculation of nuclear structure observables based on chiral effective field theory. The nuclear wave functions obtained from ChPT by *ab initio* methods such as the no-core shell model give good results of the energy spectrum as well as spectroscopic observables of light nuclei [28, 29]. Therefore, the computation of the pion photoproduction within the framework of ChPT represents a further tool to get insights into nuclear structure and to study ChPT in nuclear physics. Moreover, it can be regarded as an additional test of the nuclear wave functions.

The goal of this work is to extend the neutral pion photoproduction to a broad range of light nuclei. The relevant degrees of freedom are pions and nucleons and thus, we employ ChPT for the derivation of the relevant Feynman diagrams. The expectation value of the pion production operators from ChPT is calculated applying nuclear wave functions from the no-core shell model (NCSM). These wave functions are provided by the group of *Robert Roth*¹. Since the ChPT operators are represented in the plane wave basis and the wave functions from the NCSM are in harmonic-oscillator representation, a basis transformation between these two representations is required. For the explicit evaluation of the pion production amplitudes, we apply a density matrix approach. This allows us to calculate the pion production operator only once and then trace it with the appropriate density matrix to obtain the pion production amplitude for arbitrary nuclei.

This thesis is organized as follows: We start with a general discussion of the basic concepts of effective field theories in Chapter 2. In particular, we introduce the chiral effective field theory and the Halo EFT, which are relevant for this thesis. The NCSM is utilized especially in the pion production but also in the Halo EFT sector and thus, its basic idea is explained in Chapter 3.

In Chapter 4, we extend the Halo EFT approach to shallow *D*-wave bound states and develop a power-counting scheme for arbitrary partial wave bound states. Furthermore, we present our results for electromagnetic form factors, electromagnetic transitions as well as neutron capture reactions and apply them to the two carbon isotopes ${}^{15}\text{C}$ and ${}^{17}\text{C}$. That way, we derive universal correlations between electric

¹ TU Darmstadt, Institut für Kernphysik

observables and predict electromagnetic properties of both carbon isotopes numerically. Eventually, we discuss universality of higher partial wave bound states.

The neutral pion photoproduction at threshold is presented in Chapter 5. We explain the derivation of the relevant Feynman diagrams and outline the density matrix approach for the evaluation of pion production amplitudes. After the proof of principle calculation of the magnetic moment and the intrinsic kinetic energy, the one-nucleon and two-nucleon contributions to the pion production amplitude are computed. Finally, we compare our results with the literature and experimental data.

In the appendix, we present the explicit evaluation of selected Feynman diagrams in the Halo EFT sector. In App. A, the self energy of the D -wave propagator is derived and the Feynman rules for the inclusion of photons via minimal substitution are deduced. Moreover, we calculate the relevant Feynman diagrams that contribute to the $B(E2)$ transition from the S -to- D -wave state and to the electric form factors of the D -wave. The incorporation of P -waves in the Halo EFT approach is explicitly addressed with the example of ^{11}Be in App. B.



2 Effective Field Theories

Physical phenomena in nature take place at different length or energy scales. To be able to describe these phenomena for a certain energy range, it is convenient to apply effective field theories (EFT) [30–34]. In other words: An EFT is a low-energy approximation to some underlying, more fundamental theory that is only valid in a specific energy range.

A crucial requirement is a separation of scales in our physical description so that we are able to focus on the appropriate degrees of freedom in our EFT. Consider, for example, the Newtonian mechanics. If the relevant velocities are small compared to the speed of light, the inclusion of relativity is not required, which simplifies our calculations. Nevertheless, if we used the full theory and included relativity, we would derive the same result with very small corrections. This means our EFT is only valid in a specific regime and breaks down if we are in the range of or even beyond the high energy scale.

We want to explain the concept in more detail with the example of Fermi's theory of beta decay [32, 33]. In the standard model, the beta decay is described by the exchange of a W boson. For energies or momenta q that are much smaller compared to the mass of the exchange boson $M_W \approx 80$ GeV, we can describe the interaction by a local contact interaction with an unknown low-energy constant (LEC) G_f that has to be matched to data instead of an exchange of a virtual W boson. Hence, the massive bosons are integrated out in our EFT and the boson propagator can be replaced at leading order (LO) by

$$\frac{1}{q^2 - M_W^2} \rightarrow -\frac{1}{M_W^2} \sim G_f . \quad (2.1)$$

Accordingly, the relevant degrees of freedom differ from those of the underlying theory since the heavy bosons are excluded. The small scale is the momentum q and the break-down scale of this theory is the boson mass M_W .

To derive a more accurate approximation to the standard model, we have to expand the boson propagator in powers of q^2/M_W^2 . In principle, we get infinitely many terms with infinitely many unknown LECs, which means that our EFT is non-renormalizable. However, we restrict ourselves to a finite accuracy and stop at a certain order in our expansion. Accordingly, we only have a finite number of terms and LECs that have to be matched. This shows the systematic characteristic of an EFT. By writing down the most general Lagrangian consistent with the assumed symmetries of the underlying theory, we ensure that the observables calculated with this Lagrangian are related to those of the underlying theory [35].

In this thesis, we aim for the theoretical description of electromagnetic properties and nuclear reactions in light nuclei. Depending on the considered system, we apply two different effective field theories with distinct degrees of freedom. We first discuss the commonly used chiral effective field theory, which we will employ later in the derivation of the relevant Feynman diagrams for the pion photoproduction at threshold. In this effective theory, the relevant degrees of freedom are pions and nucleons.

Second, we elaborate the Halo effective field theory (Halo EFT) approach, which exploits the separation of scales between a tightly bound core and a shallowly bound halo nucleon. In Halo EFT, the pions are integrated out and the relevant degrees of freedom are the core and the halo nucleons.

2.1 Chiral Effective Field Theory

Chiral effective field theory (χ EFT) has proven to be a very useful tool in the derivation of the nuclear force in the low-energy regime [4, 36]. By exploiting the symmetries in Quantum Chromodynamics (QCD), especially the chiral symmetry, χ EFT establishes a direct connection to the underlying theory of nuclear interactions. A major requirement for the development of an EFT is the separation of scales. In χ EFT, this separation of scales is given by the large gap in the hadron spectrum between the pion mass $m_\pi \approx 140$ MeV and the rho mass $m_\rho \approx 770$ MeV. The pion mass sets the soft scale and the break-down scale (Λ_χ) is given by the rho mass. Hence, the soft scale can be expanded over the break-down scale to obtain a systematic description of the nuclear force with pions and nucleons as relevant degrees of freedom.

2.1.1 Chiral Symmetry

The separation of scales is a consequence of the chiral symmetry breaking in QCD [4, 33, 36]. QCD is a non-abelian $SU(3)_{\text{color}}$ gauge theory with six flavors of quarks, three of them being light (u, d, s) and the other three heavy (c, b, t). The Lagrangian of QCD including the light quarks is written as

$$\mathcal{L}_{\text{QCD}} = \sum_f \bar{q}_f i\gamma^\mu D_\mu q_f - \frac{1}{2} \text{Tr} G_{\mu\nu} G^{\mu\nu} - \bar{q}_f m_f q_f = \mathcal{L}_{\text{QCD}}^0 - \sum_f \bar{q}_f m_f q_f, \quad (2.2)$$

where q_f denotes the quark Dirac fields of the light quark flavors (u,d,s) with masses [37]

$$m_u = 2.15(15) \text{ MeV}, \quad m_d = 4.70(20) \text{ MeV}, \quad m_s = 93.5(2) \text{ MeV}. \quad (2.3)$$

In the Lagrangian above, the gluons are introduced by eight gauge potentials $A_{\mu,a}$, which denote the gluon fields and preserve the invariance of the Lagrangian under local transformations

$$A_\mu = \sum_{a=1}^8 \frac{\lambda_a}{2} A_{\mu,a}, \quad (2.4)$$

with the Gell-Mann-matrices λ_a . The gauge-covariant derivative is given by $D_\mu = \partial_\mu + igA_\mu$, where g is the quark-gluon coupling constant and the gluon field strength tensor is $G_{\mu\nu} = \partial_\mu A_\nu - \partial_\nu A_\mu + ig[A_\mu, A_\nu]$.

Restricting ourselves to the two lightest quarks (u, d), we can discuss the QCD Lagrangian (2.2) in the limit of vanishing quark masses where only $\mathcal{L}_{\text{QCD}}^0$ contributes. In the case of massless quarks, $\mathcal{L}_{\text{QCD}}^0$

is invariant under separate unitary global transformations of the left- and right-hand quark fields, the so-called chiral rotations, $q_I \rightarrow U_I q_I$ and $I \in L, R$, with

$$U_I = \exp\left(-i\Theta_i^I \frac{\tau_i}{2}\right), \quad (2.5)$$

and the usual Pauli isospin matrices τ_i . By applying Noether's Theorem, this yields six conserved currents, three right-handed and three left-handed currents

$$R_i^\mu = \bar{q}_R \gamma^\mu \frac{\tau_i}{2} q_R, \quad L_i^\mu = \bar{q}_L \gamma^\mu \frac{\tau_i}{2} q_L, \quad (2.6)$$

with $\partial_\mu R_i^\mu = \partial_\mu L_i^\mu = 0$.

This implies that the right- and left-handed components of massless quarks do not mix. Using group theory, this can be expressed as $SU(2)_R \times SU(2)_L$ symmetry, which is also referred to as chiral symmetry. The chiral symmetry of the Lagrangian of QCD is spontaneously broken down to its vector subgroup $SU(2)_{V=L+R}$ in the ground state of the system. Evidence of the spontaneous breakdown of the chiral symmetry comes from the hadron spectrum. The isospin symmetry is well observed in experimental data, e.g., the masses of protons and neutrons are approximately equal. However, two hadrons with the same mass but different parity do not appear in the hadron spectrum.

Due to the spontaneously broken symmetry, there exist three massless Goldstone bosons, the pions, which interact weakly at low energies. Since the quarks are not massless, the mass term in Eq. (2.2) breaks the symmetry explicitly and therefore, the pions are not massless either. Furthermore, the isospin symmetry is not exact because $m_u \neq m_d$.

2.1.2 Chiral Perturbation Theory

For the derivation of the nuclear interaction using χ EFT, the most general Lagrangian including the symmetries of QCD is constructed and nucleons are included in our theory [4, 36, 38–40]. The relevant degrees of freedom are pions and nucleons and an expansion can be done in terms of $(Q/\Lambda_\chi)^\nu$, where $Q \approx m_\pi$ is the momentum, $\Lambda_\chi \approx m_\rho$ the break-down scale, and ν the power [41]. Thus, a systematic description of the nuclear force can be obtained considering only the most important contributions of the infinitely many terms of our Lagrangian up to a specific order ν .

In principle, our effective Lagrangian consists of three different parts: pion-pion dynamics, nucleon-pion interactions and nucleon contact terms

$$\mathcal{L}_{\text{eff}} = \mathcal{L}_{\pi\pi} + \mathcal{L}_{\pi N} + \mathcal{L}_{NN} + \dots, \quad (2.7)$$

where the ellipsis stands for terms that involve two nucleons plus pions and three or more nucleons with or without pions. The three different parts can be expanded in powers of derivatives or pion mass insertions that are denoted by the superscripts in the following

$$\mathcal{L}_{\pi\pi} = \mathcal{L}_{\pi\pi}^{(2)} + \mathcal{L}_{\pi\pi}^{(4)} + \mathcal{L}_{\pi\pi}^{(6)} + \dots, \quad (2.8)$$

$$\mathcal{L}_{\pi N} = \mathcal{L}_{\pi N}^{(1)} + \mathcal{L}_{\pi N}^{(2)} + \mathcal{L}_{\pi N}^{(3)} + \dots, \quad (2.9)$$

$$\mathcal{L}_{NN} = \mathcal{L}_{NN}^{(0)} + \mathcal{L}_{NN}^{(2)} + \mathcal{L}_{NN}^{(4)} + \dots, \quad (2.10)$$

where nucleon contact interactions come only in even powers of derivatives due to parity. Since Goldstone bosons can interact only when they carry momentum, only even powers of $\mathcal{L}_{\pi\pi}$ are allowed because of Lorentz invariance.

The nucleon-pion interactions describe the long- and medium-range potential of the nuclear force. The short-range potential is parametrized by contact terms. Such contact terms are needed to renormalize loop integrals and to obtain results that are reasonably independent of regulators. Moreover, they imitate the high-energy states that are integrated out and contain low-energy constants to parametrize the unresolved short-range dynamics. The LECs are obtained by low-energy fits to experimental data.

Treating the baryons relativistically leads to the problem that the time derivative of a relativistic hadron field generates a factor $E \approx m_N$, which is about the same size as our χ EFT breaking scale Λ_χ . This can be solved by considering the baryons as heavy static sources [42], the so-called heavy baryon formalism, such that only the baryon momenta which are small relative to their rest mass are relevant. The expansion is then carried out in terms of these small momenta over the large baryon mass. A more detailed description of this approach can be found in Ref. [36].

As pointed out before, we can construct infinitely many diagrams involving nucleons and pions from our effective Lagrangian (2.7). To be able to analyze the diagrams in terms of powers of $(Q/\Lambda_\chi)^v$ and such to sort them order by order, we need to establish a power-counting scheme. By applying dimensional analysis, we obtain Q^{-1} for a nucleon propagator, Q^{-2} for a pion propagator, Q for each derivative in any interaction, and Q^4 for each four-momentum loop integration. Combined with some topological identities, Weinberg derived a power-counting scheme for arbitrary diagrams [41, 43]. This yields for a given connected irreducible diagram [4]

$$\nu = -4 + 2N + 2L + \sum_i V_i \Delta_i \quad \text{and} \quad \Delta_i = d_i + \frac{n_i}{2} - 2, \quad (2.11)$$

where N denotes the number of nucleons, L the number of pion loops, n_i is the number of nucleon field operators at the vertex V_i of type i and d_i the number of derivatives and/or insertions of m_π . We refer to Refs. [4, 36, 40] for more details.

Analyzing the different terms of the Lagrangian with the power-counting scheme in (2.11) leads to a hierarchy of nuclear forces in chiral perturbation theory (ChPT), which is shown in Fig. 2.1. The two-nucleon interactions are present at leading order (LO) and

$$\nu = -4 + 2 \times 2 + 2 \times 0 + 0 = 0, \quad (2.12)$$

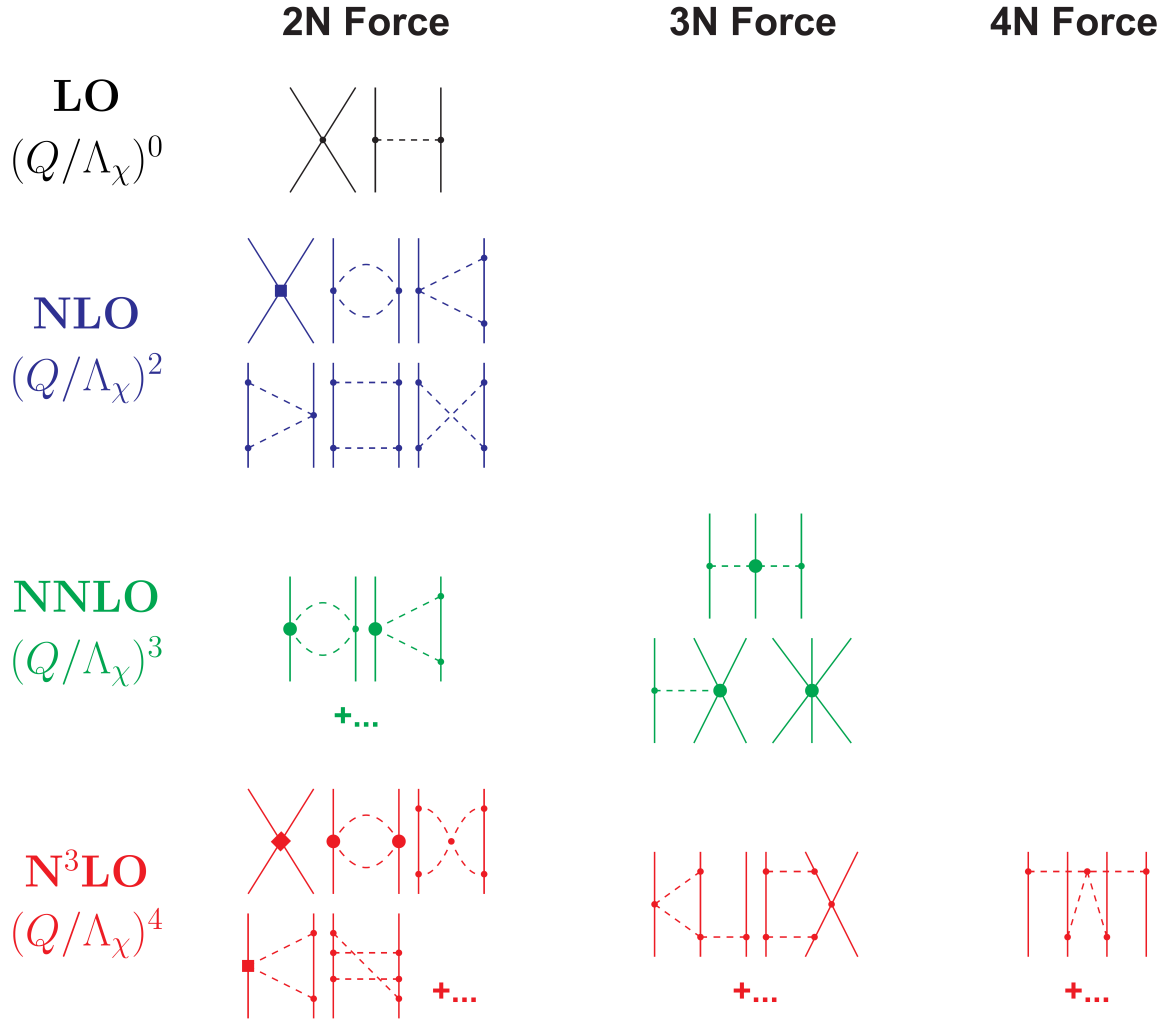


Figure 2.1.: Hierarchy of nuclear forces in ChPT from Ref. [36]. Solid lines denote nucleons and dashed lines pions. Small dots, large solid dots, solid squares, and solid diamonds represent different vertices.

where only vertices with $\Delta_i = 0$ contribute. At LO, the only contributions are from tree level diagrams, cf. Fig. 2.1. They can be constructed from the LO Lagrangian, which has the following form in the heavy-baryon formalism [4]

$$\mathcal{L}_{\pi\pi}^{(0)} = \frac{F_\pi^2}{4} \text{Tr} \left[\partial_\mu U \partial^\mu U^\dagger + 2B(\mathcal{M}U^\dagger + \mathcal{M}^\dagger U) \right], \quad (2.13)$$

$$\mathcal{L}_{\pi N}^{(0)} = \bar{N} (i v \cdot D + g_A u \cdot S) N, \quad (2.14)$$

$$\mathcal{L}_{NN}^{(0)} = -\frac{1}{2} C_S (\bar{N} N)(\bar{N} N) + 2C_T (\bar{N} S N) \cdot (\bar{N} S N), \quad (2.15)$$

where N , v_μ and $S_\mu \equiv (1/2)i\gamma_5\sigma_{\mu\nu}v^\nu$ denote the large component of the nucleon field, the nucleon four-velocity and the covariant spin vector, respectively. Moreover, Tr denotes the trace in flavor space,

while F_π and g_A refer to the chiral-limit values of the pion decay and the nucleon axial vector coupling constants. The unitary 2×2 matrix $U(\boldsymbol{\pi}) = u^2(\boldsymbol{\pi})$ in the flavor space collects the pion fields

$$U = \exp\left(i \frac{\boldsymbol{\pi} \cdot \boldsymbol{\tau}}{F_\pi}\right), \quad (2.16)$$

which can be expanded in numbers of pion fields and τ_i being the isospin Pauli matrices. The constant B is related to the value of the scalar quark condensate in the chiral limit, $\langle 0 | \bar{u}u | 0 \rangle = -F^2 B$, and connects the pion mass m_π to the quark mass m_q via $m_\pi = 2Bm_q + \mathcal{O}(m_q^2)$. Furthermore, $\mathcal{M} = \text{diag}(m_u, m_d)$ contains the quark masses due to the explicit chiral symmetry breaking. The covariant derivatives of the nucleon and pion fields are defined by

$$D_\mu = \partial_\mu + \frac{[u^\dagger, \partial_\mu u]}{2} \quad \text{and} \quad u_\mu = i(u^\dagger \partial_\mu u - u \partial_\mu u^\dagger). \quad (2.17)$$

The LO NN Lagrangian has no derivatives and C_S and C_T are unknown LECs, which are determined by a fit to the NN data.

From this effective Lagrangian at LO it follows that the only possible connected two-nucleon diagrams are the one-pion exchange and the contact tree diagram as depicted in Fig. 2.1. They yield the following two-nucleon potential in the center-of-mass system (CMS) [4]

$$V_{2N}^{(0)} = -\frac{g_A^2}{4F_\pi^2} \frac{\boldsymbol{\sigma}_1 \cdot \mathbf{q} \boldsymbol{\sigma}_2 \cdot \mathbf{q}}{q^2 + m_\pi^2} \boldsymbol{\tau}_1 \cdot \boldsymbol{\tau}_2 + C_S + C_T \boldsymbol{\sigma}_1 \cdot \boldsymbol{\sigma}_2, \quad (2.18)$$

where σ_i denote the Pauli spin matrices and $\mathbf{q} = \mathbf{p}' - \mathbf{p}$ is the nucleon momentum transfer of the initial (\mathbf{p}) and final nucleon momenta (\mathbf{p}') in the CMS. Furthermore, $F_\pi = 92.4$ MeV and $g_A = 1.267$ denote the pion decay and the nucleon axial coupling constants, respectively.

Taking a closer look at Fig. 2.1, we find that two-nucleon forces show up at LO, whereas the three-nucleon interactions which contribute to the nuclear interaction emerge first at next-to-next-to leading order (N²LO) and $\nu = 3$, four-nucleon forces at (N³LO) and $\nu = 4$, et cetera. This indicates that two-nucleon forces are more important than three-nucleon forces and explains the dominance of two-nucleon interactions observed in nuclear physics.

To calculate phase shifts and NN observables, we need to insert the nuclear potentials from χ EFT in the Lippmann-Schwinger equation to obtain the T -matrix. As described above, ChPT is a low-momentum expansion for $Q \ll \Lambda_\chi$. Therefore, the potentials require a cutoff $\Lambda \approx 0.5$ GeV regularization to exclude high momenta. This is realized by multiplying the derived potentials with a regulator function [36, 44]

$$f(p', p) = \exp\left[-\left(\frac{p}{\Lambda}\right)^{2n} - \left(\frac{p'}{\Lambda}\right)^{2n}\right], \quad (2.19)$$

where p and p' denote the magnitudes of the initial and final nucleon momenta in the CMS and the exponent $2n$ is chosen sufficiently large such that only the desired orders of ν are affected. Since the

results of the T -matrix can depend sensitively on the choice of the cutoff, we need the contact terms to account for the excluded high-momentum effects and to remove systematically the dependence of the cutoff or in other words, to renormalize our EFT.

2.2 Halo Effective Field Theory

In the previous sections, we have discussed the nuclear interaction derived from χ EFT, where the considered momenta are comparable to the pion mass. We now consider momenta that are even smaller than the pion mass $Q \ll m_\pi$. In this energy regime, even the longest-ranged part of the NN force, due to the one-pion exchange, appears short-ranged and dynamical pions are integrated out in this pionless EFT [32, 34, 45]. Since the explicit pion exchange cannot be resolved, the only degrees of freedom are nucleons and only local contact interactions between nucleons remain. These contact interactions account not only for the unresolved pion exchange but also for the unresolved short-distance physics for which they already exist in χ EFT.

First, we outline the pionless EFT approach for the two-nucleon system and then extend it to halo nuclei and discuss its implications.

2.2.1 Pionless Effective Field Theories

In this section, we introduce the Lagrangian for a two-nucleon S -wave system, calculate the scattering amplitude and match the unknown LECs to the effective range expansion (ERE). The LO Lagrangian for such a two-nucleon S -wave system is written as [34, 45]

$$\mathcal{L} = N^\dagger \left(i\partial_0 + \frac{\nabla^2}{2M_N} + \dots \right) N - C_{0,s} (N^T \hat{P}_s N)^\dagger (N^T \hat{P}_s N) - C_{0,t} (N^T \hat{P}_t N)^\dagger (N^T \hat{P}_t N) + \dots, \quad (2.20)$$

where N denotes the nucleon field, the ellipses stand for terms with higher number of derivatives that contribute at higher orders and the projectors of the 1S_0 and 3S_1 NN channels are given by

$$(\hat{P}_s)^\lambda = \frac{1}{\sqrt{8}} \sigma_2 \tau_2 \tau^\lambda \quad \text{and} \quad (\hat{P}_t)^i = \frac{1}{\sqrt{8}} \sigma_2 \sigma^i \tau_2, \quad (2.21)$$

respectively. The Pauli matrices for the spin space are denoted by σ and for the isospin space by τ . The unknown coupling constants $C_{0,s}$ and $C_{0,t}$ also refer to the 1S_0 and 3S_1 NN channels, respectively. The first term in Eq. (2.20) denotes the kinetic part of the Lagrangian. Since the nucleon momenta in our EFT are smaller than the pion mass and therefore, much smaller than their rest mass M_N , the nucleons are treated non-relativistically.

The nucleon-nucleon scattering amplitude reads

$$T(k) = \frac{4\pi}{M_N} \frac{1}{k \cot \delta_0(k) - ik}, \quad (2.22)$$

$$= \frac{4\pi}{M_N} \frac{1}{-\frac{1}{a_0} + \frac{r_0}{2}k^2 + \dots - ik}, \quad (2.23)$$

with the S -wave phase shift δ_0 . In the second step of the equation above, $k \cot \delta_0(k)$ is replaced by the effective range expansion for small k with corresponding ERE parameters a_0 , r_0 , and the ellipsis indicates further ERE parameters with higher powers of k [46].

The relevant diagrams which are generated by the Lagrangian in Eq. (2.20) and contributing to the NN scattering amplitude are shown in Fig. 2.2.

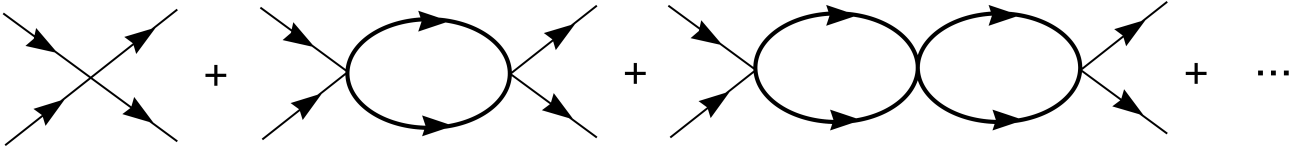


Figure 2.2.: Feynman diagrams contributing to the NN scattering amplitude. Figure taken from Ref. [45].

Every additional loop adds one extra loop integration, two additional nucleon propagators, and one further C_0 vertex. Hence, each NN bubble contains a linearly divergent part. By resumming all bubble diagrams and using dimensional regularization, i.e. the power divergence subtraction (PDS) [47, 48] with scale μ , we derive for the scattering amplitude [32]

$$T(k) = -\frac{4\pi}{M_N} \frac{1}{\frac{4\pi}{M_N C_0} + \mu + ik}. \quad (2.24)$$

After matching the equation above to the amplitude of the ERE in Eq. (2.23), we deduce

$$\frac{1}{a} = \frac{4\pi}{M_N C_0} + \mu. \quad (2.25)$$

We will give a more detailed description of the regularization and renormalization procedure of such a shallowly bound two-body system in Sec. 4.3, where we discuss one-neutron halo nuclei.

As a first application, the deuteron is such a shallowly bound two-nucleon system. It consists of a neutron and a proton and can be considered the lightest halo nucleus. Applying pionless EFT to the deuteron system, *Chen et al.* calculated low-energy observables such as electric and magnetic form factors as well as the neutron capture cross section [49, 50]. This demonstrates the usefulness of the pionless EFT approach.

2.2.2 Halo Nuclei

Halo nuclei are weakly-bound states of a few valence nucleons and a tightly-bound core nucleus [8, 9, 51–54]. They demonstrate the occurrence of new degrees of freedom close to the neutron and proton drip lines and away from the valley of stability. Halo nuclei were discovered at radioactive ion beam facilities [55] and are characterized by a long tail in the density distribution of the nucleus and the decoupling of the halo wave function from the core [9]. As shown in Fig. 2.3, halo nuclei can be found for various isotopes near the drip line. Because of the Coulomb barrier, neutron halos are more common than proton halos.

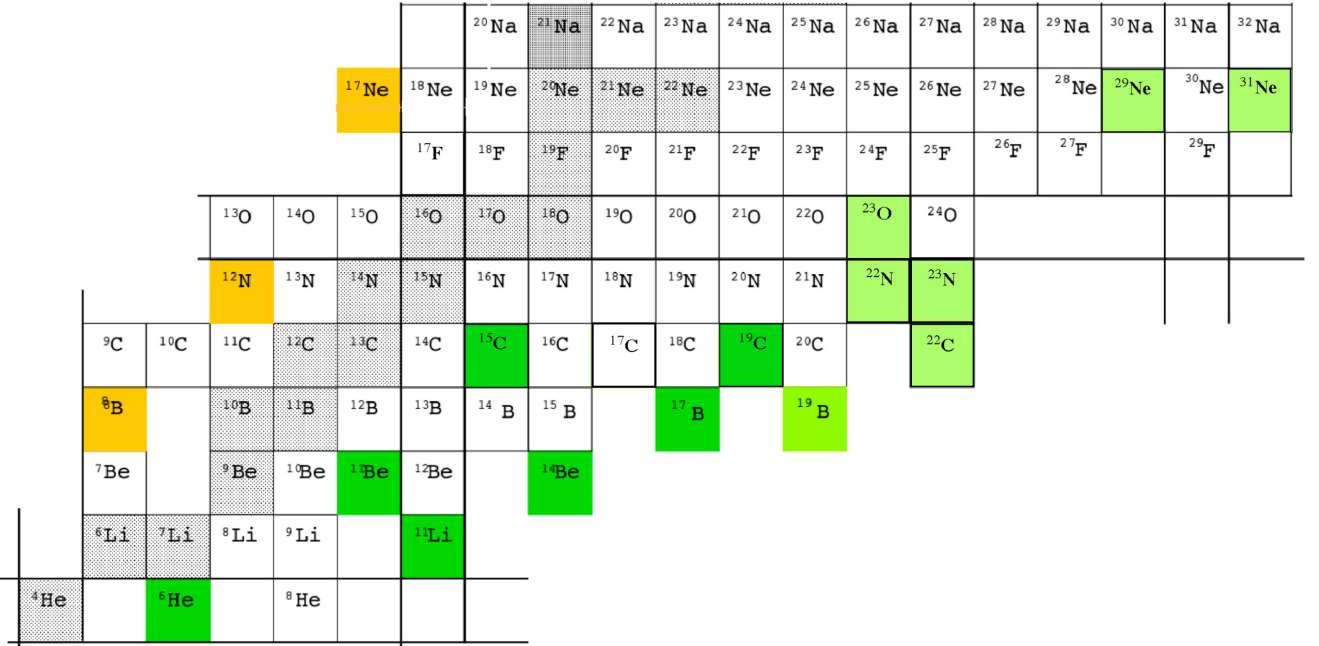


Figure 2.3.: Confirmed and suggested halo nuclei. Neutron halo nuclei are represented by green squares and candidates of neutron halos are depicted by light green. Orange squares show the proton halos. Figure taken from Ref. [9].

In this thesis, we focus on one-neutron halo nuclei and use the Halo EFT approach [14] to calculate static properties and reactions of such shallowly bound systems. As mentioned before, the deuteron can be considered as the simplest example of a halo nucleus, consisting of one halo neutron with a proton core, since its root-mean-square charge radius is about three times as large as the size of the constituent proton. A more complex one-neutron halo nucleus is ${}^{11}\text{Be}$. It has two bound states, a $J^P = 1/2^+$ *S*-wave ground state and a $1/2^-$ *P*-wave first excited state, with the one-neutron separation energies of 500 keV and 180 keV [56], respectively. Compared to that, the first excitation of the ${}^{10}\text{Be}$ core is 3.4 MeV above the ground state. Since exotic nuclei close to the drip line are difficult to describe in *ab initio* approaches, e.g., coupled cluster theory [57, 58] or the no-core shell model [5, 59], we employ the Halo EFT approach to study halo nuclei [16, 17].

Halo EFT is a systematic approach to these systems that exploits the separation of scales between the small nucleon separation energy of the halo neutron and the large excitation energy of the core nucleus. The small separation energy of the halo nucleus is directly connected to the large radius of the

system. For this reason, we can convert the energy separation into a length scale separation between the large halo radius R_{halo} and the short core radius R_{core} . Halo EFT provides a systematic expansion of low-energy observables in powers of $R_{\text{core}}/R_{\text{halo}}$. Therefore, predictions made in Halo EFT can be improved systematically through the calculation of additional orders in the low-energy expansion. Since the core and the halo neutron are the relevant degrees of freedom, Halo EFT is an extension of pionless EFT for few-nucleon systems. The strong interaction between the core and the valence nucleons is parametrized by contact interactions tuned to reproduce a few low-energy observables.

To adapt the Lagrangian in Eq. (2.20) to the two-body halo system, we introduce independent field operators for the halo neutron (n) and the core (c)

$$\mathcal{L} = c^\dagger \left(i\partial_t + \frac{\nabla^2}{2M} \right) c + n^\dagger \left(i\partial_t + \frac{\nabla^2}{2m} \right) n, \quad (2.26)$$

where M , m denotes the mass of the core and the neutron, respectively. Furthermore, we employ an auxiliary dimer field for the nc system to include the strong interaction in the Lagrangian. We demonstrate this for a dimer field (σ), where the halo neutron is in an S -wave relative to the core

$$\mathcal{L}_{nc} = \sigma^\dagger \left[\eta_0 \left(i\partial_t + \frac{\nabla^2}{2M_{nc}} \right) + \Delta_0 \right] \sigma - g_0 \left([nc]_{s,\beta}^\dagger \sigma_{s,\beta} + \sigma_{s,\beta}^\dagger [nc]_{s,\beta} \right), \quad (2.27)$$

with the residual mass Δ_0 of the σ field, the mass of the nc system $M_{nc} = M + m$, $\eta = \pm 1$ gives the appropriate sign to the S -wave effective range, and g_0 denotes the S -wave dimer coupling constant. The notation $[nc]_{s,\beta}$ represents the spin coupling of the core and halo neutron through Clebsch-Gordan coefficients to total spin s and appropriate projection β . As outlined in App. B for P -waves and in Sec. 4 for D -waves, higher partial wave states can be incorporated in a similar way.

The fact that the core neutrons are no active degrees of freedom means that the halo nucleons are not antisymmetrized with nucleons in the core. This is illustrated by the example of ^{11}Be in Fig. 2.4.

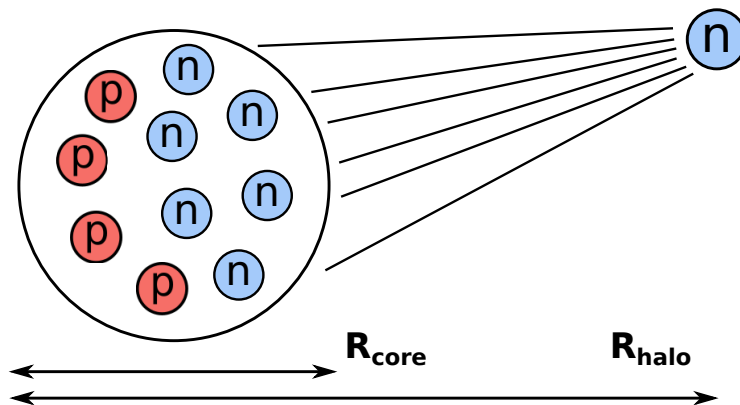


Figure 2.4. Illustration of the antisymmetrization of neutrons in the halo nucleus ^{11}Be . Figure from Ref. [14] adapted to ^{11}Be .

The hypothetical exchange of a neutron from the core with the valence neutron depends on the overlap of the wave functions of the core and the halo neutron, which is determined by R_{core} and R_{halo} , respectively.

Therefore, these effects are subsumed in low-energy constants and included perturbatively in the expansion of $R_{\text{core}}/R_{\text{halo}}$.

For proton halos with two or more charged particles, the repulsive Coulomb interaction between the core and the halo proton has to be additionally incorporated in the Halo EFT. Furthermore, the extension to two-neutron halos is straightforward [14]. Naturally, the three-body system is more complex and new universal few-body correlations such as the Efimov effect [60] emerge. Similar EFT approaches can be used for systems of atoms and nucleons at low energies [61, 62].

In order to be able to make numerical predictions, Halo EFT needs additional experimental and/or theoretical input to tune the contact interactions and additional counterterms [63]. The benefit of this approach is the reduction of the complexity of the system in terms of degrees of freedom, i.e. from an A -body to a two-body system. This reduction simplifies the search for universal correlations between observables since the separation of scales is not explicit in the parameters of the *ab initio* methods, which employ interactions from χ EFT. The structure of such correlations is universal in the sense that it is independent of the specific neutron separation energies and applies to all states with the same quantum numbers. As a consequence, Halo EFT can be considered a complementary approach to *ab initio* calculations. On the one hand, Halo EFT requires theoretical or experimental input to predict halo properties. On the other hand, the universal correlations derived from Halo EFT can be used to test *ab initio* calculations of different observables for their consistency.

In Halo EFT, electromagnetic interactions can be straightforwardly included via minimal substitution and local gauge invariant operators in the effective Lagrangian. That way, electric properties of the two S - and P -wave bound states in ^{11}Be were studied in detail in Ref. [64] using Halo EFT. The Halo EFT approach is not limited to static electromagnetic properties or electromagnetic transitions, but can be applied in the same way to calculate radiative neutron/proton capture [65–68]. Moreover, Halo EFT has been used to study various reactions and properties of halo systems. Initial studies in the strong sector have mainly focused on the universal properties of halo nuclei with S -wave [69, 70] and P -wave interactions [71, 72], including matter form factors and radii. For general reviews of Halo EFT and applications to other halo nuclei see Refs. [14, 73, 74]. In this thesis, we focus on shallowly bound D -wave states. Because of the angular momentum barrier, the probability to find a halo bound state for large relative angular momentum is decreased and thus, low relative angular momentum states occur more frequently in nature. We also find proof for that principle in our Halo EFT results in Sec. 4.5.

A more detailed discussion concerning the Halo EFT approach for one-neutron halos is presented in Sec. 4, where we explicitly derive electromagnetic observables and universal correlations for weakly-bound D -wave states.



3 No-Core Shell Model

Parts of this chapter have been taken from the author's Master's thesis [75].

Before we present our Halo EFT and pion photoproduction results, we discuss the no-core shell model as an example for an *ab initio* many-body approach to the nuclear many-body problem [5, 59]. It will be used later for the derivation of the nuclear wave function for the pion photoproduction in Chapter 5. Moreover, we consider the importance-truncated no-core shell model [76] as an extension of the no-core shell model to heavier nuclei, which will be employed to generate input data for our Halo EFT in Section 4.10.2.

Given an interaction, we aim for the solution of the nuclear many-body problem

$$\mathbf{H}|\Psi_n\rangle = E_n |\Psi_n\rangle. \quad (3.1)$$

There are several *ab initio* methods with different advantages and drawbacks to solve the Schrödinger equation, e.g., coupled cluster theory [57, 58], in-medium similarity renormalization group [7, 77] or the no-core shell model (NCSM) [5, 59]. In this chapter, we focus on the latter. The NCSM is based on the configuration interaction idea, which plays an important role in the description of quantum many-body systems in various areas of modern physics, e.g., the many-electron problem in molecular physics and quantum chemistry [78]. The common purpose of all configuration-interaction methods is the calculation of the eigenstates of the Hamiltonian for a particular model space spanned by a set of many-body states. To obtain the eigenstates, the large-scale matrix eigenvalue problem is solved numerically, where the matrix dimension is the computationally limiting factor.

The NCSM is an *ab initio* approach applicable to light nuclei [5, 59], where all A nucleons are active degrees of freedom. The model space is spanned by Slater determinants constructed from harmonic-oscillator (HO) single-particle states [59, 76]. The Hamiltonian is given in a generic form by

$$\mathbf{H}_A = \frac{1}{A} \sum_{i<j} \frac{(\mathbf{p}_i - \mathbf{p}_j)^2}{2m} + \sum_{i<j}^A \mathbf{v}_{NN,ij} + \sum_{i<j<k}^A \mathbf{v}_{NNN,ijk}, \quad (3.2)$$

and contains the intrinsic kinetic energy and two- plus three-body interactions. First, the interaction between the nucleons is derived from χ EFT. In a second step, the potentials are “softened” via the similarity renormalization group (SRG) [79] to improve the convergence in the many-body calculation [80]. This is achieved by unitary transformations that decouple high-momentum and low-momentum components.

In principle, the eigenvalue problem (3.1) has to be solved in the infinite-dimensional Hilbert space to obtain the exact energy eigenstate. Hence, the model space has to be truncated to a computationally feasible size. Therefore, only basis states with an excitation energy smaller than $N_{\max} \hbar\Omega$ are taken into account, where N_{\max} defines the HO excitation quanta of the many-body state. By increasing the model space size via $N_{\max} \hbar\Omega$ sufficiently, the results for the energy eigenvalues converge to the exact energies.

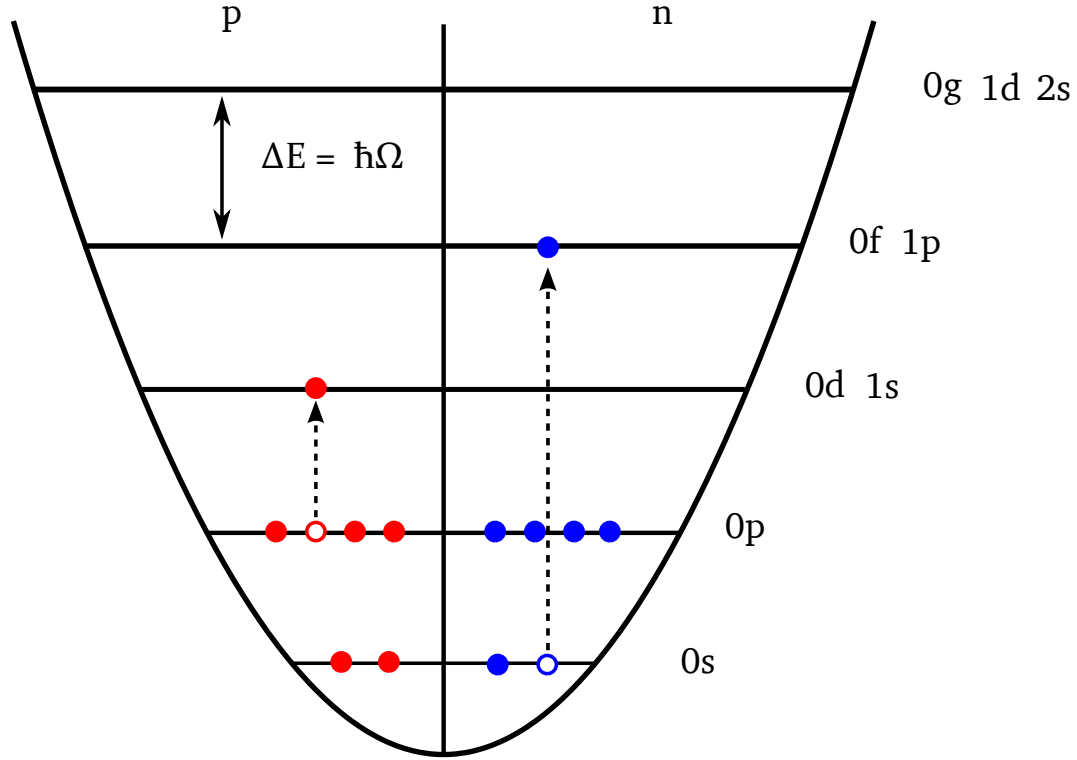


Figure 3.1.: NCSM single-particle orbits in the harmonic-oscillator potential for protons (red) and neutrons (blue). Horizontal lines indicate harmonic-oscillator shells. The energy difference between two shells is $\hbar\Omega$. In this example for ^{12}C , the total excitation energy is $4\hbar\Omega$.

The general concept of this truncation scheme is illustrated for ^{12}C in Fig. 3.1. The $A = 12$ nucleons are distributed over the different shells of the proton and neutron HO potential according to their particle species. The unperturbed Slater determinant is given by the configuration with the lowest possible HO energy. In this case, the protons and neutrons completely fill the 0s- and 0p-shell for the unperturbed ground state. Every excitation of one or multiple nucleons from this state into a higher shell yields an excitation energy of $N\hbar\Omega$, where $N = \sum_{i=1}^A (2n_i + l_i) - N_{\text{unperturbed}}$. In Fig. 3.1, a proton is excited by $1\hbar\Omega$ from the 0p-shell to the 0d, 1s-shell and a neutron is excited by $3\hbar\Omega$ from the 0s-shell into the 0f, 1p-shell. Thus, the total excitation energy is $4\hbar\Omega$. Since all Slater determinants up to an excitation energy of $N_{\text{max}}\hbar\Omega$ are included in the model space, this Slater determinant is included if $N_{\text{max}} \geq 4$.

The dimension of the model space grows factorially with N_{max} and particle number A . However, the model-space size has to be manageable for the diagonalization of the Hamilton matrix. Thus, the NCSM cannot reach convergence for heavier nuclei and works properly only up to p-shell nuclei.

3.1 Importance-Truncation Scheme

To overcome the dimensional problems arising in the NCSM, an importance-truncation (IT) scheme can be applied [76]. In general, we are only interested in a few energy eigenstates, e.g., the ground state and the first few excited states. To reduce the model-space dimension, only the most relevant basis states for the description of the target eigenstates, with respect to an *a priori* importance measure, are taken into account. Accordingly, the Hamiltonian is diagonalized in this reduced model space.

Originally, this importance-truncation concept was invented in quantum chemistry in the 1970s [81], but it is adaptable to arbitrary configuration interaction approaches. In the following, the concept of the importance-truncation scheme for the NCSM is explained in more detail.

An essential ingredient of the IT scheme is the definition of an *a priori* importance measure for the individual basis states. In this framework, the importance measure is derived from many-body perturbation theory. We start with a reference state $|\Psi_{\text{ref}}\rangle$ from a previous calculation. This reference state

$$|\Psi_{\text{ref}}\rangle = \sum_{\mu \in \mathcal{M}_{\text{ref}}} C_{\mu}^{(\text{ref})} |\Phi_{\mu}\rangle, \quad (3.3)$$

is a zeroth-order approximation for the description of the target eigenstate, where \mathcal{M}_{ref} is a subspace of the full model space spanned by the basis states $|\Phi_{\mu}\rangle$ and $C_{\mu}^{(\text{ref})}$ represents the amplitudes of the basis states for the target eigenstate, e.g., the ground state. In order to derive the importance measure, the full Hamiltonian $\mathbf{H} = \mathbf{H}_0 + \mathbf{W}$ is decomposed into an unperturbed part \mathbf{H}_0 and a perturbation \mathbf{W} with respect to $|\Psi_{\text{ref}}\rangle$

$$\mathbf{H}_0 |\Psi_{\text{ref}}\rangle = \epsilon_{\text{ref}} |\Psi_{\text{ref}}\rangle \quad \text{with} \quad \epsilon_{\text{ref}} = \langle \Psi_{\text{ref}} | \mathbf{H} | \Psi_{\text{ref}} \rangle. \quad (3.4)$$

The unperturbed Hamiltonian that satisfies the eigenvalue relation is defined as

$$\mathbf{H}_0 = \epsilon_{\text{ref}} |\Psi_{\text{ref}}\rangle \langle \Psi_{\text{ref}}| + \sum_{\nu \notin \mathcal{M}_{\text{ref}}} \epsilon_{\nu} |\Phi_{\nu}\rangle \langle \Phi_{\nu}|, \quad (3.5)$$

where ϵ_{ν} denotes the unperturbed energy for basis states outside of the reference space \mathcal{M}_{ref} .

There are different choices of the unperturbed energies and of the partitioning of the Hamiltonian. We employ the simplest Møller-Plesset-type formulation of multiconfigurational perturbation theory and define the unperturbed energies as

$$\epsilon_{\nu} = \epsilon_{\text{ref}} + \Delta\epsilon_{\nu}, \quad (3.6)$$

where, in the NCSM, $\Delta\epsilon_{\nu}$ is the excitation energy of the basis state $|\Phi_{\nu}\rangle$ computed from the single-particle HO energies $e_a = \hbar\Omega(2n_a + l_a + 3/2)$.

The choice of the unperturbed Hamiltonian defines the perturbation

$$\mathbf{W} = \mathbf{H} - \mathbf{H}_0. \quad (3.7)$$

Thus, the first-order correction of $|\Psi_{\text{ref}}\rangle$ is given by

$$|\Psi^{(1)}\rangle = - \sum_{\nu \notin \mathcal{M}_{\text{ref}}} \frac{\langle \Phi_{\nu} | \mathbf{W} | \Psi_{\text{ref}} \rangle}{\epsilon_{\nu} - \epsilon_{\text{ref}}} |\Phi_{\nu}\rangle \quad (3.8)$$

$$= - \sum_{\nu \notin \mathcal{M}_{\text{ref}}} \frac{\langle \Phi_{\nu} | \mathbf{H} | \Psi_{\text{ref}} \rangle}{\epsilon_{\nu} - \epsilon_{\text{ref}}} |\Phi_{\nu}\rangle. \quad (3.9)$$

We define the *a priori* importance measure κ_ν for the basis states $|\Phi_\nu\rangle \notin \mathcal{M}_{\text{ref}}$ by the amplitudes of the individual basis states $|\Phi_\nu\rangle$ in Eq. (3.8)

$$\kappa_\nu = -\frac{\langle \Phi_\nu | \mathbf{H} | \Psi_{\text{ref}} \rangle}{\epsilon_\nu - \epsilon_{\text{ref}}} = -\sum_{\mu \in \mathcal{M}_{\text{ref}}} C_\mu^{(\text{ref})} \frac{\langle \Phi_\nu | \mathbf{H} | \Phi_\mu \rangle}{\epsilon_\nu - \epsilon_{\text{ref}}}, \quad (3.10)$$

where relation (3.3) is used in the second step. Only those basis states $|\Phi_\nu\rangle$ with an importance measure larger than the importance threshold $|\kappa_\nu| \geq \kappa_{\text{min}}$ are included in the importance-truncated (IT) model space \mathcal{M}_{IT} . The eigenvalue problem is solved in this IT model space, which leads to an improved approximation for the target eigenstate.

The IT scheme retains the variational principle of the NCSM. Accordingly, the energies $E(\kappa_{\text{min}})$ for a certain eigenstate with importance threshold κ_{min} can be extrapolated to the exact energy $E^{\text{exact}}(\kappa_{\text{min}} = 0) \leq E(\kappa_{\text{min}})$. This is accomplished by calculating the energy for a sequence of κ_{min} values, typically of the order of 10^{-5} , and extrapolating the energy to vanishing κ_{min} .

Since this IT scheme leads to a representation of the approximate eigenstates in a shell-model basis, not only the energies but all other observables of interest, e.g., radii or transition strength, can be computed directly.

3.2 Center-of-Mass Motion

The nucleus is a finite self-bound system. There is no external potential as in many-electron systems in atomic physics, where the electrons are bound by the electromagnetic field of the nucleus, and accordingly, there is no defined reference frame. In the exact theory, the many-body state $|\Psi\rangle$ of the nucleus factorizes into the intrinsic state $|\Psi_{\text{int}}\rangle$ and a state $|\Psi_{\text{CM}}\rangle$ describing the center-of-mass (CM) motion [76]

$$|\Psi\rangle = |\Psi_{\text{int}}\rangle \otimes |\Psi_{\text{CM}}\rangle. \quad (3.11)$$

Only if this decoupling holds, the intrinsic state is translationally invariant and does not suffer from spurious center-of-mass motion. For the NCSM with a HO basis and an $N_{\text{max}}\hbar\Omega$ truncation, the exact factorization of the CM and intrinsic state is possible for all N_{max} [5, 76].

However, in the IT-NCSM, the factorization of the eigenstate into a CM and an intrinsic component is only approximate due to the additional model-space truncation with respect to the importance measure. Thus, a weak coupling between CM and intrinsic component is induced, which has to be monitored and quantified [76].

4 Halo EFT Results

Now, we have everything at hand to start with the discussion of our results. In this chapter, we explore electromagnetic properties and nuclear reactions for one-neutron halo nuclei using the Halo EFT approach. As discussed in Sec. 2.2.2, halo nuclei are exotic nuclei that can be found for various isotopes close to the drip line. The well-established *ab initio* approaches have difficulties to describe these exotic nuclei since the separation of scales between R_{core} and R_{halo} is not explicit in the parameters of the *ab initio* methods. Halo EFT exploits this separation of scales and so, it provides insights into universal correlations of such weakly-bound systems. Thus, Halo EFT can be considered a complementary approach to *ab initio* methods.

Halo EFT was successfully applied to describe shallowly bound S -wave and P -wave states [16, 64, 82]. In this work, we aim for the extension of the Halo EFT formalism to partial wave bound states beyond P -wave states, in general, and D -wave states, in particular. That way, we want to make the Halo EFT approach applicable to a broader range of halo systems and discuss universality for higher partial wave bound states.

The chapter is organized as follows: First, we introduce the two one-neutron halo nuclei, ^{15}C and ^{17}C , that we aim to describe with our Halo EFT. After writing down the effective Lagrangian, we dress the S - and D -wave dimers and develop a power-counting scenario for shallowly bound D -wave states. In the next step, photons are included in our theory to calculate electromagnetic form factors of the S - and D -wave state. Furthermore, we compute electromagnetic transitions between different states and neutron capture into the S - and D -wave state. Eventually, we apply our findings to the two carbon isotopes and discuss universal correlations between electric observables in such systems.

Parts of this chapter were already published in Refs. [1–3].

4.1 Carbon-15 and Carbon-17

In this thesis, we focus on one-neutron halo nuclei with a shallowly bound D -wave state. Two prominent examples are the two carbon isotopes ^{15}C and ^{17}C .

As illustrated in Fig. 4.1, ^{15}C has a $J^P = 1/2^+$ ground state and an excited $5/2^+$ state. While the ground state is an S -wave state, the excited state is predominantly a D -wave bound state relative to the core. The neutron separation energy of the $1/2^+$ state of ^{15}C is $S_n = 1218$ keV and the neutron separation energy of the $5/2^+$ state is $S_n = 478$ keV [83], whereas the first excitation of the ^{14}C nucleus is $E^{(\text{ex})} = 6.1$ MeV above the 0^+ ground state. This weak binding indicates the halo nature of the ground and first excited state of ^{15}C . Converting these energy scales into the relevant distance scales

$$R_{\text{core}} \approx \frac{1}{\sqrt{E^{(\text{ex})} 2m_R}} = 1.91 \text{ fm} \quad \text{and} \quad R_{\text{halo}} \approx \frac{1}{\gamma_2} = \frac{1}{\sqrt{S_n 2m_R}} = 6.81 \text{ fm} , \quad (4.1)$$

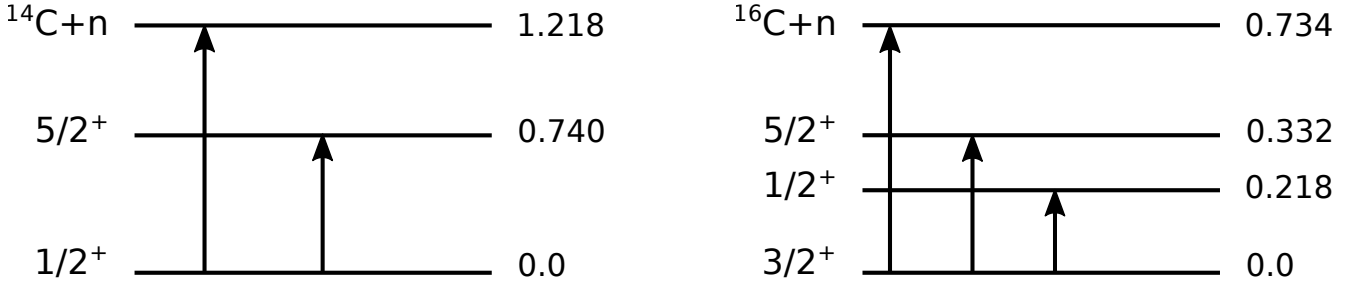


Figure 4.1.: Level schemes of ^{15}C (left) and ^{17}C (right) showing quantum numbers J^P , excitation energies in MeV, and the $^{14}\text{C} + n/^{16}\text{C} + n$ threshold.

with the reduced mass of the two-body system m_R , we obtain an approximation for the core and halo radius and can estimate the EFT expansion parameters for this system as $R_{\text{core}}/R_{\text{halo}} \approx 0.3 - 0.4$. Using the experimental values for the binding energies of the S - and D -wave states above, we deduce

$$\gamma_0 = \sqrt{S_n(1/2^+)2m_R} = 0.235 \text{ fm}^{-1} \quad \text{and} \quad \gamma_2 = \sqrt{S_n(5/2^+)2m_R} = 0.147 \text{ fm}^{-1}. \quad (4.2)$$

The electromagnetic form factors for the ground state of ^{15}C and the radiative neutron capture on ^{14}C to the $1/2^+$ ground state of ^{15}C were previously calculated using Halo EFT in Refs. [82, 84], respectively.

Next, we consider the ^{17}C nucleus. The first excitation of the ^{16}C core has an energy of $E^{(\text{ex})} = 1.766 \text{ MeV}$ [85], while the neutron separation energy of the $3/2^+$ ground state in ^{17}C is $S_n = 0.734 \text{ MeV}$ [15]. This suggests that the ground state of ^{17}C can be described as a neutron in a D -wave relative to the ^{16}C core, although the halo nature of the ground state is not commonly accepted [86, 87]. Converting these energy scales into the relevant distance scales yields $R_{\text{core}} \approx 3.53 \text{ fm}$ and $R_{\text{halo}} \approx 5.47 \text{ fm}$ that leads to an expansion parameter for this system of $R_{\text{core}}/R_{\text{halo}} \approx 0.6$. As shown in Fig. 4.1, ^{17}C also has two excited $J^P = 1/2^+$ and $5/2^+$ states with energies $E_{1/2^+}^{(\text{ex})} = 0.218 \text{ MeV}$ and $E_{5/2^+}^{(\text{ex})} = 0.332 \text{ MeV}$ [87]. In Halo EFT, these two states are described by a neutron in an S -wave and D -wave relative to the core, respectively. This yields an expansion parameter for the two excited states of $R_{\text{core}}/R_{\text{halo}} \approx 0.5$. Using the experimental values for the binding energies of the S - and D -wave states above, we find

$$\gamma_0 = 0.153 \text{ fm}^{-1}, \quad \gamma_2 = 0.183 \text{ fm}^{-1} \quad \text{and} \quad \gamma_{2'} = 0.135 \text{ fm}^{-1}, \quad (4.3)$$

for the S -wave excited state and D -wave ground and excited state, respectively.

Since the expansion parameters for all bound states of both halo nuclei are not particularly small, effects beyond LO are not negligible in our theory.

4.2 Effective Lagrangian

After the brief introduction of the two carbon isotopes, we write down the effective Lagrangian to describe the S - and D -wave states, in the following. We continue the discussion in Sec. 2.2.2 and extend the Halo EFT formalism, developed in Ref. [64] for the calculation of electric properties of S - and P -wave

systems, to D -wave states. Thus, the relevant degrees of freedom are the halo neutron, a spinor field n with spin $1/2$, and the core, a bosonic field c with spin zero, since the core of both carbon isotopes has $J^P = 0^+$. The strong S -wave and D -wave interactions are included through the incorporation of auxiliary spinor fields σ_s and d_m , which correspond to the $1/2^+$ and $5/2^+$ or $3/2^+$ states, respectively.

With the convention that repeated spin indices are summed the effective, non-relativistic Lagrangian can be written as

$$\begin{aligned}
\mathcal{L} = & c^\dagger \left(i\partial_t + \frac{\nabla^2}{2M} \right) c + n^\dagger \left(i\partial_t + \frac{\nabla^2}{2m} \right) n \\
& + \sigma_s^\dagger \left[\eta_0 \left(i\partial_t + \frac{\nabla^2}{2M_{nc}} \right) + \Delta_0 \right] \sigma_s + d_m^\dagger \left[c_2 \left(i\partial_t + \frac{\nabla^2}{2M_{nc}} \right)^2 + \eta_2 \left(i\partial_t + \frac{\nabla^2}{2M_{nc}} \right) + \Delta_2 \right] d_m \\
& - g_0 [c^\dagger n_s^\dagger \sigma_s + \sigma_s^\dagger n_s c] - g_2 \left[d_m^\dagger \left[n \overleftrightarrow{\nabla} c \right]_{J,m} + \left[c^\dagger \overleftrightarrow{\nabla} n^\dagger \right]_{J,m} d_m \right], \tag{4.4}
\end{aligned}$$

where $3/2 \leq J \leq 5/2$ denotes the total spin of the D -wave state, m is the neutron mass, M the core mass and $M_{nc} = m + M$ is the total mass of the nc system. In the equation above, the first four terms denote the kinetic energy part of the Lagrangian for the core, neutron, S - and D -wave dimer, respectively. The last two terms represent the contact interactions for the coupling of the neutron and the core to an S - or D -wave dimer with coupling constants g_0 and g_2 , respectively. The power counting for this Lagrangian depends on the underlying scales and will be discussed in Sec. 4.4. Because of the mass difference between the core and the neutron and to preserve Galilean invariance, we adopt

$$n \overleftrightarrow{\nabla} c = n \frac{(M \overleftarrow{\nabla} - m \overrightarrow{\nabla})}{M_{nc}} c. \tag{4.5}$$

For the D -wave, we have four constants in our Lagrangian: c_2, η_2, Δ_2 and g_2 . However, only three of them are linearly independent. In principle, we are free to choose which constant is set on a fixed value. In this thesis, we follow the traditional approach and set $\eta_2 = \pm 1$, but other choices, e.g., fixing g_2 , lead to the same results. For the D -wave, the additional higher-order kinetic term with constant c_2 is required to renormalize the interacting D -wave propagator in Sec. 4.3.2. We project out the $J = 5/2$ or $3/2$ part of the strong D -wave interaction employing Clebsch-Gordan coefficients

$$\left[n \overleftrightarrow{\nabla} c \right]_{J,m} = \sum_{m_s, m_l} \left(\frac{1}{2} m_s \ 2m_l \middle| Jm \right) n_{m_s} \sum_{\alpha\beta} (1\alpha \ 1\beta \middle| 2m_l) \frac{1}{2} \left(\overleftrightarrow{\nabla}_\alpha \overleftrightarrow{\nabla}_\beta + \overleftrightarrow{\nabla}_\beta \overleftrightarrow{\nabla}_\alpha \right) c. \tag{4.6}$$

In practice, we calculate D -wave observables in Cartesian coordinates and then couple the spin and relative momentum appropriately through Clebsch-Gordan coefficients. To distinguish between spherical and Cartesian coordinates, we use Greek indices to indicate spherical representation and Latin indices denote Cartesian coordinates throughout this thesis.

The Cartesian form of the strong D -wave interaction is taken from Refs. [17, 88]

$$\frac{1}{2} \left(\overleftrightarrow{\nabla}_i \overleftrightarrow{\nabla}_j + \overleftrightarrow{\nabla}_j \overleftrightarrow{\nabla}_i \right) - \frac{1}{D-1} \overleftrightarrow{\nabla}^2 \delta_{ij}, \quad (4.7)$$

where D denotes the space-time dimensions. This interaction yields 9 terms, but only 5 of them are linearly independent since Eq. (4.7) is traceless and symmetric under permutation of i and j . Accordingly, they correspond to the 5 components of a D -wave state. Thus, the D -wave part of the Lagrangian (4.7) contains all symmetries relevant in our framework. It is Galilean invariant and symmetric under permutation of two indices, which preserves gauge invariance after the inclusion of photons via minimal substitution in Sec. 4.6. Furthermore, it contains the correct number of degrees of freedom.

4.3 Dimer Propagators

After writing down the effective Lagrangian, the dressed $\sigma(d)$ propagator and the $S(D)$ -wave scattering amplitude are computed from the diagrams in Fig. 4.2 in the same way as in Ref. [64]. At first, we have to dress the dimer propagator by iteratively summing up the one-loop self energy, $\Sigma(p)$, to all orders. This is achieved through the Dyson equation illustrated in the top panel of Fig. 4.2. Subsequently, we calculate the scattering amplitude, bottom panel of Fig. 4.2, and match it to the effective range expansion (ERE) in the corresponding channel.

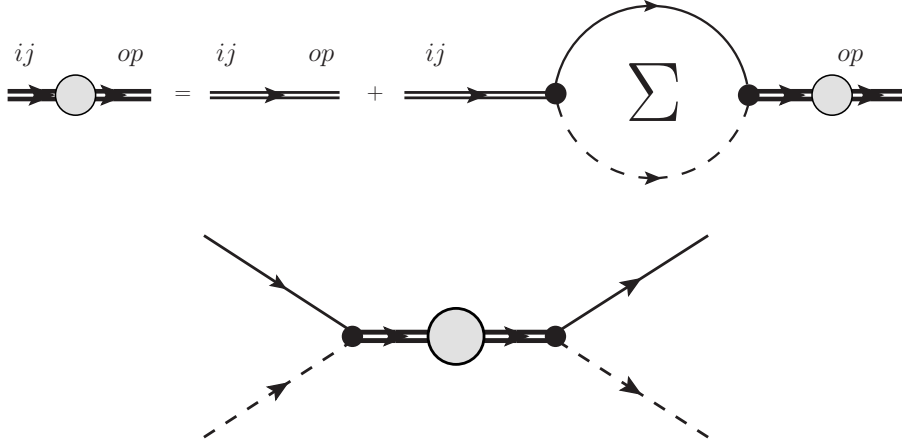


Figure 4.2.: The top panel shows the diagrammatic representation of the Dyson equation for the dressed dimer propagator and the bottom panel the neutron-core scattering amplitude with the dressed dimer propagator. The dashed line denotes the core field c , and the thin solid line the neutron. The thin double line represents the bare dimer propagator and the thick double line with the gray circle is the dressed dimer propagator.

We demonstrate this in detail only for the D -wave and refer the reader to Ref. [64] for a detailed calculation of the dressed σ propagator. Eventually, we obtain the exact solution of the effective field theory for the S - or D -wave state. In Sec. 4.4, we develop a power-counting scheme that classifies the different contributions to the dimer propagator according to their importance at low energies.

4.3.1 S-Wave Propagator

The S -wave part of the Lagrangian is well known in the literature [14, 64, 84]. Compared to the D -wave case, it contains three unknown constants η_0 , Δ_0 and g_0 . However, only two of them are linearly independent so that η_0 is chosen to be a sign, which depends on the sign of the effective range. We follow the steps in Ref. [64] to reproduce their results. Using the Dyson equation illustrated in Fig. 4.2, we calculate the one-loop self energy $\Sigma_\sigma(p)$ to obtain the full σ propagator $D_\sigma(p)$

$$\Sigma_\sigma(p) = -\frac{g_0^2 m_R}{2\pi} \left[i \sqrt{2m_R \left(p_0 - \frac{\mathbf{p}^2}{2M_{nc}} \right) + \mu} \right], \quad (4.8)$$

$$D_\sigma(p) = \frac{1}{\Delta_0 + \eta_0 [p_0 - \mathbf{p}^2/(2M_{nc}) + i\epsilon] - \Sigma_\sigma(p)}, \quad (4.9)$$

where m_R denotes the reduced mass of the neutron-core system and the power divergence subtraction (PDS) is employed as regularization scheme with scale μ [47, 48].

After matching the S -wave scattering amplitude in the two-body center-of-mass frame, $t_0(\mathbf{p}', \mathbf{p}; E) = g_0^2 D_\sigma(E, \mathbf{p})$, to the S -wave effective range expansion

$$t_0(\mathbf{p}', \mathbf{p}; E) = \frac{2\pi}{m_R} \frac{1}{1/a_0 - \frac{1}{2}r_0 k^2 + ik}, \quad (4.10)$$

with $E = k^2/(2m_R)$ and $k = |\mathbf{p}'| = |\mathbf{p}|$ for on-shell scattering, we derive the following renormalization conditions

$$\frac{1}{a_0} = \frac{2\pi}{m_R g_0^2} \Delta_0 + \mu \quad \text{and} \quad r_0 = -\frac{2\pi}{m_R^2 g_0^2} \eta_0. \quad (4.11)$$

In the vicinity of the bound state pole, the dressed S -wave propagator thus reads

$$D_\sigma(p) = Z_\sigma \frac{1}{p_0 - \frac{\mathbf{p}^2}{2M_{nc}} + B_0} + R_\sigma(p),$$

$$Z_\sigma = \frac{2\pi}{m_R^2 g_0^2} \frac{\gamma_0}{1 - r_0 \gamma_0}, \quad (4.12)$$

where Z_σ denotes the wave-function renormalization, $B_0 = \gamma_0^2/(2m_R)$ indicates the binding energy and $R_\sigma(p)$ is regular at the pole.

4.3.2 D-Wave Propagator

Now, we consider the D -wave bound state. In practice, we calculate the dressed D -wave propagator in Cartesian representation and eventually, couple the neutron spin and the relative momentum to project

out the appropriate angular momentum J . The Dyson equation for the D -wave is graphically illustrated in the top panel of Fig. 4.2 and its solution yields

$$D_d(p)_{ijop} = D_d(p) \frac{(\delta_{io}\delta_{jp} + \delta_{ip}\delta_{jo} - \frac{2}{3}\delta_{ij}\delta_{op})}{2}, \quad (4.13)$$

$$D_d(p) = \frac{1}{(D_d^0(p))^{-1} - \Sigma_d(p)}, \quad (4.14)$$

$$= \frac{1}{\Delta_2 + \eta_2 [p_0 - \mathbf{p}^2/(2M_{nc}) + i\epsilon] + c_2 [p_0 - \mathbf{p}^2/(2M_{nc}) + i\epsilon]^2 - \Sigma_d(p)}, \quad (4.15)$$

with the bare dimer propagator $D_d^0(p)$ and the one-loop self energy is computed as

$$\Sigma_d(p)_{ijop} = \Sigma_d(p) \frac{(\delta_{io}\delta_{jp} + \delta_{ip}\delta_{jo} - \frac{2}{3}\delta_{ij}\delta_{op})}{2}, \quad (4.16)$$

$$\begin{aligned} \Sigma_d(p) = & -\frac{m_R g_2^2}{15\pi} \left[\frac{2}{5\pi} \Lambda^5 + \frac{2}{3\pi} (2m_R) \left(p_0 - \frac{p^2}{2M_{nc}} \right) \Lambda^3 + \frac{2}{\pi} (2m_R)^2 \left(p_0 - \frac{p^2}{2M_{nc}} \right)^2 \Lambda \right. \\ & \left. + i(2m_R)^{5/2} \left(p_0 - \frac{p^2}{2M_{nc}} \right)^{5/2} \right], \end{aligned} \quad (4.17)$$

where $m_R = (m + M)/(mM)$ denotes the reduced mass of the neutron-core system and we employ a momentum cutoff Λ as regularization scheme. Additionally, we used the following identities for $d = 3$ space dimensions in the loop integration

$$l_i l_j = l^2 \frac{\delta_{ij}}{d}, \quad (4.18)$$

$$l_i l_j l_o l_p = l^4 \frac{\delta_{ij}\delta_{op} + \delta_{io}\delta_{jp} + \delta_{ip}\delta_{jo}}{d(d+2)}. \quad (4.19)$$

The detailed calculation of the self energy is presented in App. A.1.

In spherical coordinates the Cartesian tensor of the D -wave propagator

$$\frac{(\delta_{io}\delta_{jp} + \delta_{ip}\delta_{jo} - \frac{2}{3}\delta_{ij}\delta_{op})}{2}, \quad (4.20)$$

which is consistent with the results in [88], transforms to

$$\sum_{\alpha\beta\gamma\delta} (1\alpha \ 1\beta | 2m_l) (1\gamma \ 1\delta | 2m_l') \frac{(\delta_{\alpha\gamma}\delta_{\beta\delta} + \delta_{\alpha\delta}\delta_{\beta\gamma})}{2} = \delta_{m_l, m_l'}, \quad (4.21)$$

and eventually, the total angular momentum coupling, cf. Eq. (4.6), applied in the incoming and outgoing channel yields

$$\Sigma_d(p)_{mm'} = \sum_{m_s m_l m'_s m'_l} \left(\frac{1}{2} m_s \ 2m_l \middle| Jm \right) \left(\frac{1}{2} m'_s \ 2m'_l \middle| Jm' \right) \delta_{m_l m'_l} \delta_{m_s m'_s} \Sigma_d(p) \quad (4.22)$$

$$= \delta_{mm'} \Sigma_d(p), \quad (4.23)$$

as expected.

The D -wave scattering amplitude in the two-body center-of-mass frame with $E = k^2/(2m_R)$ and $k = |\mathbf{p}'| = |\mathbf{p}|$ for on-shell scattering

$$t_2(\mathbf{p}', \mathbf{p}; E) = g_2^2 \left[(\mathbf{p} \cdot \mathbf{p}')^2 - \frac{1}{3} \mathbf{p}^2 \mathbf{p}'^2 \right] D_d(E, \mathbf{0}), \quad (4.24)$$

is then matched to the D -wave effective range expansion

$$t_2(\mathbf{p}', \mathbf{p}; E) = \frac{15\pi}{m_R} \frac{(\mathbf{p} \cdot \mathbf{p}')^2 - \frac{1}{3} \mathbf{p}^2 \mathbf{p}'^2}{1/a_2 - \frac{1}{2} r_2 k^2 + \frac{1}{4} \mathcal{P}_2 k^4 + ik^5}, \quad (4.25)$$

and we find the following renormalization conditions

$$\frac{1}{a_2} = \frac{15\pi}{m_R g_2^2} \Delta_2 + \frac{2}{5\pi} \Lambda^5, \quad r_2 = -\frac{15\pi}{m_R^2 g_2^2} \eta_2 - \frac{2}{3\pi} \Lambda^3, \quad \mathcal{P}_2 = \frac{15\pi}{m_R^3 g_2^2} c_2 + \frac{2}{\pi} \Lambda, \quad (4.26)$$

which determine the running of the coupling constants g_2 , Δ_2 , and c_2 with the momentum cutoff Λ . Since we get cutoff dependencies with powers of 5, 3 and 1, the effective range parameters a_2 , r_2 and \mathcal{P}_2 are required for the renormalization at LO, which motivates the power-counting scheme below. In particular, we need to include the additional second-order kinetic term proportional to the coupling constant c_2 in our Lagrangian (4.4) to absorb the linear divergence [89]. If the values for these effective range parameters are known, they can be used to fix the EFT couplings Δ_2 , c_2 , and g_2 and the sign η_2 in our theory.

Near the bound state pole, the dressed d -propagator can then be written as

$$D_d(p) = Z_d \frac{1}{p_0 - \frac{\mathbf{p}^2}{2M_{nc}} + B_2} + R_d(p), \quad (4.27)$$

where $B_2 = \gamma_2^2/(2m_R)$ indicates the binding energy, $R_d(p)$ is a remainder that is regular at the pole and Z_d denotes the wave function renormalization, which is the residue of the pole obtained by

$$\frac{1}{Z_d} = i \frac{\partial}{\partial E} (iD_d(p))^{-1} \Big|_{E=-\frac{\gamma_2^2}{2m_R}, \mathbf{p}=0} \rightarrow Z_d = -\frac{15\pi}{m_R^2 g_2^2} \frac{1}{r_2 + \mathcal{P}_2 \gamma_2^2 - 5\gamma_2^3}. \quad (4.28)$$

For a D -wave bound state, Z_d is related to the asymptotic normalization constant (ANC) of the bound state wave function, whose position space representation reads

$$\psi_{2m}(\mathbf{r}) = A_2 \frac{u_2(r)}{r} Y_{2m}(\hat{\mathbf{r}}), \quad (4.29)$$

with the spherical harmonic $Y_{2m}(\hat{\mathbf{r}})$ for $l = 2$. The radial part of the wave function is given by

$$u_2(r) = \exp(-\gamma_2 r) \left(1 + \frac{3}{\gamma_2 r} + \frac{3}{(\gamma_2 r)^2} \right), \quad (4.30)$$

while A_2 denotes the ANC of the D -wave bound state

$$A_2 = \sqrt{\frac{2\gamma_2^4}{-r_2 - \mathcal{P}_2\gamma_2^2 + 5\gamma_2^3}}. \quad (4.31)$$

A_2 is not directly measured in experiments, however, it can be extracted from neutron-core scattering data by an analytic continuation of the scattering amplitudes to negative energy [14].

4.4 Power-Counting Scheme

After dressing the dimer propagators, we develop a power-counting scenario that classifies the different contributions to the propagator according to their importance in our Halo EFT expansion, $R_{\text{core}}/R_{\text{halo}}$. For the shallow S -wave bound state, we adopt the standard power counting used in Refs. [17, 64, 82]. It implies $1/\gamma_0 \sim a_0 \sim R_{\text{halo}}$ and $r_0 \sim R_{\text{core}}$, where γ_0 represents the bound state pole position, a_0 is the S -wave scattering length and r_0 the effective range. As a result, r_0 contributes at NLO in the expansion in $R_{\text{core}}/R_{\text{halo}}$.

Because of the increasing number of required effective range parameters and the weakly-bound nature of halo nuclei, the power counting for partial waves beyond S -wave states is not unique and different scenarios are conceivable [16, 17]. We apply the constraint that we use the minimal number of fine tunings possible in our power-counting scheme to absorb all power law divergences. This is motivated by the expectation that every additional fine tuning makes our scenario less likely to be found in nature, as discussed by *Bedaque et al.* in Ref. [17]. They explicitly consider P -waves and assume that $a_1 \sim R_{\text{halo}}^2 R_{\text{core}}$ and $r_1 \sim 1/R_{\text{core}}$, while higher effective range parameters scale with the appropriate power of R_{core} . This scenario requires only one fine-tuned constant for P -waves instead of two as proposed in the previous paper on Halo EFT [16].

In Ref. [17], the P -wave power counting is generalized to partial waves with $l > 0$. They suggest that also for $l > 1$ only one fine-tuned constant is sufficient. However, we find that the number of fine tunings for higher partial waves ($l > 1$) is larger than proposed in Ref. [17]. A more detailed discussion of the differences between both power countings is given in Sec. 4.5. In this work, we follow the general arguments for the P -wave case in Ref. [17] and apply them to the D -wave. To renormalize all arising divergences in the calculation of the dimer propagator, cf. Eq. (4.26), a_2, r_2 and \mathcal{P}_2 are required at LO

in the D -wave case. In the minimal scenario for the $D_d(p)$ propagator, two out of three effective range parameters need to be fine-tuned, i.e. $a_2 \sim R_{\text{halo}}^4 R_{\text{core}}$ and $r_2 \sim 1/(R_{\text{halo}}^2 R_{\text{core}})$ are both unnaturally large. This is more likely to occur than three unnaturally large parameters and three fine tunings so that we adopt $\mathcal{P}_2 \sim 1/R_{\text{core}}$. Thus, all three terms contribute at LO for typical momenta $k \sim 1/R_{\text{halo}}$. Higher effective range parameters scale with R_{core} only and are therefore suppressed by powers of $R_{\text{core}}/R_{\text{halo}}$.

Accordingly, the LO contribution to the dressed D -wave propagator (4.27), after resumming all bubble diagrams and appropriate renormalization, comes from the bare propagator only. The loop contributions are suppressed by $R_{\text{core}}/R_{\text{halo}}$ and thus, contribute at NLO. Furthermore, all imaginary parts, if present, appear in the regular part of the amplitude. Hence, the D -wave scattering amplitude will be not exactly unitary, but it respects unitarity perturbatively in the expansion in $R_{\text{core}}/R_{\text{halo}}$. This is in contrast to the S -wave case, where the bare propagator is not sufficient and the loop contributions are required at LO to determine the dressed S -wave propagator. However, the power-counting scenario depends sensitively on the details of the considered system and has to be verified by comparison with experimental data.

After the discussion above and replacing the S -wave scattering length by the pole momentum, $a_0 = 1/\gamma_0$, the relevant fit parameters in our EFT are γ_0 , γ_2 , r_2 , and \mathcal{P}_2 at LO and the following renormalization constants can be derived

$$Z_\sigma = \frac{2\pi\gamma_0}{m_R^2 g_0^2} \quad \text{and} \quad Z_d = -\frac{15\pi}{m_R^2 g_2^2} \frac{1}{r_2 + \mathcal{P}_2 \gamma_2^2}. \quad (4.32)$$

At NLO, we have to consider r_0 as additional fit parameter and we obtain

$$Z_\sigma = \frac{2\pi}{m_R^2 g_0^2} \frac{\gamma_0}{1 - r_0 \gamma_0} \quad \text{and} \quad Z_d = -\frac{15\pi}{m_R^2 g_2^2} \frac{1}{r_2 + \mathcal{P}_2 \gamma_2^2 - 5\gamma_2^3}. \quad (4.33)$$

The power counting for arbitrary l -th partial waves is presented in Sec. 4.5. For the specific case of ^{15}C , Ref. [84] indicates that effective range corrections could be large $r_0 \gamma_0 \sim 0.6$ and it could be appropriate to scale $r_0 \sim R_{\text{halo}}$ and thus, to keep it at LO. The extracted value for $r_0 = 2.67 \text{ fm}$ [84] results from a fit to one-neutron capturing data $^{14}\text{C}(n, \gamma)^{15}\text{C}$ from Ref. [90]. Therefore, we will treat r_0 as a LO parameter for ^{15}C .

After the development of our power counting, we employ, from now on, a dimensional regularization scheme with power divergence subtraction (PDS) and renormalization scale μ [47, 48] for all calculations instead of a cutoff regularization. The reason why we used the cutoff regularization in the first place was that it is more convenient for keeping track of any divergences emerging from the loop integration. However, the cutoff regularization breaks Galilean invariance, which complicates the renormalization for different substitutions in the loop integration. Therefore, dimensional regularization schemes are more favorable since they preserve Galilean invariance. In this thesis, we compute several observables with different loop integrations so that a dimensional regularization scheme is best suited for our purpose. PDS is the ideal candidate since it keeps track of linear divergences and has all the benefits of a dimensional regularization scheme, as we will discuss in more detail at the end of this section.

To start with, we apply PDS to the full D -wave propagator calculation. In PDS, the one-loop self energy is given by

$$\Sigma_d(p) = -\frac{2}{15} \frac{m_R g_2^2}{2\pi} (2m_R)^2 \left(p_0 - \frac{p^2}{2M_{nc}} \right)^2 \left[i \sqrt{2m_R \left(p_0 - \frac{p^2}{2M_{nc}} + i\epsilon \right)} - \frac{15}{8} \mu \right]. \quad (4.34)$$

After the matching to the effective range expansion, we deduce the following renormalization conditions

$$\frac{1}{a_2} = \frac{15\pi}{m_R g_2^2} \Delta_2, \quad r_2 = -\frac{15\pi}{m_R^2 g_2^2} \eta_2, \quad \mathcal{P}_2 = \frac{15\pi}{m_R^3 g_2^2} c_2 + \frac{15}{2} \mu. \quad (4.35)$$

Note that the μ dependence in the condition for $\mathcal{P}_2 \sim 1/R_{\text{core}}$ is subleading if $\mu \sim 1/R_{\text{halo}}$ and hence, can be dropped at LO. Our findings later in the form factor calculation confirm this assumption.

Dressing the D -wave propagator was already performed in the context of the $d + t \leftrightarrow n + \alpha$ reaction by *Brown and Hale* [88], where the coupling of the auxiliary field for the ${}^5\text{He}$ resonance to the αn pair with spin $3/2$ involves an internal D -wave angular momentum. Employing a similar approach for the coupling of the cn pair, we obtain the same Cartesian tensor (4.20) as *Brown and Hale*. In Ref. [88], they also use a dimensional regularization scheme, the minimal subtraction (MS) scheme [91, 92], which adds counterterms that subtract poles at $D = 4$ dimensions. In PDS, the poles at $D = 4$ and $D = 3$ are both subtracted by counterterms. If there are no poles in $D = 3$, PDS and MS yield the same result. Considering the calculation of the self energy for the D -wave propagator, there is no pole in $D = 4$ but a pole in $D = 3$. Therefore, by employing the MS scheme, it is not required to add counterterms to regularize divergences. In PDS, the pole at $D = 3$, which corresponds to power law divergences at $D = 4$, is also subtracted. The MS leads to a different power-counting scheme where all power divergences are automatically set to zero in the D -wave case and the effective range parameters r_2 and \mathcal{P}_2 are not required for the renormalization at LO. As discussed in Refs. [47, 48], the PDS scheme is better suited for such shallowly bound systems since it keeps track of power law divergences and yields the appropriate power counting that we derived from the cutoff regularization (4.17) before.

4.5 Higher Partial Waves

As a first conclusion, the basic concept for the extension of our Halo EFT to higher l -th partial waves is outlined in this section. The strong interaction terms for higher l can be derived from the traceless, symmetric Cartesian (Buckingham) multipole tensors [93] given by

$$M_{i,j,\dots,t}^{(l)} = \frac{(-1)^l}{l!} r^{2l+1} \frac{\partial^l}{\partial r_i \partial r_j \dots \partial r_t} \left(\frac{1}{r} \right) \quad i, j, \dots, t \in \{x, y, z\}. \quad (4.36)$$

To obtain the specific interaction in momentum space for a given angular momentum l , r_j is simply replaced by $i\nabla_j$. In principle, this leads to a tensor of rank l with 3^l components. However, because the tensors are traceless and symmetric in every pair of indices, only $(2l + 1)$ components of the tensor are linearly independent.

This statement can be verified by applying concepts of combination theory and linear algebra. First, we consider the $l = 2$ case and the M_{ij} tensor with $i, j \in x, y, z$. By summing over all possible values of i and j , we obtain $n^k = 3^2 = 9$ variations of M_{ij} . Since M_{ij} is symmetric under permutation of i and j , the number of distinct components is given by $\binom{n}{k} = \binom{n+k-1}{k} = \binom{4}{2} = 6$, which is equivalent to the number of ways to sample k elements from a set of n elements allowing for duplicates but disregarding different orderings. Moreover, the tensor $\text{Tr}(M_{ij}) = 0$ is traceless which further reduces the number of independent components by one and we are left with the total number of five independent components.

The same reasoning applies to higher partial waves. Considering the case of $l = 3$, we obtain $3^3 = 27$ components of M_{ijk} of which only $\binom{5}{3} = 10$ components are distinct due to symmetry. The trace of a rank r tensor can be generalized to a tensor contraction where a pair of unlike indices that are set equal are summed up according to the Einstein summation convention. The result is a new tensor whose rank $(r - 2)$ is reduced by two. Accordingly, the trace of a rank two tensor ($l = 2$) is a scalar and of a rank three tensor ($l = 3$) a vector. Since the M_{ijk} tensor is traceless, $M_{iik} = 0$, this reduces the number of independent components by three so that seven independent components remain in the end.

Initially, using Cartesian tensors and neglecting the spin simplifies the calculation of Feynman diagrams. However, we have to eventually couple the spin and the relative momentum for a given J in the appropriate way. This can become demanding for some observables that are sensitive on the spin. Therefore, it might be more convenient to apply the spherical representation for partial waves beyond P -wave throughout the calculation.

Now, we reconsider the discussion of the renormalization procedure and the power-counting scenario for arbitrary partial waves. To be able to absorb all power law divergences in the calculation of the dressed dimer propagator, the number of effective range parameters required at LO for the l -th partial wave is $(l + 1)$ [16]. Accordingly, for the S -wave only the scattering length a_0 and for the D -wave a_2 , r_2 , and \mathcal{P}_2 are necessary. As argued in Sec. 4.4, the highest ERE parameter at LO can be assumed to scale as $1/R_{\text{core}}$ for partial waves beyond the S -wave. Thus, to renormalize all power law divergences for the l -th partial wave, a minimal number of l fine-tuned parameters is required. This explains why higher partial wave bound states occur less likely in nature as mentioned in Sec. 2.2.2. For arbitrary l , the reasoning above and in Sec. 4.4 leads to the following power-counting scheme

$$a_l = \begin{cases} R_{\text{halo}}, & l = 0 \\ R_{\text{halo}}^{2l} R_{\text{core}}, & l > 0 \end{cases} \quad (4.37)$$

$$r_l = \begin{cases} R_{\text{core}}, & l = 0 \\ 1/(R_{\text{halo}}^{2l-2} R_{\text{core}}), & l > 0 \end{cases} \quad (4.38)$$

$$\mathcal{P}_l = \begin{cases} R_{\text{core}}^{3-2l}, & l \leq 1 \\ 1/(R_{\text{halo}}^{2l-4} R_{\text{core}}), & l > 1 \end{cases} \quad (4.39)$$

\vdots ,

where the l -th and higher ERE parameters in each partial wave scale with appropriate powers of R_{core} .

Accordingly, our power-counting scenario agrees with Ref. [17] up to shallow P -wave states but differs for partial waves beyond since higher ERE parameters are counted differently. Although *Bedaque et al.* [17] confirm that higher effective range parameters are required to absorb the divergences in the self energy for higher partial waves, the renormalized quantities scale differently in their power counting. The absolute scaling differs for each partial wave, but the relative scaling is always the same as for the P -wave. This means that only a_l and r_l contribute at LO and every higher parameter is smaller by two powers of $R_{\text{core}}/R_{\text{halo}}$. As a consequence, only one fine-tuned parameter is required for arbitrary partial waves. However, this would imply that the probability to find shallow bound states in higher partial waves does not decrease for larger l . This stands in contrast to the conclusion of our power counting with l fine tunings and to experimental observations. Additionally, by comparing our Halo EFT results with experimental data for ^{15}C , we find that our power counting is in better agreement than their scenario, as we will discuss in Sec. 4.10.2. Nevertheless, the scenario depends sensitively on the details of the considered system and in principle, different fine tunings are conceivable.

4.6 Electromagnetic Interactions

After dressing the dimer propagators and developing the power-counting scheme for our Halo EFT, the next step towards the calculation of electromagnetic observables is the incorporation of photons in our theory. Hence, electromagnetic interactions are included via minimal substitution in the effective Lagrangian (4.4)

$$\partial_\mu \rightarrow D_\mu = \partial_\mu + ie\hat{Q}A_\mu, \quad (4.40)$$

where the charge operator \hat{Q} acting on the ^{14}C or ^{16}C core yields $\hat{Q}c = 6c$ and on the halo neutron $\hat{Q}n = 0$. Throughout this chapter we employ Coulomb gauge, $\nabla \cdot \mathbf{A} = 0$.

We demonstrate the minimal substitution for the kinetic part of the core field

$$c^\dagger \left(i\partial_0 + \frac{\nabla^2}{2M} \right) c \rightarrow c^\dagger \left(iD_0 + \frac{\mathbf{D}^2}{2M} \right) c = c^\dagger \left(i(\partial_0 + ie\hat{Q}A_0) + \frac{(\nabla - ie\hat{Q}\mathbf{A})^2}{2M} \right) c, \quad (4.41)$$

where the corresponding Feynman rules for the coupling of a photon to the core field are given by

$$-ie\hat{Q}\epsilon_0 \quad \text{and} \quad i\frac{e\hat{Q}}{M}\boldsymbol{\epsilon} \cdot \mathbf{p}, \quad (4.42)$$

for an A_0 -photon and an \mathbf{A} -photon vertex, respectively. The photon polarization vector is denoted by $\boldsymbol{\epsilon}$. The explicit derivation of the Feynman rule for the \mathbf{A} -photon vertex that stems from the minimal substitution in the D -wave interaction is deduced in App. A.2.

In addition to the electromagnetic interactions resulting from the application of the minimal substitution in the Lagrangian, we have to consider local gauge-invariant operators involving the electric, $\mathbf{E} = -\nabla A_0 - \partial_0 \mathbf{A}$, and magnetic field, $\mathbf{B} = \nabla \times \mathbf{A}$, and the fields c , n , σ and d . Depending on the observable and respective partial wave, they contribute at different orders in our EFT. For convenience, we will introduce these additional operators for every calculation of electromagnetic observables separately in the corresponding chapters.

After the inclusion of photons in our theory, we are now in the position to calculate electromagnetic observables in our Halo EFT approach.

4.7 Electromagnetic Form Factors

We first consider the static electromagnetic properties of shallow S - and D -wave states in general and eventually apply our results to ^{15}C and ^{17}C in Sec. 4.10. Static observables are usually easier to measure experimentally than dynamical properties. Moreover, they can be calculated in *ab initio* approaches that provide the wave functions of the involved states. In particular, we will compute the electric and magnetic form factors for D -waves and review the existing results for the S -wave so that we can consider all bound states of ^{15}C and ^{17}C .

4.7.1 Electric Form Factors

The result for the electric form factor of the S -wave halo state was already discussed in Ref. [64] for ^{11}Be and in Ref. [84] for ^{15}C . We will review it briefly before discussing the D -wave form factors in detail. Up to NLO, the electric form factors are calculated from Feynman diagrams with a scalar photon between the initial and final bound state. The relevant diagrams contributing to the $A_0 d d$ interaction up to NLO are illustrated in Fig. 4.3. For the S -wave or $A_0 \sigma \sigma$ interaction, only diagram (b) contributes at LO, whereas diagram (a), which is $\sim r_0$, contributes at NLO. For the D -wave, we have to consider only diagram (a) at LO, where the photon directly couples to the dimer field, while the loop diagram (b) yields a NLO contribution.

The Lagrangian with the relevant electric two-body currents for the S - and D -wave reads

$$\begin{aligned}
\mathcal{L}_E = & -L_{C0}^{(\sigma)} \sigma_s^\dagger (\nabla^2 A_0 - \partial_0 (\nabla \cdot \mathbf{A})) \sigma_s \\
& -L_{C01}^{(d)} d_m^\dagger (\nabla^2 A_0 - \partial_0 (\nabla \cdot \mathbf{A})) d_m \\
& -L_{C02}^{(d)} d_m^\dagger \left(\frac{1}{2} m_s \ 2m_l \middle| Jm \right) \left(\frac{1}{2} m_s \ 2m_l \middle| Jm \right) (1\alpha \ 1\beta | 2m_l) (1\gamma \ 1\delta | 2m_l) \times \\
& \left[(\nabla_\alpha \nabla_\gamma \delta_{\beta\delta} A_0) - \left(\partial_0 \frac{(\nabla_\alpha A_\gamma + \nabla_\gamma A_\alpha)}{2} \delta_{\beta\delta} \right) \right] d_m, \tag{4.43}
\end{aligned}$$

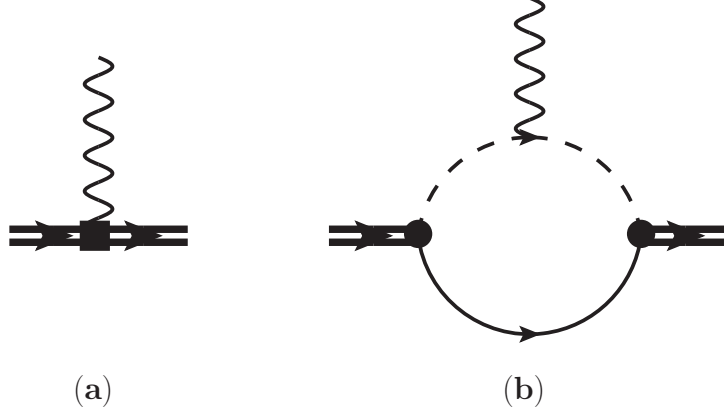


Figure 4.3.: The topologies contributing to the irreducible vertex for an A_0 -photon coupling to the core-neutron D -wave bound state up to NLO. Diagram (a) arises since r_2, \mathcal{P}_2 (minimal substitution in the bare propagator) and the local gauge-invariant operator $\sim L_{C01/2}^{(d)}$ contribute at LO, while diagram (b) emerges from the minimal substitution in the core propagator and contributes at NLO. The thick double line denotes the dressed D -wave propagator.

where repeated spin indices are summed over. For D -waves, the counterterms are required to absorb divergences not only in the calculation of the charge form factor but also in the quadrupole form factor, where the corresponding tensor structure becomes more complex, as we will see in Eq. (4.51). Hence, we derive the lengthy expression for the $L_{C02}^{(d)}$ operator, which is similar to Eq. (4.6).

To determine the order of these additional operators in the power counting, we follow the procedure from Refs. [64, 89]. The d and σ fields are rescaled so that they absorb factors of g_0, g_2 and m_R and have non-canonical dimensions

$$\tilde{d} = dg_2m_R \quad \text{and} \quad \tilde{\sigma} = \sigma g_0m_R. \quad (4.44)$$

For the rescaled σ field, we extract the non-canonical dimension from [64]: $[\tilde{\sigma}] = 2$. This can be obtained by reconsidering the matching between Eq. (4.9) and (4.10) and the power-counting scheme in Sec. 4.4

$$g_0^2m_R^2 \simeq -\frac{2\pi\eta_0}{r_0} \sim R_{\text{core}}. \quad (4.45)$$

Thus, the shallowness of the S -wave state is now encoded in the rescaled field and all the coefficients are natural in terms of $\tilde{\sigma}$. The rescaling procedure for the d field is more complicated since r_2 not only scales with powers of R_{core} but as $\sim (R_{\text{core}}R_{\text{halo}}^2)^{-1}$ adopting our power-counting scenario. In order to determine the scaling of the \tilde{d} field, we recall that the D -wave field implicitly contains two additional derivatives due to the higher angular momentum compared to the S -wave field. Thus, we assume that the non-canonical dimension of the rescaled d field is two dimensions lower than for the $\tilde{\sigma}$ field and we derive the non-canonical dimension $[\tilde{d}] = 0$. This is consistent with the finding in Ref. [64], $[\tilde{\pi}] = 1$, for the non-canonical dimension of the rescaled P -wave field, which implicitly contains one additional

derivative. Moreover, it agrees with the renormalization of the loop integral for the electric form factors of the D -wave later in this chapter.

Using naive dimensional analysis with these rescaled fields, we can determine the scaling of the operators with respect to R_{core} . As a result, the coefficients written above scale as

$$L_{C0}^{(\sigma)} \sim R_{\text{core}}^3 l_{C0}^{(\sigma)} g_0^2 m_R^2, \quad (4.46)$$

$$L_{C01}^{(d)} \sim R_{\text{core}}^{-1} l_{C01}^{(d)} g_2^2 m_R^2, \quad (4.47)$$

$$L_{C02}^{(d)} \sim R_{\text{core}}^{-1} l_{C02}^{(d)} g_2^2 m_R^2, \quad (4.48)$$

with parameters l_{\dots} all of order one. In the sections below, we will show that the operator $\sim L_{C0}^{(\sigma)}$ contributes at N³LO, while $\sim L_{C01/2}^{(d)}$ yields a LO contribution.

Electric Form Factor of the S -Wave State

First, we review the S -wave results before we consider the D -wave case. It is convenient to calculate all form factors in the Breit frame, where the photon transfers no energy, $q = (0, \mathbf{q})$, and to choose the photon to be moving in the \hat{z} direction $\mathbf{q} = |\mathbf{q}| \hat{z}$. The form factor of an S -wave one-neutron halo nucleus was calculated in Refs. [64, 84]. In this section, we review their results. From a straightforward calculation of diagram (b) in Fig. 4.3 for the $A_0 \sigma \sigma$ vertex, the electric charge form factor at LO can be derived [64]

$$G_E^{(\sigma)}(|\mathbf{q}|) = \frac{2\gamma_0}{f|\mathbf{q}|} \arctan\left(\frac{f|\mathbf{q}|}{2\gamma_0}\right), \quad (4.49)$$

with mass factor $f = m/M_{nc}$. Since the σ dimer corresponds to a spin 1/2 state, no higher form factors beyond G_E can occur. By expanding Eq. (4.49) for small values of $|\mathbf{q}|$, cf. Eq. (4.65), we can extract the charge radius relative to the electric radius of the core up to NLO

$$\langle r_E^2 \rangle^{(\sigma)} = \frac{f^2}{2\gamma_0^2(1 - r_0\gamma_0)}. \quad (4.50)$$

The LO result can be obtained by setting $r_0 = 0$ in Eq. (4.50). At NLO, we have to consider the additional operator that is proportional to $\eta_0 \sigma^\dagger A_0 \sigma$ and stems from the minimal substitution in the bare dimer propagator. This additional diagram, depicted in Fig. 4.3 (a), guarantees that $G_E(0) = 1$ if the NLO wave function renormalization (4.33) is used. At N³LO, a counterterm related to the radius of the core contributes. In the standard power counting, the factors of f are counted as $\mathcal{O}(1)$, although they can become rather small for large core masses. As a consequence, the counterterm contribution is enhanced numerically.

Since the core is assumed to be a point particle in Halo EFT, we have to add the charge radius of the core to the result of the relative charge radius in Eq. (4.50) to obtain the total charge radius of the halo nucleus.

Electric Form Factors of the D -Wave State

Next, we compute the D -wave form factors by calculating the contribution to the irreducible vertex for $A_0 dd$ interactions up to NLO shown in Fig. 4.3. The first diagram represents three different direct couplings of the photon to the D -wave propagator. Two couplings emerge from the minimal substitution in Eq. (4.4) since r_2 and \mathcal{P}_2 contribute at LO. The last one are the counterterms $\sim L_{C01/2}^{(d)}$ entering at LO that come out of Eq. (4.43). The second diagram stems from minimal substitution in the core propagator in Eq. (4.4) and contributes at NLO. The computation is carried out in the Breit frame, $q = (0, \mathbf{q})$, and the irreducible vertex for the A_0 -photon coupling to the D -wave state in Cartesian coordinates yields

$$\langle ij | J^0 | op \rangle = -ieQ_c \left[G_E(|\mathbf{q}|) E_{ij,op} + \frac{1}{2M_{nc}^2} G_Q(|\mathbf{q}|) Q_{ij,op} + \frac{1}{4M_{nc}^4} G_H(|\mathbf{q}|) H_{ij,op} \right], \quad (4.51)$$

with the three-momentum of the virtual photon $\mathbf{q} = \mathbf{p}' - \mathbf{p}$ and three different D -wave tensors for each form factor $E_{ij,op} \sim q^0$, $Q_{ij,op} \sim q^2$ and $H_{ij,op} \sim q^4$. Compared to the S -wave state, we get contributions to the electric G_E , quadrupole G_Q and hexadecupole form factor G_H for the D -wave. Evidently, the hexadecupole form factor is only observable for the $5/2^+$ D -wave state and unobservable for the $3/2^+$ state. This can be straightforwardly verified by considering the appropriate Clebsch-Gordan coefficients to couple the spin and angular momentum to total J for the two D -wave states in combination with $H_{ij,op}$ in spherical coordinates.

For reasons of simplicity, the calculation is carried out in Cartesian coordinates and the Cartesian tensors that come out automatically of our calculation are given below

$$\tilde{Q}_{ij,op} = \frac{1}{4} \left(q_j q_p \delta_{io} + q_j q_o \delta_{ip} + q_i q_p \delta_{jo} + q_i q_o \delta_{jp} - \frac{4}{3} q_i q_j \delta_{op} - \frac{4}{3} q_o q_p \delta_{ij} + \frac{4}{9} q^2 \delta_{ij} \delta_{op} \right), \quad (4.52)$$

$$\tilde{H}_{ij,op} = \left(q_i q_j q_o q_p - \frac{1}{3} q^2 q_i q_j \delta_{op} - \frac{1}{3} q^2 q_o q_p \delta_{ij} + \frac{1}{9} q^4 \delta_{ij} \delta_{op} \right). \quad (4.53)$$

However, the appropriate Cartesian tensors $E_{ij,op}$, $Q_{ij,op}$, and $H_{ij,op}$ have to fulfill the following constraints

$$E_{ij,op} E_{ij,op} = 5, \quad \delta_{ij} E_{ij,op} = \delta_{op} E_{ij,op} = 0, \quad (4.54)$$

$$E_{ij,op} Q_{ij,op} = 0, \quad \delta_{ij} Q_{ij,op} = \delta_{op} Q_{ij,op} = 0, \quad (4.55)$$

$$E_{ij,op} H_{ij,op} = 0, \quad Q_{ij,op} H_{ij,op} = 0, \quad \delta_{ij} H_{ij,op} = \delta_{op} H_{ij,op} = 0, \quad (4.56)$$

that are derived from the definition of the tensor structure for the respective partial wave and corresponding form factor. The $E_{ij,op}$ tensor, which we deduced in the dimer calculation (4.20) before, represents the number of D -wave polarizations

$$E_{ij,op} = \frac{(\delta_{io} \delta_{jp} + \delta_{ip} \delta_{jo} - \frac{2}{3} \delta_{ij} \delta_{op})}{2}. \quad (4.57)$$

Hence, under consideration of the constraints in Eq. (4.55) and (4.56), we obtain the appropriate quadrupole and hexadecupole tensors

$$Q_{ij,op} = \frac{3}{5}\tilde{Q}_{ij,op} - \frac{1}{5}q^2 E_{ij,op}, \quad (4.58)$$

$$H_{ij,op} = \frac{3}{2}\tilde{H}_{ij,op} - \frac{30}{35}q^2\tilde{Q}_{ij,op} + \frac{3}{35}q^4 E_{ij,op}. \quad (4.59)$$

Note that the neutron spin is unaffected by the charge operator up to the order considered here.

LO results

In the following, we present the LO results for the D -wave state before discussing the NLO effects. At LO, only topology (a) in Fig. 4.3 contributes and we find for the electric $G_E(|\mathbf{q}|)$, quadrupole $G_Q(|\mathbf{q}|)$ and hexadecupole $G_H(|\mathbf{q}|)$ form factors

$$G_E(|\mathbf{q}|) = \frac{1}{r_2 + \mathcal{P}_2\gamma_2^2} \left[\left(\tilde{L}_{C01}^{(d)LO} + \frac{4}{3}\tilde{L}_{C02}^{(d)LO} \right) |\mathbf{q}|^2 + \gamma_2^2 \mathcal{P}_2 + r_2 \right], \quad (4.60)$$

$$G_Q(|\mathbf{q}|) = \frac{2M_{nc}^2}{r_2 + \mathcal{P}_2\gamma_2^2} \left[\frac{20}{3}\tilde{L}_{C02}^{(d)LO} \right], \quad (4.61)$$

$$G_H(|\mathbf{q}|) = 0, \quad (4.62)$$

where $L_{C01/2}^{(d)LO}$ represents the finite LO pieces of the local gauge-invariant operators $L_{C01/2}^{(d)}$ from Eq. (4.43). At NLO, these operators have a finite piece $L_{C01/2}^{(d)NLO}$ as well as μ -dependent part that cancels the renormalization scale dependence from the loop contribution. For a better readability, we absorb some prefactors in the definition of the counterterms and define

$$\tilde{L}_{C01}^{(d)} = \frac{15\pi}{eQ_c g_2^2 m_R^2} L_{C01}^{(d) \text{fin}}, \quad (4.63)$$

$$\tilde{L}_{C02}^{(d)} = \frac{15\pi}{eQ_c g_2^2 m_R^2} L_{C02}^{(d) \text{fin}}. \quad (4.64)$$

A more detailed discussion of the evaluation of the Feynman diagrams in Fig. 4.3 (a) is presented in App. A.4.1.

The electric form factor for $|\mathbf{q}| \rightarrow 0$ is normalized such that

$$G_E(|\mathbf{q}|) \approx 1 - \frac{1}{6} \langle r_E^2 \rangle |\mathbf{q}|^2 + \dots, \quad (4.65)$$

and an expansion of Eq. (4.60) yields $G_E(0) = 1$ and an electric radius of the D -wave state at LO

$$\langle r_E^2 \rangle^{(d)} = -\frac{6}{r_2 + \mathcal{P}_2\gamma_2^2} \left(\tilde{L}_{C01}^{(d)LO} + \frac{4}{3}\tilde{L}_{C02}^{(d)LO} \right), \quad (4.66)$$

which means that the electric radius is not a prediction.

Moreover, the quadrupole and hexadecupole form factors can be expanded for small $|\mathbf{q}|$ as

$$\frac{1}{M_{nc}^2} G_Q(|\mathbf{q}|) \approx \mu_Q \left(1 - \frac{1}{6} \langle r_Q^2 \rangle |\mathbf{q}|^2 + \dots \right), \quad (4.67)$$

$$\frac{1}{M_{nc}^4} G_H(|\mathbf{q}|) \approx \mu_H \left(1 - \frac{1}{6} \langle r_H^2 \rangle |\mathbf{q}|^2 + \dots \right). \quad (4.68)$$

Thus, we expand Eq. (4.61) and find for the quadrupole moment at LO

$$\mu_Q^{(d)} = \frac{40 \tilde{L}_{C02}^{(d)LO}}{3(r_2 + \mathcal{P}_2 \gamma_2^2)}, \quad (4.69)$$

which also contains an unknown counterterm.

NLO results

At NLO, diagram (b) in Fig. 4.3 also contributes. The detailed calculation of the loop diagram is shown in App. A.4.2. After adjusting $L_{C01/2}^{(d)NLO}$ to satisfy the renormalization conditions (4.66) and (4.69), we obtain

$$G_E(|\mathbf{q}|) = -\frac{1}{6} \langle r_E^2 \rangle^{(d)} |\mathbf{q}|^2 + \frac{1}{r_2 + \mathcal{P}_2 \gamma_2^2 - 5\gamma_2^3} \left[\frac{77\gamma_2 f^2 |\mathbf{q}|^2}{48} - \frac{19\gamma_2^3}{4} + \gamma_2^2 \mathcal{P}_2 + r_2 \right. \\ \left. - \arctan\left(\frac{f|\mathbf{q}|}{2\gamma_2}\right) \left(\frac{21f^3 |\mathbf{q}|^3}{32} + \frac{13\gamma_2^2 f |\mathbf{q}|}{4} + \frac{\gamma_2^4}{2f |\mathbf{q}|} \right) \right], \quad (4.70)$$

$$G_Q(|\mathbf{q}|) = M_{nc}^2 \mu_Q^{(d)} + \frac{2M_{nc}^2}{r_2 + \mathcal{P}_2 \gamma_2^2 - 5\gamma_2^3} \left[\frac{125\gamma_2 f^2}{42} - \frac{25\gamma_2^3}{7|\mathbf{q}|^2} \right. \\ \left. - \arctan\left(\frac{f|\mathbf{q}|}{2\gamma_2}\right) \left(\frac{75f^3 |\mathbf{q}|}{28} + \frac{75\gamma_2^2 f}{14|\mathbf{q}|} - \frac{50\gamma_2^4}{7f |\mathbf{q}|^3} \right) \right], \quad (4.71)$$

$$G_H(|\mathbf{q}|) = \frac{2}{3} \frac{4M_{nc}^4}{r_2 + \mathcal{P}_2 \gamma_2^2 - 5\gamma_2^3} \left[-\frac{45\gamma_2 f^2}{64|\mathbf{q}|^2} + \frac{45\gamma_2^3}{16|\mathbf{q}|^4} \right. \\ \left. - \arctan\left(\frac{f|\mathbf{q}|}{2\gamma_2}\right) \left(\frac{45f^3}{128|\mathbf{q}|} - \frac{15\gamma_2^2 f}{16|\mathbf{q}|^3} + \frac{45\gamma_2^4}{8f |\mathbf{q}|^5} \right) \right], \quad (4.72)$$

with $f = m_R/M$. From the loop diagram in Fig. 4.3, a divergence emerges that is absorbed by \mathcal{P}_2 from the direct photon coupling in diagram (a) and two more that are absorbed by the μ -dependent parts of the counterterms $L_{C02}^{(d)}$ and $L_{C01}^{(d)}$ at NLO. We expand Eq. (4.72) and derive the hexadecupole moment

$$\mu_H^{(d)} = -\frac{2f^4}{3\gamma_2(r_2 + \mathcal{P}_2 \gamma_2^2)}, \quad (4.73)$$

as a prediction. The electric radius $\langle r_E^2 \rangle^{(d)}$ and the quadrupole moment $\mu_Q^{(d)}$ are not predicted. They are used to fix the counterterms $L_{C02}^{(d)}$ and $L_{C01}^{(d)}$. The quadrupole and hexadecupole radii yield

$$\langle r_Q^2 \rangle^{(d)} = \frac{27}{28} \frac{f^4}{\gamma_2 \tilde{L}_{C02}^{(d)}}, \quad (4.74)$$

$$\langle r_H^2 \rangle^{(d)} = \frac{9}{14} \frac{f^2}{\gamma_2^2}, \quad (4.75)$$

where the hexadecupole radius is predicted by Halo EFT and the quadrupole radius depends on the counterterm $L_{C02}^{(d)}$, fixed by the quadrupole moment. Thus, we can predict the quadrupole radius if the quadrupole moment is known.

We continue with the calculation of magnetic form factors, while the explicit application of our Halo EFT results to ^{15}C and ^{17}C is presented in Sec. 4.10.

4.7.2 Magnetic Moments

The magnetic properties of shallow bound states are predominantly determined by the magnetic moments of its degrees of freedom. The magnetic moment of a single particle is introduced into the Lagrangian through an additional magnetic one-body operator [49, 84]. An additional counterterm enters via a two-body current. Assuming a spin-0 core, the effective Lagrangian is written as

$$\mathcal{L}_M = \kappa_n \mu_N n^\dagger \boldsymbol{\sigma} \cdot \mathbf{B} n + 2\mu_N L_M^J \Phi^\dagger \mathbf{S}_J \cdot \mathbf{B} \Phi, \quad (4.76)$$

where Φ is a place holder for the relevant auxiliary field ($\sigma_s, \pi_s, d_{J,M}, \dots$), \mathbf{S}_J is the corresponding spin matrix for spin J , $\boldsymbol{\sigma}$ represents the Pauli matrices, μ_N denotes the nuclear magneton, and L_M^J the coupling constant for the magnetic two-body current. For the anomalous magnetic moment of the neutron we use $\kappa_n = -1.913$ [37].

The corresponding Feynman rule for the coupling of the photon to the magnetic moment of the neutron is given by

$$-\kappa_n \mu_N \boldsymbol{\sigma}_{m_s, m'_s} \cdot (\mathbf{k} \times \boldsymbol{\epsilon}), \quad (4.77)$$

with the photon momentum \mathbf{k} , the photon polarization vector $\boldsymbol{\epsilon}$ and the Pauli matrices $\boldsymbol{\sigma}$. The incoming and outgoing spin polarizations of the neutron are denoted by m_s and m'_s , respectively.

Compared to the electric form factors, magnetic form factors are calculated from Feynman diagrams with a vector photon between the initial and final bound state. Furthermore, the photon not only couples to the electric charge of the core but also to the magnetic moment of the halo neutron. As before, we review the S -wave result of the magnetic moment before we consider the D -wave state.

Magnetic Moment of the S-Wave State

We reproduce the results obtained by *Fernando et al.* [84] who calculated electromagnetic form factors for S -wave states of one-neutron halo nuclei. Up to NLO, only the two last diagrams in Fig. 4.4 contribute

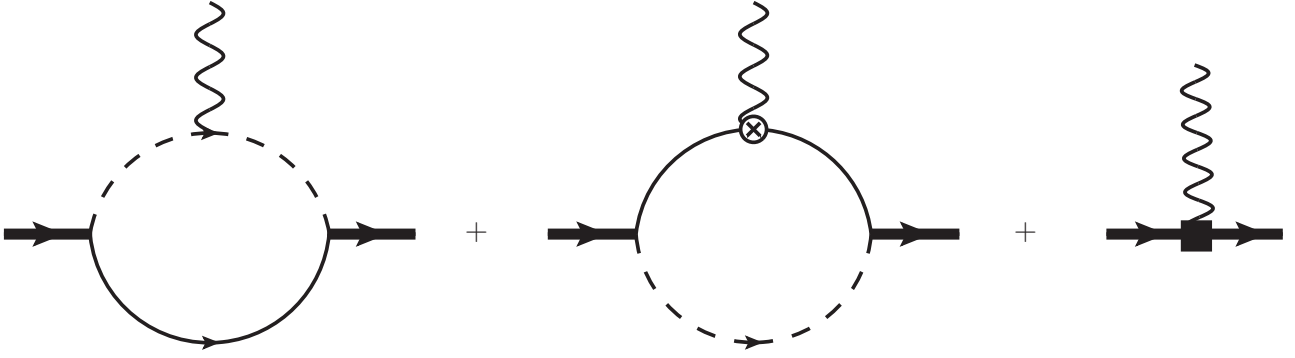


Figure 4.4.: Diagrams contributing to the magnetic moment. The first diagram is the coupling of a vector photon to the charge of the core arising from minimal substitution in the Lagrangian. The second diagram displays a vector photon coupling to the magnetic moment of the neutron. The last diagrams shows a two-body current. The thick solid line denotes the dressed σ -propagator.

to the magnetic form factor in the Breit frame and we derive for the magnetic form factor

$$\frac{eQ_c}{2M_{nc}} G_M(|\mathbf{q}|) = Z_\sigma \mu_N \left(g_0^2 \kappa_n \frac{mm_R}{\pi|\mathbf{q}|} \arctan \left[\frac{|\mathbf{q}|m_R}{2m\gamma_0} \right] + L_M^\sigma \right), \quad (4.78)$$

with the NLO wave function renormalization

$$Z_\sigma = \frac{2\pi\gamma_0}{m_R^2 g_0^2 (1 - r_0 \gamma_0)} \quad \text{and we define} \quad \tilde{L}_M^\sigma = \frac{2\pi L_M^\sigma}{m_R^2 g_0^2}. \quad (4.79)$$

The magnetic moment κ_σ is obtained by evaluating the form factor at $|\mathbf{q}| = 0$

$$\kappa_\sigma = \frac{eQ_c}{2M_{nc}} G_M(0) = \frac{\kappa_n + \tilde{L}_M^\sigma \gamma_0}{1 - r_0 \gamma_0}, \quad (4.80)$$

where κ_σ is given in units of μ_N . Naive dimensional analysis with rescaled fields, $[\tilde{\sigma}] = 2$, determines the scaling of the counterterm $\tilde{L}_M^\sigma \sim R_{\text{core}}$. As a consequence, \tilde{L}_M^σ contributes at NLO. At LO, we set $r_0 = 0$ and the magnetic moment of the S -wave state is thus given by the magnetic moment of the neutron, κ_n .

Magnetic Moments of the D -Wave State

In the case of the D -wave, the only contribution to the magnetic moment at LO is the two-body current in Eq. (4.76), which corresponds to the last diagram in Fig. 4.4. Hence, we obtain for the magnetic form factor

$$\frac{eQ_c}{2M_{nc}} G_M(|\mathbf{q}|) = Z_d \mu_N L_M^d = -\frac{\mu_N \tilde{L}_M^d}{r_2 + \mathcal{P}_2 \gamma_2^2}, \quad (4.81)$$

with the wave function renormalization at LO

$$Z_d = -\frac{15\pi}{m_R^2 g_2^2} \frac{1}{r_2 + \mathcal{P}_2 \gamma_2^2} \quad \text{and we adopt} \quad \tilde{L}_M^d = \frac{15\pi L_M^d}{m_R^2 g_2^2}. \quad (4.82)$$

The expansion of Eq. (4.81) for small $|\mathbf{q}|$ yields for the magnetic form factor at LO

$$\kappa_d = \frac{eQ_c}{2M_{nc}} G_M(0) = -\frac{\tilde{L}_M^d}{r_2 + \mathcal{P}_2 \gamma_2^2}, \quad (4.83)$$

where κ_d is given in units of μ_N as before. Because of the unknown counterterm, κ_d cannot be predicted. Beyond LO, we also need to consider the loop diagrams in Fig. 4.4. Therefore, additional counterterms are required to renormalize the corresponding divergences. This complicates predictions even further and for that reason, we do not calculate the NLO contribution to the magnetic form factors for the D -wave state explicitly.

In general, the magnetic moment of the D -wave states will thus differ significantly from the magnetic moment of the neutron since κ_n is a NLO contribution.

4.8 Electromagnetic Transitions

After investigating the static electromagnetic properties of halo states, we consider E2 and M1 transitions between S - and D -wave states in this chapter. In this case, the amplitudes are calculated from Feynman diagrams with a real vector photon between the initial and final bound state. Moreover, the initial and final states are no longer identical. We start with the calculation of the S -to- D state E2 transition and then consider the M1 transitions from S -to- D and D -to- D' state.

4.8.1 E2 Transitions

The diagrams contributing to the irreducible vertex for the E2 transition from the S -wave state to the D -wave state up to NLO are depicted in Fig. 4.5. At LO, only the two loop diagrams (a) from minimal substitution contribute and at NLO, an additional counterterm (b) enters.

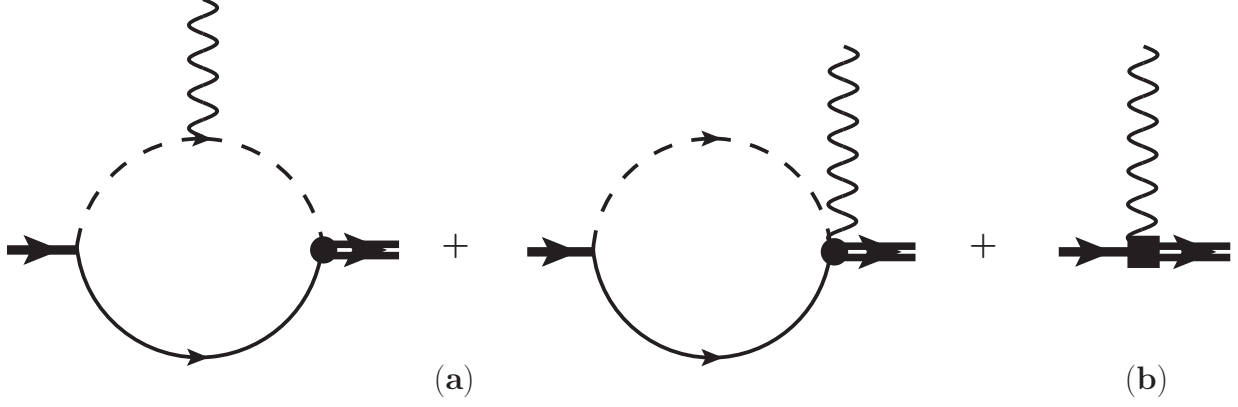


Figure 4.5.: The diagrams contributing to the irreducible vertex that determines the S -to- D state transition in Halo EFT up to NLO. The thick double line denotes the dressed D -wave propagator and the thick single line the dressed S -wave propagator.

The additional local operator with one power of the photon field for the B(E2) transition strength is given by

$$\mathcal{L}_E = -L_{E2}^{(sd)} \sigma_m d_{m'}^\dagger \left(\frac{1}{2} m J m' \middle| 2m_l \right) (1\alpha \ 1\beta \middle| 2m_l) \left[\nabla_\alpha \nabla_\beta A_0 - \partial_0 \frac{(\nabla_\alpha A_\beta + \nabla_\beta A_\alpha)}{2} \right], \quad (4.84)$$

where repeated spin indices are summed over. Using the rescaled fields $\tilde{\sigma}$ and \tilde{d} (4.44), we can determine the scaling of the operator with respect to R_{core} from naive dimensional analysis

$$L_{E2}^{(sd)} \sim R_{\text{core}} l_{E2}^{(5/2)} g_0 g_2 m_R^2, \quad (4.85)$$

with $l_{E2}^{(5/2)}$ of order one. Below we show that the operator $\sim L_{E2}^{(sd)}$ yields a NLO contribution.

LO result

We start with the presentation of the LO results and then discuss the NLO effects. The photon has a four momentum of $k = (\omega, \mathbf{k})$ and its polarization index is denoted by ν . The computation of the relevant diagrams yields a vertex function $\Gamma_{m' m_s \nu}$, where m' is the total angular momentum projection of the D -wave state and m_s denotes the spin projection of the S -wave state. The detailed evaluation of both Feynman diagrams is shown in App. A.3. Since the neutron spin is unaffected by this transition, we calculate the vertex function with respect to the specific components of the D -wave interaction

$$\Gamma_{m' m_s \nu} = \sum_{m_l} \left(\frac{1}{2} m_s \ 2m_l \middle| J m' \right) \sum_{\alpha\beta} (1\alpha \ 1\beta \middle| 2m_l) \tilde{\Gamma}_{\alpha\beta \nu}, \quad (4.86)$$

where J denotes the total spin of the D -wave state. In the case of $m_s = m' = \pm 1/2$, only $m_l = 0$

contributes to the sum in Eq. (4.86) and we derive for $J = 5/2$

$$\Gamma_{++\nu} = \Gamma_{--\nu} = \sqrt{\frac{2}{5}}\tilde{\Gamma}_{00\nu} + \sqrt{\frac{1}{10}}\tilde{\Gamma}_{1-1\nu} + \sqrt{\frac{1}{10}}\tilde{\Gamma}_{-11\nu}, \quad (4.87)$$

where \pm denotes the total angular momentum projection $\pm 1/2$. We calculate the irreducible vertex in Coulomb gauge so that we have $\mathbf{k} \cdot \boldsymbol{\epsilon} = 0$ for real photons with the photon polarization vector $\boldsymbol{\epsilon}$. Additionally, we choose, without loss of generality, $\mathbf{k} \cdot \mathbf{p} = 0$ to simplify the calculation, where \mathbf{p} denotes the incoming momentum of the S -wave state. As a result, the space-space components of the vertex function in Cartesian coordinates can be written as

$$\tilde{\Gamma}_{ijk} = \Gamma_E \frac{1}{2} (k_j \delta_{ik} + k_i \delta_{jk}) + \Gamma_M p_k \left(k_i k_j - \frac{1}{3} \delta_{ij} k^2 \right). \quad (4.88)$$

By choosing the photon to be traveling in \hat{z} direction, we obtain

$$\tilde{\Gamma}_{333} = \Gamma_E \omega, \quad \text{with } |\mathbf{k}| = k_z = \omega. \quad (4.89)$$

By comparing the definitions for the transition rate depending on B(E2) and the transition rate as a function of the irreducible vertex Γ_E [94], we deduce the following dependence for arbitrary multipolarity λ

$$B(E\lambda) = \frac{1}{2\pi} \frac{1}{k^{2\lambda}} \frac{\lambda [(2\lambda + 1)!!]^2}{(\lambda + 1)(2\lambda + 1)} |\Gamma_{m'm_s\nu}|^2. \quad (4.90)$$

Hence, in the case of B(E2) and if we replace $\Gamma_{m'm_s\nu}$ with Eq. (4.87) and (4.89), it follows

$$B(E2: 1/2^+ \rightarrow 5/2^+) = \frac{15}{\pi} \left(\frac{\Gamma_{++3}}{\omega^2} \right)^2 = \frac{6}{\pi} \left(\frac{\bar{\Gamma}_E}{\omega} \right)^2, \quad (4.91)$$

with the renormalized, irreducible vertex $\bar{\Gamma}_E = \sqrt{Z_\sigma Z_d} \Gamma_E$. At LO, Z_σ and Z_d are given in Eq. (4.32). Using the result of the calculation for Γ_E from the diagrams in Fig. 4.5 (a), App. A.3, we derive at LO

$$B(E2: 1/2^+ \rightarrow 5/2^+) = \frac{4}{5\pi} \frac{Z_{\text{eff}}^2 e^2 \gamma_0}{-r_2 - \mathcal{P}_2 \gamma_2^2} \left[\frac{3\gamma_0^2 + 9\gamma_0 \gamma_2 + 8\gamma_2^2}{(\gamma_0 + \gamma_2)^3} \right]^2, \quad (4.92)$$

where γ_2 , r_2 , and \mathcal{P}_2 are the parameters of the $5/2^+$ state and the effective charge, $Z_{\text{eff}} = \left(\frac{m}{M_{nc}} \right)^2 Q_c$, comes out of the calculation automatically and is given for arbitrary multipolarity λ by [95]

$$Z_{\text{eff}}^{(\lambda)} = Z_n \left(\frac{M}{M_{nc}} \right)^\lambda + Z_c \left(-\frac{m}{M_{nc}} \right)^\lambda. \quad (4.93)$$

Consequently, we can predict the B(E2) transition in Halo EFT at LO once γ_0 , γ_2 and the wave function renormalization constants are known.

The renormalized B(E2) matrix element scales as $\sim R_{\text{halo}} \sqrt{R_{\text{core}} R_{\text{halo}}}$, whereas the operator $\sim L_{E2}^{(sd)}$ scales as $\sim R_{\text{core}} \sqrt{R_{\text{core}} R_{\text{halo}}}$ and therefore, contributes at NLO. Both diagrams in Fig. 4.5 (a) are divergent. However, the divergences cancel each other. This is expected since gauge invariance precludes additional counterterms that could absorb divergences at this order.

Alternatively, the same result for $\tilde{\Gamma}_E$ can be derived using current conservation

$$\omega \tilde{\Gamma}_{ij0} = k_k \tilde{\Gamma}_{ijk}, \quad (4.94)$$

if we calculate the space-time components of the vertex function $\tilde{\Gamma}$. In contrast to $\tilde{\Gamma}_{ijk}$, we have to consider only the left diagram in Fig. 4.5 with an A_0 -photon vertex for $\tilde{\Gamma}_{ij0}$ at LO.

The calculation of the transition to the $3/2^+$ state can be carried out in the same way. The only difference is a relative factor of $2/3$ for B(E2) because of the different Clebsch-Gordan coefficient in Eq. (4.87)

$$\text{B(E2: } 1/2^+ \rightarrow 3/2^+) = \frac{8}{15\pi} \frac{Z_{\text{eff}}^2 e^2 \gamma_0}{-r_2 - \mathcal{P}_2 \gamma_2^2} \left[\frac{3\gamma_0^2 + 9\gamma_0 \gamma_2 + 8\gamma_2^2}{(\gamma_0 + \gamma_2)^3} \right]^2, \quad (4.95)$$

where γ_2 , r_2 , and \mathcal{P}_2 are now the parameters of the $3/2^+$ state.

NLO result

To obtain the NLO result for the $1/2^+$ to the $5/2^+$ transition, we have to take the additional counterterm for B(E2), Eq. (4.84) or diagram (b) in Fig. 4.5, into account and use the NLO expressions for Z_σ and Z_d in Eq. (4.33)

$$\text{B(E2: } 1/2^+ \rightarrow 5/2^+) = \frac{6\gamma_0/\pi}{(r_2 + \mathcal{P}_2 \gamma_2^2 - 5\gamma_2^3)(r_0 \gamma_0 - 1)} \left(\frac{\sqrt{2} Z_{\text{eff}} e}{\sqrt{15}} \left[\frac{3\gamma_0^2 + 9\gamma_0 \gamma_2 + 8\gamma_2^2}{(\gamma_0 + \gamma_2)^3} \right] + \frac{2m_R \tilde{L}_{E2}^{(sd)}}{\gamma_0^2 - \gamma_2^2} \right)^2, \quad (4.96)$$

with the definition

$$\tilde{L}_{E2}^{(sd)} = \frac{\sqrt{30}\pi}{m_R^2 g_0 g_2} L_{E2}^{(sd)}. \quad (4.97)$$

Because of the additional counterterm that has to be fitted, numerical predictions for the NLO result are currently not possible. As before, the expression for the transition to the $3/2^+$ state differs by a relative factor of $2/3$.

In principle, we can also calculate the E2 transition for $D \rightarrow D'$. However, we do not present the result here since the relevant diagram diverges cubically and therefore, additional counterterms are required for this observable already at LO. Instead, we continue with the M1 transitions.

4.8.2 M1 Transitions

The selection rules for M1 transitions, i.e. parity conservation and $\Delta J = 0, \pm 1$, allow only transitions from $3/2^+ \rightarrow 1/2^+$ or $3/2^+ \rightarrow 5/2^+$ and vice versa for S - and D -wave states. As there are no relevant M1 transitions in ^{15}C , we focus on ^{17}C in this section.

$S \rightarrow D$ Transition

We will first consider the M1 transition strength from the $3/2^+$ ground state (D -wave) to the first excited $1/2^+$ state (S -wave) in ^{17}C since it was measured in Refs. [86, 87]. The experimental result is small compared with typical M1 transition strengths in nuclei

$$B(\text{M1: } 1/2^+ \rightarrow 3/2^+) = 1.04_{-0.12}^{+0.03} \times 10^{-2} \mu_N^2 \quad (4.98)$$

$$= 0.58 \times 10^{-2} \text{ W.u.} , \quad (4.99)$$

expressed in Weisskopf units and taken from Ref. [87].

In the neutron-core picture of Halo EFT, the M1 transition from a D -wave to an S -wave state is forbidden for one-body currents, which agrees with the experimental suppression of the transition. The non-zero transition strength can only be accounted for by a two-body current that takes short-ranged (core) physics into account. We therefore include the gauge-invariant counterterm

$$\mathcal{L}_M = -\mu_N L_{M1}^{\sigma d} \sigma_m^\dagger d_{m'} \left(\frac{1}{2} m 1 i \left| \frac{3}{2} m' \right. \right) B_i . \quad (4.100)$$

By rescaling the fields to absorb unnaturally large coupling constants, leading to $[\tilde{\sigma}] = 2$, $[\tilde{d}] = 0$, and using naive dimensional analysis for the rescaled fields, we derive $L_{M1}^{\sigma d} \sim R_{\text{core}}^{-1} l_{M1}^{\sigma d} g_0 g_2 m_R^2$ with $l_{M1}^{\sigma d}$ of order one. To obtain the magnetic transition amplitude, we calculate the vertex function

$$\Gamma_{mm'i} = \left(\frac{1}{2} m 1 i \left| \frac{3}{2} m' \right. \right) \mu_N \tilde{L}_{M1}^{\sigma d} \epsilon_{ijk} k_j , \quad (4.101)$$

where we adopt

$$\tilde{L}_{M1}^{\sigma d} = \frac{\sqrt{30}\pi}{m_R^2 g_0 g_2} L_{M1}^{\sigma d} . \quad (4.102)$$

If we consider the case $m = -m' = \pm 1/2$ and choose the photon to be traveling in \hat{z} direction, we obtain

$$\tilde{\Gamma}_{\pm\mp, \mp 1} = \mp \frac{\mu_N}{\sqrt{3}} \tilde{L}_{M1}^{\sigma d} \omega . \quad (4.103)$$

This yields for the M1 transition strength

$$B(M1: 1/2^+ \rightarrow 3/2^+) = \frac{3}{4\pi} \left(\frac{\bar{\Gamma}_{\pm\mp, \mp 1}}{\omega} \right)^2 = -\frac{1}{4\pi} \frac{\gamma_0}{r_2 + \mathcal{P}_2 \gamma_2^2} (\tilde{L}_{M1}^{\sigma d})^2 \mu_N^2. \quad (4.104)$$

Because of the additional counterterm at LO, we cannot predict $B(M1)$ numerically to compare our Halo EFT result with the experimental data.

$D' \rightarrow D$ Transition

The M1 transition strength from the $3/2^+$ ground state (D -wave) to the second excited $5/2^+$ state (D' -wave) in ^{17}C was also measured in Ref. [86]

$$B(M1: 5/2^+ \rightarrow 3/2^+) = 7.12_{-0.96}^{+1.27} \times 10^{-2} \mu_N^2. \quad (4.105)$$

Compared to the D -to- S -state M1 transition strength, it is around one order of magnitude larger. This agrees with the fact that M1 transitions are allowed for neutron-core systems with one-body currents by the usual selection rules. We calculate both loop diagrams in Fig. 4.6 and find that we need additional counterterms to absorb all divergences. Moreover, we obtain results for the M3 and M5 transition. Two different counterterms are required for the M1 transition and two more for the M3 transition.

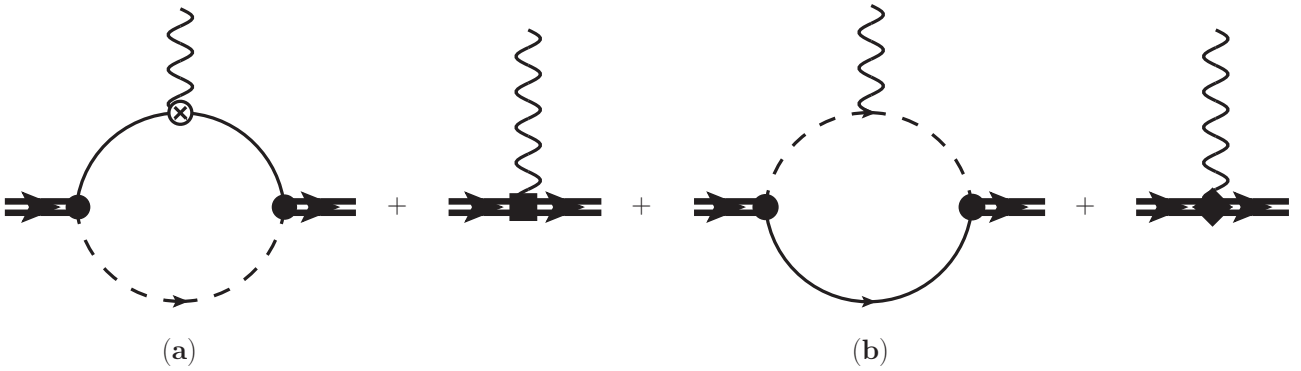


Figure 4.6.: Relevant diagrams for the M1 transition. In the diagram (a) a vector photon couples to the magnetic moment of the neutron and in (b) to the electric charge of the core. In the two remaining diagrams the photon couples directly to the D -wave dimers. For a more detailed description of the lines, see Fig. 4.2.

In the following, we concentrate the discussion on the M1 transition. In this case, the two counterterms are given by

$$\mathcal{L}_M = -L_{M1a}^{dd'} \mu_N d_{ij}^\dagger d'_{ij} \sigma_k^{m_s m_s'} B_k - L_{M1b}^{dd'} \mu_N d_{ij}^\dagger \nabla \cdot \mathbf{A} d'_{ij}. \quad (4.106)$$

The first counterterm is needed to renormalize the scale dependence from diagram (a) with the magnetic

photon coupling to the neutron and the second one renormalizes the scale for the vector photon coupling in diagram (b), respectively. For a better readability, we absorb some prefactors in the definition of the counterterms and adopt

$$\tilde{L}_{M1a}^{dd'} = \frac{15\pi}{m_R^2 g_{2'} g_2} L_{M1a}^{dd' \text{ fin}}, \quad (4.107)$$

$$\tilde{L}_{M1b}^{dd'} = \frac{15\pi}{m_R^2 g_{2'} g_2} L_{M1b}^{dd' \text{ fin}}, \quad (4.108)$$

which represent the finite pieces of the local gauge-invariant operators. The μ -dependent part of $L_{M1a}^{dd'}$ and $L_{M1b}^{dd'}$ cancels the renormalization scale dependence from the loop contribution.

As before, the photon has a four-momentum $k = (\omega, \mathbf{k})$ and its polarization index is denoted by ν . The computation of both diagrams leads to a vertex function $\Gamma_{mm'\nu}$, where m is the total angular momentum projection of the $3/2^+$ state and m' denotes the spin projection of the $5/2^+$ state. The computation of the vertex function with respect to the specific components of the D -wave interaction yields

$$\Gamma_{mm'\nu} = \sum_{\alpha\beta\delta\eta m_l m_l' m_s m_s'} \left(\frac{1}{2} m_s 2m_l \middle| \frac{3}{2} m \right) (1\alpha 1\beta | 2m_l) \left(\frac{1}{2} m_s' 2m_l' \middle| \frac{5}{2} m' \right) (1\delta 1\eta | 2m_l') \tilde{\Gamma}_{\alpha\beta\delta\eta\nu}. \quad (4.109)$$

We calculate the irreducible vertex in Coulomb gauge so that we have $\mathbf{k} \cdot \boldsymbol{\epsilon} = 0$ for real photons. Additionally, we choose $\mathbf{k} \cdot \mathbf{p} = 0$, where \mathbf{p} denotes the incoming momentum of the D -wave state. As a result, the space-space components of the vertex function in Cartesian coordinates for the left diagram can be written as

$$\tilde{\Gamma}_{ijopk} = \Gamma_M^{(a)} \epsilon_{abk} \sigma_a^{m_s m_s'} k_b \left(\frac{\delta_{io} \delta_{jp} + \delta_{ip} \delta_{jo}}{2} - \frac{1}{3} \delta_{ij} \delta_{op} \right), \quad (4.110)$$

and for the right one

$$\tilde{\Gamma}_{ijopk} = \Gamma_M^{(b)} p_k \left(\frac{\delta_{io} \delta_{jp} + \delta_{ip} \delta_{jo}}{2} - \frac{1}{3} \delta_{ij} \delta_{op} \right) + \Gamma_{E2} \left[k_i \left(\frac{\delta_{jp} \delta_{ko} + \delta_{jo} \delta_{kp}}{2} - \frac{1}{3} \delta_{jk} \delta_{op} \right) + \dots \right], \quad (4.111)$$

where the ellipsis inside the bracket stands for further terms with permuted indices. In the left diagram, the photon couples to the spin of the neutron and we get a spin flip $m_s \neq m_s'$. In the case of the right diagram, there is no spin flip so that $m_s = m_s'$. By choosing the photon to be traveling in \hat{z} direction, it follows from the tensor structure of $\tilde{\Gamma}_{ijop\nu}$ that $m_l = m_l'$ and $\nu \neq 0$. For the case that $m = \pm 1/2 = -m'$, we derive

$$-\Gamma_{-+,1} = \Gamma_{+,-,1} = \frac{\sqrt{6}}{5} \Gamma_M^{(a)} \sqrt{2}\omega, \quad (4.112)$$

and for $m = m'$, we get zero for all possible values. This yields for the B(M1: $3/2^+ \rightarrow 5/2^+$) transition

$$B(\text{M1: } 3/2^+ \rightarrow 5/2^+) = \frac{3}{4\pi} \left(\frac{\Gamma_{+,-,-1}}{\omega} \right)^2 = \frac{9}{25\pi} \left(\frac{\bar{\Gamma}_M^{(a)} \omega}{\omega} \right)^2 \quad (4.113)$$

$$= \frac{9\mu_N^2}{25\pi} \frac{1}{r_2 + \mathcal{P}_2 \gamma_2^2} \frac{1}{r_{2'} + \mathcal{P}_{2'} \gamma_{2'}^2} \left[\tilde{L}_{M1a}^{dd'} + \frac{2\gamma_{2'}^4 \kappa_n}{(\gamma_{2'} + \gamma_2)} + 2\kappa_n (\gamma_2 \gamma_{2'}^2 + \gamma_2^3) \right]^2, \quad (4.114)$$

with the renormalized, irreducible vertex $\bar{\Gamma}_M = \sqrt{Z_d Z_{d'}} \Gamma_M$. By rescaling the fields, $[\tilde{d}] = [\tilde{d}'] = 0$, and using dimensional analysis, we find that the counterterm scales as

$$L_{M1a/b}^{dd'} \sim R_{\text{core}}^{-3} l_{M1a/b}^{dd'} g_2 g_{2'} m_R^2, \quad (4.115)$$

with $l_{M1a/b}^{dd'}$ of order one. In contrast, the contribution from the loop scales as R_{halo}^{-3} , which means that at LO, only the counterterm contributes to the M1 transition and the loop diagram is suppressed by $(R_{\text{core}}/R_{\text{halo}})^3$. Thus, the M1 transition is strongly dominated by short-range physics. As a consequence, a numerical prediction for the M1 transition for the $D' \rightarrow D$ case is generally difficult and at the moment, not possible for ^{17}C due to the lack of data.

4.9 Neutron Capture

An important process providing insight into the properties of halo nuclei is neutron capture or the time-reversed process, photodissociation. In contrast to the standard *ab initio* approaches, Halo EFT allows for the calculation of static observables as well as nuclear reactions within the same theoretical framework. In this chapter, we compute cross sections for the E1 and M1 neutron capture reaction on one-neutron halo nuclei into the S - and D -wave state. Because of the detailed balance theorem [96], the time-reversed process, i.e. breakup reactions through photodissociation, can also be described without further calculations.

The cross section for the neutron capturing process, $n + c \rightarrow A_{nc} + \gamma$, in the center-of-mass system is related to the squared matrix element \mathcal{M} by the following relation

$$\sigma^{(\text{inelastic})} = \frac{1}{|\mathbf{v}_n - \mathbf{v}_c|} |\mathcal{M}|^2 \Phi_2 = \frac{2m_R}{|\mathbf{p}|} |\mathcal{M}|^2 \Phi_2, \quad (4.116)$$

where A_{nc} represents the nucleus of the composite neutron-core system, $\mathbf{v}_n - \mathbf{v}_c$ indicates the relative neutron and core velocity and \mathbf{p} is the relative momentum of the nc pair. Moreover, Φ_2 denotes the

two-particle phase space and is given by

$$\Phi_2 = \int \frac{d^3 \mathbf{p}_{A_{nc}}}{(2\pi)^3} \int \frac{d^3 \mathbf{k}}{(2\pi)^3} \frac{1}{2\omega} (2\pi)^3 \delta^{(3)}(\mathbf{p}_{A_{nc}} + \mathbf{k}) (2\pi) \delta \left(\frac{p^2}{2m_R} - \omega + B_E - \frac{p_{A_{nc}}^2}{2M_{nc}} \right) \quad (4.117)$$

$$= \int \frac{d^3 \mathbf{k}}{(2\pi)^3} \frac{1}{2\omega} (2\pi) \delta \left(\frac{p^2}{2m_R} - \omega + B_E - \frac{\omega^2}{2M_{nc}} \right) \quad (4.118)$$

$$= \int \frac{d\omega \omega^2}{(2\pi)^3} \int d\Omega \frac{1}{2\omega} (2\pi) \delta \left(\frac{p^2}{2m_R} - \omega + B_E - \frac{\omega^2}{2M_{nc}} \right) \quad (4.119)$$

$$= \frac{1}{2\pi} M_{nc} \left(1 - \sqrt{\frac{M_{nc}}{M_{nc} + \left(B_E + \frac{p^2}{2m_R} \right)}} \right), \quad (4.120)$$

where B_E denotes the binding energy of the A_{nc} system, $\omega = |\mathbf{k}|$ the photon energy and \mathbf{k} the photon momentum. By exploiting the energy conservation

$$\frac{p^2}{2m} + \frac{p^2}{2M} = \omega - B_E + \frac{\omega^2}{2M_{nc}}, \quad (4.121)$$

and by replacing $\left(B_E + \frac{p^2}{2m_R} \right)$ with $\left(\omega + \frac{\omega^2}{2M_{nc}} \right)$, it follows

$$\Phi_2 = \frac{1}{2\pi} \frac{\omega M_{nc}}{\omega + M_{nc}}. \quad (4.122)$$

The total cross section thus reads

$$\sigma^{(\text{inelastic})} = \frac{1}{\pi} \frac{m_R}{p} \frac{M_{nc} \omega}{\omega + M_{nc}} |\mathcal{M}|^2 \approx \frac{m_R}{\pi} \frac{\omega}{p} |\mathcal{M}|^2, \quad (4.123)$$

where we used in the last step that $\omega \ll M_{nc}$.

4.9.1 E1 Neutron Capture

We start with E1 neutron capture, which generally dominates over M1 capture. For ^{15}C , E1 neutron capture was already considered in Ref. [82]. In their studies, *Rupak et al.* included P -waves as initial state interactions. Their power counting, however, differs from ours for shallow bound states beyond S -wave so that P -wave initial state interactions are LO in Ref. [82] but NLO contributions in our power-counting scheme, cf. Ref. [64] and App. B. In the following, we calculate the neutron capture cross section at LO and therefore, neglect diagrams including P -wave states. First, we discuss E1 capture into the S -wave state and then consider D -wave states.

E1 Capture into the S-Wave State

E1 capture proceeds dominantly through the vector coupling of the photon to the halo core. The corresponding LO operator is generated through minimal substitution in Eq. (4.4), cf. Eq. (4.42). The diagram that contributes at LO to this process is shown in Fig. 4.7. It is the time-reversed diagram of the photodissociation reaction considered in Ref. [64].

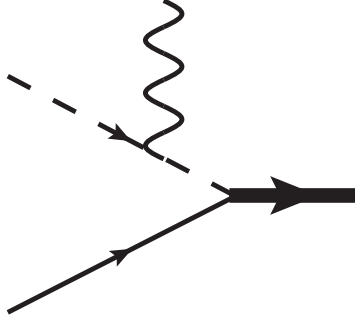


Figure 4.7.: Relevant diagram contributing to the E1 capture amplitude to S-wave states at LO. For a more detailed description of the lines, see Fig. 4.2 and 4.4.

At LO, the E1 neutron capture amplitude yields

$$\bar{\Gamma}^i = \frac{\sqrt{Z_\sigma} e Q_c g_0}{M} \left[E - \frac{(\mathbf{p} - \mathbf{k})^2}{(2M)} \right]^{-1} \epsilon^i \cdot \mathbf{p} \quad (4.124)$$

$$= -\frac{\epsilon^i \cdot \mathbf{p}}{M} \frac{\sqrt{Z_\sigma} e Q_c g_0 2m_R}{\gamma_0^2 + (\mathbf{p} - \frac{m}{M_{nc}} \mathbf{k})^2}, \quad (4.125)$$

where i is the photon polarization, \mathbf{p} denotes the relative momentum of the nc pair, ω the photon energy and \mathbf{k} the photon momentum. Throughout this section, we choose the nc pair to be traveling in \hat{z} direction, which means that $\mathbf{p} = |\mathbf{p}| \mathbf{e}_z$. Moreover, the energy of the core propagator between the photon vertex and the nc -S-wave interaction is given by

$$E = \frac{p^2}{2M} - \omega. \quad (4.126)$$

In the last step of Eq. (4.125) we exploited the energy conservation and used

$$E = \frac{p^2}{2M} - \omega = -\frac{p^2}{2m} - B_0 + \frac{\omega^2}{2M_{nc}} \quad \text{with} \quad B_0 = \frac{\gamma_0^2}{2m_R}. \quad (4.127)$$

Since m/M_{nc} is small and it follows from power counting that $p \sim \gamma_0 \sim R_{\text{halo}}^{-1}$ and $\omega \sim R_{\text{core}}/R_{\text{halo}}^2$, we can neglect the recoil term $\sim \mathbf{p} \cdot \mathbf{k}$ in the denominator. By averaging over the neutron spin and

photon polarization and summing over the outgoing S -wave spin, we obtain at LO using $\frac{m}{M_{nc}}\omega \ll p$

$$\frac{d\sigma^{\text{cap}}}{d\Omega} = \frac{m_R}{4\pi^2} \frac{\omega}{p} |\mathcal{M}^{(1/2)}|^2 = \frac{e^2 Z_{\text{eff}}^2 p \gamma_0 \sin^2 \theta}{\pi m_R^2 (p^2 + \gamma_0^2)}, \quad (4.128)$$

with the LO approximation $\omega \approx (p^2 + \gamma_0^2)/2m_R$, the angle between $\hat{\mathbf{k}} \cdot \hat{\mathbf{p}} = \cos \theta$, the effective charge $Z_{\text{eff}} = (m_R/M)Q_c$, and

$$|\mathcal{M}^{(1/2)}|^2 = \frac{1}{2} \sum_{i, m_s, M} |\bar{\Gamma}^i|^2 \delta_{m_s, M}, \quad (4.129)$$

where m_s denotes the neutron spin and M the S -wave polarization. For the photon polarization sum, the following identity was used

$$\sum_i \epsilon_\alpha^i \epsilon_\beta^{i*} = \delta_{\alpha\beta} - \frac{k_\alpha k_\beta^*}{k^2}. \quad (4.130)$$

As the neutron spin is unaffected by this reaction, m_s and M have to be the same. After integration over $d\Omega$, we derive

$$\sigma^{\text{cap}} = \frac{m_R}{\pi} \frac{\omega}{p} |\mathcal{M}^{(1/2)}|^2 \quad (4.131)$$

$$= \frac{8e^2 Z_{\text{eff}}^2}{3m_R^2} \frac{p\gamma_0}{(p^2 + \gamma_0^2)} = \frac{32\pi\alpha Z_{\text{eff}}^2}{3m_R^2} \frac{p\gamma_0}{(p^2 + \gamma_0^2)}, \quad (4.132)$$

with the fine-structure constant $\alpha = e^2/(4\pi)$.

Exploiting the detailed balance theorem, the capture cross section σ^{cap} can be related to the photodissociation cross section σ^{dis} [96] as follows

$$\sigma^{\text{cap}} = \frac{2(2J_{nc} + 1)}{(2j_n + 1)(2j_c + 1)} \frac{\omega^2}{p^2} \sigma^{\text{dis}} = 2 \frac{\omega^2}{p^2} \sigma^{\text{dis}}. \quad (4.133)$$

E1 Capture into the D -Wave State

Next, we consider D -wave states and calculate E1 neutron capture into the $3/2^+$ and $5/2^+$ states. The relevant diagrams that emerge from minimal substitution in our Lagrangian (4.4) are shown in Fig. 4.8.

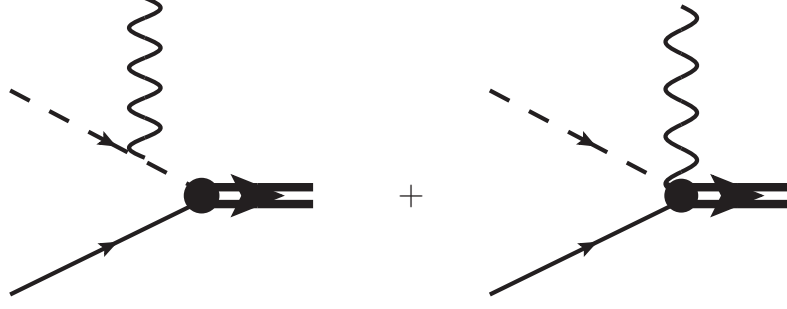


Figure 4.8.: Relevant diagrams for E1 capture to D -wave states at LO. For a more detailed description of the lines, see Fig. 4.2.

They yield

$$\bar{\Gamma}_{m_s JM}^i = - \sum_{m_s' m_l} \left(\frac{1}{2} m_s' 2m_l \middle| JM \right) \sum_{\alpha\beta} (1\alpha 1\beta | 2m_l) \sqrt{Z_d} g_2 e Q_c \frac{2m_R}{M} \times$$

$$\left[\frac{\left(\mathbf{p} - \frac{m}{M_{nc}} \mathbf{k} \right)_\alpha \left(\mathbf{p} - \frac{m}{M_{nc}} \mathbf{k} \right)_\beta}{\gamma_2^2 + \left(\mathbf{p} - \frac{m}{M_{nc}} \mathbf{k} \right)^2} \boldsymbol{\epsilon}^i \cdot \mathbf{p} + \epsilon_\alpha^i \left(p_\beta - \frac{m}{2M_{nc}} k_\beta \right) \right] \delta_{m_s m_s'}, \quad (4.134)$$

with the charge of the core Q_c , the photon momentum \mathbf{k} , the relative momentum of the incoming nc pair \mathbf{p} , the photon polarization i and JM denoting the spin and polarization of the D -wave, respectively. Note that the neutron spin is unaffected by the E1 capture process up to this order.

By projecting out the $J = 3/2$ part of the amplitude $M^{(3/2)}$ and by averaging (summing) over incoming (outgoing) spins, respectively, we finally obtain the differential cross section for the E1 capture process at LO using $\frac{m}{M_{nc}} \omega \ll p$

$$\frac{d\sigma^{\text{cap}}}{d\Omega} = \frac{m_R}{4\pi^2} \frac{\omega}{p} \left| \mathcal{M}^{(3/2)} \right|^2 \quad (4.135)$$

$$= \frac{15}{2\pi} \frac{(p^2 + \gamma_2^2)}{m_R^2 p} \frac{e^2 Z_{\text{eff}}^2}{-r_2 - \mathcal{P}_2 \gamma_2^2} X(\theta) = \frac{30\alpha Z_{\text{eff}}^2}{-r_2 - \mathcal{P}_2 \gamma_2^2} \frac{(p^2 + \gamma_2^2)}{m_R^2 p} X(\theta), \quad (4.136)$$

with the fine-structure constant α , $Z_{\text{eff}} = (m_R/M)Q_c$, the squared amplitude

$$\left| \mathcal{M}^{(3/2)} \right|^2 = \frac{1}{2} \sum_{i, m_s, M} \left| \bar{\Gamma}_{m_s, 3/2 M}^i \right|^2, \quad (4.137)$$

and the function that contains the θ dependency

$$X(\theta) = \frac{1}{15} \left[2p^2(13 - \cos(2\theta)) + \frac{4p^4 \sin^2(\theta)}{(\gamma_2^2 + p^2)} \left(\frac{p^2}{(\gamma_2^2 + p^2)} + 2 \right) \right]. \quad (4.138)$$

After integrating over $d\Omega$, we eventually derive for the total cross section

$$\sigma^{\text{cap}} = \frac{\alpha Z_{\text{eff}}^2}{-r_2 - \mathcal{P}_2 \gamma_2^2} \frac{32\pi p}{3m_R^2} \frac{(5\gamma_2^4 + 11p^4 + 14\gamma_2^2 p^2)}{(\gamma_2^2 + p^2)}. \quad (4.139)$$

From an experimental measurement of the capture (or dissociation) cross section, we can therefore extract the numerical value of the combination of D -wave effective range parameters $1/(-r_2 - \mathcal{P}_2 \gamma_2^2)$.

For the $5/2^+$ state we project out the $J = 5/2$ part of the amplitude $M^{(5/2)}$ and obtain

$$\frac{d\sigma^{\text{cap}}}{d\Omega} = \frac{m_R}{4\pi^2} \frac{\omega}{p} |\mathcal{M}^{(5/2)}|^2 \quad (4.140)$$

$$= \frac{45}{4\pi} \frac{(p^2 + \gamma_{2'}^2)}{m_R^2 p} \frac{e^2 Z_{\text{eff}}^2}{-r_{2'} - \mathcal{P}_{2'} \gamma_{2'}^2} X(\theta) = \frac{45\alpha Z_{\text{eff}}^2}{-r_{2'} - \mathcal{P}_{2'} \gamma_{2'}^2} \frac{(p^2 + \gamma_{2'}^2)}{m_R^2 p} X(\theta), \quad (4.141)$$

where $X(\theta)$ is the same as for the $J = 3/2$ cross section. After integrating over $d\Omega$, we deduce for the total cross section

$$\sigma^{\text{cap}} = \frac{\alpha Z_{\text{eff}}^2}{-r_{2'} - \mathcal{P}_{2'} \gamma_{2'}^2} \frac{16\pi p}{m_R^2} \frac{(5\gamma_{2'}^4 + 11p^4 + 14\gamma_{2'}^2 p^2)}{(\gamma_{2'}^2 + p^2)}, \quad (4.142)$$

which is the same result as the $J = 3/2$ cross section multiplied by a factor of $3/2$ and different numerical values for γ_2 , r_2 and \mathcal{P}_2 .

4.9.2 M1 Neutron Capture

After the calculation of the E1 neutron capture, we consider the M1 neutron capture process. In particular, we compute the cross section for M1 capture first into the S - and then into the D -wave state.

M1 Capture into the S -Wave State

The calculation of the M1 capture cross section is similar to the E1 capture in the previous section. The main difference between both processes is the parity conservation in the M1 matrix element. Therefore, the loop diagram (b), shown in Fig. 4.9, is also relevant at LO for M1 capture since initial state interactions in the S -wave channel have to be taken into account. Additionally, the photon now couples to the magnetic moment of the halo neutron in diagrams (a) and (b). In principle, we also need to consider diagrams that arise from minimal substitution. This is illustrated in the third diagram (c), where the photon couples to the charged core. In the S -wave case, however, diagram (c) yields no contribution to the M1 capture process.

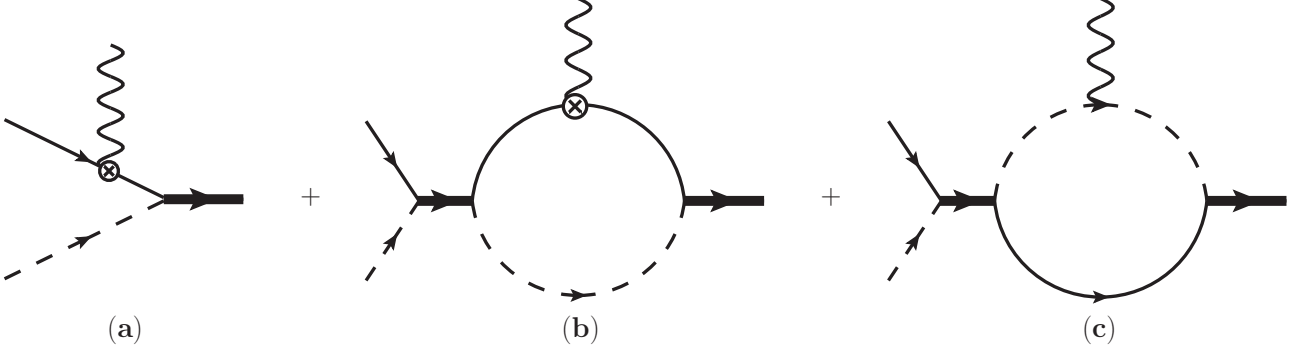


Figure 4.9.: Relevant diagrams contributing to M1 capture at LO. For a more detailed description of the lines, see Fig. 4.2 and 4.4.

For diagram (a) in Fig. 4.9, we obtain

$$\bar{\Gamma}_{im_s m_{s'}}^{(a)} = -2\sqrt{Z_\sigma} \kappa_n \mu_N g_0 m_R \frac{\sigma_j^{m_s m_{s'}} (\mathbf{k} \times \boldsymbol{\epsilon}^i)_j}{\gamma_0^2 + \left(\mathbf{p} - \frac{M}{M_{nc}} \mathbf{k}\right)^2}, \quad (4.143)$$

with the Pauli matrices σ_j , the photon polarization index i , and the relative momentum of the incoming nc pair \mathbf{p} . Since the power counting stipulates $p \sim \gamma_0 \sim R_{\text{halo}}^{-1}$ and $\omega \sim R_{\text{core}}/R_{\text{halo}}^2$, we can neglect the recoil term $\sim \mathbf{p} \cdot \mathbf{k}$ in the denominator of Eq. (4.143)

$$\bar{\Gamma}_{im_s m_{s'}}^{(a)} = -2\sqrt{2\pi} \gamma_0 \kappa_n \mu_N \frac{\sigma_j^{m_s m_{s'}} (\mathbf{k} \times \boldsymbol{\epsilon}^i)_j}{\gamma_0^2 + p^2}. \quad (4.144)$$

Considering diagram (b) with the intermediate S -wave state, we derive

$$\bar{\Gamma}_{im_s m_{s'}}^{(b)} = -\sqrt{Z_\sigma} g_0^3 \kappa_n \mu_N \frac{2\pi}{g_0^2 m_R} \frac{\sigma_j^{m_s m_{s'}} (\mathbf{k} \times \boldsymbol{\epsilon}^i)_j}{\frac{1}{a_0} - \frac{r_0}{2} p^2 + ip} \int \frac{d^3 l}{(2\pi)^3} \frac{2m_R}{p^2 - l^2} \frac{2m_R}{\gamma_0^2 + \left(\mathbf{l} + \frac{m_R}{m} \mathbf{k}\right)^2}, \quad (4.145)$$

with the loop momentum \mathbf{l} . This leads at LO to

$$\bar{\Gamma}_{im_s m_{s'}}^{(b)} = 2\sqrt{2\pi} \gamma_0 \kappa_n \mu_N \frac{\sigma_j^{m_s m_{s'}} (\mathbf{k} \times \boldsymbol{\epsilon}^i)_j}{\gamma_0 + ip} \frac{1}{\gamma_0 - ip} = -\bar{\Gamma}_{im_s m_{s'}}^{(a)}. \quad (4.146)$$

As a consequence, both diagrams cancel each other at LO. In coordinate space, this process is given by an overlap integral between two orthogonal wave functions. At NLO, there is an additional contribution from the effective range r_0 as discussed for the E1 capture process before, which will give a correction of order $\gamma_0 r_0 \approx 40\%$ depending on the specific value of the expansion parameter $R_{\text{core}}/R_{\text{halo}}$. Moreover, a two-body current enters at NLO with an additional counterterm that has to be fixed from data, similar to the case of magnetic moments discussed in Sec. 4.7.2. This demonstrates once again that counterterms play a more dominant role in the magnetic sector than in the electric one.

Recoil corrections

Subleading recoil corrections are usually dropped in EFT calculations for capture reactions such as this one. Taking recoil corrections into account, the first diagram (a) will give non-zero contributions to higher multipoles through higher partial waves in the initial state. The second diagram (b) in Fig. 4.9 contributes only when the core and the nucleon are in a relative S -wave in the initial state.

The denominator in Eq. (4.143) for diagram (a) can be written in coordinate space as

$$\frac{1}{\gamma_0^2 + \left(\mathbf{p} - \frac{M}{M_{nc}}\mathbf{k}\right)^2} = \int d^3r \frac{\exp(-\gamma_0 r)}{4\pi r} \exp\left[i\left(\mathbf{p} - \frac{M}{M_{nc}}\mathbf{k}\right) \cdot \mathbf{r}\right]. \quad (4.147)$$

The expression on the right-hand side can be viewed as the overlap integral of the halo wave function, a plane wave scattering wave function, and the current operator $\exp(i\frac{M}{M_{nc}}\mathbf{k} \cdot \mathbf{r})$. After spherically expanding the plane wave scattering wave function, we obtain for the different partial waves

$$\frac{1}{\gamma_0^2 + \left(\mathbf{p} - \frac{M}{M_{nc}}\mathbf{k}\right)^2} = -\sum_l (2l+1)i^{2l} P_l(\hat{\mathbf{p}} \cdot \hat{\mathbf{k}}) \frac{M_{nc}}{2M\omega p} \mathcal{R}e\left\{Q_l\left(-\frac{M_{nc}}{2Mp}k\left(p^2 + \frac{M^2}{M_{nc}^2}\omega^2 + \gamma_0^2\right)\right)\right\}, \quad (4.148)$$

where $Q_l(x)$ denotes the Legendre function of the second kind and we used

$$\exp(i\mathbf{p} \cdot \mathbf{r}) = 4\pi \sum_{l=0}^{\infty} \sum_{m=-l}^l i^l j_l(pr) Y_{lm}(\hat{\mathbf{p}}) Y_{lm}^*(\hat{\mathbf{r}}). \quad (4.149)$$

As an example, we consider the S -wave result for Eq. (4.148)

$$-\frac{1}{a} \ln\left(1 - \frac{a}{\gamma_0^2 + \left(p + \frac{M}{M_{nc}}\omega\right)^2}\right), \quad (4.150)$$

with $a = M_{nc}/(4M\omega p)$, which agrees with Eq. (4.144) if we set $\omega \sim 0$ and expand the logarithm.

After averaging and summing over incoming and outgoing spins, respectively, we obtain for the differential cross section the general result

$$\frac{d\sigma^{\text{cap}}}{d\Omega} = \frac{m_R}{4\pi^2} \frac{\omega}{p} |\mathcal{M}^{(1/2)}|^2 = \frac{m_R}{m^2} \frac{\omega^3}{p} \frac{4\alpha\kappa_n^2\gamma_0}{\left[\gamma_0^2 + \left(\mathbf{p} - \frac{M}{M_{nc}}\mathbf{k}\right)^2\right]^2}, \quad (4.151)$$

with the fine structure constant α and the squared amplitude

$$|\mathcal{M}^{(1/2)}|^2 = \frac{1}{2} \sum_{i,m_s,m_{s'}} \left| \bar{\Gamma}_{im_s m_{s'}}^{(a)} \right|^2. \quad (4.152)$$

M1 Capture into the D -Wave State

Next, we consider D -wave states and calculate M1 neutron capture from the continuum into the $3/2^+$ or $5/2^+$ states. Compared to the $1/2^+$ case in the previous section, there are additional contributions from two-body currents for the D -wave case at LO and NLO

$$\begin{aligned} \mathcal{L}_M = & -\mu_N L_{M1cap}^{d'd} d_m^\dagger d_m' B_i \left(\frac{5}{2} m1i \left| \frac{3}{2} m' \right. \right) - \mu_N L_{M1cap}^{dd} d_m^\dagger d_m B_i \left(\frac{3}{2} m1i \left| \frac{3}{2} m' \right. \right) \\ & - \mu_N L_{M1cap}^{d'd'} d_m'^\dagger d_m' B_i \left(\frac{5}{2} m1i \left| \frac{5}{2} m' \right. \right) - \mu_N L_{M1cap}^{\sigma d} d_m^\dagger \sigma_m B_i \left(\frac{1}{2} m1i \left| \frac{3}{2} m' \right. \right). \end{aligned} \quad (4.153)$$

By rescaling the fields to absorb unnaturally large coupling constants, leading to $[\tilde{\sigma}] = 2$, $[\tilde{d}] = [\tilde{d}'] = 0$, and using naive dimensional analysis for the rescaled fields, we obtain

$$L_{M1cap}^{d'd} \sim R_{core}^{-3} l_{M1cap}^{d'd} g_2' g_2 m_R^2, \quad L_{M1cap}^{d^{(\prime)}d^{(\prime)}} \sim R_{core}^{-3} l_{M1cap}^{d^{(\prime)}d^{(\prime)}} g_2^{2(\prime)} m_R^2, \quad \text{and} \quad L_{M1cap}^{\sigma d} \sim R_{core}^{-1} l_{M1cap}^{\sigma d} g_0 g_2 m_R^2, \quad (4.154)$$

with the constants l_{M1cap}^{\dots} all of order one.

The corresponding diagrams are shown in Fig. 4.10. The first diagram (a) represents the first three terms in Eq. (4.153), where the two-body current is between two D -wave states. This is the LO contribution to the M1 capture process. The second diagram (b) belongs to the last term in Eq. (4.153) and is only relevant for the $3/2^+$ state. This yields a NLO contribution.

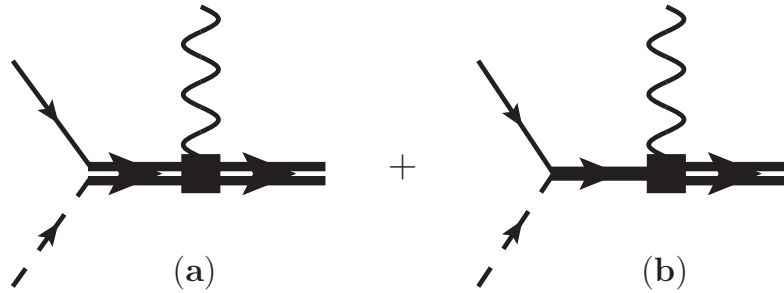


Figure 4.10.: Relevant diagrams contributing to M1 capture into the D -wave up to NLO. The thick double line denotes the dressed D -wave dimer and the thick single line the dressed S -wave dimer. For a description of the other lines, see Figs. 4.2 and 4.4. The solid squares denote different vertices from two-body currents.

The diagram (a) in the previous Fig. 4.9, where the photon couples to the magnetic moment of the neutron, contributes at $N^2\text{LO}$ and the two loop diagrams at $N^3\text{LO}$. Since we get additional counterterms L_{M1cap} that have to be matched to data, predictions for the M1 capture in the D -wave case become even more complicated.

Therefore, we concentrate on the LO result which yields for the $5/2^+$ state

$$\begin{aligned} \bar{\Gamma}_{m_s \frac{5}{2} M}^i &= \sum_{m_s m_l} \left(\frac{1}{2} m_s \ 2m_l \left| \frac{5}{2} M' \right. \right) \sum_{\alpha\beta} (1\alpha \ 1\beta | 2m_l) \frac{P_\alpha P_\beta}{\sqrt{r_{2'} + \mathcal{P}_{2'} \gamma_{2'}^2}} \times \\ &\quad \mu_N \sum_{M'\gamma} \left(\frac{5}{2} M' 1\gamma \left| \frac{5}{2} M \right. \right) (\mathbf{k} \times \boldsymbol{\epsilon}^i)_\gamma \frac{\tilde{L}_{M1cap}^{d'd'}}{\frac{1}{a_{2'}} - \frac{r_{2'}}{2} p^2 + \frac{\mathcal{P}_{2'}}{4} p^4}, \end{aligned} \quad (4.155)$$

with the D -wave polarizations α and β , the photon momentum \mathbf{k} , photon polarization i , the relative momentum of the incoming nc pair \mathbf{p} , and we define

$$\tilde{L}_{M1cap}^{d'd'} = \frac{(15\pi)^{3/2}}{m_R^2 g_{2'}^2} L_{M1cap}^{d'd'}. \quad (4.156)$$

For the $3/2^+$ state, we derive

$$\begin{aligned} \bar{\Gamma}_{m_s \frac{3}{2} M}^i &= (1\alpha \ 1\beta | 2m_l) \frac{P_\alpha P_\beta \mu_N (\mathbf{k} \times \boldsymbol{\epsilon}^i)_\gamma}{\sqrt{r_2 + \mathcal{P}_2 \gamma_2^2}} \left[\left(\frac{1}{2} m_s \ 2m_l \left| \frac{3}{2} M' \right. \right) \left(\frac{3}{2} M' 1\gamma \left| \frac{3}{2} M \right. \right) \frac{\tilde{L}_{M1cap}^{dd}}{\frac{1}{a_2} - \frac{r_2}{2} p^2 + \frac{\mathcal{P}_2}{4} p^4} + \right. \\ &\quad \left. \left(\frac{1}{2} m_s \ 2m_l \left| \frac{5}{2} M' \right. \right) \left(\frac{5}{2} M' 1\gamma \left| \frac{3}{2} M \right. \right) \frac{\tilde{L}_{M1cap}^{d'd'}}{\frac{1}{a_{2'}} - \frac{r_{2'}}{2} p^2 + \frac{\mathcal{P}_{2'}}{4} p^4} \right], \end{aligned} \quad (4.157)$$

where we implicitly summed over repeated indices and we adopted

$$\tilde{L}_{M1cap}^{dd} = \frac{(15\pi)^{3/2}}{m_R^2 g_2^2} L_{M1cap}^{dd} \quad \text{and} \quad \tilde{L}_{M1cap}^{d'd'} = \frac{(15\pi)^{3/2}}{m_R^2 g_{2'}^2 g_2} L_{M1cap}^{d'd'}. \quad (4.158)$$

The differential cross section for the M1 capture process at LO for $J = 3/2$ or $5/2$ is then given by

$$\frac{d\sigma^{\text{cap}}}{d\Omega} = \frac{m_R}{4\pi^2} \frac{\omega}{p} |\mathcal{M}^{(J)}|^2, \quad \text{with} \quad |\mathcal{M}^{(J)}|^2 = \frac{1}{2} \sum_{i, m_s, M} \left| \bar{\Gamma}_{m_s J M}^i \right|^2. \quad (4.159)$$

4.10 Results for Carbon-15 and Carbon-17

Up to this point, all the results are universal and not specific to ^{15}C or ^{17}C . In this section, we combine our Halo EFT results with experimental data and *ab initio* data from the IT-NCSM [76] to predict electromagnetic properties for the two carbon isotopes ^{15}C and ^{17}C , shown in Fig. 4.1. Moreover, we investigate universal relations between different observables for shallow D -wave bound states predicted by the Halo EFT.

4.10.1 S-Wave Charge Radius

We start the discussion by considering the relative charge radius of the S -wave state in Eq. (4.50). *Fernando et al.* already discussed the result for ^{15}C in Ref. [84]

$$\langle r_E^2 \rangle_{^{15}\text{C}}^{1/2^+} - \langle r_E^2 \rangle_{^{14}\text{C}} = 0.103 \text{ fm}^2, \quad (4.160)$$

where we employed the binding momentum $\gamma_0 = 0.235 \text{ fm}^{-1}$ from Sec. 4.1 and the extracted value for $r_0 = 2.67 \text{ fm}$ is taken from Ref. [84]. To make a numerical prediction for the full charge radius of ^{15}C , we use the charge radius of the ^{14}C core, $\langle r_E^2 \rangle_{^{14}\text{C}}^{1/2^+} = 2.503(9) \text{ fm}^2$ [97], and add it to our Halo EFT result which yields

$$\sqrt{\langle r_E^2 \rangle_{^{15}\text{C}}^{1/2^+}} = 2.523(9) \text{ fm}. \quad (4.161)$$

We compare this value to the measured point-proton radius of ^{15}C in Ref. [98]. For this purpose we convert the point-proton radius R_p into the charge radius

$$\sqrt{\langle r_E^2 \rangle_{^{15}\text{C}}^{1/2^+}} = \sqrt{\left(R_p^{^{15}\text{C}}\right)^2 + r_p^2 + \frac{3}{4m^2} + \frac{N}{Z}r_n^2} = 2.50(3) \text{ fm}, \quad (4.162)$$

where we used the formula for the charge radius from Ref. [99] including the Darwin-Foldy term and the neutron charge radius as corrections. Furthermore, we employed the proton, $r_p = 0.875 \text{ fm}$, and neutron charge radii, $r_n^2 = -0.116 \text{ fm}^2$ [100], and $N = 9$ ($Z = 6$) denotes the number of neutrons (protons) of ^{15}C . The derived radius agrees with our Halo EFT result. However, the effect of the relative charge radius is in the same order as the experimental error.

Considering ^{17}C , we obtain for the charge radius of the excited S -wave state of ^{17}C relative to the charge radius of ^{16}C at LO

$$\langle r_E^2 \rangle_{^{17}\text{C}}^{1/2^+} - \langle r_E^2 \rangle_{^{16}\text{C}} = 0.074 \text{ fm}^2, \quad (4.163)$$

where we used $\gamma_0 = 0.218 \text{ fm}^{-1}$ from Sec. 4.1. The error from NLO corrections is about 50%. As before, we have to add the charge radius of ^{16}C , $\langle r_E^2 \rangle_{^{16}\text{C}}$, to our result to predict the full charge radius of ^{17}C numerically. Hence, we use the point-proton radius R_p from Ref. [98] to derive

$$\sqrt{\langle r_E^2 \rangle_{^{17}\text{C}}^{1/2^+}} = \sqrt{\left(R_p^{^{16}\text{C}}\right)^2 + r_p^2 + \frac{3}{4m^2} + \frac{N}{Z}r_n^2 + 0.074 \text{ fm}^2} = 2.53(5) \text{ fm}, \quad (4.164)$$

where $N = 11$ ($Z = 6$) indicates the number of neutrons (protons) of ^{17}C . The error bar includes both the experimental and the Halo EFT uncertainties.

To date, there is no experimental data for the charge radius of the $1/2^+$ excited state to compare with. As a consistency check, we compare it with the experimental value for the $3/2^+$ ground state of ^{17}C extracted in Ref. [98], $\sqrt{\langle r_E^2 \rangle_{^{17}\text{C}}^{3/2^+}} = 2.54(4) \text{ fm}$, which is very close to our result for the $1/2^+$ excited

state. Note that the difference between the charge radius of ^{17}C and ^{16}C is smaller than the experimental error from Ref. [98] for this quantity.

4.10.2 D -Wave E2 Transition and Form Factors

In the D -wave sector, we start with the E2 transition in ^{15}C . It was measured experimentally and the result is used to extract the denominator of the D -wave renormalization constant at LO and subsequently, to predict several electric observables numerically. The E2 strength for the transition from $5/2^+ \rightarrow 1/2^+$ in ^{15}C is $B(\text{E}2) = 0.44(1)$ W.u. [83]. This yields $B(\text{E}2) = 2.90(7) e^2\text{fm}^4$ for the transition from $1/2^+ \rightarrow 5/2^+$ that we calculated in Sec. 4.8.1. As argued for the power counting in Sec. 4.4, r_0 is treated as a LO parameter for ^{15}C so that Eq. (4.92) has to be modified by a factor of $1/(1 - r_0\gamma_0)$, originating from the renormalization constant of the S -wave state in Eq. (4.33). Using the experimental value for the binding momenta from Sec. 4.1 $\gamma_0 = 0.235 \text{ fm}^{-1}$, $\gamma_2 = 0.147 \text{ fm}^{-1}$ and the extracted value for $r_0 = 2.67 \text{ fm}$ [84], we are able to derive the numerical value for

$$Z_d m_R^2 g_2^2 \sim \frac{1}{r_2 + \mathcal{P}_2 \gamma_2^2} = -181(4) \text{ fm}^3, \quad (4.165)$$

for ^{15}C . Moreover, the denominator with the effective range parameters is related to the Asymptotic Normalization Coefficient (ANC) of the D -wave state, $A_2 = \sqrt{2\gamma_2^4 / (-r_2 - \mathcal{P}_2 \gamma_2^2)}$, as discussed in Sec. 4.3.2.

With the numerical result for $Z_d m_R^2 g_2^2$ we can check if our power-counting scenario, leading to the scaling $Z_d m_R^2 g_2^2 \sim R_{\text{halo}}^2 R_{\text{core}}$, can be confirmed or if the scenario of Ref. [17] yields better agreement. By employing the experimental values for $R_{\text{halo}} \approx 6.81 \text{ fm}$ and $R_{\text{core}} \approx 1.91 \text{ fm}$ from Sec 4.1, we predict $Z_d m_R^2 g_2^2 \sim R_{\text{halo}}^2 R_{\text{core}} \approx 90 \text{ fm}^3$. This value is by a factor of 2 smaller than the one extracted from $B(\text{E}2)$ and thus in reasonable agreement. The power counting of Ref. [17] leads to the scaling

$$Z_d m_R^2 g_2^2 \sim \frac{1}{r_2} \sim R_{\text{core}}^3 \approx 7 \text{ fm}^3, \quad (4.166)$$

which is around 26 times smaller than the extracted result. These numbers indicate that our power-counting scenario is better suited for ^{15}C .

Using our LO and NLO results from the previous electric form factor calculation in Sec. 4.7.1, we obtain

$$\tilde{L}_{C01}^{(d)\text{LO}} + \frac{4}{3} \tilde{L}_{C02}^{(d)\text{LO}} = \langle r_E^2 \rangle^{(d)} / 1088(25) \text{ fm}^{-1}, \quad \tilde{L}_{C02}^{(d)\text{LO}} = -\mu_Q^{(d)} / 2418(55) \text{ fm}^{-1}, \quad (4.167)$$

for the LO piece of the counterterms. At NLO, no new physics input enters as these counterterms have a finite and a μ -dependent piece which are completely determined by the renormalization condition applied to the form factors. For the hexadecupole moment and radius we derive the following predictions

$$\mu_H^{(d)} = 1.68(4) \times 10^{-2} e\text{fm}^4, \quad \text{and} \quad \langle r_H^2 \rangle^{(d)} = 0.135(3) \text{ fm}^2. \quad (4.168)$$

Comparing our findings with Ref. [64], we deduce, as a general rule, that the highest multipole form factor is always independent of additional parameters from short-range counterterms. Moreover, the second highest multipole form factor requires one additional counterterm for the respective moment, the third highest one for the respective moment and one for the respective radius, et cetera. As a consequence, we can always find a smooth correlation between the highest radius and the neutron separation energy S_n

$$\langle r_H^2 \rangle^{(d)} = \frac{9}{28} \frac{f^2}{m_R S_n^{(d)}}. \quad (4.169)$$

In the P -wave case, we obtain

$$\langle r_E^2 \rangle^{(p)} = -\frac{5}{2} \mu_Q^{(p)}, \quad (4.170)$$

as an additional correlation since the electric form factor is normalized to $G_E(0) = 1$.

For the D -wave, we can derive several linear correlations between different combinations of multipole moments and radii. This is illustrated in Fig. 4.11, where the red cross denotes the numerical prediction of the corresponding quantity for ^{15}C . Therefore, by measuring one of these observables, we can immediately predict the correlated quantity. These correlations are universal and can be found in arbitrary one-neutron D -wave halo nuclei or similar weakly-bound systems.

The ground state and the two excited states of ^{17}C have positive parity and differ at most by 2 units in total angular momentum. All states can therefore be connected by E2 transitions. In the case of ^{17}C , there is, however, no experimental data to compare with since M1 transitions seem to be more dominant than E2 transitions [86, 87]. Thus, we cannot extract the renormalization constant $Z_d m_R^2 g_2^2$ of the D -wave states in the same way as before for ^{15}C to be able to predict electric observables numerically.

Nevertheless, by combining Eqs. (4.104) and (4.95), we find a correlation between B(E2) and B(M1)

$$\text{B(E2: } 1/2^+ \rightarrow 3/2^+) = \frac{32}{15} \frac{Z_{\text{eff}}^2 e^2}{(\tilde{L}_{M1}^{\sigma d})^2 \mu_N^2} \left[\frac{3\gamma_0^2 + 9\gamma_0\gamma_2 + 8\gamma_2^2}{(\gamma_0 + \gamma_2)^3} \right]^2 \text{B(M1: } 1/2^+ \rightarrow 3/2^+). \quad (4.171)$$

If we use the experimental result for $\text{B(M1: } 1/2^+ \rightarrow 3/2^+) = 1.04_{-0.12}^{+0.03} \times 10^{-2} \mu_N^2$ [87] and employ naive dimensional analysis for the counterterm $\tilde{L}_{M1}^{\sigma d} \sim R_{\text{core}}^{-1} \approx 0.28 \text{ fm}^{-1}$, we obtain a rough prediction for B(E2)

$$\text{B(E2: } 1/2^+ \rightarrow 3/2^+) \approx 3 \times 10^{-2} e^2 \text{fm}^4, \quad (4.172)$$

where we applied the numerical values for γ_0 and γ_2 from Sec. 4.1.

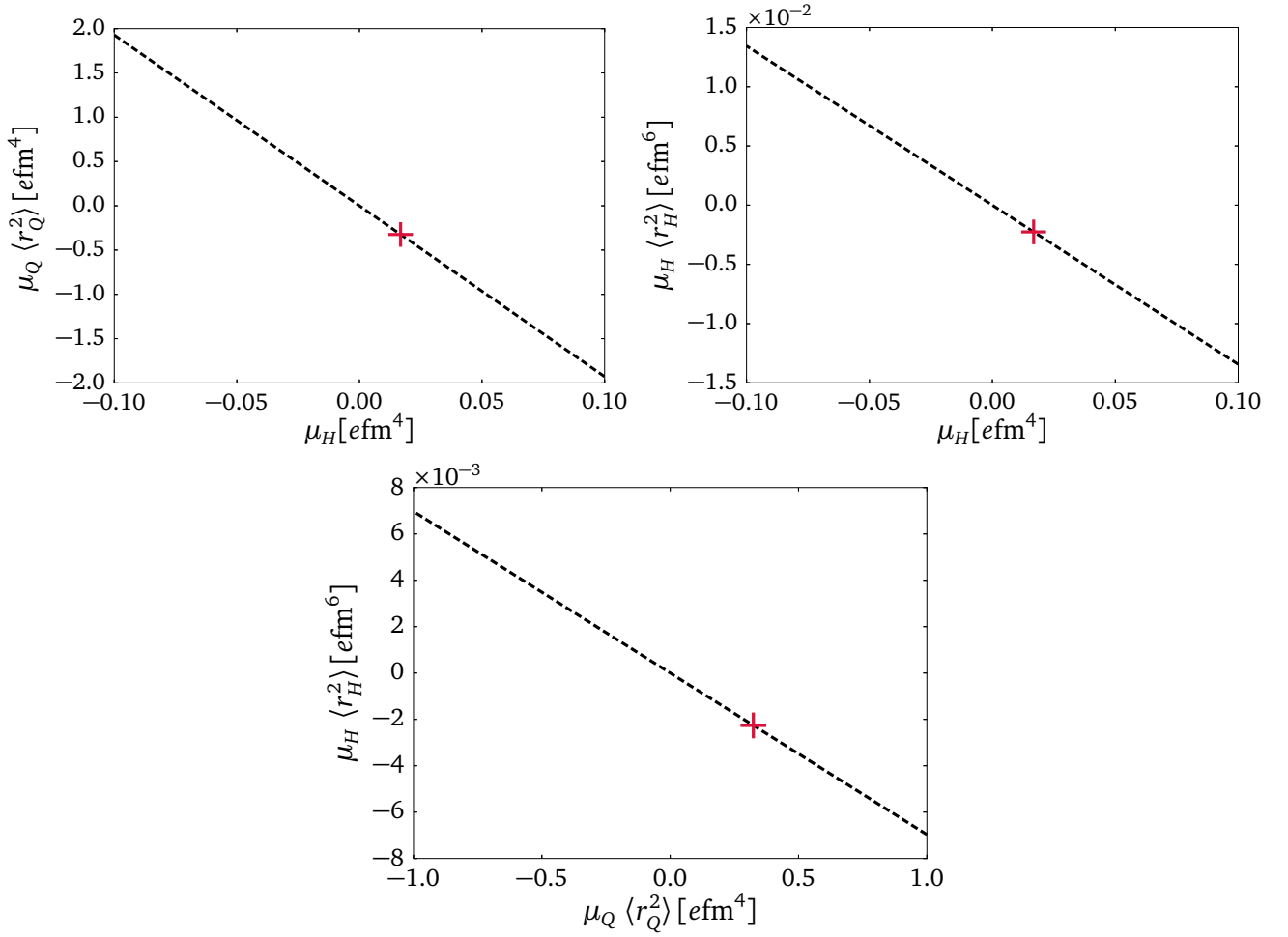


Figure 4.11.: Linear correlations between the hexadecupole moment and the quadrupole moment times quadrupole radius (top left), the hexadecupole moment and the hexadecupole moment times hexadecupole radius (top right) and between the quadrupole moment times quadrupole radius and hexadecupole moment times hexadecupole radius (bottom). The red cross denotes the numerical prediction for ^{15}C .

Moreover, the M1 and E2 transition strengths for ^{17}C can be compared considering the corresponding transition rates [94]

$$T(R\lambda) = \frac{8\pi(\lambda+1)}{\lambda[(2\lambda+1)!!]^2} \omega^{2\lambda+1} B(R\lambda), \quad (4.173)$$

that have, in contrast to $B(M1)$ and $B(E2)$, the same units. Here, R stands for E or M, λ denotes the order of the transition and ω defines the photon energy which, in this case, is 0.218 MeV. Using the naive dimensional analysis result for $\tilde{L}_{M1}^{\sigma d}$ from above, we find

$$\frac{T(E2)}{T(M1)} = \frac{32\omega^2}{125} \frac{Z_{\text{eff}}^2 e^2}{(\tilde{L}_{M1}^{\sigma d})^2 \mu_N^2} \left[\frac{3\gamma_0^2 + 9\gamma_0\gamma_2 + 8\gamma_2^2}{(\gamma_0 + \gamma_2)^3} \right]^2 \approx 1 \times 10^{-5}, \quad (4.174)$$

which implies that the M1 transition strongly dominates over E2 for ^{17}C .

Correlations between E2 Observables

Two prominent examples for universal correlations in light nuclei are the Phillips line [101], a correlation between the binding energy of ${}^3\text{H}$ and the neutron-deuteron scattering length, and the Tjon line [102], a linear relation between 3N and 4N binding energies for different nuclear interactions, see, e.g., Ref. [103] for an explicit example. In general, universal correlations are easier to find in Halo EFT than in *ab initio* methods since Halo EFT employs the relevant degrees of freedom with respect to the separation of scales between R_{core} and R_{halo} .

In this section, we combine our Halo EFT results with experimental data and *ab initio* data from the IT-NCSM [76] to predict the electric quadrupole moment for ${}^{15}\text{C}$. In a second step, the correlations obtained in Halo EFT are compared to the E2 correlation based on the rotational model by Bohr and Mottelson [104]. To derive the correlation between the quadrupole transition from the $5/2^+$ to the $1/2^+$ state and the quadrupole moment of the $5/2^+$ state, we combine Eqs. (4.69) and (4.92) and apply a factor $2/6$ to account for the different multiplicity of the initial and final states. As discussed before, we have to include the S -wave effective range r_0 in Eq. (4.92) since r_0 contributes at LO for ${}^{15}\text{C}$. Eventually, we obtain a linear dependence between $B(\text{E}2)$ for the transition $5/2^+ \rightarrow 1/2^+$ and the quadrupole moment at LO

$$B(\text{E}2: 5/2^+ \rightarrow 1/2^+) = -\frac{1}{50\pi} \frac{Z_{\text{eff}}^2 e^2 \gamma_0}{(1 - r_0 \gamma_0)} \left[\frac{3\gamma_0^2 + 9\gamma_0 \gamma_2 + 8\gamma_2^2}{(\gamma_0 + \gamma_2)^3} \right]^2 \frac{\mu_Q^{(d)}}{\tilde{L}_{C02}^{(d)\text{LO}}}, \quad (4.175)$$

where $\tilde{L}_{C02}^{(d)\text{LO}}$ is treated as fit parameter and γ_0 and γ_2 are taken from experiment [83].

A similar correlation between the quadrupole transition and the quadrupole moment can be deduced from the rotational model by Bohr and Mottelson [104]. The quadrupole moment for a rigid rotor with static intrinsic quadrupole moment $Q^{0,s}$

$$\mu_Q(J) = \frac{3K^2 - J(J+1)}{(J+1)(2J+3)} Q^{0,s}, \quad (4.176)$$

is combined with the $B(\text{E}2)$ transition of such a rigid rotor

$$B(\text{E}2, J_i \rightarrow J_f) = \frac{5}{16\pi} (J_i K \ 20 | J_f K)^2 (Q^{0,t})^2, \quad (4.177)$$

where K denotes the projection of the total angular momentum on the symmetry axis of the intrinsically deformed nucleus and $Q^{0,t}$ is the transition intrinsic quadrupole moment. Consequently, we derive the correlation between the E2 transition and the quadrupole moment in the rigid rotor model

$$B(\text{E}2, J_i \rightarrow J_f) = \frac{5}{16\pi} \frac{((J+1)(2J+3))^2}{(3K^2 - J(J+1))^2} (J_i K \ 20 | J_f K)^2 \left(\frac{Q^{0,t}}{Q^{0,s}} \right)^2 \mu_Q(J)^2, \quad (4.178)$$

with $K = 1/2$ for ${}^{15}\text{C}$. For an ideal rigid rotor, both intrinsic quadrupole moments would be equal $Q^{0,s} = Q^{0,t} = Q^0$.

The idea to employ this simple model is motivated by observations of *Calci and Roth* [29], who found a robust correlation between this pair of quadrupole observables in *ab initio* calculations for light nuclei. In the simple rigid rotor model the ratio $Q^{0,t}/Q^{0,s}$ is expected to be one. The results of Ref. [29] indicate that the correlation is robust as long as the ratio $Q^{0,t}/Q^{0,s}$ is treated as a fit parameter.

We use IT-NCSM data of ^{15}C , provided by *Robert Roth* and generated by different χEFT interactions and different model spaces, to check the quadratic and linear correlations and predict the quadrupole moment of ^{15}C numerically. This is demonstrated in Fig. 4.12.

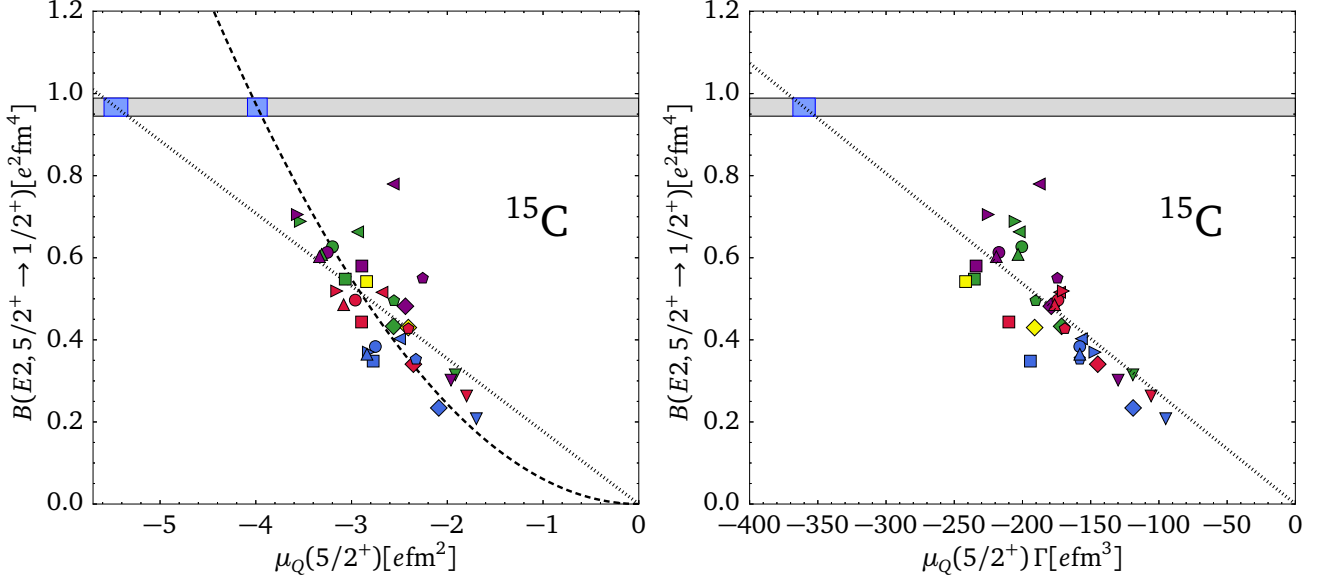


Figure 4.12.: Correlation between $B(E2)$ and the quadrupole moment μ_Q . The IT-NCSM data is obtained with different $NN + 3N$ χEFT interactions: EM with cutoffs $\{400, 400, 500\}$ MeV/c (square, diamond, triangle down), and EGM with cutoffs $(\Lambda_\chi/\tilde{\Lambda}_\chi) = \{(450/500), (600/500), (550/600), (450/700), (600/700)\}$ MeV/c (triangle left, pentagon, circle, triangle right, and triangle up) with oscillator frequency $\hbar\Omega = 16$ MeV for all IT-NCSM calculations except for the diamond and triangle down data where $\hbar\Omega = 20$ MeV. Different colors denote different $N_{\text{max}} = 2$ (blue), 4 (red), 6 (green), 8 (violet), and 10 (yellow) values. Left panel: Rigid rotor model with quadratic fit of $Q^{0,t}/Q^{0,s}$ ratio (dashed line, $\chi_{\text{red}}^2 = 110$) and linear Halo EFT fit of $\tilde{L}_{C02}^{(d)}$ with fixed γ_2 from experiment (dotted line, $\chi_{\text{red}}^2 = 123$). Right panel: Linear Halo EFT fit with $\gamma_0^2 - \gamma_2^2$ from IT-NCSM calculation and rescaled μ_Q/Γ (dotted line, $\chi_{\text{red}}^2 = 80$), where $\Gamma = \gamma_0(3\gamma_0^2 + 9\gamma_0\gamma_2 + 8\gamma_2^2)^2/(1 - r_0\gamma_0)/(\gamma_0 + \gamma_2)^6$ divides out dependence on γ_0 and γ_2 . The gray shaded area indicates the error band of the experimental $B(E2)$ [83]. The blue shaded area corresponds to the prediction for μ_Q .

The varying symbols denote different $NN + 3N$ χEFT interactions which are similar to the ones used in Ref. [29]. We employ the NN interaction developed by Entem and Machleidt (EM) [44] at N^3LO with a cutoff of 500 MeV/c for the nonlocal regulator function. This NN force is combined with the local 3N force at N^2LO using a cutoff of 400 or 500 MeV/c [105]. The second NN interaction by Epelbaum, Glöckle, Meißner (EGM) [106] at N^2LO uses a nonlocal regularization with a cutoff Λ_χ and an additional spectral function regularization with cutoff $\tilde{\Lambda}_\chi$. The EGM NN forces are combined with a consistent nonlocal 3N force at N^2LO used in several applications to neutron matter [107–109]. For reasons of

convergence, the $NN + 3N$ potentials are softened by a similarity renormalization group evolution where all contributions up to the three-body level are included.

The different colors in Fig. 4.12 denote different N_{\max} values. Since the IT-NCSM results are not fully converged and the results differ for different N_{\max} values, the ordering of the ground and first excited state is exchanged for some data points. Leaving out the data sets with exchanged ordering does not significantly improve the fit. The plot on the left side employs the experimental values for the neutron separation energy as input for γ_0 and γ_2 . For the plot on the right side, we apply the excitation energy of the first excited state from the IT-NCSM to determine $\gamma_0^2 - \gamma_2^2$ and for γ_0 we use the experimental value.

We emphasize that in the *ab initio* calculations, both, the interactions (including short distance physics) and the model spaces are varied. If the *ab initio* calculations were (i) fully converged and (ii) all interactions and electromagnetic operators were unitarily equivalent, they would fall on a single point. However, neither (i) nor (ii) is the case here. So, naively, one would expect the calculations for B(E2) and μ_Q to fill the whole plane. Halo EFT and the rotational model, however, predict a one parameter correlation between B(E2) and μ_Q based on certain assumptions. If these assumptions, such as shallow binding and a corresponding separation of scales in the case Halo EFT, are satisfied in the *ab initio* calculations, they should also show the correlation even if they are not converged and/or have different short distance physics.

An additional complication here is the appearance of the two-body coupling $L_{C02}^{(d)}$ in Eq. (4.43) which could vary for the different *ab initio* data sets. In our analysis of the *ab initio* data, we explicitly assume that $L_{C02}^{(d)}$ varies only slowly and can be approximated by a constant for the *ab initio* data considered. Under this assumption, it becomes possible to decide between the type of correlation using the *ab initio* data for ^{15}C . A similar assumption is made in the analysis of three-body recombination rates for ultracold atoms near a Feshbach resonance to observe the Efimov effect. There the scattering length varies strongly with the magnetic field \mathbf{B} while the three-body parameter is assumed to stay approximately constant [61]. Since the two parameters are independent, it would be very unnatural if both had a resonance at the same value of \mathbf{B} .

From the left plot, we obtain $\mu_Q^{(d)} \approx -3.98(5) \text{efm}^2$ for the quadratic fit and $\mu_Q^{(d)} \approx -5.46(12) \text{efm}^2$ for the linear fit, where the uncertainties from B(E2) are given in parenthesis. For both fits, we find for the two-body current operator $\tilde{L}_{C02}^{(d)\text{LO}} R_{\text{core}} \approx 10^{-3}$, which is significantly smaller than expected from Eq. (4.43). Part of this suppression is due to mass factors that are not accounted for in the power counting in $R_{\text{core}}/R_{\text{halo}}$. Specifically, a suppression of order 10^{-2} comes from the effective charge $Z_{\text{eff}} \sim (m/M_{nc})^2$ which is implicitly contained in $\tilde{L}_{C02}^{(d)\text{LO}}$. Taking this into account, the value of $\tilde{L}_{C02}^{(d)\text{LO}}$ is much more natural. The remaining deviation from unity could be due to a conspiracy of numerical factors or an additional fine tuning.

From the fits, we cannot decide which scenario describes the IT-NCSM data more appropriately since both lead to similar reduced χ^2 values. The ratio $Q^{0,t}/Q^{0,s}$ should be equal to 1 for an ideal rigid rotor. Since the quadratic fit yields a ratio of $Q^{0,t}/Q^{0,s} \approx 0.5$, we assume that ^{15}C is not a good example of a rigid rotor. Perhaps for larger N_{\max} values, and thus better converged results, the matching between fit curves and data points would improve.

In the linear case, the slope of the fit depends also on the neutron separation energies of both states, which differ for each data point from the IT-NCSM. From the excitation energy obtained in the IT-NCSM

calculation, we know only the difference between the neutron separation energies of the ground and excited state. Thus, one experimental input is still required to fix γ_0 and γ_2 from the IT-NCSM data since we did not perform explicit calculations for ^{14}C . In the right plot of Fig. 4.12, we determine $\gamma_0^2 - \gamma_2^2$ from IT-NCSM data and take γ_0 from experiment. The reduced χ^2 value for the linear fit then slightly improves compared to the fit using experimental values only. This leads to $\mu_Q^{(d)} \approx -4.21(10) \text{ efm}^2$, which is closer to the value from the quadratic fit. The deviations of the data points from the linear fit might decrease further if consistent values for both neutron separation energies could be extracted from the IT-NCSM. However, within the 30% LO uncertainty from Halo EFT both values for $\mu_Q^{(d)}$ agree.

With the extracted results of $\mu_Q^{(d)}$, we can predict the quadrupole radius, $\langle r_Q^2 \rangle^{(d)} = 5.93(13) \times 10^{-2} \text{ fm}^2$ from the left linear fit and $\langle r_Q^2 \rangle^{(d)} = 7.70(17) \times 10^{-2} \text{ fm}^2$ from the right linear fit in Fig. 4.12, by Halo EFT.

Finally, we note that the correlation between the LO result for μ_Q and B(E2) previously discussed does not persist at NLO because two different counterterms enter into μ_Q and B(E2) at this order. Hence, this correlation is only expected to hold up to corrections of order $R_{\text{core}}/R_{\text{halo}} \approx 0.3$.

Similar to the correlation between $\mu_Q^{(d)}$ and B(E2) above, we find a smooth correlation between $\langle r_E^2 \rangle^{(d)}$ and $\mu_Q^{(d)}$

$$\mu_Q^{(d)} = -\frac{20}{9} \frac{\tilde{L}_{C02}^{(d)\text{LO}}}{\left(\tilde{L}_{C01}^{(d)\text{LO}} + \frac{4}{3}\tilde{L}_{C02}^{(d)\text{LO}}\right)} \langle r_E^2 \rangle^{(d)}, \quad (4.179)$$

which implies that *ab initio* calculations with different phaseshift-equivalent interactions should show a linear correlation between the quadrupole moment and the charge radius.

4.10.3 Neutron Capture

Eventually, we focus on neutron capture into ^{15}C and ^{17}C in this section. E1 neutron capture was already considered for ^{15}C by *Rupak et al.* in Ref. [82]. In ^{15}C , there is an experimentally measured $1/2^-$ P -wave resonance with a resonance energy of $E_r \approx 1.885 \text{ MeV}$ and a width of $\Gamma_r \approx 40 \text{ keV}$ [83]. As discussed in Sec. 4.9.1, *Rupak et al.* incorporated P -wave initial state interactions by including the resonant $^2P_{1/2}$ state with ERE parameters, $a_1^{(1)}$ and $r_1^{(2)}$, determined from the resonance data and the non-resonant $^2P_{3/2}$ state with undetermined ERE parameters, $a_1^{(2)} = -n_1/Q^3$, $r_1^{(2)} = 2n_2Q$, where n_1 and n_2 are expected to be $\mathcal{O}(1)$ and $Q = 40 \text{ MeV}$. Note that Q is equivalent to $1/R_{\text{halo}}$ in our Halo EFT. They estimated the scattering parameters in the $^2P_{3/2}$ channel from the direct capture and Coulomb dissociation data [90, 110]. *Rupak et al.* included the P -wave contributions at LO because their power counting differs from ours for shallow P -wave states. We neglect these diagrams since they contribute at NLO in our power counting. For ^{17}C , there exists no data concerning P -wave states.

Our numerical results for the E1 capture into ^{17}C , Eq. (4.131), and photodissociation of ^{17}C , using Eq. (4.133), at LO are shown in the top panel of Fig. 4.13. At NLO, there is an additional contribution from the effective range r_0 . By assuming that r_0 scales as R_{core} , we can estimate the size of the NLO contribution by multiplying the LO result by a factor of $1/(1 \pm \gamma_0 R_{\text{core}})$ and add an error band to our LO results in Fig. 4.13.

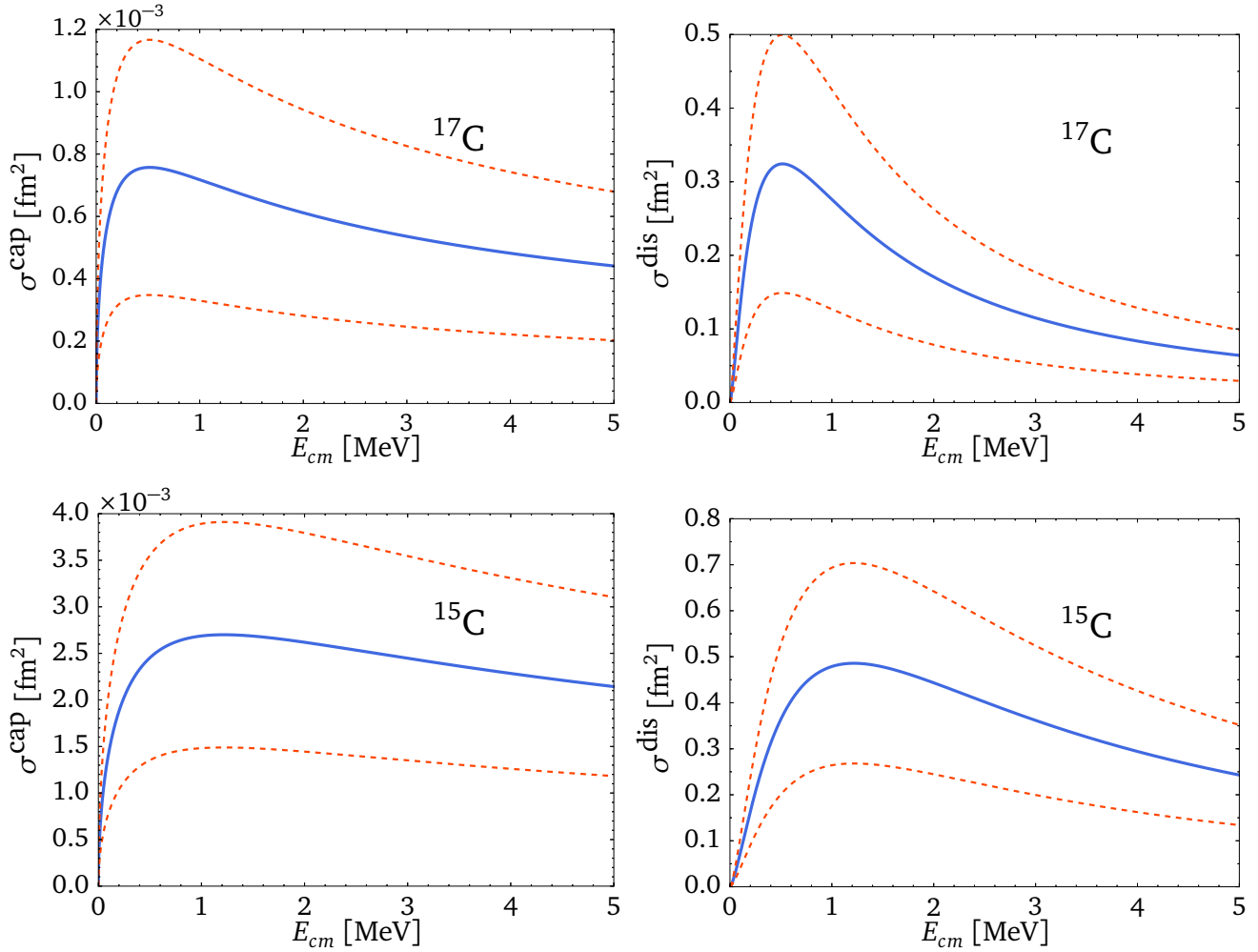


Figure 4.13.: Left panel: E1 capture cross section into the $1/2^+$ state of ^{17}C (top panel) and ^{15}C (bottom panel) as a function of the center-of-mass energy E_{cm} . Right panel: E1 photodissociation cross section as a function of E_{cm} . The solid (blue) line denotes the LO result and the dashed (red) lines show an estimate of the NLO corrections.

The numerical capture and photodissociation results for ^{15}C are illustrated in the bottom panel of Fig. 4.13. Note that we have to add a factor of $1/(1 - r_0\gamma_0)$ to the LO result in Eq. (4.131) since r_0 contributes at LO for ^{15}C . We can estimate NLO contributions, e.g., from P -wave initial state interactions, by a relative factor of $R_{\text{core}}/R_{\text{halo}} \approx 0.45$ from our Halo EFT expansion. This leads to the error bands shown in the bottom panel of Fig. 4.13. Our capture cross section into the S -wave state of ^{15}C is qualitatively consistent with the findings of *Rupak et al.*, see Fig. 4.14, if we disregard the peak in the cross section in the region of $1.5 \text{ MeV} < E_{cm} < 2.0 \text{ MeV}$ due to the implicit inclusion of the P -wave resonance. Furthermore, our predicted cross section at LO is slightly larger than their prediction. Since we neglected the contributions of P -wave initial state interactions, we expect deviations in the order of the estimate of the NLO corrections. Including the estimate of the NLO effects, depicted by the dashed red curve in Fig. 4.14, our prediction, i.e. the lower dashed red curve, reasonably agrees with the findings of *Rupak* and also with the experimental data [90, 110] plotted in the left graph of Fig. 4.14. Although we cannot reproduce the resonance peak without explicitly including P -wave initial state interactions, the experimental data, with a few exceptions, lie within the NLO correction.

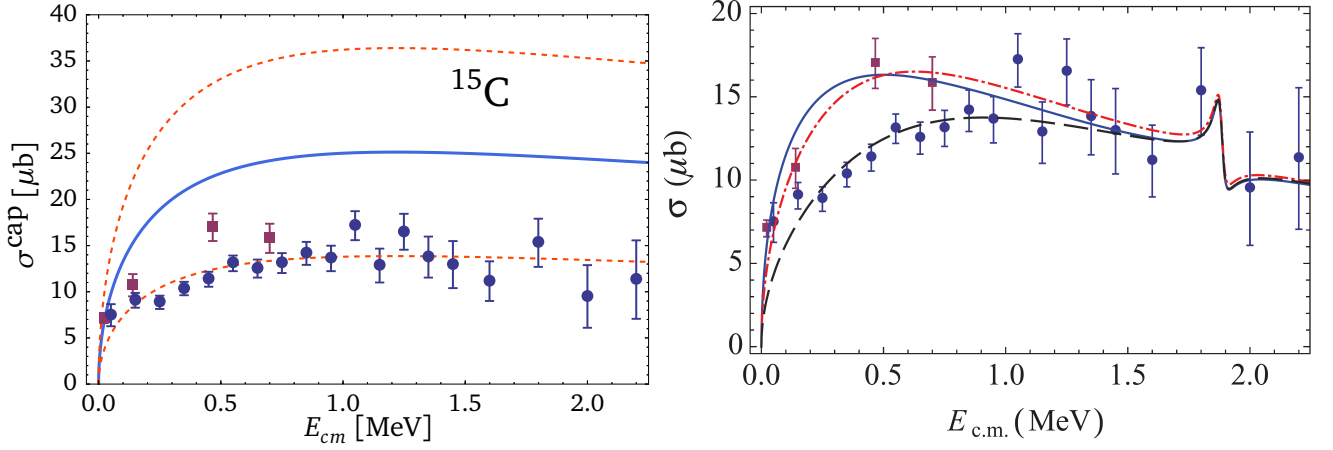


Figure 4.14.: The E1 capture cross section into the $1/2^+$ state of ^{15}C as a function of the CM energy E_{cm} is compared to the findings of *Rupak et al.* [82] and experimental data [90, 110]. Left panel: Our predicted cross section. The solid (blue) line denotes the LO result and the dashed (red) lines show an estimate of the NLO corrections. Right panel: Calculated cross section taken from Ref. [82] with undetermined ERE parameters for the $^2P_{3/2}$ channel $a_1^{(2)} = -n_1/(Q^3)$, $r_1^{(2)} = 2n_2Q$, and $Q = 40$ MeV. Q is equivalent to $1/R_{\text{halo}}$. The solid (blue) curve uses $(n_1, n_2) = (2, 1.5)$; the dot-dashed (red) curve uses $(n_1, n_2) = (1.5, 1.2)$; the dashed (black) curve uses $(n_1, n_2) = (0.818, 1.12)$. The calculated cross sections are compared with square (maroon) direct capture data from Ref. [110] and with circle (dark blue) Coulomb dissociation data from Ref. [90].

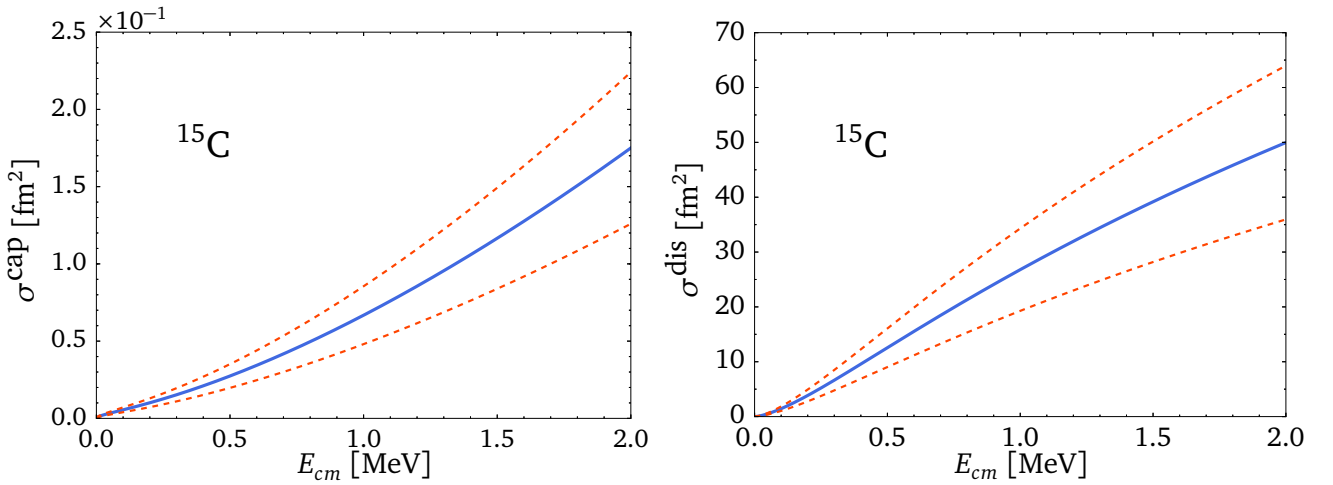


Figure 4.15.: Left panel: E1 capture cross section into the $5/2^+$ state of ^{15}C as a function of the center-of-mass energy E_{cm} . Right panel: E1 photodissociation cross section as a function of E_{cm} . The solid (blue) line denotes the LO result and the dashed (red) lines show an estimate of the NLO corrections.

Using the numerical result of $Z_d m_R^2 g_2^2 \sim 1/(r_2 + \mathcal{P}_2 \gamma_2^2) = -181(4) \text{ fm}^3$ for the $5/2^+$ state of ^{15}C , extracted from the B(E2) transition in Sec. 4.10.2, we can predict the E1 neutron capture cross section for the D -wave state in ^{15}C numerically. This is illustrated in Fig. 4.15. Compared to the S -wave cross section in Fig. 4.13, the D -wave cross section steadily increases for increasing E_{cm} . This can be explained by the fact that the unitary cut $\sim ik^5$ in Eq. (4.25), which leads to a decrease in the cross section for

large energies, is a NLO contribution in the D -wave case, while it is a LO contribution for the S -wave. The ik^5 contribution, however, dominates for energies beyond $E_{\text{cm}} \gtrsim 0.8$ MeV for the D -wave so that we cannot expect our results to be accurate for larger E_{cm} values.

Eventually, we briefly discuss M1 capture into the D -wave state. Since we need at least four additional input parameters to be able to predict the M1 capture process into the D -wave state already at LO, cf. Eqs. (4.155) and (4.157), numerical predictions are currently not possible.

This shows the limitations of Halo EFT for higher partial waves especially in the magnetic sector, where additional counterterms typically contribute at LO.

4.11 Conclusion

We extended the Halo EFT approach for the calculation of electromagnetic observables introduced by *Hammer and Phillips* [64] to shallow bound states beyond the P -wave. In particular, we considered D -wave states to describe the two carbon isotopes ^{15}C and ^{17}C . Since the neutron separation energy is large compared to the first excitation energy of the core, both carbon isotopes can be assumed to be one-neutron halo nuclei. We exploited this separation of scales and developed a new power-counting scheme for shallow D -wave and higher partial wave bound states. For the D -wave state in particular, we assumed that $a_2 \sim R_{\text{halo}}^4 R_{\text{core}}$ and $r_2 \sim 1/(R_{\text{halo}}^2 R_{\text{core}})$ while all other parameters scale with R_{core} . In general, we find that the number of fine-tuned parameters increases for higher partial waves which explains why S - and P -wave states are observed more frequently in nature than shallow bound states with larger l . This power-counting scheme differs from the general scenario proposed by *Bedaque et al.* in Ref. [17]. The *Bedaque* scheme requires only one fine tuning in the leading order parameter set, but further fine tunings appear through higher order power law divergences that have to be canceled. Our scheme requires two fine tunings for the D -wave case, but is better adapted to the scale hierarchy in ^{15}C than the scheme of Ref. [17].

Using our power-counting scheme, we computed the electric, quadrupole and hexadecupole form factors of the D -wave state up to NLO. We found that for the D -wave, the local gauge-invariant operators become more important than in lower partial waves and counterterms are required in the electric and quadrupole form factors already at LO. This continues the trend, observed in Ref. [64], that the counterterms enter in lower orders at larger l . We also computed the $B(E2)$ strength for the transition from the S -to- D state up to NLO and found that the first counterterm emerges at NLO. The occurrence of counterterms in low orders limits the predictive power of Halo EFT for D -waves since the number of matching parameters increases. However, this limitation can be overcome by considering universal correlations between observables, as discussed in particular for ^{15}C . Considering ^{15}C , the lack of experimental data for the first excited $5/2^+$ state complicates numerical predictions. We can, however, use the experimentally measured $B(E2)$ transition to extract the combination of unknown effective range parameters of the wave function renormalization. Hence, we were able to predict the hexadecupole moment $\mu_H^{(d)} = 1.68(4) \times 10^{-2} \text{ efm}^4$ and the hexadecupole radius $\langle r_H^2 \rangle^{(d)} = 0.135(3) \text{ fm}^2$. Unfortunately, there is not enough experimental data to predict the form factors for the $3/2^+$ and $5/2^+$ state in ^{17}C .

Furthermore, we cannot directly predict the charge radius, quadrupole moment and quadrupole radius at LO since the expressions (4.66), (4.69) and (4.74) contain unknown counterterms. Nevertheless, we determined a value for the quadrupole moment for ^{15}C , $\mu_Q^{(d)} \approx -4.21(10) \text{ efm}^2$, by exploiting the

linear correlation between the reduced E2 transition strength $B(E2)$ and the quadrupole moment in our Halo EFT, fitting the unknown counterterm to *ab initio* data from the IT-NCSM. With the result for the quadrupole moment, we also predicted the quadrupole radius for ^{15}C , $\langle r_Q^2 \rangle^{(d)} \approx 7.70(17) \times 10^{-2} \text{ fm}^2$, using correlations from Halo EFT. These correlations are not obvious in *ab initio* approaches because the separation of scales is not explicit in the parameters of the theory. This demonstrates the complementary character of Halo EFT towards *ab initio* methods. In principle, the universal correlations allow to extract information even from unconverged *ab initio* calculations since the correlations are universal. We compared the linear Halo EFT correlation to the quadratic correlation based on the simple rotational model by Bohr and Mottelson. The value for the quadrupole moment, $\mu_Q^{(d)} \approx -3.98(5) \text{ efm}^2$, obtained from the quadratic correlation deviates from the linear result by 5% – 30% depending on the input used for $\gamma_0^2 - \gamma_2^2$. Within the accuracy of LO EFT this is still consistent.

In the Halo EFT approach, static observables and nuclear reactions can be calculated in the same framework. Therefore, we also considered E1 neutron capture and photodissociation into the S - and D -wave states at LO. In the case of ^{15}C , we used the values for the effective range parameters of the D -wave renormalization extracted from $B(E2)$ to compute the cross section for both reactions into the S - and D -wave bound state. E1 capture into the S -wave state was already considered by *Rupak et al.* [82], who compared their result to experimental data. Our result is consistent with their findings taking our estimate of NLO corrections into account and disregarding the peak in the cross section due to the inclusion of the P -wave resonance by *Rupak*. The latter yields a NLO contribution in our power-counting scenario. In the case of ^{17}C , the lack of experimental data complicates numerical predictions so that our predictions are limited to the S -wave bound state.

We also calculated static observables and nuclear reaction in the magnetic sector. As a general rule, the counterterms are even more dominant for magnetic observables than in the electric case. This further complicates numerical predictions. Consider the S -wave magnetic form factor for example, the counterterm enters already at NLO, while for the electric form factor the counterterm yields a N^3LO contribution [64]. In the case of the D -wave, neither the magnetic moment nor the M1 transition from the D -wave ground state to the excited S -wave or D -wave bound state in ^{17}C can be predicted because of the emerging counterterms at LO. Furthermore, the two diagrams at LO for the M1 neutron capture into the S -wave state cancel each other and another unknown counterterm enters at NLO. In the D -wave sector, the counterterms contribute already at LO and due to the lack of experimental data, we cannot predict the cross section numerically.

As exotic nuclei are difficult to describe by *ab initio* methods, our results show the usefulness and complementary character of the Halo EFT approach even for D -wave bound states. Although we predicted several observables, in particular in the electric sector, the dominant role of counterterms and the increasing number of matching parameters demonstrate the limiting factors for the extension to higher partial waves beyond D -waves.



5 Pion Photoproduction

In this chapter, we shift our focus to the threshold pion photoproduction off light nuclei employing χ EFT. Pion production off nucleons and nuclei is a useful tool to study and test ChPT and to obtain further insights into nuclear structure. Our work is motivated by the previous calculation of threshold neutral pion photoproduction off ${}^3\text{He}$ and ${}^3\text{H}$ by *Lenkewitz et al.* [26, 111, 112]. They used ${}^3\text{He}$ as a neutron-like target and extracted the S -wave pion production amplitude in order to verify the counterintuitive ChPT prediction that $E_{0+}^{\pi^0 n} = +2.13 \times 10^{-3}/M_{\pi^+}$ is larger in magnitude than $E_{0+}^{\pi^0 p} = -1.16 \times 10^{-3}/M_{\pi^+}$ [23, 27]. In a similar approach, pion photoproduction off ${}^2\text{H}$ was studied before in Ref. [113]. Instead of a hadron physics motivation, our goal is to further test ChPT in the sense of nuclear physics and to extend the calculation of the pion production to a broad number of light nuclei.

To analyze the pion photoproduction off nuclei, we have to calculate the nuclear matrix element of the pion production operator $\langle M'_J | \hat{O} | M_J \rangle_\Psi$, where M_J (M'_J) denotes the magnetic quantum number of the initial (final) nuclear wave function, Ψ , corresponding to the total angular momentum, J . *Lenkewitz et al.* evaluated the matrix element numerically using Monte Carlo integration and wave functions from ChPT at the appropriate order. We employ a different approach that is more convenient for the extension to a broad number of nuclei. As explained in Chapter 3, the nuclear wave functions are obtained by the (IT)-NCSM from *Robert Roth* [76] employing nuclear interactions from ChPT. These wave functions are given in the harmonic oscillator (HO) basis. Since our pion production operator obtained from ChPT is given in the plane wave (PW) basis, we transform the pion production operator into the HO basis and apply a density matrix approach to extract the relevant information from the many-body HO wave functions for the relevant one-nucleon (1N) and two-nucleon (2N) pion production operators. The exact procedure is discussed in more detail in the following sections. This approach has the benefit that we have to calculate the pion production operator in HO basis only once. Then the pion production amplitude for arbitrary nuclei can be derived at no additional computational cost except for the respective density matrix calculation.

Experimentally, the pion production off light nuclei was studied at Saskatoon [19, 20] for ${}^2\text{H}$, ${}^4\text{He}$ and ${}^{12}\text{C}$ and at MAMI [21, 22] for ${}^7\text{Li}$ and H , respectively. For a review of this topic see Ref. [18].

5.1 Pion Photoproduction at Threshold

The pion photoproduction describes the nuclear process of the creation of a pion (π^0, π^\pm) through absorption of a photon (γ) by the nucleus (A) with proton number (Z). This reaction is illustrated in Fig. 5.1 and given by

$$\gamma + A(Z) \rightarrow \pi^0 + A'(Z) \quad (5.1)$$

$$\gamma + A(Z) \rightarrow \pi^\pm + A'(Z \mp 1) . \quad (5.2)$$

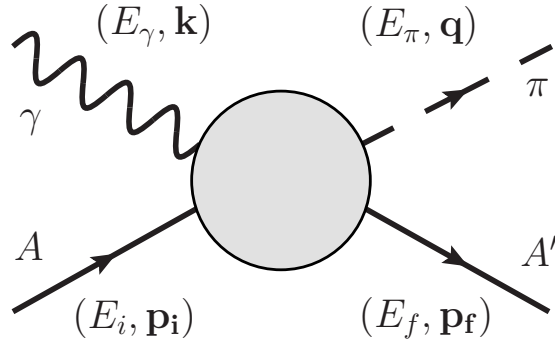


Figure 5.1.: Pion photoproduction. The photon (γ) is absorbed by the nucleus (A) and a pion (π) is produced. The corresponding energies and momenta are given in parenthesis, respectively.

Since the photon requires enough energy to produce a pion with mass $m_{\pi^0} \approx 134.97$ MeV or $m_{\pi^\pm} \approx 139.57$ MeV [37], there is a threshold above which pion production becomes possible. Due to energy and momentum conservation, the threshold photon energy is slightly higher than the bare pion mass and converges to m_π for increasing mass number of the nucleus because the recoil effect becomes negligible. In this work, we concentrate on the pion production at threshold, where the momentum of the produced pion is zero ($\mathbf{q} = \mathbf{0}$). Hence, we deduce from momentum and energy conservation

$$\mathbf{p}_i + \mathbf{k} = \mathbf{p}_f, \quad (5.3)$$

$$E_\gamma^{\text{thresh}} = E_f - E_i + m_\pi \quad \text{with} \quad E_{f/i} = \frac{p_{f/i}^2}{2m_A}, \quad (5.4)$$

with the mass of the nucleus m_A , \mathbf{k} indicates the photon momentum and \mathbf{p}_i (\mathbf{p}_f) denotes the initial (final) momentum of the nucleus. If we consider the initial nucleus to be at rest ($\mathbf{p}_i = \mathbf{0}$) such that $\mathbf{p}_f = \mathbf{k}$, we obtain for the threshold energy depending on the mass of the nucleus

$$E_\gamma^{\text{thresh}}(m_A) = m_A - \sqrt{m_A^2 - 2m_A m_\pi} \approx m_\pi + \mathcal{O}(m_\pi^2/m_A), \quad (5.5)$$

where we exploited in the last step that $m_\pi \ll m_A$.

Depending on the incoming multipolarity of the photon RL , where R stands for E or M and L denotes the multipole, and the spin of the nucleus S , the outgoing pion-nucleus system can be only in distinct outgoing channels such that angular momentum J and parity are conserved [114]

$$|L \pm S| = J = |l \pm S|, \quad (5.6)$$

where l denotes the orbital momentum of the pion relative to the recoiling nucleus. At threshold, the dominant contribution comes from the S -wave multipole E_{0+} of the pion-nucleus system, which corresponds to an incoming $E1$ photon and an orbital momentum of the pion of $l = 0$. Above threshold, where the momentum of the produced pion differs from zero $|\mathbf{q}| > 0$, contributions from P -wave and

even higher multipoles become important. For more details concerning the derivation of multipole amplitudes for the pion production see, e.g., Refs. [115–117].

In this work, we consider the threshold neutral pion photoproduction, where only the S -wave amplitude is relevant at LO. In Refs. [118–120] the S - and P -wave amplitudes for the pion production off the proton and ${}^2\text{H}$ are derived. We follow their approach and extract the S -wave amplitude for neutral pion production, which is consistent with Ref. [112],

$$\mathcal{M}^\lambda =: 2iE_{0+}^{\pi^0}(\boldsymbol{\epsilon}^\lambda \cdot \mathbf{J}) + 2i(L_{0+}^{\pi^0} - E_{0+}^{\pi^0})(\boldsymbol{\epsilon}^\lambda \cdot \hat{\mathbf{k}})(\hat{\mathbf{k}} \cdot \mathbf{J}) \quad (5.7)$$

$$= 2iE_{0+}^{\pi^0}(\boldsymbol{\epsilon}_T^\lambda \cdot \mathbf{J}) + 2iL_{0+}^{\pi^0}(\boldsymbol{\epsilon}_L^\lambda \cdot \mathbf{J}), \quad (5.8)$$

where $\boldsymbol{\epsilon}_T^\lambda = \boldsymbol{\epsilon}^\lambda - (\boldsymbol{\epsilon}^\lambda \cdot \hat{\mathbf{k}})\hat{\mathbf{k}}$ and $\boldsymbol{\epsilon}_L^\lambda = (\boldsymbol{\epsilon}^\lambda \cdot \hat{\mathbf{k}})\hat{\mathbf{k}}$ denote the transverse and longitudinal part of the photon polarization vector $\boldsymbol{\epsilon}^\lambda$, respectively. The nuclear spin vector is given by \mathbf{J} and the photon momentum by \mathbf{k} . In principle, there are also longitudinal multipoles $\sim L_{0+}$ that can be calculated using longitudinal polarized photons. Since we focus on the photoproduction and not on the electroproduction of pions, we employ transverse polarized photons ($\boldsymbol{\epsilon}^\lambda \cdot \mathbf{k} = 0$), where the longitudinal parts are zero.

5.2 Neutral and Charged Pion Photoproduction

The next step in the calculation of pion photoproduction amplitudes is the derivation of the relevant Feynman diagrams at LO for neutral and charged pion production. We follow the power counting in Refs. [112, 113] for Feynman diagrams from chiral perturbation theory (Sec. 2.1.2) to deduce the relevant Feynman diagrams at LO. The chiral order for a given diagram is given by

$$\nu = 4 - A - 2C + 2L + \sum_i V_i \Delta_i, \quad \text{with} \quad \Delta_i = d_i + \frac{N_i}{2} - 2, \quad (5.9)$$

where A denotes the total number of nucleon lines in the initial or final state, C the number of separately connected pieces, L the number of loops and V_i vertices of type i with dimension Δ_i . The latter is derived from N_i which denotes the number of nucleon lines attaching a vertex of type i and from d_i which is the dimension of the meson ($\mathcal{L}_{\pi\pi}$), meson-baryon Lagrangian ($\mathcal{L}_{\pi N}$) as described in Sec 2.1.2. For more details regarding the vertices V_i and corresponding Feynman rules we refer the reader to Ref. [24] appendix A.

Similar to the hierarchy of nuclear forces in Fig. 2.1, we find that one-nucleon contributions start to appear earlier in the chiral order than two-nucleon contributions, et cetera. The lowest order contribution for pion photoproduction contains the maximum number of disconnected pieces ($C = A$), no loops ($L = 0$), one vertex with $\Delta_i = -1$, which is the lower bound from chiral symmetry after the inclusion of photons via minimal substitution, and any number of vertices with $\Delta_i = 0$

$$\nu = 4 - A - 2A + 0 - 1 = 3 - 3A. \quad (5.10)$$

At this order, the prominent Kroll-Ruderman term contributes [121]. The NLO contribution has one additional vertex with $\Delta_i = 1$

$$\nu = 4 - A - 2A = 4 - 3A. \quad (5.11)$$

At NNLO, we get one-nucleon contributions with $L = 0$ and $\sum_i V_i \Delta_i = 1$, where $\Delta_i = 2, 1, 0, -1$, and with $L = 1$, one vertex with $\Delta_i = -1$ and any number of vertices with $\Delta_i = 0$. Moreover, the two-nucleon contributions start to appear at this order with $C = A - 1$, $L = 0$, one vertex with $\Delta_i = -1$ and any number of vertices with $\Delta_i = 0$. Since the lowest order of N -nucleon contribution differs only in $C = A - N$, we deduce that the next higher $(N + 1)$ -nucleon contributions starts two orders beyond the leading N -nucleon contribution.

Not all possible diagrams, however, contribute to the neutral pion photoproduction at threshold. For example, all the LO graphs, as the Kroll-Ruderman term, vanish for neutral pion production which is not the case for charged pion production [122]. As a consequence, the cross section for neutral pion production is smaller than for charged pions. Since we employ Coulomb gauge ($\epsilon \cdot k = 0$), only the two diagrams (a) and (b) survive in the two-nucleon sector, illustrated in Fig. 5.2.

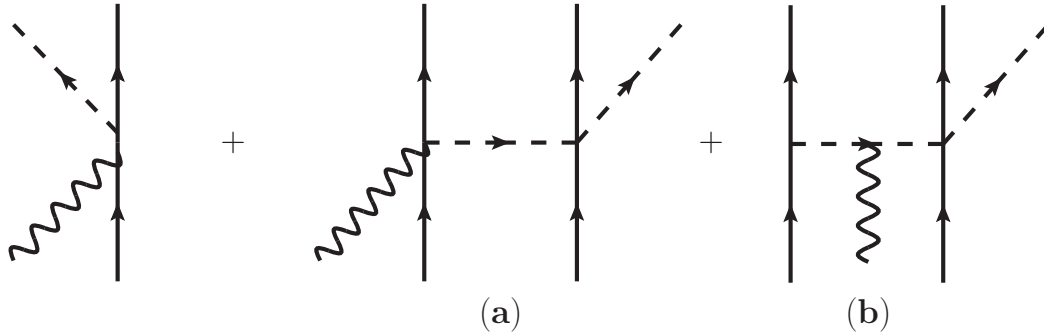


Figure 5.2.: Relevant diagrams at LO for the neutral pion photoproduction at threshold. Solid, dashed and wiggly lines denote nucleons, pions and photons, respectively. In the left panel, the one-nucleon contribution is shown, while in the right panel the two-nucleon diagrams (a) and (b) are illustrated.

Accordingly, we have one-nucleon and two-nucleon contributions for neutral pion photoproduction at LO or at chiral order q^3 , where q is a generic symbol for a small momentum or the pion mass. The relevant diagrams at this order are shown in Fig. 5.2. In contrast, charged pion photoproduction at threshold is well described by the one-nucleon contribution from the Kroll-Ruderman term at LO [123].

At order q^4 , there are additional contributions in the one- and two-nucleon sector for neutral pion photoproduction at threshold. We briefly discuss these corrections and refer the reader to Refs. [26, 112] for more details. First, there are boost corrections that emerge from the relative motion of the nucleons inside the nucleus. This leads to a slight shift in the pion production threshold compared to a single nucleon and essentially induces P -wave contributions due to the lowering of the threshold. Second, there are further corrections in the two-nucleon sector which can be grouped into static and recoil corrections. The former are tree graphs that contain exactly one insertion from the dimension two

pion-nucleon Lagrangian ($\mathcal{L}_{\pi N}^{(2)}$), while recoil corrections involve only insertions from the dimension one pion-nucleon Lagrangian.

5.3 Density Matrix Approach

As briefly discussed in the introduction to this chapter, we employ the (IT)-NCSM (Sec. 3) to obtain the nuclear wave functions and apply a density matrix approach to calculate the pion production amplitude for the considered nucleus. In principle, the nucleus is an A -body system where up to A particles can be involved in the pion production process. This is illustrated in the top panel of Fig. 5.3, where the so-called integral kernel is sandwiched with the initial and final nuclear wave function.

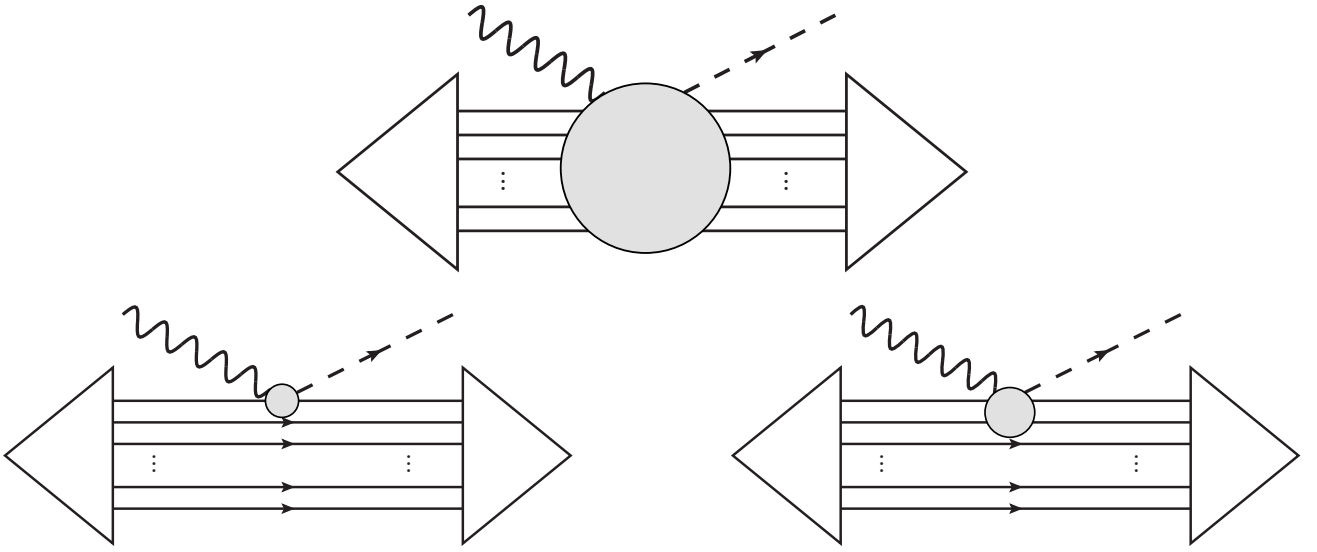


Figure 5.3.: Pion photoproduction off the nucleus. The gray bubble denotes the integral kernel that is sandwiched with the initial and final nuclear wave function denoted by the triangles. Solid, dashed and wiggly lines denote nucleons, pions and photons, respectively. In the top panel, the generalized integral kernel is shown, where in the bottom panel the two relevant topologies for threshold neutral pion photoproduction at LO are illustrated.

The integral kernel contains all possible diagrams from Sec. 5.2. For the threshold neutral pion photoproduction, only 1N- and 2N-topologies contribute at LO. This is shown in the bottom panel of Fig. 5.3, where the nucleons that are not involved in the pion production act as spectators. Since we are interested in pion photoproduction off a broad range of light nuclei, employing the (IT)-NCSM is convenient. As explained in Chapter 3, the wave functions $|\Psi^{\text{HO}}\rangle$ obtained by the (IT)-NCSM are a superposition of many-body Slater determinants $|\Phi_i\rangle$ in HO basis

$$|\Psi^{\text{HO}}\rangle = \sum_i c_i |\Phi_i^{\text{HO}}\rangle = \sum_i c_i |s_1^{\text{HO}} s_2^{\text{HO}} \dots s_A^{\text{HO}}\rangle_i, \quad (5.12)$$

where the correct normalization of the total wave function is ensured by the c_i constants, the single-particle HO eigenstates are indicated by $|s_i^{\text{HO}}\rangle$ and A denotes the total number of nucleons.

To calculate the pion production amplitude with the (IT)-NCSM wave functions provided by *Robert Roth*, we use one-particle and two-particle density matrices. Density matrices are an expedient tool from second quantization to reduce the information from a many-body state to the relevant information for 1N- or 2N-operators. It is an alternative representation of the many-body state that encodes all the relevant information of the system.

The 1N-density matrix for a many-body state $|\Psi\rangle$ in a single-particle basis $|s\rangle$ is defined as

$$\rho_{s,s'}^{(1N)} = \langle \Psi | \hat{a}_{s'}^\dagger \hat{a}_s | \Psi \rangle , \quad (5.13)$$

where \hat{a}_s^\dagger and \hat{a}_s are the creation and annihilation operators for a single-particle state s , respectively. Summing up the diagonal elements of $\rho^{(1N)}$ yields the particle number N of the many-body system

$$\text{Tr}(\rho^{(1N)}) = \sum_s \rho_{s,s}^{(1N)} = N . \quad (5.14)$$

Likewise, the 2N-density matrix is defined as

$$\rho_{s_1 s_2, s'_1 s'_2}^{(2N)} = \langle \Psi | \hat{a}_{s'_1}^\dagger \hat{a}_{s'_2}^\dagger \hat{a}_{s_1} \hat{a}_{s_2} | \Psi \rangle . \quad (5.15)$$

The trace of the 2N-density matrix yields the number of pairs of the many-body system, i.e. all possible combinations, times two

$$\text{Tr}(\rho^{(2N)}) = \sum_{s_1 s_2} \rho_{s_1 s_2, s_1 s_2}^{(2N)} = N(N-1) . \quad (5.16)$$

Moreover, ρ is Hermitian so that $\rho_{s,s'}^{(1N)} = \rho_{s',s}^{(1N)}$ and because of the antisymmetric two-particle basis states, we deduce

$$\rho_{s_1 s_2, s'_1 s'_2}^{(2N)} = -\rho_{s_2 s_1, s'_1 s'_2}^{(2N)} = -\rho_{s_1 s_2, s'_2 s'_1}^{(2N)} = \rho_{s_2 s_1, s'_2 s'_1}^{(2N)} . \quad (5.17)$$

In addition, the trace of the density matrix does not change under unitary transformations since the trace is invariant under cyclic permutations

$$\text{Tr}(\mathbf{U}\rho\mathbf{U}^\dagger) = \text{Tr}(\mathbf{U}^\dagger\mathbf{U}\rho) = \text{Tr}(\rho) . \quad (5.18)$$

This will be used later to validate if our basis transformation matrix from plane wave to HO basis states indeed satisfies unitarity.

After calculating the density matrix for the HO many-body wave function, we can use it to compute

any expectation value for a given 1N-operator $\hat{O}^{(1N)}$

$$\langle \Psi_f | \hat{O}^{(1N)} | \Psi_i \rangle = \sum_{ss'} \langle \Psi_f | s' \rangle \langle s' | \hat{O} | s \rangle \langle s | \Psi_i \rangle = \sum_{ss'} o_{s',s} \langle \Psi_f | \hat{a}_{s'}^\dagger \hat{a}_s | \Psi_i \rangle = \sum_{ss'} o_{s',s} \rho_{s,s'}^{(1N)} = \text{Tr} \left(\mathbf{O}^{(1N)} \boldsymbol{\rho}_{\Psi_f \Psi_i}^{(1N)} \right), \quad (5.19)$$

with $\hat{O}^{(1N)} = \sum_{ss'} o_{s',s} \hat{a}_{s'}^\dagger \hat{a}_s$.

The expectation value of a 2N-operator can be calculated likewise using the 2N-density matrix

$$\langle \Psi_f | \hat{O}^{(2N)} | \Psi_i \rangle = \text{Tr} \left(\mathbf{O}^{(2N)} \boldsymbol{\rho}_{\Psi_f \Psi_i}^{(2N)} \right). \quad (5.20)$$

5.4 Plane Wave to Harmonic-Oscillator Basis Transformation

Up to this point, we derived the relevant Feynman diagrams contributing to the pion production at LO and discussed the density matrix approach to evaluate the expectation value of the pion production operator with the nuclear wave functions obtained by the (IT)-NCSM. Since the derived pion production operators are represented in plane wave (PW) basis, while the wave functions from the (IT)-NCSM are in harmonic-oscillator (HO) basis, the next step towards the calculation of the amplitude is the necessary basis transformation of the pion production operator from PW into HO representation

$$\langle \Psi_f | \hat{O} | \Psi_i \rangle = \text{Tr} \left(\mathbf{U} \mathbf{O} \mathbf{U}^\dagger \boldsymbol{\rho}_{\Psi_i \Psi_f} \right), \quad (5.21)$$

with the transformation matrix \mathbf{U} .

The transformation matrix between the PW and HO single-particle states (s_i) reads

$$U_{ab} = \langle s_a^{\text{HO}} | s_b^{\text{PW}} \rangle := \langle (nlm_l)_a | \mathbf{k} \rangle_b = i^l \Phi_{nl}(k) Y_{lm_l}^*(\Omega_k), \quad (5.22)$$

with the spherical HO quantum numbers (nlm_l) , the PW momentum $k = |\mathbf{k}|$, the spherical harmonics $Y_{lm_l}(\Omega)$ and the spherical harmonic-oscillator wave function in momentum space [124]

$$\Phi_{nl}(k) = (-1)^n \sqrt{\frac{2n!}{\Gamma(n+l+\frac{3}{2})}} (k^l b^{l+3/2}) \exp\left(-\frac{1}{2}(kb)^2\right) L_n^{(l+1/2)}((kb)^2). \quad (5.23)$$

Here, $b = \sqrt{\hbar/(m_N \omega)}$ denotes the oscillator length, depending on the oscillator frequency ω and nucleon mass $m_N \approx 939$ MeV, while $L_n^{(k)}(x)$ represents the generalized Laguerre polynomials.

The expression for the transformation matrix in Eq. (5.22) can be derived by repeatedly inserting identity operators

$$\langle nlm_l | \mathbf{k} \rangle = \int_0^\infty dk' k'^2 \sum_{l'm'_l} \langle nlm_l | k'l'm'_l \rangle \langle k'l'm'_l | \mathbf{k} \rangle \quad (5.24)$$

$$= \int_{-\infty}^\infty d^3\mathbf{r} \int_0^\infty dk' k'^2 \sum_{l'm'_l} \Phi_{nl}(k') \langle k'l'm'_l | \mathbf{r} \rangle \langle \mathbf{r} | \mathbf{k} \rangle \quad (5.25)$$

$$= \int_0^\infty dr r^2 \int d\Omega_r \int_0^\infty dk' k'^2 \sum_{l'm'_l} \Phi_{nl}(k') \sqrt{\frac{2}{\pi}} j_{l'}(k'r) Y_{l'm'_l}^*(\Omega_r) \frac{1}{(2\pi)^{3/2}} \exp(i\mathbf{k} \cdot \mathbf{r}), \quad (5.26)$$

with the spherical HO momentum basis $|klm_l\rangle$ and the spherical Bessel functions j_l . After spherically expanding the plane wave

$$\exp(i\mathbf{k} \cdot \mathbf{r}) = 4\pi \sum_{l''=0}^\infty \sum_{m''=-l''}^{l''} i^{l''} j_{l''}(kr) Y_{l''m''}(\hat{\mathbf{k}}) Y_{l''m''}^*(\hat{\mathbf{r}}), \quad (5.27)$$

and exploiting the orthogonality of the spherical harmonics and spherical Bessel functions, we eventually obtain the result of Eq. (5.22).

Furthermore, the spin projection, m_s , and isospin projection, m_t , have to be included as additional quantum numbers in the single-particle basis. Since these quantum numbers are identical in both bases, we have neglected them in the transformation above

$$|s^{\text{HO}}\rangle_i = |nlm_l m_s m_t\rangle_i \quad |s^{\text{PW}}\rangle_i = |\mathbf{k} m_s m_t\rangle_i. \quad (5.28)$$

However, the HO single-particle states from the (IT)-NCSM are coupled to total angular momentum $j = |l \pm s|$. Therefore, we have to decouple the HO single-particle states with the corresponding Clebsch-Gordan coefficients which yields for the transformation

$$U_{ab} = \langle s_a^{\text{HO}} | s_b^{\text{PW}} \rangle := \langle (n(ls)jm_j m_t)_a | (\mathbf{k} m_s m_t)_b \rangle \quad (5.29)$$

$$= i^l \Phi_{nl}(k) \sum_{m_l} \left(\frac{1}{2} m_s \ l m_l \left| j m_j \right. \right) Y_{lm_l}^*(\Omega_k) \quad (5.30)$$

$$= i^l \Phi_{nl}(k) \left(\frac{1}{2} m_s \ l(m_j - m_s) \left| j m_j \right. \right) Y_{l(m_j - m_s)}^*(\Omega_k). \quad (5.31)$$

In principle, the PW basis is continuous in \mathbf{k} while $|\mathbf{k}|$ goes from minus infinity to plus infinity. For the numerical integration of the matrix element, however, we need to discretize our basis and employ a

momentum grid

$$1 = \int_{-\infty}^{\infty} d^3\mathbf{k} |\mathbf{k}\rangle \langle \mathbf{k}| \rightarrow \sum_{\mathbf{k}, |\mathbf{k}| \leq k_{\max}} \Delta_{\mathbf{k}}^3 |\mathbf{k}\rangle \langle \mathbf{k}|, \quad (5.32)$$

with grid length k_{\max} and grid spacing $\Delta_{\mathbf{k}}^3 = \Delta_{k_x} \Delta_{k_y} \Delta_{k_z}$. The simplest method for the grid generation is the application of an equidistant grid for the momentum basis. For an appropriate number of momentum basis states, this leads to consistent results. However, to improve the convergence with the same number of basis states, it is convenient to employ a more sophisticated ansatz to decrease the step size in the dominant region or increase the step size in the less important domain and weighting every point individually. Therefore, we apply the Gauss-Legendre n -point quadrature formula for the grid generation [125], where the weights for the j -th grid point can be expressed as

$$w_j = \frac{2}{(1-x_j^2)[P'_n(x_j)]^2}, \quad (5.33)$$

with the Legendre Polynomials $P_n(x)$ and x_j denotes the j -th root of P_n adapted to the employed grid length. If the grid domain goes from -1 to $+1$, x_j would be exactly the j -th root of P_n .

Using a distinct momentum grid instead of a continuous momentum basis from minus infinity to plus infinity, we have to take care of ultraviolet errors due to an undersized grid domain and of infrared errors because of an insufficient grid spacing. To specify the appropriate grid dimensions, we calculate $UU^\dagger \stackrel{!}{=} 1$ to cross check our grid resolution for a given HO basis with $|s_i^{\text{HO}}\rangle = |(n(ls)jm_t)_i\rangle$

$$1 = \langle s_i^{\text{HO}} | s_i^{\text{HO}} \rangle = \sum_{m_s} \int d^3\mathbf{k} \langle s_i^{\text{HO}} | \mathbf{k} m_s m_t \rangle \langle \mathbf{k} m_s m_t | s_i^{\text{HO}} \rangle \quad (5.34)$$

$$= \sum_{m_s} \sum_{\mathbf{k}} \Delta_{\mathbf{k}}^3 \langle s_i^{\text{HO}} | \mathbf{k} m_s m_t \rangle \langle \mathbf{k} m_s m_t | s_i^{\text{HO}} \rangle \quad (5.35)$$

$$= \sum_j \Delta_{\mathbf{k}_j}^3 \langle s_i^{\text{HO}} | (\mathbf{k} m_s m_t)_j \rangle \langle (\mathbf{k} m_s m_t)_j | s_i^{\text{HO}} \rangle \quad (5.36)$$

$$= \sum_j \Delta_{\mathbf{k}_j}^3 U_{ij} U_{ji}^\dagger, \quad (5.37)$$

where $\Delta_{\mathbf{k}_j}^3 = w_{k_x,j} w_{k_y,j} w_{k_z,j}$ denotes the weights from the Gauss-Legendre algorithm (5.33) of the j -th plane wave state $|(\mathbf{k} m_s m_t)_j\rangle$. Since the HO single-particle states are orthonormal, the off diagonal entries in U should yield zero. In terms of precision, three digits are sufficient for our numerical accuracy.

In the (IT)-NCSM, the HO single-particle basis is truncated in the single-particle energy e_{\max} , which is chosen such that it matches the many-body N_{\max} truncation. The HO single-particle energy is defined as $e = 2n + l$. Depending on the dimension of the HO single-particle basis, we have to adapt our grid dimensions for a consistent numerical precision. In general, we find that grid spacing values below 0.5 fm^{-1} are reasonable and an appropriate grid limit is around 4.5 fm^{-1} . Note that the grid dimensions are not explicitly applied since they are used as input for the Gauss-Legendre algorithm that generates

the grid points with individual weights and varying grid spacings. However, they set the total number of grid points generated by the algorithm.

5.5 One-Nucleon Results

In this chapter, we explicitly discuss the computation of one-body operators with the density approach described above. The nuclear wave functions employed in this thesis are provided by the group of *Robert Roth*. We start with a proof of concept calculation for the magnetic moments and then present our results of the one-nucleon contribution to the neutral pion photoproduction amplitude at threshold and compare them with the literature. Throughout the entire discussion of our one-nucleon and two-nucleon results, the IT scheme is not required for the NCSM calculation of the nuclear wave functions since the many-body problem for the nuclei under consideration can be solved numerically without the additional importance truncation for sufficiently large N_{\max} model spaces. However, our approach can also be applied to nuclear wave functions obtained by the IT-NCSM.

5.5.1 Magnetic Moment Benchmark

As a first cross check of our numerical procedure, we calculate the 1N contribution to the magnetic dipole moment for different nuclei and compare them to the corresponding NCSM result and the results obtained by *Lenkewitz* [112].

The 1N operator for the magnetic moment in spin and isospin space has the generic form [112]

$$\hat{\mu}^{1N} = \hat{\mu}_1 + \hat{\mu}_2 + \cdots + \hat{\mu}_A, \quad (5.38)$$

$$\hat{\mu}_i = \boldsymbol{\sigma}_i \left(\frac{1 + \tau_i^z}{2} \mu_p + \frac{1 - \tau_i^z}{2} \mu_n \right) + l_i \frac{1 + \tau_i^z}{2} \mu_N, \quad (5.39)$$

where $\boldsymbol{\sigma}$ denotes the spin operator represented by the Pauli matrices, τ^z is the z -component of the isospin operator and $\mu_p = 2.79 \mu_N$, $\mu_n = -1.91 \mu_N$ are the magnetic moments of the proton and neutron, respectively, in units of nuclear magneton μ_N . The last term proportional to the angular momentum l , which is generated by the rotating proton charges, is expected to be small. However, it should become more important for nuclei where the total spin of the nucleus J is not dominated by the S -wave contribution with $L = 0$.

The expectation value is then given by

$$\langle M'_J | \hat{\mu}^{1N} | M_J \rangle_\Psi = \sum_{s_i} \sum_{s_j} \sum_{m_s, m'_s} \int d^3 \mathbf{k} \int d^3 \mathbf{k}' U_{s_j, k' m'_s} \mathbf{o}_{m'_s m'_t, m_s m_t} \delta^{(3)}(\mathbf{k} - \mathbf{k}') U_{s_i, k m_s}^\dagger \boldsymbol{\rho}_{s_i, s_j}^{1N} \quad (5.40)$$

$$= \sum_{s_i, s_j} \sum_{m_s, m'_s} \sum_{\mathbf{k}} \Delta_{\mathbf{k}}^3 U_{s_j, k m'_s} \mathbf{o}_{m'_s m'_t, m_s m_t} U_{s_i, k m_s}^\dagger \boldsymbol{\rho}_{s_i, s_j}^{1N} \quad (5.41)$$

$$= \text{Tr} \left(\mathbf{U} \mathbf{O} \mathbf{U}^\dagger \boldsymbol{\rho}_{M_J M'_J}^{1N} \right), \quad (5.42)$$

where $\mathbf{o}_{m'_s m'_t, m_s m_t}$ denotes the single-particle operator of the magnetic moment in PW basis that reads

$$\mathbf{o}_{m'_s m'_t, m_s m_t} = \left\langle \mathbf{k} m'_s m'_t \left| \boldsymbol{\sigma} \left(\frac{1 + \tau^z}{2} \mu_p + \frac{1 - \tau^z}{2} \mu_n \right) + l \frac{1 + \tau^z}{2} \mu_N \right| \mathbf{k} m_s m_t \right\rangle. \quad (5.43)$$

In principle, different choices for M_J and M'_J yield different results for the expectation value $\langle M'_J | \hat{\boldsymbol{\mu}}^{1N} | M_J \rangle_\Psi$. However, the results are proportional to the spin matrices for a given nuclear spin, J , so that we can cross check our numerical outcome. As a consequence, we find for the tensor structure of the expectation value for $\boldsymbol{\mu}^{1N}$

$$\langle M'_J | \hat{\boldsymbol{\mu}}^{1N} | M_J \rangle_\Psi =: \frac{J_{M'_J M_J}}{J} \boldsymbol{\mu}_\Psi^{1N}, \quad (5.44)$$

where $\boldsymbol{\mu}_\Psi^{1N}$ indicates the result of the magnetic dipole moment for the nuclear state denoted by $|\Psi\rangle$ and $J_{M'_J M_J}$ is the entry of the spin matrix for the nuclear spin J at the position M'_J, M_J .

In the next step, our results for the magnetic moment are compared with the NCSM results from *Robert Roth* and with the results obtained by *Lenkewitz* in Ref. [112]. As a first remark, by varying the boundaries and density of our momentum grid, we can monitor the convergence behavior of our results. Moreover, we find that the grid values obtained from our unity matrix validation above are also appropriate for the magnetic moment calculation.

We compute the magnetic moment for arbitrary nuclei and find that our values are consistent with the results from the NCSM up to the desired accuracy. In Ref. [112], *Lenkewitz* neglects the last term in Eq. (5.39), which is proportional to the angular momentum l . This is legitimate for ${}^3\text{H}$ and ${}^3\text{He}$, where contributions from this term are indeed negligible. However, for nuclei with dominant $L \neq 0$ contributions to the nuclear wave function this leads to significant deviations.

The results for ${}^2\text{H}$, ${}^3\text{H}$ and ${}^3\text{He}$ are shown in Tab. 5.1 for an NCSM calculation with $\hbar\omega = 20$ MeV and $N_{\text{max}} = e_{\text{max}} = 12$. We employ the NN interaction developed by Entem and Machleidt (EM) [44] at N^3LO with a cutoff of 500 MeV/c for the nonlocal regulator function. This NN force is combined with the local 3N force at N^2LO [105]. In order to improve the convergence in the many-body calculation, the potentials derived from ChPT are “softened” via unitary transformations that decouple high-momentum and low-momentum components. We achieve this by applying the similarity renormalization group (SRG) [79] where the SRG evolution of the Hamiltonian is carried out with a flow parameter $\alpha = 0.12 \text{ fm}^4$.

Table 5.1.: Numerical results for the magnetic dipole moment $\boldsymbol{\mu}^{1N}$ in units of $\boldsymbol{\mu}_N$ for different nuclei.

nucleus	our result	NCSM	Ref. [112]
${}^2\text{H}$	0.866	0.865	
${}^3\text{H}$	2.692	2.695	2.582(42)
${}^3\text{He}$	-1.833	-1.836	-1.810(34)
${}^6\text{Li}$	0.843	0.843	

Unless otherwise stated, we consistently use the same nuclear wave functions for all calculations throughout Chapter 5.

Note that we use different wave functions than in Ref. [112], which explains the small deviations. Hence, we are consistent with the numerical results. Furthermore, we extend the calculation to ${}^6\text{Li}$. The same interactions from ChPT are employed as before and the nuclear wave function is calculated by the NCSM for $N_{\text{max}} = 8$. The value for the magnetic moment of ${}^6\text{Li}$ is also consistent with the NCSM result.

5.5.2 One-Nucleon Contribution to the Neutral Pion Photoproduction

We have now all the tools at hand to calculate the one-body contribution to the neutral pion photoproduction at threshold. Following the approach in Ref. [112], we initially compute the transverse form factors $F_T^{S\pm V}$ before stating the final result for the S -wave amplitude E_{0+}^{1N} . This has the advantage that we gain further insights into the neutron and proton properties of the composite nucleus and can directly compare our results with *Lenkewitz et al.* As described in Sec. 5.2, the one-nucleon contribution at LO is illustrated in the first diagram from the left in Fig. 5.2. In this impulse approximation, the nucleons are considered to be coupling independently to the electromagnetic current.

Similar to the magnetic moment calculation, the 1N pion production operator is given by [112]

$$\mathcal{M}_{1N}^\lambda = \sum_{i=1}^A \mathcal{M}_i^\lambda \quad \text{with} \quad \mathcal{M}_i^\lambda = i\epsilon_T^\lambda \cdot \boldsymbol{\sigma}_i \left(\frac{1 + \tau_i^z}{2} E_{0+}^{\pi^0 p} + \frac{1 - \tau_i^z}{2} E_{0+}^{\pi^0 n} \right), \quad (5.45)$$

where ϵ_T^λ denotes the transverse photon polarization vector for a given polarization λ and $E_{0+}^{\pi^0 p}, E_{0+}^{\pi^0 n}$ are the pion production amplitudes off the proton and the neutron, respectively. For the elementary S -wave neutral pion production amplitudes at threshold, we take the predictions from the chiral perturbation theory calculation to order $\mathcal{O}(q^4)$ from Refs. [23, 126]

$$E_{0+}^{\pi^0 p} = -1.16 \times 10^{-3} / M_{\pi^+} \quad \text{and} \quad E_{0+}^{\pi^0 n} = +2.13 \times 10^{-3} / M_{\pi^+}, \quad (5.46)$$

given in the usual units. Note that the values above are order $\mathcal{O}(q^4)$ predictions in ChPT, while the chiral order of the LO contribution to the pion production is $\mathcal{O}(q^3)$. There are two reasons for this: First, we want to compare our numerical results for ${}^2\text{H}$, ${}^3\text{H}$ and ${}^3\text{He}$ with the values of Refs. [26, 113], which use the same predictions as in Eq. (5.46). Second, the order $\mathcal{O}(q^3)$ value for the threshold amplitudes disagrees with the experimentally measured S -wave amplitude at threshold [127]

$$E_{0+}^{\pi^0 p} = (-1.23 \pm 0.08 \pm 0.03) \times 10^{-3} / M_{\pi^+}, \quad (5.47)$$

since the E_{0+} amplitude is only slowly converging in ChPT [23]. The same predictions as in Eq. (5.46) can be derived by averaging the values of Refs. [27, 128]. Furthermore, the E_{0+} amplitudes above are consistent with the results of the chiral unitary approach in Ref. [25]. Since the elementary S -wave amplitudes from ChPT vary by about 5% in Refs. [27, 126, 128], we consequently assign a

5% uncertainty to the E_{0+} amplitudes. Even under consideration of the experimental value above, this seems to be a reasonable assumption. Moreover, this is consistent with the arguments in Ref. [26].

As described in Sec. 5.1 and shown in Eq. (5.8), the S -wave pion production amplitude can be extracted from the expectation value of the pion production operator

$$\langle M'_J | \mathcal{M}_{1N}^\lambda | M_J \rangle_\Psi =: 2iE_{0+}^{1N} (\boldsymbol{\epsilon}_T^\lambda \cdot \mathbf{J}) = 2i \left(E_{0+}^{\pi^0 p} \frac{F_T^{S+V}}{2} + E_{0+}^{\pi^0 n} \frac{F_T^{S-V}}{2} \right) (\boldsymbol{\epsilon}_T^\lambda \cdot \mathbf{J}) . \quad (5.48)$$

First, we calculate the transverse form factors

$$\langle M'_J | \hat{O}_{1N}^\lambda | M_J \rangle_\Psi = \left\langle M'_J \left| \sum_{i=1}^A \boldsymbol{\epsilon}_T^\lambda \cdot \boldsymbol{\sigma}_i \frac{1 \pm \tau_i^z}{2} \right| M_J \right\rangle_\Psi =: F_T^{S\pm V} (\boldsymbol{\epsilon}_T^\lambda \cdot \mathbf{J}) . \quad (5.49)$$

The corresponding expectation value is given by

$$\langle M'_J | \hat{O}_{1N}^\lambda | M_J \rangle_\Psi = \sum_{s_i, s_j} \sum_{m_s, m'_s} \int d^3 \mathbf{k} \int d^3 \mathbf{k}' U_{s_j, \mathbf{k}' m'_s} \mathbf{o}_{m'_s m'_t, m_s m_t}^\lambda \delta^{(3)}(\mathbf{k} + \mathbf{k}_\gamma - \mathbf{k}') U_{s_i, \mathbf{k} m_s}^\dagger \boldsymbol{\rho}_{s_i, s_j}^{1N} \quad (5.50)$$

$$= \sum_{s_i, s_j} \sum_{m_s, m'_s} \sum_{\mathbf{k}} \Delta_{\mathbf{k}}^3 U_{s_j, (\mathbf{k} + \mathbf{k}_\gamma) m'_s} \mathbf{o}_{m'_s m'_t, m_s m_t}^\lambda U_{s_i, \mathbf{k} m_s}^\dagger \boldsymbol{\rho}_{s_i, s_j}^{1N} \quad (5.51)$$

$$= \text{Tr} \left(\mathbf{U} \mathbf{O}^\lambda \mathbf{U}^\dagger \boldsymbol{\rho}_{M_J M'_J}^{1N} \right) , \quad (5.52)$$

where \mathbf{k}_γ denotes the photon momentum with $\boldsymbol{\epsilon}_T^\lambda \cdot \mathbf{k}_\gamma = 0$ and the single-particle operator for the transverse form factors in PW basis reads

$$\mathbf{o}_{m'_s m'_t, m_s m_t}^\lambda = \left\langle \mathbf{k} m'_s m'_t \left| \boldsymbol{\epsilon}_T^\lambda \cdot \boldsymbol{\sigma} \frac{(1 \pm \tau^z)}{2} \right| \mathbf{k} m_s m_t \right\rangle , \quad (5.53)$$

where \pm determines the appropriate transverse form factor $F_T^{S\pm V}$.

As explained in Sec. 3.2, the total many-body wave function factorizes into an intrinsic and a CM state

$$|\Psi_{\text{HO}}\rangle = |\Psi_{\text{int}}\rangle \otimes |\Psi_{\text{CM}}\rangle . \quad (5.54)$$

Compared to the magnetic moment operator, we have a momentum transfer from the photon to the nucleus in the pion photoproduction. Hence, the center-of-mass (CM) momentum is shifted by the incoming photon momentum $\mathbf{k}_\gamma \approx m_{\pi^0}$, cf. Eq. (5.5), due to the recoil of the nucleus. This poses an issue in the NCSM approach since the center-of-mass part of the wave function is expected to remain unchanged for the initial and final wave function.

Therefore, we have to modify our result to account for the shift in the CM momentum. Using

Eq. (5.54), the expectation value above (5.52) reads

$$\langle \Psi_f | \hat{O}_{1N}^\lambda | \Psi_i \rangle = \langle \Psi_f^{\text{int}} | \hat{O}_{1N}^\lambda | \Psi_i^{\text{int}} \rangle \langle \Psi_f^{\text{CM}} | \hat{O}_{1N}^\lambda | \Psi_i^{\text{CM}} \rangle = \text{Tr} \left(\mathbf{U} \mathbf{O}^\lambda \mathbf{U}^\dagger \boldsymbol{\rho}_{\Psi_i \Psi_f}^{1N} \right). \quad (5.55)$$

However, we are only interested in the intrinsic contribution to the pion production. For that reason, we have to divide our result by the CM contribution. In general, the CM state in the NCSM wave function occupies always the HO ground state $|NLM\rangle = |000\rangle$, where we use capital letters for the quantum numbers to indicate the CM state. In the case of the pion production, the overlap of the initial and final CM wave function thus yields

$$\langle \Psi_f^{\text{CM}} | \hat{O}_{1N}^\lambda | \Psi_i^{\text{CM}} \rangle = \langle 000 | \hat{O}_{1N}^\lambda | 000 \rangle = \int d^3 \mathbf{P}' \int d^3 \mathbf{P} \langle 000 | \mathbf{P}' \rangle \delta^{(3)}(\mathbf{P} + \mathbf{k}_\gamma - \mathbf{P}') \langle \mathbf{P} | 000 \rangle \quad (5.56)$$

$$= \int d^3 \mathbf{P} \langle 000 | \mathbf{P} + \mathbf{k}_\gamma \rangle \langle \mathbf{P} | 000 \rangle \quad (5.57)$$

$$= \int d^3 \mathbf{P} \Phi_{00}(|\mathbf{P} + \mathbf{k}_\gamma|) Y_{00}^*(\Omega_{\mathbf{P} + \mathbf{k}_\gamma}) \Phi_{00}(|\mathbf{P}|) Y_{00}(\Omega_{\mathbf{P}}) \quad (5.58)$$

$$= \exp\left(-\frac{1}{4} B^2 k_\gamma^2\right), \quad (5.59)$$

where \mathbf{P} denotes the CM momentum and $B = \sqrt{\hbar/(Am_N\omega)}$ the HO length for the composite system, depending on the number of nucleons A . For ${}^3\text{H}$, we have to divide our result by a factor of $\langle \Psi_f^{\text{CM}} | \hat{O}_{1N}^\lambda | \Psi_i^{\text{CM}} \rangle \approx 0.92$ to obtain only the intrinsic contribution. For increasing A , this factor converges to 1 since the recoil effect becomes negligible. In the case of the magnetic moment, we ignored the CM contribution because $\mathbf{k}_\gamma = 0$ and the CM part therefore yields $\langle \Psi_f^{\text{CM}} | \hat{O} | \Psi_i^{\text{CM}} \rangle = 1$.

From Eq. (5.49) we can then deduce the general S -wave amplitude. To account for the change in the phase space from the one-nucleon to the A -nucleon system, we have to multiply E_{0+}^{1N} by a kinematical factor [112]

$$K_{1N}(m_A) = \frac{m_N + m_\pi}{m_A + m_\pi} \frac{m_A}{m_N}, \quad (5.60)$$

which depends on the nuclear mass m_A . Thus, the S -wave amplitude for a given nucleus with A nucleons yields

$$E_{0+}^{1N} = \frac{K_{1N}(m_A)}{2} \left(E_{0+}^{\pi^0 p} F_T^{S+V} + E_{0+}^{\pi^0 n} F_T^{S-V} \right). \quad (5.61)$$

At threshold, we obtain non-vanishing amplitudes for all nuclei with spin J unequal to zero. Since the 1N calculation is not computationally exhausting, we can employ large momentum grids so that infrared and ultraviolet errors are negligible. Furthermore, we obtain consistent results for different combinations of initial M_J and final M_J' and varying photon polarizations λ . We also compare the results for different N_{max} (e_{max}) values and find that the pion production operator is not very sensitive

to different HO model spaces. In the case of ${}^3\text{H}$, we already reach convergence for $N_{\text{max}} = 10$ while the deviation of the $N_{\text{max}} = 2$ from the $N_{\text{max}} = 12$ result is about 5%. A similar behavior is observed for ${}^2\text{H}$, where the deviation of the $N_{\text{max}} = 2$ from the $N_{\text{max}} = 12$ pion production amplitude is about 7%. Moreover, the results are not very sensitive to different values of $\hbar\omega$ or varying flow parameters in the SRG evolution of the interaction. We expect both errors to be in the single-digit percentage range. Since we want to apply the pion production operator at threshold to a broad range of light nuclei, we have to choose a distinct photon momentum $k_\gamma \approx m_{\pi^0}$ that suits all nuclei. Due to the small deviation from this value induced by the recoil term $\sim k_\gamma/m_A$, we get a systematic error that is below 1% for the nuclei considered here. With these considerations, we estimate the total error to be in range of 5%. Additionally, we have to consider the 5% uncertainty from the ChPT prediction for the single-nucleon amplitudes $E_{0+}^{\pi^0 p/n}$.

As before, our numerical results for ${}^3\text{H}$ and ${}^3\text{He}$ are compared with Ref. [26] and for ${}^2\text{H}$ with Ref. [113] in Tab. 5.2. Taking the uncertainties into account, our values are consistent with the literature.

Table 5.2.: Numerical results of the one-nucleon contribution to the pion production amplitude at threshold for different nuclei. The numbers in parenthesis denote the errors. In the case of two consecutive parentheses, the first error represents the 5% estimation due to different chiral interactions and photon momenta while the second error indicates the uncertainty from the single-nucleon amplitudes. The NCSM calculation is performed for $N_{\text{max}} = 8$ in the case of ${}^6\text{Li}$ and in all other cases for $N_{\text{max}} = 12$. The literature results are taken from Refs. [26, 113].

nucleus	our result			literature		
	F_T^{S+V}	F_T^{S-V}	$E_{0+}^{1N} [10^{-3}/M_{\pi^+}]$	F_T^{S+V}	F_T^{S-V}	$E_{0+}^{1N} [10^{-3}/M_{\pi^+}]$
${}^2\text{H}$	0.773(39)	0.773(39)	0.40(5)(5)	0.72	0.72	0.37(5) [113]
${}^3\text{H}$	1.551(78)	0.039(2)	-0.94(5)(5)	1.493(25)	0.012(13)	-0.93(3)(5) [26]
${}^3\text{He}$	0.041(2)	1.544(77)	1.77(9)(9)	0.017(13)	1.480(26)	1.71(4)(9) [26]
${}^6\text{Li}$	0.476(24)	0.479(24)	0.26(3)(3)			

Moreover, we calculate the pion production amplitude for ${}^6\text{Li}$, which has the same nuclear spin structure $J^P = 1^+$ as ${}^2\text{H}$. By comparing the result of ${}^6\text{Li}$ to the computed values for ${}^2\text{H}$, ${}^3\text{H}$, and ${}^3\text{He}$, we find that the result of ${}^6\text{Li}$ differs significantly from the values for ${}^3\text{H}$ and ${}^3\text{He}$, while the calculated amplitude of ${}^6\text{Li}$ is only 35% smaller than the value for ${}^2\text{H}$. Furthermore, the transverse form factors of ${}^6\text{Li}$ are qualitatively similar to those of ${}^2\text{H}$. The numerical result for ${}^6\text{Li}$ can be explained if we consider that the production amplitude for ${}^4\text{He}$ is zero at threshold and ${}^6\text{Li}$ can be approximated as a composite system of ${}^6\text{Li} = {}^4\text{He} + {}^2\text{H}$.

As pointed out before, we have to evaluate the pion production operator in HO basis only once for arbitrary nuclei and then multiply it with the appropriate density matrix for the considered nucleus. If we have the nuclear wave function from the NCSM, we can immediately obtain the pion production amplitude at almost zero additional costs. This is the advantage of this density method compared to the Monte Carlo integration of *Lenkewitz et al.*

So far, we applied the density approach to nuclei with spin $J = 0, 1/2,$ and $1,$ but in principle, our approach is applicable to arbitrary nuclei.

5.5.3 Charged Pion Photoproduction

In this section, we briefly discuss the charged pion photoproduction at threshold. In contrast to the neutral pion production, the so-called Kroll-Ruderman term [121], which contributes at LO to the charged pion production (Sec. 5.2), does not vanish and describes the charged pion production fairly well [123]. This simplifies the LO calculation for charged pions since the computationally exhausting two-nucleon production operator contributes at higher orders.

We can straightforwardly follow the steps in the previous section for neutral pion production. From Eqs. (5.52) and (5.61), we can calculate the transverse form factors for charged pion production by replacing the S -wave amplitudes for neutral pion production off the proton and the neutron with the ones derived for the charged pion production from the Kroll-Ruderman term [123]

$$E_{0+}^{\pi^+n} = \frac{eg_{\pi N}}{4\pi\sqrt{2}m(1+\mu)^{3/2}} = 27.6 \times 10^{-3}/M_{\pi^+} \quad (5.62)$$

$$E_{0+}^{\pi^-p} = -\frac{eg_{\pi N}}{4\pi\sqrt{2}m(1+\mu)^{1/2}} = -31.7 \times 10^{-3}/M_{\pi^+}, \quad (5.63)$$

with $\mu = M_{\pi^+}/m$ and using $g_{\pi N}^2/(4\pi) = 14.28$ for the pion-nucleon coupling constant, $e^2/(4\pi) = 1/137.036$ for the fine-structure constant, $m = 928.27$ MeV and $M_{\pi^+} = 139.57$ MeV. The amplitudes for charged pion production are one order in magnitude larger than the neutral pion production amplitudes and hence, the cross section for charged pion production is also more pronounced. Including chiral corrections to the Kroll-Ruderman theorem up to order $\mathcal{O}(q^3)$ yields only small deviations of the values for the S -wave amplitudes [123]

$$E_{0+}^{\pi^+n} = (28.2 \pm 0.6) \times 10^{-3}/M_{\pi^+} \quad (5.64)$$

$$E_{0+}^{\pi^-p} = (-32.7 \pm 0.6) \times 10^{-3}/M_{\pi^+}, \quad (5.65)$$

since the chiral expansion shows a rapid convergence. The minor mass difference between m_{π^0} and m_{π^\pm} leads to slightly larger photon energies at threshold. However, the main difference in the calculation comes from the fact that the initial and final nucleus differ because of charge conservation, cf. Eq. (5.2). Therefore, we have to consider the transition density matrix from the initial nuclear state Ψ_i to the final nuclear state Ψ'_f

$$\rho_{s,s'}^{(1N,\text{trans})} = \langle \Psi'_f | \hat{a}_{s'}^\dagger \hat{a}_s | \Psi_i \rangle. \quad (5.66)$$

This can complicate the computation, especially if the initial and the final nuclear spin are also different. Moreover, employing the NCSM, we are limited to nuclear reactions between bound states. For the reasons mentioned above, the charged pion photoproduction is not explicitly evaluated in this thesis.

Instead, we will address the two-nucleon contribution to the neutral pion photoproduction in the next section.

5.6 Two-Nucleon Results

In this chapter, we demonstrate the computation of two-nucleon operators employing the density approach. As a first test case, we start with the calculation of the intrinsic kinetic energy. Eventually, we present our results for the 2N pion production amplitude at threshold and compare them with the literature.

At first, we discuss the extension of the single-particle basis to a two-particle basis required for the calculation of two-body operators. The HO and PW two-particle basis are composed from the single-particle basis states and since we are dealing with fermions, they satisfy antisymmetry

$$|s_1 s_2\rangle_a = \frac{|s_1 s_2\rangle - |s_2 s_1\rangle}{\sqrt{2}}. \quad (5.67)$$

Due to the fact that the two-particle basis grows approximately quadratically with the number of single-particle basis states, the calculations in the two-particle sector become computationally exhausting, even for small values of e_{\max} . This is illustrated in Fig. 5.4, where the number of single-particle and two-particle HO basis states are plotted as a function of e_{\max} . Since the computation time scales approximately quadratically with the number of basis states, we expect the calculation for $e_{\max} = 2$ in the 2N sector to take significantly longer than for $e_{\max} = 16$ in the one-nucleon contribution. In this assumption, however, we did not consider that the PW basis also grows quadratically with the number of PW single-particle states. As a consequence, even the calculation of the 2N contribution for $e_{\max} = 2$ is barely feasible on a personal computer.

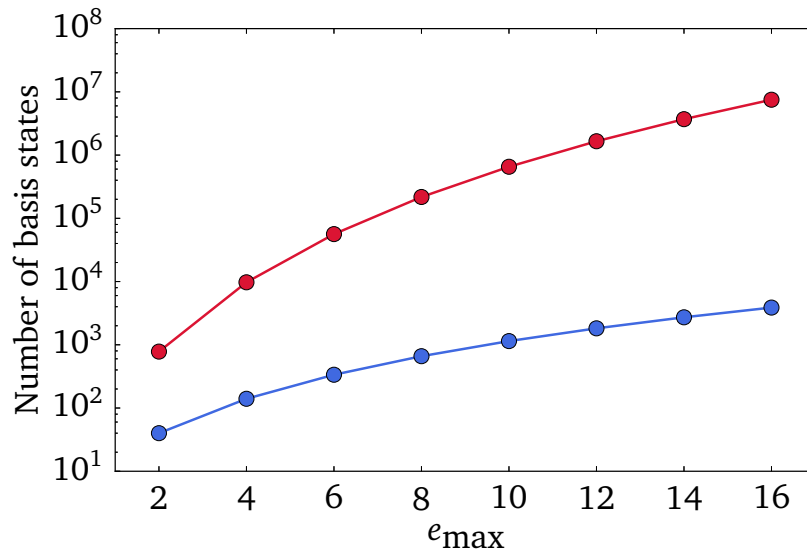


Figure 5.4.: Number of HO basis states as a function of the single-particle energy e_{\max} on a logarithmic scale. The blue colored data points denote the number of single-particle basis states while the red colored data points represent the number of antisymmetrized two-particle states.

5.6.1 Intrinsic Kinetic Energy Benchmark

Similar to the benchmark of the magnetic moments, we apply the intrinsic kinetic energy operator, $\hat{T}_{\text{int}} = \hat{T} - \hat{T}_{\text{CM}}$, as a first cross check in the two-nucleon sector. There are two reasons for this: First, it is already implemented in the (IT)-NCSM code of *Robert Roth's* group and second, \hat{T}_{int} can be straightforwardly calculated in the PW basis

$$\hat{T}_{\text{int}} = \frac{1}{2} \sum_{ij} \frac{2}{A} \frac{\mathbf{P}_{ij,\text{rel}}^2}{2\mu} = \frac{(\mathbf{k}_i - \mathbf{k}_j)^2}{4Am_N} \quad \text{with} \quad \mathbf{P}_{ij,\text{rel}} = \frac{(\mathbf{k}_i - \mathbf{k}_j)}{2}, \quad (5.68)$$

where A denotes the total number of nucleons, $\mathbf{P}_{ij,\text{rel}}$ the relative momentum and $\mu = m_N/2$ the reduced mass between the two nucleons.

The expectation value then reads

$$\begin{aligned} \langle M'_J | \hat{T}_{\text{int}}^{2N} | M_J \rangle_{\Psi} &= \sum_{s_i s_j} \sum_{s'_i s'_j} \sum_{m_{s_1} m_{s_2}} \sum_{m'_{s_1} m'_{s_2}} \int d^3 \mathbf{k}_1 \int d^3 \mathbf{k}_2 \int d^3 \mathbf{k}'_1 \int d^3 \mathbf{k}'_2 \delta^{(3)}(\mathbf{k}_1 - \mathbf{k}'_1) \delta^{(3)}(\mathbf{k}_2 - \mathbf{k}'_2) \times \\ &\quad \mathbf{U}_{s'_i, \mathbf{k}'_1 m'_{s_1}} \mathbf{U}_{s'_j, \mathbf{k}'_2 m'_{s_2}} \mathbf{t}_{\mathbf{k}_1 \mathbf{k}_2, \mathbf{k}'_1 \mathbf{k}'_2}^{(\text{int})} \delta_{m_{s_1}, m'_{s_1}} \delta_{m_{s_2}, m'_{s_2}} \mathbf{U}_{s_i, \mathbf{k}_1 m_{s_1}}^{\dagger} \mathbf{U}_{s_j, \mathbf{k}_2 m_{s_2}}^{\dagger} \rho_{s_i s_j, s'_i s'_j}^{2N} \end{aligned} \quad (5.69)$$

$$= \sum_{s_i s_j} \sum_{s'_i s'_j} \sum_{m_{s_1} m_{s_2}} \sum_{\mathbf{k}_1 \mathbf{k}_2} \Delta_{\mathbf{k}_1}^3 \Delta_{\mathbf{k}_2}^3 \mathbf{U}_{s'_i, \mathbf{k}_1 m_{s_1}} \mathbf{U}_{s'_j, \mathbf{k}_2 m_{s_2}} \mathbf{t}_{\mathbf{k}_1 \mathbf{k}_2, \mathbf{k}_1 \mathbf{k}_2}^{(\text{int})} \mathbf{U}_{s_i, \mathbf{k}_1 m_{s_1}}^{\dagger} \mathbf{U}_{s_j, \mathbf{k}_2 m_{s_2}}^{\dagger} \rho_{s_i s_j, s'_i s'_j}^{2N} \quad (5.70)$$

$$= \text{Tr} \left(\mathbf{U} \mathbf{T}_{\text{int}} \mathbf{U}^{\dagger} \rho_{M_J M'_J}^{2N} \right), \quad (5.71)$$

where $\mathbf{t}_{\mathbf{k}_1 \mathbf{k}_2, \mathbf{k}_1 \mathbf{k}_2}^{(\text{int})}$ represents the two-particle operator for the intrinsic kinetic energy in PW basis, which is given by

$$\mathbf{t}_{\mathbf{k}_1 \mathbf{k}_2, \mathbf{k}_1 \mathbf{k}_2}^{(\text{int})} = \left\langle \mathbf{k}_1 m_{s_1} m_{t_1}, \mathbf{k}_2 m_{s_2} m_{t_2} \left| \frac{(\mathbf{k}_1 - \mathbf{k}_2)^2}{4Am_N} \right| \mathbf{k}_1 m_{s_1} m_{t_1}, \mathbf{k}_2 m_{s_2} m_{t_2} \right\rangle. \quad (5.72)$$

The tensor structure of the expectation value is a scalar so that the extraction of the T_{int} result is straightforward. Since the HO and PW two-particle basis grow approximately quadratically with the number of single-particle states, calculations become computationally exhausting to reach convergence. While reaching convergence is still feasible for the calculation of the two-nucleon $\mathbf{U} \mathbf{U}^{\dagger} = \mathbf{1}$ unitary matrix and for T_{int} employing small e_{max} model spaces, the computation of the two-nucleon pion production amplitude will become a hard nut to crack. This is because of the additional integrals or sums over HO and PW basis states, as we will discuss in the next chapter. For this reason, we calculate the expectation value of T_{int} only for $N_{\text{max}} = 2$ and $\hbar\omega = 20$ MeV for ${}^2\text{H}$, ${}^3\text{H}$, ${}^3\text{He}$ and ${}^6\text{Li}$ and compare it to the NCSM results. The results are shown in Tab. 5.3 and are consistent with the values of the NCSM.

Employing small values of e_{max} not only decreases the HO model space size but also the PW basis required to represent the HO basis in order to satisfy the unitary condition $\mathbf{U} \mathbf{U}^{\dagger} = \mathbf{1}$. In the 2N sector, we

find that a grid length of $k_{\max} = 2.5 \text{ fm}^{-1}$ and a grid spacing of 0.4 fm^{-1} as input for the Gauss-Legendre algorithm lead to reasonable results with a three digits precision for $UU^\dagger = 1$.

Table 5.3.: Numerical results for the intrinsic kinetic energy T_{int} in units of MeV for different nuclei.

nucleus	our result	NCSM
^2H	13.75	13.74
^3H	28.62	28.60
^3He	28.38	28.37
^6Li	86.69	86.66

5.6.2 Two-Nucleon Contribution to the Neutral Pion Photoproduction

After the successful benchmark in the 2N sector for T_{int} , we are now in the position to calculate the relevant two-nucleon diagrams contributing at LO in Fig. 5.2. In Coulomb gauge, all possible contact terms vanish at this order and only the two relevant one-pion-exchange diagrams (a) and (b) in Fig. 5.2 remain at threshold, as discussed in Sec. 5.2. Since the two-nucleon contributions are dominant over the one-nucleon effects for ^2H [113] and ^3H , ^3He [26], these contributions are not negligible and are expected to yield a significant contribution to the pion production amplitude at LO for arbitrary light nuclei.

In principle, the two-body contribution can be evaluated in the same way as in the one-body sector. Following the approach in Ref. [26], the S -wave pion production amplitude can be extracted from the expectation value of the pion production operator in the 2N sector

$$\langle M'_J | \mathcal{M}_{2N}^{\lambda,a} + \mathcal{M}_{2N}^{\lambda,b} | M_J \rangle_\Psi =: 2iE_{0+}^{2N} (\epsilon_T^\lambda \cdot \mathbf{J}) = 2iK_{2N} (F_T^a - F_T^b) (\epsilon_T^\lambda \cdot \mathbf{J}), \quad (5.73)$$

$$\text{with } \mathcal{M}_{2N}^{\lambda,a} + \mathcal{M}_{2N}^{\lambda,b} = \frac{1}{2} \sum_{ij} (\mathcal{M}_{ij}^{\lambda,a} + \mathcal{M}_{ij}^{\lambda,b}). \quad (5.74)$$

The prefactor K_{2N} , which depends on the nuclear mass, reads

$$K_{2N}(m_A) = \frac{m_\pi e g_A m_A}{16\pi(m_A + m_\pi)(2\pi)^3 F_\pi^3}, \quad (5.75)$$

with the axial-vector coupling constant $g_A = 1.26$ and the pion decay constant $F_\pi = 93 \text{ MeV}$. Note that we use the old values for g_A and F_π to be consistent with Refs. [26, 112] and with the evaluation of the single-nucleon multipoles in Eq. (5.46). Moreover, we define the transverse form factors

$$\langle M'_J | \mathcal{M}_{2N}^{\lambda,x} | M_J \rangle_\Psi =: K_{2N} \langle M'_J | \hat{O}_{2N}^{\lambda,x} | M_J \rangle_\Psi = K_{2N} F_T^x (\epsilon_T^\lambda \cdot \mathbf{J}), \quad (5.76)$$

where x is a placeholder for diagram (a) or (b). The expectation value is then given by

$$\begin{aligned} \langle M'_J | \hat{O}_{2N}^{\lambda,x} | M_J \rangle_\Psi &= \sum_{s_i s_j} \sum_{s'_i s'_j} \sum_{m_{s_1} m_{s_2}} \sum_{m'_{s_1} m'_{s_2}} \int d^3 \mathbf{k}_1 \int d^3 \mathbf{k}_2 \int d^3 \mathbf{k}'_1 \int d^3 \mathbf{k}'_2 \delta^{(3)}(\mathbf{k}_1 + \mathbf{k}_2 + \mathbf{k}_\gamma - \mathbf{k}'_1 - \mathbf{k}'_2) \times \\ &\quad \mathbf{U}_{s'_i, \mathbf{k}'_1 m'_{s_1}} \mathbf{U}_{s'_j, \mathbf{k}'_2 m'_{s_2}} \mathbf{o}_{s_1^{\text{PW}} s_2^{\text{PW}}, s_1^{\text{PW}'} s_2^{\text{PW}'}}{}^{\lambda,x} \mathbf{U}_{s_i, \mathbf{k}_1 m_{s_1}}^\dagger \mathbf{U}_{s_j, \mathbf{k}_2 m_{s_2}}^\dagger \boldsymbol{\rho}_{s_i s_j, s'_i s'_j}^{2N} \end{aligned} \quad (5.77)$$

$$\begin{aligned} &= \sum_{s_i s_j} \sum_{s'_i s'_j} \sum_{m_{s_1} m_{s_2}} \sum_{m'_{s_1} m'_{s_2}} \sum_{\mathbf{k}_1 \mathbf{k}_2} \sum_{\mathbf{k}'_1} \Delta_{\mathbf{k}_1}^3 \Delta_{\mathbf{k}_2}^3 \Delta_{\mathbf{k}'_1}^3 \mathbf{U}_{s'_i, \mathbf{k}'_1 m'_{s_1}} \mathbf{U}_{s'_j, (\mathbf{k}_1 + \mathbf{k}_2 + \mathbf{k}_\gamma - \mathbf{k}'_1) m'_{s_2}} \times \\ &\quad \mathbf{o}_{s_1^{\text{PW}} s_2^{\text{PW}}, s_1^{\text{PW}' } s_2^{\text{PW}'}}{}^{\lambda,x} \mathbf{U}_{s_i, \mathbf{k}_1 m_{s_1}}^\dagger \mathbf{U}_{s_j, \mathbf{k}_2 m_{s_2}}^\dagger \boldsymbol{\rho}_{s_i s_j, s'_i s'_j}^{2N} \end{aligned} \quad (5.78)$$

$$= \text{Tr} \left(\mathbf{U} \mathbf{O}_{2N}^{\lambda,i} \mathbf{U}^\dagger \boldsymbol{\rho}_{M_J M'_J}^{2N} \right), \quad (5.79)$$

where $|s_i^{\text{PW}}\rangle = |k_i, m_{s_i}, m_{t_i}\rangle$, \mathbf{k}_γ denotes the photon momentum and $\mathbf{o}^{\lambda,x}$ represents the two-particle operator in PW basis. The two-particle operator reads for diagram (a) [26]

$$\mathbf{o}_{s_1^{\text{PW}} s_2^{\text{PW}}, s_1^{\text{PW}' } s_2^{\text{PW}'}}{}^{\lambda,a} = \left\langle s_1^{\text{PW}' } s_2^{\text{PW}' } \left| \frac{\boldsymbol{\epsilon}_T^\lambda \cdot (\boldsymbol{\sigma}_1 + \boldsymbol{\sigma}_2) (\boldsymbol{\tau}_1 \cdot \boldsymbol{\tau}_2 - \tau_1^z \tau_2^z)}{4q^2} \right| s_1^{\text{PW}} s_2^{\text{PW}} \right\rangle, \quad (5.80)$$

and for diagram (b)

$$\mathbf{o}_{s_1^{\text{PW}} s_2^{\text{PW}}, s_1^{\text{PW}' } s_2^{\text{PW}'}}{}^{\lambda,b} = \left\langle s_1^{\text{PW}' } s_2^{\text{PW}' } \left| \frac{(\boldsymbol{\tau}_1 \cdot \boldsymbol{\tau}_2 - \tau_1^z \tau_2^z) [(\mathbf{q} - \mathbf{k}) \cdot (\boldsymbol{\sigma}_1 + \boldsymbol{\sigma}_2)] [\boldsymbol{\epsilon}_T^\lambda \cdot \mathbf{q}]}{2[(\mathbf{q} - \mathbf{k}_\gamma)^2 + m_{\pi^+}^2] q^2} \right| s_1^{\text{PW}} s_2^{\text{PW}} \right\rangle, \quad (5.81)$$

where $\mathbf{q} = (\mathbf{k}_1 - \mathbf{k}_2 - \mathbf{k}'_1 + \mathbf{k}'_2 + \mathbf{k}_\gamma)/2$ denotes the momentum of the exchanged pion, which simplifies to

$$\mathbf{q} = \mathbf{k}_1 - \mathbf{k}'_1 + \mathbf{k}_\gamma = \mathbf{k}'_2 - \mathbf{k}_2, \quad (5.82)$$

after applying the momentum conservation via the delta function in Eq. (5.77).

As previously discussed for the 1N pion production in Sec. 5.5.2, the two-nucleon result also has to be divided by a factor of

$$\langle \Psi_f^{\text{CM}} | \hat{O}_{2N}^\lambda | \Psi_i^{\text{CM}} \rangle = \exp\left(-\frac{1}{4} B^2 k_\gamma^2\right), \quad (5.83)$$

due to the recoil effect that leads to a shift in the CM momentum. Here, $B = \sqrt{\hbar/(Am_N \omega)}$ denotes the HO length of the nucleus.

Compared to the one-nucleon contribution, the computation in the 2N sector is computationally very exhausting. There are two reasons for this: First, the two-particle HO and PW model space dimensions grow approximately quadratically with respect to the single-particle basis, which leads in each case to

twice as many sums as in the one-nucleon contribution. Second, the delta function eliminates only the sum over the outgoing PW basis \mathbf{k}'_2 while the additional sum over \mathbf{k}'_1 remains. These difficulties can be tackled head-on. The code is easy to parallelize and the matrix calculation of $\mathbf{U}\mathbf{O}_{2N}^{\lambda,x}\mathbf{U}^\dagger$ can be conveniently split into smaller matrix blocks. This enables large scale calculations on clusters that shifts the feasibility to larger model spaces.

Another complication is induced by the denominator in Eqs. (5.80), (5.81) since the integral for the form factors contains an integrable singularity for $\mathbf{q} \rightarrow \mathbf{0}$. There are several possibilities to deal with this. As one possibility, we can remove the singularity by an appropriate variable transformation

$$\int d^3\mathbf{k}_1 \int d^3\mathbf{k}'_1 \frac{1}{\mathbf{q}^2} = - \int d^3\mathbf{k}_1 \int d^3\mathbf{q} \frac{1}{\mathbf{q}^2}, \quad (5.84)$$

where we exploited that $\mathbf{q} = \mathbf{k}_1 - \mathbf{k}'_1 + \mathbf{k}_\gamma$. Then we can cancel the denominator and obtain

$$- \int d^3\mathbf{k}_1 \int d^3\mathbf{q} \frac{1}{\mathbf{q}^2} = - \int d^3\mathbf{k}_1 \int d\Omega_{\mathbf{q}} d\mathbf{q} \frac{\mathbf{q}^2}{\mathbf{q}^2}. \quad (5.85)$$

This has the downside that it is not straightforwardly compatible with our numerical approach of summing over the PW basis in Cartesian representation. First, this would require another variable transformation from Cartesian to spherical PW representation and second, the new integral boundaries would become more complex.

Therefore, we follow the idea of *Lenkewitz* [112] and introduce an additional mass scale Λ in the denominator to avoid division-by-zero terms

$$\frac{1}{\mathbf{q}^2} \rightarrow \frac{1}{\mathbf{q}^2 + \Lambda^2}. \quad (5.86)$$

To extract the result that is independent of Λ , we have to extrapolate $\Lambda \rightarrow 0$. Hence, we evaluate the form factors for different values of Λ and extrapolate exponentially to zero. In the following, we briefly motivate this exponential ansatz.

We start with the integral for the form factor in momentum space

$$\mathcal{M}_{\lambda,a}^\Lambda(\boldsymbol{\epsilon}_T^\lambda, \mathbf{k}_\gamma) = \int d^3\mathbf{k} \int d^3\mathbf{k}' \Psi^\dagger(\mathbf{k}') \frac{\boldsymbol{\epsilon}_T^\lambda \cdot \mathbf{S}}{\left(\mathbf{k} - \mathbf{k}' + \frac{\mathbf{k}_\gamma}{2}\right)^2 + \Lambda^2} \Psi(\mathbf{k}), \quad (5.87)$$

with $\mathbf{S} = \boldsymbol{\sigma}_1 + \boldsymbol{\sigma}_2$. This expression can be Fourier transformed into

$$\mathcal{M}_{\lambda,a}^\Lambda(\boldsymbol{\epsilon}_T^\lambda, \mathbf{k}_\gamma) = 2\pi^2 \int d^3\mathbf{r} \Psi^\dagger(\mathbf{r}) \frac{\boldsymbol{\epsilon}_T^\lambda \cdot \mathbf{S}}{|\mathbf{r}|} \Psi(\mathbf{r}) \exp\left(i\frac{\mathbf{k}_\gamma}{2} \cdot \mathbf{r}\right) \exp(-|\Lambda||\mathbf{r}|) \quad (5.88)$$

$$= 2\pi^2 \int d^3\mathbf{r} f(\mathbf{r}) \exp(-|\Lambda||\mathbf{r}|), \quad (5.89)$$

with

$$f(\mathbf{r}) = \Psi^\dagger(\mathbf{r}) \frac{\boldsymbol{\epsilon}_T^\lambda \cdot \mathbf{S}}{|\mathbf{r}|} \Psi(\mathbf{r}) \exp\left(i \frac{\mathbf{k}_\gamma}{2} \cdot \mathbf{r}\right), \quad (5.90)$$

and we employed the following identities

$$\Psi(\mathbf{k}) = \frac{1}{(2\pi)^{3/2}} \int d^3\mathbf{r} \exp(-i\mathbf{k} \cdot \mathbf{r}) \Psi(\mathbf{r}), \quad (5.91)$$

$$\frac{1}{\left(\mathbf{k} - \mathbf{k}' + \frac{\mathbf{k}_\gamma}{2}\right)^2 + \Lambda^2} = \frac{1}{4\pi} \int d^3\mathbf{r} \frac{\exp\left(i\left(\mathbf{k} - \mathbf{k}' + \frac{\mathbf{k}_\gamma}{2}\right) \cdot \mathbf{r}\right)}{|\mathbf{r}|} \exp(-|\Lambda||\mathbf{r}|), \quad (5.92)$$

$$\int d^3\mathbf{k} \exp(i(\mathbf{r} - \mathbf{r}') \cdot \mathbf{k}) = (2\pi)^3 \delta^{(3)}(\mathbf{r} - \mathbf{r}'). \quad (5.93)$$

Under the assumption that $f(\mathbf{r})$ denotes a function with a distinctive peak at the typical nuclear length scale $\mathbf{r} = \mathbf{r}_0$, we can replace \mathbf{r} with \mathbf{r}_0 in Eq. (5.89) and write

$$\mathcal{M}_{\lambda,a}^\Lambda(\boldsymbol{\epsilon}_T^\lambda, \mathbf{k}_\gamma) = 2\pi^2 f(\mathbf{r}_0) \exp(-|\Lambda||\mathbf{r}_0|) \int d^3\mathbf{r} \quad (5.94)$$

$$= 2\pi^2 f(\mathbf{r}_0) \exp(-|\Lambda||\mathbf{r}_0|) V, \quad (5.95)$$

with $V = \int d^3\mathbf{r}$. When we explicitly discuss our numerical results, we will see that r_0 is indeed in the typical nuclear length scale.

The exponential ansatz is also confirmed by comparing with our numerical results for different values of Λ in the range of $0.5 - 1.0 \text{ fm}^{-1}$, as illustrated in Figs. 5.5 and 5.6. The reasoning behind the choice of the upper and lower limit for Λ is as follows: For large values of Λ , the integral converges to zero, while for small values of Λ , the integral diverges and the distinctive peak of $f(\mathbf{r})$ at r_0 becomes negligible compared to the Λ contribution. We apply a logarithmic scale and obtain from Eq. (5.95)

$$\ln\left(\mathcal{M}_{\lambda,a}^\Lambda(\boldsymbol{\epsilon}_T^\lambda, \mathbf{k}_\gamma)\right) = \ln(2\pi^2 f(\mathbf{r}_0) V) - |\Lambda||\mathbf{r}_0| \quad (5.96)$$

$$= \ln(\mathcal{M}_a(\boldsymbol{\epsilon}_T, \mathbf{k}_\gamma)) - |\Lambda||\mathbf{r}_0|. \quad (5.97)$$

Then we extrapolate exponentially Λ to zero. This is shown in Fig. 5.5 and 5.6, where all data points for $1.0 \text{ fm}^{-1} \geq \Lambda \geq 0.5 \text{ fm}^{-1}$ lie approximately on a linear curve. Here, the slope of the linear curve is given by r_0 and the result for $\Lambda \rightarrow 0$ is denoted by $\mathcal{M}_a(\boldsymbol{\epsilon}_T, \mathbf{k}_\gamma)$. In Fig. 5.5, the data points are not fully converged with respect to the PW model space since we intentionally decreased the number of grid points to reduce the computation time. Therefore, the corresponding result for $(F_T^a - F_T^b)$ is about 20% smaller than for the converged data set in Fig. 5.6. As explained above, for small values of Λ the singularity destroys the linear behavior and the outcome is very sensitive to small changes in our momentum grid.

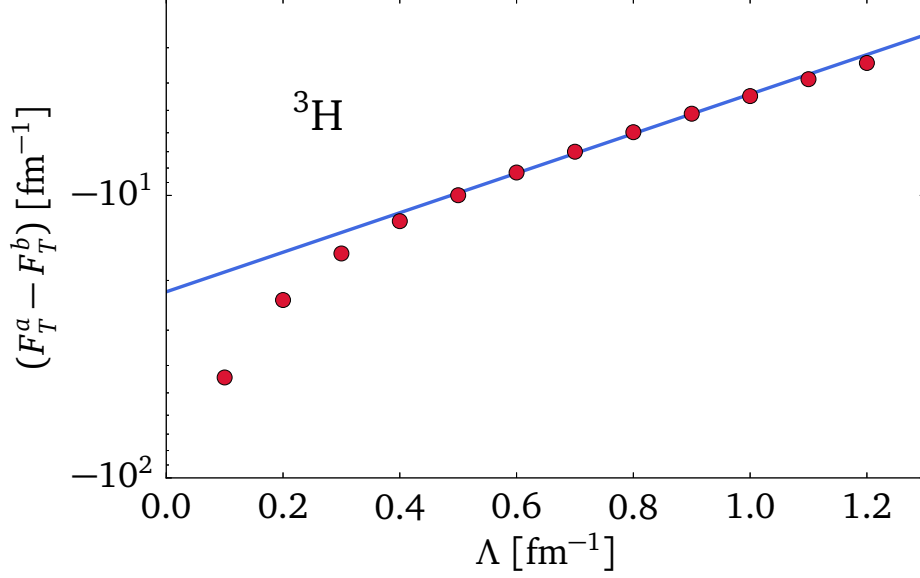


Figure 5.5.: The numerical result of $(F_T^a - F_T^b)$ is plotted for different values of Λ (red data points) on a logarithmic scale for ${}^3\text{H}$. The blue curve is the exponential fit (in the data range of $\Lambda = 0.5 - 1.0 \text{ fm}^{-1}$) to vanishing Λ for extracting the result of the form factor. The data points are not fully converged with respect to the PW model space. The NCSM wave function is calculated for an $N_{\text{max}} = 2$ model space and accordingly, the applied HO single-particle energy is $e_{\text{max}} = 2$.

For large values of Λ the linear behavior is more robust, but the expectation value eventually goes to zero because the Λ term dominates.

The converged results are illustrated in Fig. 5.6. In contrast to the one-nucleon contribution, the NCSM calculation is performed in an $N_{\text{max}} = 2$ model space for all nuclei since, at the moment, we are computationally limited to single-particle model spaces with $e_{\text{max}} = 3$ in the two-nucleon sector. As a consequence, our results are not fully converged with respect to e_{max} (N_{max}). Due to our findings for the one-nucleon contribution, we do not expect our results to be strongly sensitive to e_{max} . Compared to the converged result for $e_{\text{max}} = 10$, the deviation for $e_{\text{max}} = 2$ is about 5% in the case of ${}^3\text{H}$ and ${}^3\text{He}$ and about 7% for ${}^2\text{H}$. The largest uncertainty stems from the $\Lambda \rightarrow 0$ extrapolation. By varying the fitting range of Λ in both directions we estimate the uncertainty to be in order of 10%. Because of the logarithmic scale, even small changes in the slope of the linear curve lead to significant deviations of the extrapolated result. The other uncertainties discussed for the 1N contribution, e.g, the change in the photon momentum for different nuclei due to the recoil term, are negligible in the two-nucleon sector. Employing the formula for the Gaussian propagation of uncertainty, we expect the total error for all nuclei to be in the range of 12% since the 2N contribution is not as sensitive to the varying number of neutrons and protons inside the nucleus as the 1N effect before.

The numerical results for the two-nucleon contribution are shown in Tab. 5.4. Comparing our values with the results of *Lenkewitz et al.* and *Beane et al.*, we find that our numerical results are around 10% smaller in magnitude for all nuclei compared to the ones in the papers, i.e. ${}^2\text{H}$, ${}^3\text{H}$ and ${}^3\text{He}$. However, including the uncertainties, our values are consistent with the literature.

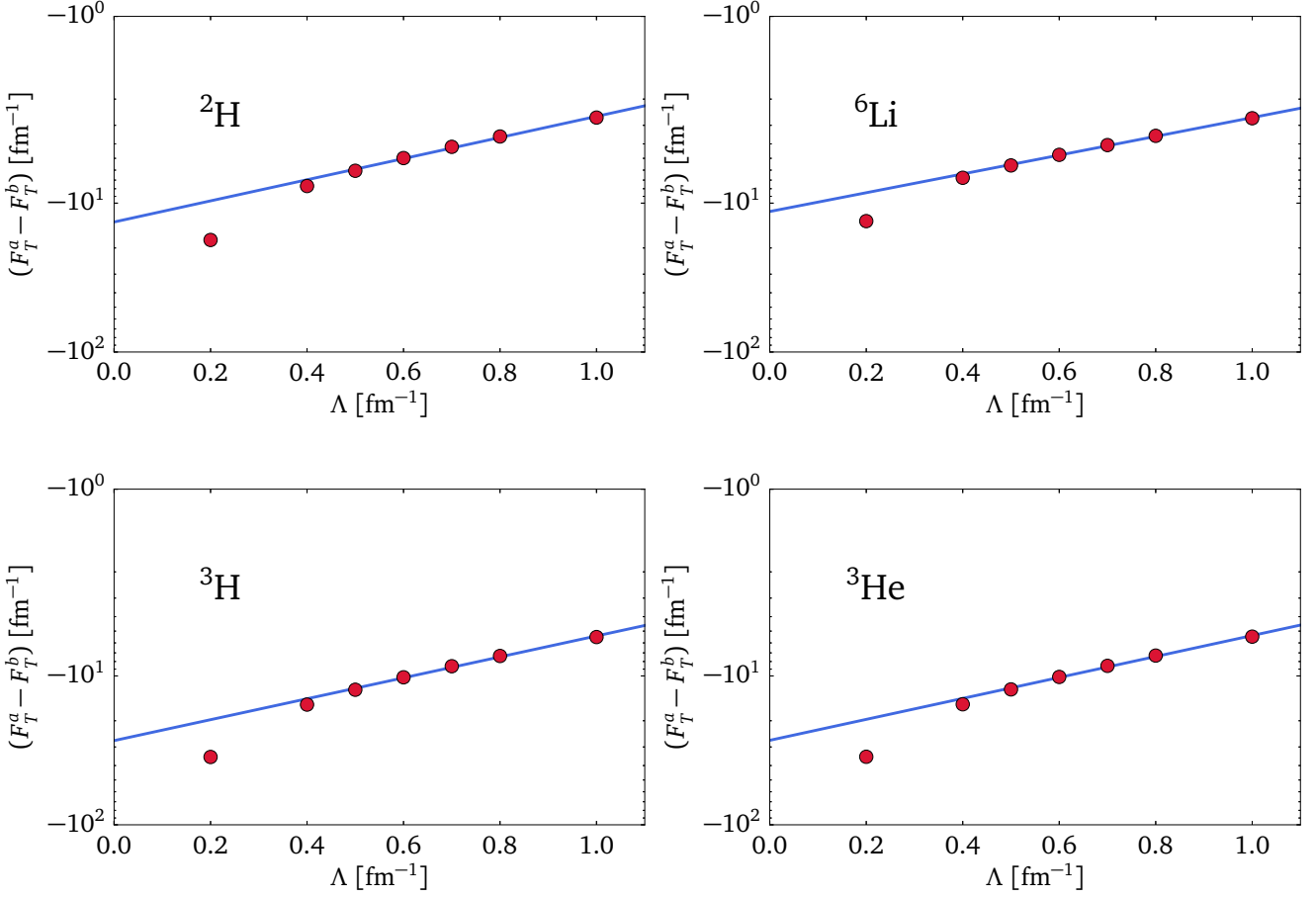


Figure 5.6.: The numerical result of $(F_T^a - F_T^b)$ is plotted for different values of Λ (red data points) on a logarithmic scale. The blue curve is the exponential fit (in the data range of $\Lambda = 0.5 - 1.0 \text{ fm}^{-1}$) to vanishing Λ for extracting the result of the form factor. The respective NCSM wave functions are calculated for an $N_{\text{max}} = 2$ model space and e_{max} is chosen accordingly. In the top panel, the extrapolation for the two $J^P = 1^+$ nuclei ${}^2\text{H}$ and ${}^6\text{Li}$ is shown while in the bottom panel ${}^3\text{H}$ and ${}^3\text{He}$ with $J^P = 1/2^+$ are illustrated.

Table 5.4.: Numerical results of the two-nucleon contribution to the pion production amplitude at threshold for different nuclei. The numbers in parenthesis denote the errors. The NCSM calculations are performed for $N_{\text{max}} = 2$. The literature results are taken from Refs. [26, 113].

nucleus	our result		literature	
	$F_T^a - F_T^b [\text{fm}^{-1}]$	$E_{0+}^{2N} [10^{-3}/M_{\pi^+}]$	$F_T^a - F_T^b [\text{fm}^{-1}]$	$E_{0+}^{2N} [10^{-3}/M_{\pi^+}]$
${}^2\text{H}$	-13.4(16)	-1.71(20)		-1.90 [113]
${}^3\text{H}$	-27.2(33)	-3.55(43)	-29.7(3)	-4.01(3) [26]
${}^3\text{He}$	-27.1(33)	-3.53(42)	-29.3(3)	-3.95(3) [26]
${}^6\text{Li}$	-11.4(14)	-1.52(18)		

As mentioned before, we employ different nuclear wave functions than *Lenkewitz* and *Beane*, which can lead to small deviations. Furthermore, our amplitudes are not expected to be converged with respect to e_{\max} . This is one possible explanation for the fact that our amplitudes are systematically smaller in magnitude than the literature results. Moreover, the numerical uncertainties for the 2N contribution of *Lenkewitz et al.* appear to be an overoptimistic estimation. They apply a similar approach for the extrapolation to vanishing Λ and assume that their error is one order in magnitude smaller than our estimation. As a further validation of our extrapolation procedure, we extract r_0 from the slope of our linear fit. We find for all nuclei considered in Fig. 5.6 that $r_0 \approx 1.6$ fm, which is consistent with the typical nuclear length scale.

5.7 Results of the Neutral Pion Photoproduction at Threshold

The total S -wave amplitudes derived from the 1N and 2N contributions for threshold neutral pion photoproduction at LO for ${}^2\text{H}$, ${}^3\text{H}$, ${}^3\text{He}$, and ${}^6\text{Li}$ are shown in Tab. 5.5.

Table 5.5.: Numerical results of the total S -wave neutral pion production amplitude at threshold E_{0+} for different nuclei. The numbers in parenthesis denote the errors. The literature results are taken from Refs. [26, 113].

nucleus	$E_{0+} [10^{-3}/M_{\pi^+}]$	
	our result	literature
${}^2\text{H}$	-1.31(22)	-1.53(5) [113]
${}^3\text{H}$	-4.48(43)	-4.94(5) [26]
${}^3\text{He}$	-1.77(44)	-2.25(4) [26]
${}^6\text{Li}$	-1.26(19)	

The calculated 2N contributions are smaller in magnitude than in the literature and dominate over the 1N effects. Thus, the deduced total amplitudes are also smaller in magnitude than the literature results. Including the uncertainties, they are consistent with Refs. [26, 113].

Furthermore, we can compare our results with experimental data from the Saskatchewan Accelerator Laboratory (SAL) for the neutral pion photoproduction off ${}^2\text{H}$ in the threshold region [19]. They extrapolated their data to threshold and concluded for the threshold pion photoproduction amplitude of ${}^2\text{H}$

$$E_{0+} = (-1.45 \pm 0.09) \times 10^{-3}/M_{\pi^+}, \quad (5.98)$$

which is about 11% larger than our prediction and about 5% lower than the prediction by *Beane* [113].

Finally, we briefly discuss the NLO effects. The relevant contributions at order $\mathcal{O}(q^4)$ are outlined in the last paragraph of Sec. 5.2. *Beane* and *Lenkewitz* calculated the neutral pion photoproduction amplitudes at threshold up to NLO. By comparing their LO predictions with their results at NLO, we can estimate the NLO contribution to our computed values. We observe an increase in magnitude of

the pion production amplitude from LO to NLO for all considered nuclei, i.e. ${}^2\text{H}$, ${}^3\text{H}$ and ${}^3\text{He}$. The pion production amplitude up to NLO of ${}^2\text{H}$ is 17% larger in magnitude than the result at LO [113] while the NLO amplitudes of ${}^3\text{H}$ and ${}^3\text{He}$ are 7% and 10% larger in magnitude, respectively, than the LO values [26]. Consequently, we assume that the NLO contribution to our results is of the same size. In the case of ${}^6\text{Li}$, a similar effect as for ${}^2\text{H}$ is expected.

5.8 Conclusion

We combined the threshold neutral pion photoproduction operators from ChPT at LO with nuclear wave functions from the NCSM in a density matrix approach. Thus, we extended the calculation of S -wave pion production amplitudes to a broad range of light nuclei. In particular, we calculated the threshold neutral pion photoproduction amplitude at LO for ${}^2\text{H}$, ${}^3\text{H}$, and ${}^3\text{He}$ to compare it with the literature [26, 113] and we further extended the calculation to ${}^6\text{Li}$. The advantage of this density approach is that the pion production operator has to be evaluated only once for arbitrary nuclei. The pion production amplitude can then be directly derived by tracing the resulting matrix with the appropriate density matrix for the considered nucleus. This approach works smoothly in the one-nucleon sector, where the computation time is negligible and the results for the neutral pion photoproduction amplitude at threshold $E_{0+}^{1N} = [0.40(5), -0.94(5), 1.77(9)] \times 10^{-3}/M_{\pi^+}$ for ${}^2\text{H}$, ${}^3\text{H}$, and ${}^3\text{He}$, respectively, agree with the literature. We further predicted the neutral pion photoproduction amplitude at threshold $E_{0+}^{1N} = 0.26(3) \times 10^{-3}/M_{\pi^+}$ for ${}^6\text{Li}$. This value can be explained by considering ${}^6\text{Li}$ as a composite system of ${}^4\text{He} + {}^2\text{H}$. At threshold, all amplitudes for nuclei with $J = 0$ such as ${}^4\text{He}$ vanish. Thus, we expect the amplitude of ${}^6\text{Li}$ to yield a similar result as for ${}^2\text{H}$.

The calculation in the two-nucleon sector was more challenging. On the one hand, the matrix dimensions become very large so that the calculation of the pion production operator is computationally exhausting even on large clusters. On the other hand, the integral contains an integrable singularity. To avoid division-by-zero terms, we included an additional mass scale in the denominator that has to be extrapolated to zero. This induces extrapolation errors and requires multiple calculations with different values for the mass scale. Nevertheless, we were able to calculate the two-body contribution to the neutral pion photoproduction amplitude at threshold $E_{0+}^{2N} = [-1.71(20), -3.55(43), -3.53(42)] \times 10^{-3}/M_{\pi^+}$ for ${}^2\text{H}$, ${}^3\text{H}$, and ${}^3\text{He}$, respectively. Taking the uncertainties into account, our values are consistent with the literature. Furthermore, we predicted the two-nucleon amplitude $E_{0+}^{2N} = -1.52(18) \times 10^{-3}/M_{\pi^+}$ for ${}^6\text{Li}$. This result can be explained as before by considering the approximation ${}^6\text{Li} = {}^4\text{He} + {}^2\text{H}$ and comparing it with the value of ${}^2\text{H}$.

At LO in ChPT, one-nucleon and two-nucleon effects contribute to the S -wave neutral pion production amplitude. Our results confirm that the two-nucleon contribution is dominant over the one-nucleon effect, as suggested by the literature. Incorporating the uncertainties, we are consistent with the total amplitudes in the literature for ${}^2\text{H}$, ${}^3\text{H}$, and ${}^3\text{He}$ and with the experimental data for ${}^2\text{H}$ [19]. The experimental result for the threshold pion production amplitude is about 11% larger than our prediction, while it is about 5% lower than the prediction of Ref. [113]. Our calculated amplitudes are systematically smaller in magnitude than the theoretical and experimental reference values. One explanation for this could be that our results of the dominant two-nucleon contribution are not fully converged with respect to e_{max} . For ${}^6\text{Li}$, we predicted the threshold pion photoproduction amplitude $E_{0+} = -1.26(26) 10^{-3}/M_{\pi^+}$

at LO in ChPT for the first time. By comparing the pion photoproduction amplitudes from the literature at LO with the appropriate NLO results, we estimate the NLO effects to be about 10%, depending on the considered nucleus.

In principle, this density approach can be applied to any light nucleus for which the (IT)-NCSM is capable of calculating the nuclear wave function to immediately predict the threshold neutral pion photoproduction amplitude at LO. However, there is still an unresolved issue related to the computation time of the pion production operator in the two-nucleon sector. For harmonic-oscillator single-particle model spaces with $e_{\max} > 4$, our density approach in its current version reaches its computational limit even on large clusters. However, especially for nuclei beyond ${}^6\text{Li}$, neither the energy of the nuclear wave function nor the corresponding pion production amplitude are fully converged in these small e_{\max} model spaces.



6 Conclusion and Outlook

In this work, we employed two different effective field theories for the description of electromagnetic properties and reactions in light nuclei depending on the effective degrees of freedom in the considered system. We applied the pionless Halo EFT to calculate electromagnetic form factors, electromagnetic transitions as well as the neutron capture cross section for the two carbon isotopes ^{15}C and ^{17}C . Both carbon isotopes can be assumed to be one-neutron halo nuclei, where the effective degrees of freedom are the halo neutron and a tightly bound carbon core. Furthermore, they both have shallow D -wave bound states. We extended the Halo EFT approach to higher partial wave bound states and to D -wave states in particular. Moreover, we predicted several electromagnetic observables such as the quadrupole moment exploiting the universal correlation between the quadrupole moment and the $B(E2)$ transition. In this sense, Halo EFT can be regarded as a complementary approach to *ab initio* methods, where these correlations are not obvious since the separation of scales is not explicit in the parameters of the theory. We generally find that counterterms become more dominant for higher partial waves, which complicates numerical predictions. In the magnetic sector, in particular, unknown counterterms that have to be matched to theoretical or experimental data enter already at LO. We also outlined the extension of the Halo EFT approach to partial waves beyond the D -wave. However, we propose the application of the spherical representation throughout the calculation of electromagnetic observables beyond the P -wave instead of employing Cartesian coordinates as in this work. Especially in the magnetic sector, where observables are more sensitive to the spin of the neutron, we expect a significant simplification in the evaluation of observables from the spherical representation. Moreover, we could extend our considerations to systems with two halo neutrons. In such three-body systems, new universal few-body correlations, such as the Efimov effect [60], emerge. Another field of study are one-proton halo nuclei. Because of the Coulomb interaction between the charged core and halo proton, the long-range Coulomb photon exchange has to be explicitly included in the effective Lagrangian in addition to the short-range strong interaction. Some of these extensions are already being considered by our group.

Through the inclusion of pions in addition to nucleons as effective degrees of freedom in our theory, we employed ChPT and a density matrix approach to evaluate the threshold neutral pion photoproduction amplitudes at LO for several light nuclei. The density approach enables us to immediately predict the pion production amplitude for a broad range of nuclei with the appropriate density matrix since the evaluation of the pion production operator is required only once. This is the advantage of our density approach compared to the Monte Carlo integration of *Lenkewitz et al.* So far, we applied the density method to nuclei with spin $J = 0, 1/2, \text{ and } 1$, but in principle, our approach is applicable to arbitrary nuclei. The S -wave amplitudes for ^2H , ^3H , and ^3He were already predicted in the literature [26, 113]. We compared our results with the predictions in the literature and found that we are in agreement about the one- and two-nucleon contribution to the S -wave amplitudes. The experimental result for the pion photoproduction off ^2H [19] is about 11% larger than our prediction. This deviation can be explained by considering that the dominant two-nucleon results are not fully converged with respect to e_{max} .

Therefore, we have to reconsider our numerical approach in the two-body sector. Currently, we are limited to $e_{\max} \leq 4$ model spaces so that we cannot reach full convergence in our pion production amplitude, especially for nuclei beyond the s-shell. In addition, there are several natural extensions to this work such as the investigation of higher order contributions to the threshold neutral pion photoproduction and the calculation of pion production amplitudes above threshold. Since experimental setups generally measure the pion production above threshold, the extension to this energy regime would simplify the comparison with experimental data. Furthermore, this would enable us to describe even more nuclei since the pion production amplitude above threshold yields non-vanishing results even for spin zero nuclei, such as ${}^4\text{He}$. Further work in this direction is in progress.

A more detailed conclusion on the Halo EFT and the pion production results can be found separately at the end of each chapter, i.e. in Sec. 4.11 and 5.8, respectively.

A Halo EFT Calculations

A.1 Self Energy of the D -Wave Propagator

We calculate the one-loop self energy of the D -wave propagator, depicted in the top panel of Fig. 4.2, in Cartesian representation, cf. Sec. 4.3.2. The incoming and outgoing relative momentum indices for the D -wave polarization are denoted by i, j and o, p , respectively. Eventually, we couple the neutron spin with the relative momentum and project out the appropriate total angular momentum J . The self energy reads

$$\begin{aligned}
 -i\Sigma_{ij,op}^d(p) = & (-ig_2)^2 \int \frac{d^4l}{(2\pi)^4} \frac{i}{\frac{M}{M_{nc}}E + l_0 - \frac{\left(\frac{M}{M_{nc}}\mathbf{p}+1\right)^2}{2M} + i\epsilon} \frac{i}{\frac{m}{M_{nc}}E - l_0 - \frac{\left(\frac{m}{M_{nc}}\mathbf{p}-1\right)^2}{2m} + i\epsilon} \times \\
 & \frac{1}{M_{nc}^2} \left(\frac{1}{2} \left[M i \left(\frac{m}{M_{nc}}\mathbf{p}-1 \right) - m i \left(\frac{M}{M_{nc}}\mathbf{p}+1 \right) \right]_j \left[\cdots \right]_i + \frac{1}{2} \left[\cdots \right]_i \left[\cdots \right]_j - \frac{1}{d} \left[\cdots \right]^2 \delta_{ij} \right) \times \\
 & - \frac{1}{M_{nc}^2} \left(\frac{1}{2} \left[M i \left(\frac{m}{M_{nc}}\mathbf{p}-1 \right) - m i \left(\frac{M}{M_{nc}}\mathbf{p}+1 \right) \right]_o \left[\cdots \right]_p + \frac{1}{2} \left[\cdots \right]_p \left[\cdots \right]_o - \frac{1}{d} \left[\cdots \right]^2 \delta_{po} \right), \tag{A.1}
 \end{aligned}$$

where the ellipses stand for the same momentum terms as in the first bracket inside the corresponding parenthesis and d denotes the space dimension. We divide the calculation into the evaluation of the numerator and the integration over l_0 .

For the numerator in the equation above, i.e. the last two lines only, we derive

$$N = (-i)^2 \left(l_i l_j - \frac{1}{d} l^2 \delta_{ij} \right) (-i)^2 \left(l_o l_p - \frac{1}{d} l^2 \delta_{op} \right) \tag{A.2}$$

$$= l_i l_j l_o l_p - \frac{l_i l_j}{d} l^2 \delta_{op} - \frac{l_o l_p}{d} l^2 \delta_{ij} + \frac{1}{d^2} l^4 \delta_{ij} \delta_{op} \tag{A.3}$$

$$= \frac{l^4}{d(d+2)} \left(\delta_{io} \delta_{jp} + \delta_{ip} \delta_{jo} - \frac{2}{d} \delta_{ij} \delta_{op} \right), \tag{A.4}$$

where we used the following identities

$$l_i l_j = l^2 \frac{\delta_{ij}}{d} \tag{A.5}$$

$$l_i l_j l_o l_p = l^4 \frac{\delta_{ij} \delta_{op} + \delta_{io} \delta_{jp} + \delta_{ip} \delta_{jo}}{d(d+2)}. \tag{A.6}$$

The integration over l_0 yields

$$I = \int \frac{d^4 l}{(2\pi)^4} \frac{i}{\frac{M}{M_{nc}} E + l_0 - \frac{\left(\frac{M}{M_{nc}} \mathbf{p} + 1\right)^2}{2M} + i\epsilon} \frac{i}{\frac{m}{M_{nc}} E - l_0 - \frac{\left(\frac{m}{M_{nc}} \mathbf{p} - 1\right)^2}{2m} + i\epsilon} \quad (\text{A.7})$$

$$= i^2 (-2\pi i) \int \frac{d^3 l}{(2\pi)^4} \frac{1}{E - \frac{p^2}{2M_{nc}} - \frac{l^2}{2m_R} + i\epsilon}. \quad (\text{A.8})$$

After defining

$$\Sigma_{ij,op}^d(p) = \Sigma^d(p) \frac{(\delta_{io} \delta_{jp} + \delta_{ip} \delta_{jo} - \frac{2}{d} \delta_{ij} \delta_{op})}{2}, \quad (\text{A.9})$$

we obtain for the self energy

$$-i\Sigma^d(p) = -ig_2^2 \frac{2}{d(d+2)} (-2m_R) \int \frac{d^3 l}{(2\pi)^3} \frac{l^4}{l^2 - 2m_R \left(E - \frac{p^2}{2M_{nc}}\right) + i\epsilon} \quad (\text{A.10})$$

$$= -ig_2^2 \frac{2}{15} \frac{2m_R}{4\pi} \left[2m_R \left(E - \frac{p^2}{2M_{nc}}\right)\right]^2 \left(\sqrt{-2m_R \left(E - \frac{p^2}{2M_{nc}}\right)} - \frac{15}{8} \mu\right), \quad (\text{A.11})$$

where we employed PDS as regularization scheme. In PDS, also the poles in $d = 2$, which correspond to power law divergences at $d = 3$, are subtracted

$$I = \left(\frac{\mu}{2}\right)^{3-d} \frac{2}{d(d+2)} \int \frac{d^d l}{(2\pi)^d} \frac{l^4}{l^2 - a} \quad (\text{A.12})$$

$$= (4\pi)^{-d/2} \Gamma(1 - d/2 - 2) \frac{\Gamma(d/2 + 2)}{\Gamma(d/2)} (-a)^{2+d/2-1} \left(\frac{\mu}{2}\right)^{3-d} \frac{2}{d(d+2)}, \quad (\text{A.13})$$

with $a = 2m_R \left(E - p^2/(2M_{nc})\right)$. Thus, we deduce for $d = 3$ under consideration of the pole in $d = 2$

$$I = -\frac{1}{4\pi} \frac{2}{15} a^2 \left[(-a)^{1/2} - \frac{15}{8} \mu\right]. \quad (\text{A.14})$$

A.2 Minimal Substitution in the D -Wave Interaction

Photons are included via minimal substitution in the effective Lagrangian (4.4) in our theory. The D -wave Galilean invariant interaction in Cartesian representation is given by

$$-g_2 \left[d_{s,ij}^\dagger n_s \left(\frac{1}{2} \left[\overleftrightarrow{\nabla}_j \overleftrightarrow{\nabla}_j + \overleftrightarrow{\nabla}_j \overleftrightarrow{\nabla}_i \right] - \frac{1}{d} \overleftrightarrow{\nabla}^2 \delta_{ij} \right) c + h.c. \right], \quad (\text{A.15})$$

where we ensure Galilean invariance with the adoption

$$n \overleftrightarrow{\nabla} c = n \frac{\left(M \overleftarrow{\nabla} - m \overrightarrow{\nabla} \right)}{M_{nc}} c. \quad (\text{A.16})$$

The left and right arrows indicate operators acting on the neutron and core fields, respectively. For the inclusion of photons we replace $\partial_\mu \rightarrow D_\mu = \partial_\mu + ie\hat{Q}A_\mu$, which leads to

$$n \left[M \overleftarrow{\nabla} - m \overrightarrow{\nabla} \right] c \rightarrow n \left[M \overleftarrow{D} - m \overrightarrow{D} \right] c = n \left[M \overleftarrow{\nabla} - m \overrightarrow{\nabla} + imeQ_c \mathbf{A} \right] c, \quad (\text{A.17})$$

where we used that the charge operator acting on the neutron field yields zero and on the core $\hat{Q}c = Q_c c$. Thus, for the term in Eq. (A.15) it follows

$$\begin{aligned} n \left[M \overleftarrow{D} - m \overrightarrow{D} \right]_i \left[M \overleftarrow{D} - m \overrightarrow{D} \right]_j c &= n \left(M^2 \overleftarrow{D}_i \overleftarrow{D}_j - M m \overleftarrow{D}_i \overrightarrow{D}_j - M m \overrightarrow{D}_i \overleftarrow{D}_j + m^2 \overrightarrow{D}_i \overrightarrow{D}_j \right) c \\ &= n \left[M^2 \overleftarrow{\nabla}_i \overleftarrow{\nabla}_j - M m \overleftarrow{\nabla}_i \overrightarrow{\nabla}_j - M m \overrightarrow{\nabla}_i \overleftarrow{\nabla}_j + m^2 \overrightarrow{\nabla}_i \overrightarrow{\nabla}_j + M m ieQ_c \overleftarrow{\nabla}_i \mathbf{A}_j \right. \\ &\quad \left. + M m ieQ_c \mathbf{A}_i \overleftarrow{\nabla}_j - m^2 ieQ_c \left(\overrightarrow{\nabla}_i \mathbf{A}_j + \mathbf{A}_i \overrightarrow{\nabla}_j - ieQ_c \mathbf{A}_i \mathbf{A}_j \right) \right] c. \end{aligned} \quad (\text{A.18})$$

In Coulomb gauge, $\nabla \cdot \mathbf{A} = 0$, and if we consider only vertices contributing to the one-photon exchange, we deduce from the equation above

$$n \left(M m ieQ_c \overleftarrow{\nabla}_i \mathbf{A}_j + M m ieQ_c \mathbf{A}_i \overleftarrow{\nabla}_j - m^2 ieQ_c \left[\overrightarrow{\nabla}_i \mathbf{A}_j + \mathbf{A}_i \overrightarrow{\nabla}_j \right] \right) c. \quad (\text{A.20})$$

This yields the following Feynman rule for the one \mathbf{A} -photon exchange derived from the D -wave interaction in Eq. (A.15)

$$(-g_2) \left(i \frac{eQ_c m}{M_{nc}^2} \right) \left[(m\mathbf{p}_c - M\mathbf{p}_n)_i \epsilon_j + (m\mathbf{p}_c - M\mathbf{p}_n)_j \epsilon_i - \frac{2}{d} \delta_{ij} (m\mathbf{p}_c - M\mathbf{p}_n) \cdot \boldsymbol{\epsilon} + \frac{m}{2} (\mathbf{k}_i \epsilon_j + \mathbf{k}_j \epsilon_i) \right], \quad (\text{A.21})$$

with the photon momentum \mathbf{k} , the photon polarization vector $\boldsymbol{\epsilon}$, and the neutron and core momentum \mathbf{p}_n and \mathbf{p}_c , respectively.

In the following sections of App. A we will discuss the calculation of Feynman diagrams that contribute to electric transitions and electric form factors. In principle, the Feynman diagrams that contribute to the equivalent magnetic observables are similar. The evaluation follows the same steps as outlined in the electric sector and thus, is not explicitly presented in this work. The main difference is the additional vertex due to the coupling of the photon to the magnetic moment of the halo neutron in Eq. (4.76) and further local gauge-invariant operators in the magnetic sector.

A.3 B(E2) Transition from the S-to-D-Wave State

In this section, we calculate the diagrams that contribute to the B(E2) transition from the S-to-D-wave state at LO. The two relevant Feynman diagrams for this process are shown in Fig. 4.5 (a). We divide the calculation into three subsections. In the first two subsections, the two diagrams in Fig. 4.5 (a), which contribute to the space-space vertex function, are computed with an A-photon vertex while in the last subsection, the corresponding space-time vertex function with an A₀-photon vertex is evaluated, which yields the same result using current conservation.

A.3.1 First Loop Diagram

We start with the left diagram in Fig. 4.5 (a), where the Feynman rule for the A-photon vertex is given in Eq. (4.42). This yields for the total amplitude in Cartesian coordinates

$$D1 = (-ig_0)(-ig_2) \left(i \frac{eQ_c}{M} \right) \int \frac{d^4l}{(2\pi)^4} \frac{i}{l_0 - \frac{(\mathbf{p}+\mathbf{l})^2}{2M} + i\epsilon} \frac{i}{l_0 + \omega - \frac{(\mathbf{p}+\mathbf{l}+\mathbf{k})^2}{2M} + i\epsilon} \frac{i}{E - l_0 - \frac{l^2}{2m} + i\epsilon} \times$$

$$\left[\frac{1}{2} \left(\left[i \frac{M}{M_{nc}} (-1) - i \frac{m}{M_{nc}} (\mathbf{1} + \mathbf{p} + \mathbf{k}) \right]_i \left[\dots \right]_j + \left[\dots \right]_j \left[\dots \right]_i \right) - \frac{1}{d} \left[\dots \right]^2 \delta_{ij} \right] \boldsymbol{\epsilon} \cdot (\mathbf{1} + \mathbf{p}), \quad (\text{A.22})$$

where the ellipses inside the brackets stand for the same momentum term as in the first bracket, ω denotes the photon energy and i, j are the relative angular momentum indices of the D-wave polarization.

First, we consider the part that depends on l_0 and integrate over l_0

$$I1 = \int \frac{d^4l}{(2\pi)^4} \frac{i}{l_0 - \frac{(\mathbf{p}+\mathbf{l})^2}{2M} + i\epsilon} \frac{i}{l_0 + \omega - \frac{(\mathbf{p}+\mathbf{l}+\mathbf{k})^2}{2M} + i\epsilon} \frac{i}{E - l_0 - \frac{l^2}{2m} + i\epsilon} \quad (\text{A.23})$$

$$= - \int \frac{d^3l}{(2\pi)^3} \frac{1}{E - \frac{(\mathbf{p}+\mathbf{l})^2}{2M} - \frac{l^2}{2m} + i\epsilon} \frac{1}{E + \omega - \frac{(\mathbf{p}+\mathbf{l}+\mathbf{k})^2}{2M} - \frac{l^2}{2m} + i\epsilon}. \quad (\text{A.24})$$

Then, the Feynman parameters are employed

$$\frac{1}{AB} = \int_0^1 dx [Ax + B(1-x)]^{-2}, \quad (\text{A.25})$$

and we derive

$$I1 = - \int \frac{d^3l}{(2\pi)^3} \int_0^1 dx \frac{(-2m_R)^2}{\left[l^2 - 2m_R \left(E - \frac{p^2}{2M} + \omega(1-x) - \frac{k^2}{2M}(1-x) - \frac{\mathbf{l}\cdot\mathbf{k}}{M}(1-x) - \frac{\mathbf{p}\cdot\mathbf{k}}{M}(1-x) - \frac{\mathbf{l}\cdot\mathbf{p}}{M} \right) \right]^2}. \quad (\text{A.26})$$

With the following variable substitution

$$\mathbf{l} = \mathbf{l}' - \frac{m_R}{M} \mathbf{k}(1-x) - \frac{m_R}{M} \mathbf{p}, \quad (\text{A.27})$$

we consequently obtain

$$I1 = - \int \frac{d^3 l}{(2\pi)^3} \int_0^1 dx \frac{(-2m_R)^2}{[l^2 - a(x)]^2}, \quad (\text{A.28})$$

where we adopt the following definition

$$-a(x) = -2m_R \left(E - \frac{p^2}{2M_{nc}} + \omega(1-x) - \frac{k^2}{2M_{nc}} - \frac{k^2}{2M} \left(\frac{M-m}{M_{nc}} x + \frac{m_R}{M} x^2 \right) - \frac{\mathbf{p} \cdot \mathbf{k}}{M_{nc}} (1-x) \right). \quad (\text{A.29})$$

In the heavy baryon approximation, $k^2/(2M_{nc}) \approx 0$ and $k^2/(2M) \approx 0$, and with the assumption $\mathbf{p} \cdot \mathbf{k} = 0$, the expression above simplifies to

$$-a(x) \approx -2m_R \left(E - \frac{p^2}{2M_{nc}} + \omega(1-x) \right) \quad (\text{A.30})$$

$$= \gamma_0^2 x + \gamma_2^2 (1-x), \quad (\text{A.31})$$

where we used in the last step that

$$E - \frac{p^2}{2M_{nc}} = -B_0, \quad \omega = B_0 - B_2, \quad \text{and} \quad B_i = \frac{\gamma_i^2}{2m_R}. \quad (\text{A.32})$$

For the numerator that we neglected so far it follows

$$N1 = (-i)^2 \left(\left[\mathbf{1} + \frac{m}{M_{nc}} (\mathbf{p} + \mathbf{k}) \right]_i \left[\dots \right]_j - \frac{1}{d} \left[\dots \right]^2 \delta_{ij} \right) \epsilon \cdot (\mathbf{1} + \mathbf{p}), \quad (\text{A.33})$$

and after the substitution in Eq. (A.27) we derive

$$N1 = (-i)^2 \left(\left[\mathbf{1} + \mathbf{k} \frac{m_R}{M} x \right]_i \left[\dots \right]_j - \frac{1}{d} \left[\dots \right]^2 \delta_{ij} \right) \epsilon_k \cdot \left(\mathbf{1} + \mathbf{p} \frac{M}{M_{nc}} \right)_k \quad (\text{A.34})$$

$$= (-i)^2 \left[\frac{l^2}{d} \frac{m_R}{M} x (\epsilon_k k_j \delta_{ik} + \epsilon_k k_i \delta_{jk}) + \frac{M m^2}{M_{nc}^3} x^2 \epsilon \cdot \mathbf{p} \left(k_i k_j - \frac{1}{d} \delta_{ij} k^2 \right) \right]. \quad (\text{A.35})$$

In the last step, Eq. (A.5) was used and we exploited that

$$\int_{-\infty}^{\infty} dl_i \frac{l_i}{l^2} = 0. \quad (\text{A.36})$$

Combining the results for $I1$ and $N1$, the total integral reads

$$D1 = -i g_0 g_2 \frac{e Q_c}{M} \int \frac{d^3 l}{(2\pi)^3} \int_0^1 dx \frac{(-2m_R)^2}{[l^2 - a(x)]^2} \times \\ (-i)^2 \left[\frac{l^2}{d} \frac{m_R}{M} x (\epsilon_k k_j \delta_{ik} + \epsilon_k k_i \delta_{jk}) + \frac{M m^2}{M_{nc}^3} x^2 \boldsymbol{\epsilon} \cdot \mathbf{p} \left(k_i k_j - \frac{1}{d} \delta_{ij} k^2 \right) \right]. \quad (\text{A.37})$$

First, we consider the integration over l and divide the integral into two parts. The first part is proportional to l^2 and the second proportional to l^0 .

In PDS, the part proportional to l^2 in the numerator yields

$$L2 = \left(\frac{\mu}{2} \right)^{3-d} \int \frac{d^d l}{(2\pi)^d} \frac{l^2}{[l^2 - a(x)]^2} \quad (\text{A.38})$$

$$= (4\pi)^{-d/2} \Gamma(2 - d/2 - 1) \frac{\Gamma(d/2 + 1)}{\Gamma(d/2)} (-a)^{1+d/2-2} \left(\frac{\mu}{2} \right)^{3-d}. \quad (\text{A.39})$$

Under consideration of the pole in $d = 2$, we obtain for $d = 3$

$$L2 = -\frac{1}{4\pi} \frac{3}{2} \left[(-a(x))^{1/2} - \frac{2}{3} \mu \right]. \quad (\text{A.40})$$

The second part proportional to l^0 in the numerator reads

$$L0 = \left(\frac{\mu}{2} \right)^{3-d} \int \frac{d^d l}{(2\pi)^d} \frac{1}{[l^2 - a(x)]^2} \quad (\text{A.41})$$

$$= (4\pi)^{-d/2} \Gamma(2 - d/2) (-a)^{d/2-2} \left(\frac{\mu}{2} \right)^{3-d}. \quad (\text{A.42})$$

There are no poles in $d = 3$ or in $d = 2$ and thus, we derive

$$L0 = \frac{1}{8\pi} (-a(x))^{-1/2}. \quad (\text{A.43})$$

Then we integrate over x and eventually deduce the total amplitude

$$D1 = i g_0 g_2 \frac{e Q_c}{M} \frac{1}{8\pi} (4m_R^3) \left[\frac{1}{M} (\epsilon_k k_j \delta_{ik} + \epsilon_k k_i \delta_{jk}) \left(\frac{2}{15} \frac{3\gamma_0^3 + 6\gamma_0^2 \gamma_2 + 4\gamma_0 \gamma_2^2 + 2\gamma_2^3}{(\gamma_0 + \gamma_2)^2} - \frac{1}{3} \mu \right) \right. \\ \left. - \frac{m}{M_{nc}^2} \boldsymbol{\epsilon} \cdot \mathbf{p} \left(k_i k_j - \frac{1}{3} \delta_{ij} k^2 \right) \frac{2}{15} \frac{3\gamma_0^2 + 9\gamma_0 \gamma_2 + 8\gamma_2^2}{(\gamma_0 + \gamma_2)^3} \right]. \quad (\text{A.44})$$

A.3.2 Second Loop Diagram

Next, we consider the right diagram in Fig. 4.5 (a)

$$D2 = (-i g_0) \left(-i g_2 \frac{e Q_c m}{M_{nc}^2} \right) \int \frac{d^4 l}{(2\pi)^4} \frac{i}{l_0 - \frac{(\mathbf{1}+\mathbf{p})^2}{2M} + i\epsilon} \frac{i}{E - l_0 - \frac{l^2}{2m} + i\epsilon} \times \\ \left[(m(\mathbf{1}+\mathbf{p})_i + M l_i) \epsilon_j + (m(\mathbf{1}+\mathbf{p})_j + M l_j) \epsilon_i - \frac{2}{d} \delta_{ij} (m(\mathbf{1}+\mathbf{p}) + M \mathbf{l}) \cdot \boldsymbol{\epsilon} + \frac{m}{2} (k_i \epsilon_j + k_j \epsilon_i) \right], \quad (\text{A.45})$$

where the Feynman rule for the photon vertex was derived in Eq. (A.21). First, the integration over l_0 yields

$$D2 = -i g_0 g_2 \frac{e Q_c m}{M_{nc}^2} \int \frac{d^3 l}{(2\pi)^3} \frac{1}{E - \frac{(\mathbf{1}+\mathbf{p})^2}{2M} - \frac{l^2}{2m} + i\epsilon} \times \\ \left[(M_{nc} l_i + m p_i) \epsilon_j + (M_{nc} l_j + m p_j) \epsilon_i - \frac{2}{3} \delta_{ij} (M_{nc} \mathbf{l} + m \mathbf{p}) \cdot \boldsymbol{\epsilon} + \frac{m}{2} (k_i \epsilon_j + k_j \epsilon_i) \right]. \quad (\text{A.46})$$

With the substitution

$$\mathbf{l} = \mathbf{l}' - \frac{m_R}{M} \mathbf{p}, \quad (\text{A.47})$$

and under consideration of Eq. (A.36), we derive

$$D2 = -i g_0 g_2 \frac{e Q_c m}{M_{nc}} \int \frac{d^3 l}{(2\pi)^3} \frac{(-2m_R)}{l^2 - 2m_R \left(E - \frac{p^2}{2M_{nc}} \right) + i\epsilon} \frac{m}{2M_{nc}} (k_i \epsilon_j + k_j \epsilon_i). \quad (\text{A.48})$$

We employ PDS and obtain

$$L0 = \left(\frac{\mu}{2} \right)^{3-d} \int \frac{d^d l}{(2\pi)^d} \frac{1}{l^2 - a} = (4\pi)^{-d/2} \Gamma(1-d/2) (-a)^{d/2-1} \left(\frac{\mu}{2} \right)^{3-d}, \quad (\text{A.49})$$

where we adopted the definition

$$-a = -2m_R \left(E - \frac{p^2}{2M_{nc}} \right) = \gamma_0^2. \quad (\text{A.50})$$

In $d = 3$ and taking the pole in $d = 2$ into account, this yields

$$L0 = -\frac{1}{4\pi} [(-a)^{1/2} - \mu]. \quad (\text{A.51})$$

The total result for the second diagram then reads

$$D2 = -ig_0g_2eQ_c \frac{1}{4\pi} \frac{Mm^3}{M_{nc}^3} (k_i\epsilon_j + k_j\epsilon_i) [\gamma_0 - \mu]. \quad (\text{A.52})$$

Combining both results for the left (A.44) and right diagram (A.52) in Fig. 4.5 (a), we find that the divergent parts cancel each other. This is expected since gauge invariance precludes additional counterterms that could absorb divergences at this order. The remaining steps in the derivation of the B(E2) transition are discussed in Sec. 4.8.1.

A.3.3 A_0 Diagram

Eventually, we calculate the diagram with an A_0 -photon vertex that contributes to the B(E2) transition. Hence, we reconsider the left diagram in Fig. 4.5 (a). In principle, the computation is similar to the $D1$ calculation in Sec. A.3.1, but we replace the A -photon vertex with the A_0 -photon vertex, cf. Eq. (4.42), to derive

$$D3 = (-ig_0)(-ig_2)(-ieQ_c\epsilon_0) \int \frac{d^4l}{(2\pi)^4} \frac{i}{l_0 - \frac{(\mathbf{p}+\mathbf{l})^2}{2M} + i\epsilon} \frac{i}{l_0 + \omega - \frac{(\mathbf{p}+\mathbf{l}+\mathbf{k})^2}{2M} + i\epsilon} \frac{i}{E - l_0 - \frac{l^2}{2m} + i\epsilon} \times$$

$$\left[\frac{1}{2} \left(\left[i \frac{M}{M_{nc}} (-1) - i \frac{m}{M_{nc}} (\mathbf{1} + \mathbf{p} + \mathbf{k}) \right]_i \left[\dots \right]_j + \left[\dots \right]_j \left[\dots \right]_i \right) - \frac{1}{3} \left[\dots \right]^2 \delta_{ij} \right], \quad (\text{A.53})$$

where the ellipses inside the brackets stand for the same momentum term as in the first bracket.

We follow the steps in the $D1$ calculation, i.e. l_0 integration, Feynman parameterization and substitution in Eq. (A.27), and we consequently deduce for the numerator

$$N3 = (-i)^2 \left(\frac{m}{M_{nc}} \right)^2 x^2 \left[k_i k_j - \frac{1}{3} \delta_{ij} k^2 \right]. \quad (\text{A.54})$$

The total integral thus reads

$$D3 = (-ig_0)(-ig_2)(-ieQ_c\epsilon_0) \int \frac{d^3l}{(2\pi)^3} \int_0^1 dx \frac{(-2m_R)^2}{[l^2 - a(x)]^2} \left(\frac{m}{M_{nc}}\right)^2 x^2 \left[k_i k_j - \frac{1}{3} \delta_{ij} k^2 \right], \quad (\text{A.55})$$

where a was defined in Eq. (A.31).

In PDS, the integral over l yields

$$L0 = \left(\frac{\mu}{2}\right)^{3-d} \int \frac{d^d l}{(2\pi)^d} \frac{1}{[l^2 - a(x)]^2} = (4\pi)^{-d/2} \Gamma(2 - d/2) (-a)^{d/2-2} \left(\frac{\mu}{2}\right)^{3-d}. \quad (\text{A.56})$$

There are no poles in $d = 3$ or in $d = 2$ so that we obtain for $d = 3$

$$L0 = \frac{1}{8\pi} (-a)^{-1/2}. \quad (\text{A.57})$$

After the integration over x , the total result for the A_0 vertex is eventually given by

$$D3 = ig_0 g_2 e Q_c \epsilon_0 \frac{1}{2\pi} \left(\frac{m_R m}{M_{nc}}\right)^2 \left[k_i k_j - \frac{1}{3} \delta_{ij} k^2 \right] \frac{2}{15} \left[\frac{3\gamma_0^2 + 9\gamma_0\gamma_2 + 8\gamma_2^2}{(\gamma_0 + \gamma_2)^3} \right].$$

Using current conservation

$$k^\mu \Gamma_{ij,\mu} = 0 \quad (\text{A.58})$$

$$k_k \Gamma_{ij,k} = \omega \Gamma_{ij,0}, \quad (\text{A.59})$$

we derive the same result for Γ_E from the A_0 -photon vertex as from the A -photon vertex, cf. Sec 4.8.1.

A.4 Electric Form Factors

In this section, we calculate the Feynman diagrams contributing to the electric form factors in Fig. 4.3 (a) and (b). For a better readability, we divide the calculation of the left and right diagram into two subsections.

A.4.1 Direct Photon Coupling

We start with diagram (a) in Fig. 4.3. It represents three different topologies for the coupling of an A_0 -photon. Two diagrams stem from the minimal substitution in the bare D -wave propagator in Eq. (4.4), while the last one arises from the local gauge-invariant operator in Eq. (4.43).

We consider only terms with one A_0 -photon and evaluate the diagrams in the Breit frame, where the photon carries no energy $q = (0, \mathbf{q})$. The diagram proportional to η_2 thus reads

$$D1 = -ieQ_c\eta_2 \frac{(\delta_{io}\delta_{jp} + \delta_{ip}\delta_{jo} - \frac{2}{3}\delta_{ij}\delta_{op})}{2}, \quad (\text{A.60})$$

with the relative angular momentum indices i, j and o, p for the incoming and outgoing polarization of the D -wave state, respectively.

For the derivation of the Feynman rule for the vertex proportional to c_2 , we evaluate

$$d_{op}^\dagger c_2 \left(iD_0 + \frac{D^2}{2M_{nc}} \right)^2 d_{ij} = d_{op}^\dagger c_2 \left(-D_0^2 + iD_0 \frac{D^2}{2M_{nc}} + i \frac{D^2}{2M_{nc}} D_0 \right) d_{ij} \quad (\text{A.61})$$

$$= d_{op}^\dagger c_2 \left(-i\partial_0 eQ_c A_0 - ieQ_c A_0 \partial_0 + i^2 eQ_c A_0 \frac{\nabla^2}{2M_{nc}} + i^2 \frac{\nabla^2}{2M_{nc}} eQ_c A_0 \right) d_{ij}, \quad (\text{A.62})$$

where we considered only the relevant terms for the one A_0 -photon exchange. Under consideration that the energy of the photon is zero and that the energy of the D -wave state is given by

$$E = \frac{q^2}{4} \frac{1}{2M_{nc}} - \frac{\gamma_2^2}{2m_R}, \quad (\text{A.63})$$

we eventually obtain the result for the diagram proportional to c_2

$$D2 = ieQ_c c_2 \frac{\gamma_2^2}{m_R} \frac{(\delta_{io}\delta_{jp} + \delta_{ip}\delta_{jo} - \frac{2}{3}\delta_{ij}\delta_{op})}{2}. \quad (\text{A.64})$$

The additional diagrams for the two local gauge-invariant operators, $L_{C01}^{(d)}$ and $L_{C02}^{(d)}$, yield in Cartesian coordinates

$$D3 = i \left(q^2 L_{C01}^{(d)} \frac{(\delta_{io}\delta_{jp} + \delta_{ip}\delta_{jo} - \frac{2}{3}\delta_{ij}\delta_{op})}{2} + L_{C02}^{(d)} \tilde{Q}_{ij,op} \right), \quad (\text{A.65})$$

where $\tilde{Q}_{ij,op}$ was defined in Eq. (4.52). These counterterms are required to absorb the divergences from the loop diagram in the next section.

A.4.2 Loop Diagram

In this section, we consider the loop diagram (b) in Fig. 4.3. In principle, we calculated a similar diagram in Sec. A.3.3 before. This time, however, there is an incoming and outgoing D -wave dimer with momentum $\mp \mathbf{q}/2$, respectively, while the photon momentum is \mathbf{q} . This yields

$$\begin{aligned} D4 = & (-ig_2)^2 (-ieQ_c \epsilon_0) \int \frac{d^4 l}{(2\pi)^4} \frac{i}{l_0 - \frac{(-\mathbf{q}/2 + \mathbf{l})^2}{2M} + i\epsilon} \frac{i}{l_0 - \frac{(\mathbf{q}/2 + \mathbf{l} + \mathbf{k})^2}{2M} + i\epsilon} \frac{i}{E - l_0 - \frac{l^2}{2m} + i\epsilon} \times \\ & \left[\frac{1}{2} \left(\left[-i \frac{M}{M_{nc}} (-1) + i \frac{m}{M_{nc}} \left(1 - \frac{\mathbf{q}}{2} \right) \right]_i \left[\dots \right]_j + \left[\dots \right]_j \left[\dots \right]_i \right) - \frac{1}{3} \left[\dots \right]^2 \delta_{ij} \right] \times \\ & \left[\frac{1}{2} \left(\left[i \frac{M}{M_{nc}} (-1) - i \frac{m}{M_{nc}} \left(1 + \frac{\mathbf{q}}{2} \right) \right]_o \left[\dots \right]_p + \left[\dots \right]_p \left[\dots \right]_o \right) - \frac{1}{3} \left[\dots \right]^2 \delta_{op} \right], \end{aligned} \quad (\text{A.66})$$

where the ellipses in the brackets stand for the same momentum terms as in the first bracket of the corresponding line.

After the l_0 integration, the application of Feynman parameters, and the following substitution

$$l = l' + \frac{m_R}{2M} \mathbf{q} (2x - 1), \quad (\text{A.67})$$

we obtain

$$D4 = -(-ig_2)^2 (-ieQ_c) \int_0^1 dx \int \frac{d^3 l}{(2\pi)^3} \frac{(-2m_R)^2}{[l^2 + a(x)]^2} \times N4, \quad (\text{A.68})$$

with the appropriate expression for the numerator

$$\begin{aligned} N4 = & (-1) \left(\left[l + \frac{m_R}{M} \mathbf{q} x \right]_i \left[l + \frac{m_R}{M} \mathbf{q} x \right]_j - \frac{1}{d} \delta_{ij} \left[l + \frac{m_R}{M} \mathbf{q} x \right]^2 \right) \times \\ & (-1) \left(\left[l + \frac{m_R}{M} \mathbf{q} (x - 1) \right]_o \left[l + \frac{m_R}{M} \mathbf{q} (x - 1) \right]_p - \frac{1}{d} \delta_{op} \left[l + \frac{m_R}{M} \mathbf{q} (x - 1) \right]^2 \right). \end{aligned} \quad (\text{A.69})$$

Moreover, we adopt the definition

$$a(x) = -2m_R \left[E - \frac{q^2}{8M} \left(1 - \frac{m_R}{M} (2x - 1)^2 \right) \right] \quad (\text{A.70})$$

$$= \gamma_2^2 + q^2 f^2 x(1-x), \quad (\text{A.71})$$

where the energy of the D -wave state is given by Eq. (A.63) and we further set $f = m_R/M$.

The expansion of the numerator $N4$ above yields several terms that can be grouped into three different subgroups proportional to l^4 , l^2 , and l^0 .

l^4 Part

For the tensor structure of the l^4 part, we find (cf. Sec A.1)

$$N4L4 = \frac{2}{d(d+2)} l^4 \frac{(\delta_{io}\delta_{jp} + \delta_{ip}\delta_{jo} - \frac{2}{3}\delta_{ij}\delta_{op})}{2} \quad (\text{A.72})$$

$$:= \frac{2l^4}{d(d+2)} E_{ij,op}. \quad (\text{A.73})$$

Employing PDS for the integration over l , it follows

$$L4 = \left(\frac{\mu}{2} \right)^{3-d} \frac{2}{d(d+2)} \int \frac{d^d l}{(2\pi)^d} \frac{l^4}{[l^2 + a(x)]^2} \quad (\text{A.74})$$

$$= (4\pi)^{-d/2} \Gamma(2 - d/2 - 2) \frac{\Gamma(d/2 + 2)}{\Gamma(d/2)} (a(x))^{2+d/2-2} \left(\frac{\mu}{2} \right)^{3-d} \frac{2}{d(d+2)}. \quad (\text{A.75})$$

Under consideration of the pole in $d = 2$, we obtain in $d = 3$

$$L4 = \frac{1}{12\pi} a(x) \left[\sqrt{a(x)} - \frac{3}{2}\mu \right]. \quad (\text{A.76})$$

After the integration over x , we eventually derive

$$D4L4 = -\frac{ieQ_c g_2^2 m_R^2}{3\pi} \int_0^1 dx (\gamma_2^2 + (fq)^2 x(1-x)) \left[\sqrt{\gamma_2^2 + (fq)^2 x(1-x)} - \frac{3}{2}\mu \right] E_{ij,op} \quad (\text{A.77})$$

$$= -\frac{ieQ_c g_2^2 m_R^2}{192\pi f q} \left[3 \arctan \left(\frac{fq}{2\gamma_2} \right) ((fq)^2 + 4\gamma_2^2)^2 + 2fq(3(fq)^2 + 20\gamma_2^3 - 8(fq)^2\mu - 48\gamma_2^2\mu) \right] E_{ij,op}. \quad (\text{A.78})$$

Hence, the part that depends on the PDS scale μ is given by

$$D4L4\mu = \frac{ieQ_c g_2^2 m_R^2}{2\pi} \left(\frac{f^2}{6} q^2 + \gamma_2^2 \right) \mu E_{ij,op}. \quad (\text{A.79})$$

The part proportional to γ_2^2 is renormalized by $D2$ in Eq. (A.64) if we reconsider the matching procedure to the effective range expansion in Eq. (4.35)

$$P_2 = \frac{15\pi}{g_2^2 m_R^3} c_2 + \frac{15}{2} \mu. \quad (\text{A.80})$$

The μ scale of the second part proportional to q^2 is absorbed by the counterterm $L_{C01}^{(d)}$ in Eq. (A.65).

l^2 Part

Next, we consider the tensor structure of the l^2 part

$$N4L2 = \frac{4f^2 x(x-1)}{d} l^2 \tilde{Q}_{ij,op}, \quad (\text{A.81})$$

where we adopt the definition of $\tilde{Q}_{ij,op}$ in Eq. (4.52). The integration over \mathbf{l} , employing PDS, yields

$$L2 = \left(\frac{\mu}{2} \right)^{3-d} \frac{1}{d} \int \frac{d^d l}{(2\pi)^d} \frac{l^2}{[l^2 + a(x)]^2} \quad (\text{A.82})$$

$$= (4\pi)^{-d/2} \Gamma(2 - d/2 - 1) \frac{\Gamma(d/2 + 1)}{\Gamma(d/2)} (a(x))^{1+d/2-2} \left(\frac{\mu}{2} \right)^{3-d} \frac{1}{d}. \quad (\text{A.83})$$

Taking the pole in $d = 2$ into account, it follows in $d = 3$

$$L2 = -\frac{1}{8\pi} \left[\sqrt{a(x)} - \mu \right]. \quad (\text{A.84})$$

Subsequently, we integrate over x and finally derive

$$D4L2 = \frac{ieQ_c 4g_2^2 m_R^2}{8\pi} \int_0^1 dx \left[\sqrt{\gamma_2^2 + (fq)^2 x(1-x)} - \frac{3}{2} \mu \right] f^2 x(x-1) \tilde{Q}_{ij,op} \quad (\text{A.85})$$

$$= -\frac{ieQ_c g_2^2 m_R^2}{384\pi f q^3} \left[3 \arctan\left(\frac{fq}{2\gamma_2}\right) (3(fq)^4 + 8(fq)^2 \gamma_2^2 - 16\gamma_2^4) + \right. \\ \left. 18(fq)^3 \gamma_2 + 24fq \gamma_2^3 - 32(fq)^3 \mu \right] \tilde{Q}_{ij,op}. \quad (\text{A.86})$$

Thus, we obtain for the μ dependent part only

$$D4L2\mu = \frac{ieQ_c g_2^2 m_R^2}{2\pi} \frac{f^2}{6} \mu \tilde{Q}_{ij,op}, \quad (\text{A.87})$$

where the divergence is absorbed by the counterterm $L_{C02}^{(d)}$ in Eq. (A.65).

l^0 Part

Eventually, the tensor structure of the l^0 part is given by

$$N4L0 = f^4 x^2 (x-1)^2 \tilde{H}_{ij,op}, \quad (\text{A.88})$$

with $\tilde{H}_{ij,op}$ defined in Eq. (4.53). Employing PDS, we obtain for the integration over l

$$L0 = \left(\frac{\mu}{2}\right)^{3-d} \int \frac{d^d l}{(2\pi)^d} \frac{1}{[l^2 + a(x)]^2} = (4\pi)^{-d/2} \Gamma(2-d/2) (a(x))^{d/2-2} \left(\frac{\mu}{2}\right)^{3-d}, \quad (\text{A.89})$$

which yields in $d = 3$

$$L0 = \frac{1}{8\pi} \frac{1}{\sqrt{a(x)}}. \quad (\text{A.90})$$

After the integration over x , we finally derive

$$D4L0 = -\frac{ieQ_c 4g_2^2 m_R^2}{8\pi} \int_0^1 dx \frac{f^4 x^2 (x-1)^2}{\sqrt{\gamma_2^2 + (fq)^2 x(1-x)}} \tilde{H}_{ij,op} \quad (\text{A.91})$$

$$= -\frac{ieQ_c g_2^2 m_R^2}{128\pi f q^5} \left[\arctan\left(\frac{fq}{2\gamma_2}\right) (3(fq)^4 - 8(fq)^2 \gamma_2^2 + 48\gamma_2^4) + 6fq\gamma_2 ((fq)^2 - 4\gamma_2^2) \right] \tilde{H}_{ij,op}. \quad (\text{A.92})$$

The remaining steps for the extraction of the form factors at LO and NLO are explained in Sec. 4.7.1.

B *P*-Wave State in Beryllium-11

As discussed in the introduction to halo nuclei in Sec. 2.2.2, ^{11}Be is an example of a one-neutron halo nucleus with a weakly-bound $1/2^+$ *S*-wave ground state and an $1/2^-$ *P*-wave first excited state. In this section, we review parts of the work on ^{11}Be by *Hammer and Phillips* in Ref. [64]. They computed electric form factors, E1 transitions, and the B(E1) strength for the Coulomb dissociation of the ^{11}Be nucleus to the continuum up to NLO in Halo EFT. Based on their results, we outline the inclusion of *P*-wave states in the effective Lagrangian (4.4) of the Halo EFT approach.

Similar to the discussion of the *S*-wave and *D*-wave interaction in Sec. 4.3, the strong *P*-wave interaction of the halo neutron with the core is incorporated through the auxiliary field π_s , which corresponds to the $J^P = 1/2^-$ state. With the convention that repeated spin indices are summed, the *P*-wave part of the non-relativistic Lagrangian is then written as [64]

$$\mathcal{L} = \pi_s^\dagger \left[\eta_1 \left(i\partial_t + \frac{\nabla^2}{2M_{nc}} \right) + \Delta_1 \right] \pi_s - g_1 \left[\pi_s^\dagger \left[ni\overleftrightarrow{\nabla}c \right]_{\frac{1}{2},s} + \left[c^\dagger i\overleftrightarrow{\nabla}n^\dagger \right]_{\frac{1}{2},s} \pi_s \right], \quad (\text{B.1})$$

where the Galilean invariant derivative is defined as

$$\left[ni\overleftrightarrow{\nabla}c \right]_{\frac{1}{2},s} = \sum_{\beta_j} \left(\frac{1}{2} \beta 1j \left| \frac{1}{2}s \right. \right) n_\beta \frac{\left(M\overleftrightarrow{\nabla}_j - m\overleftrightarrow{\nabla}_j \right)}{M_{nc}} c. \quad (\text{B.2})$$

The *P*-wave Lagrangian contains three unknown constants η_1 , Δ_1 , and g_1 . However, only two of them are linearly independent. We follow the traditional approach and set $\eta_1 = \pm 1$, which depends on the sign of the *P*-wave effective range r_1 .

The dressed propagator of the π_s field is derived by summing the bubble diagrams for the g_1 -interaction to all orders, cf. Fig. 4.2. We quote only some key results and refer the reader to Ref. [64] for more details. The *P*-wave propagator takes the form

$$D_\pi(\tilde{p}_0)_{ij} = -\frac{6\pi}{m_R g_1^2} \left[-\frac{6\pi}{m_R g_1^2} (\Delta_1 + \eta_1 \tilde{p}_0) + 2m_R \tilde{p}_0 \left[i\sqrt{2m_R \tilde{p}_0} + \mu \right] \right]^{-1} \delta_{ij}, \quad (\text{B.3})$$

with the Galilean invariant energy $\tilde{p}_0 = p_0 - \mathbf{p}^2/(2M_{nc})$ and i, j denote the polarization of the incoming and outgoing relative momentum of the *P*-wave, respectively. After matching the *P*-wave scattering amplitude to the effective range expansion for this channel

$$t_1(\mathbf{p}', \mathbf{p}; E) = \frac{6\pi}{m_R} \frac{\mathbf{p}' \cdot \mathbf{p}}{1/a_1 - \frac{1}{2}r_1 k^2 + ik^3}, \quad (\text{B.4})$$

with $E = k^2/(2m_R)$ and $k = |\mathbf{p}'| = |\mathbf{p}|$ for on-shell scattering, we obtain the dressed P -wave propagator near the bound state pole

$$D_\pi(p) = Z_\pi \frac{1}{p_0 - \frac{\mathbf{p}^2}{2M_{nc}} + B_1} + R_\pi(p) \quad \text{with} \quad Z_\pi = -\frac{6\pi}{m_R^2 g_1^2} \frac{1}{r_1 + 3\gamma_1}, \quad (\text{B.5})$$

where Z_π denotes the wave-function renormalization, $B_1 = \gamma_1^2/(2m_R)$ denotes the binding energy and $R_\sigma(p)$ is regular at the pole. Following the power-counting scheme in Sec. 4.4, only r_1 contributes at LO in the denominator in Eq. (B.5) since we assume that $r_1 \sim 1/R_{\text{core}}$ and $\gamma_1 \sim 1/R_{\text{halo}}$. This assumption can be verified in the case of ^{11}Be because *Hammer and Phillips* extracted the P -wave effective range from the B(E1) transition strength at LO and found that $r_1 = 0.66 \text{ fm}^{-1}$ [64]. Compared to the expectation from the power-counting scheme that $r_1 \sim 1/R_{\text{core}} = 0.39 \text{ fm}^{-1}$, this is consistent up to the 40% corrections of this Halo EFT.

List of Figures

2.1. Hierarchy of nuclear forces in ChPT [36]	9
2.2. Feynman diagrams contributing to the NN scattering amplitude [45]	12
2.3. Confirmed and suggested halo nuclei [9]	13
2.4. Illustration of the antisymmetrization of neutrons in the halo nucleus ^{11}Be [14]	14
3.1. NCSM single-particle orbits in the harmonic-oscillator potential	18
4.1. Level schemes of ^{15}C and ^{17}C	22
4.2. Diagrammatic representation of the Dyson equation and the nc -scattering amplitude	24
4.3. Topologies contributing to the irreducible vertex for an A_0 -photon	34
4.4. Diagrams contributing to the magnetic moment	40
4.5. Diagrams contributing to the S -to- D state transition	42
4.6. Relevant diagrams for the M1 transition	46
4.7. Relevant diagrams for E1 capture to S -wave states	50
4.8. Relevant diagrams for E1 capture to D -wave states	52
4.9. Relevant diagrams contributing to M1 capture at LO	54
4.10. Relevant diagrams contributing to M1 capture into the D -wave up to NLO	56
4.11. Linear correlations between electric observables	61
4.12. Correlation between $B(E2)$ and the quadrupole moment	63
4.13. E1 capture and photodissociation cross section into the $1/2^+$ state of ^{17}C and ^{15}C	66
4.14. E1 capture cross section into the $1/2^+$ state of ^{15}C compared to [82]	67
4.15. E1 capture and photodissociation cross section into the $5/2^+$ state of ^{15}C	67
5.1. Pion photoproduction	72
5.2. Relevant diagrams at LO for the neutral pion photoproduction at threshold	74
5.3. Pion photoproduction off the nucleus	75
5.4. Number of HO basis states as a function of the single-particle energy	87
5.5. Numerical result of $(F_T^a - F_T^b)$ for different values of Λ for ^3H	93
5.6. The numerical result of $(F_T^a - F_T^b)$ for different values of Λ and different nuclei	94



List of Tables

5.1. Numerical results for the magnetic dipole moment	81
5.2. Numerical results of the one-nucleon contribution to the pion production amplitude	85
5.3. Numerical results for the intrinsic kinetic energy	89
5.4. Numerical results of the two-nucleon contribution to the pion production amplitude	94
5.5. Numerical results of the total <i>S</i> -wave neutral pion production amplitude	95



Bibliography

- [1] J. Braun and H.-W. Hammer. *Electric Properties of One-Neutron Halo Nuclei in Halo EFT*. In: *Few Body Syst.* 58.2 (2017), p. 94.
- [2] J. Braun, R. Roth, and H. W. Hammer. *Universal correlations in shallow D-wave systems*. In: *arXiv preprint arXiv:1803.02169* (2018).
- [3] J. Braun, H.-W. Hammer, and L. Platter. *Halo structure of ^{17}C* . In: *Eur. Phys. J.* A54.11 (2018), p. 196.
- [4] E. Epelbaum, H.-W. Hammer, and U.-G. Meissner. *Modern Theory of Nuclear Forces*. In: *Rev. Mod. Phys.* 81 (2009), pp. 1773–1825.
- [5] P. Navratil et al. *Recent developments in no-core shell-model calculations*. In: *J. Phys.* G36 (2009), p. 083101.
- [6] G. Hagen et al. *Benchmark calculations for H-3, He-4, O-16 and Ca-40 with ab-initio coupled-cluster theory*. In: *Phys. Rev.* C76 (2007), p. 044305.
- [7] K. Tsukiyama, S. K. Bogner, and A. Schwenk. *In-Medium Similarity Renormalization Group for Nuclei*. In: *Phys. Rev. Lett.* 106 (2011), p. 222502.
- [8] A. S. Jensen et al. *Structure and reactions of quantum halos*. In: *Rev. Mod. Phys.* 76 (2004), pp. 215–261.
- [9] I. Tanihata, H. Savajols, and R. Kanungo. *Recent experimental progress in nuclear halo structure studies*. In: *Prog. Part. Nucl. Phys.* 68 (2013), pp. 215–313.
- [10] I. Tanihata et al. *Measurements of Interaction Cross-Sections and Nuclear Radii in the Light p Shell Region*. In: *Phys. Rev. Lett.* 55 (1985), pp. 2676–2679.
- [11] I. Tanihata et al. *Measurements of Interaction Cross-Sections and Radii of He Isotopes*. In: *Phys. Lett.* 160B (1985), pp. 380–384.
- [12] P. G. Hansen and B. Jonson. *The Neutron halo of extremely neutron-rich nuclei*. In: *Europhys. Lett.* 4 (1987), pp. 409–414.
- [13] C. Bachelet et al. *New Binding Energy for the Two-Neutron Halo of Li-11*. In: *Phys. Rev. Lett.* 100 (2008), p. 182501.
- [14] H.-W. Hammer, C. Ji, and D. R. Phillips. *Effective field theory description of halo nuclei*. In: *J. Phys.* G44.10 (2017), p. 103002.
- [15] M. Wang et al. *The AME2016 atomic mass evaluation (II). Tables, graphs and references*. In: *Chinese Physics C* 41.3 (2017), p. 030003.
- [16] C. A. Bertulani, H. W. Hammer, and U. Van Kolck. *Effective field theory for halo nuclei*. In: *Nucl. Phys.* A712 (2002), pp. 37–58.
- [17] P. F. Bedaque, H. W. Hammer, and U. van Kolck. *Narrow resonances in effective field theory*. In: *Phys. Lett.* B569 (2003), pp. 159–167.
- [18] B. Krusche. *Photoproduction of mesons off nuclei*. In: *Eur. Phys. J.* ST 198 (2011), p. 199.
- [19] J. C. Bergstrom et al. *Measurement of the H-2 (gamma, pi0) reaction near threshold*. In: *Phys. Rev.* C57 (1998), pp. 3203–3219.
- [20] M. G. Barnett et al. *Near threshold (gamma, pi0) reactions for He-4 and C-12*. In: *Phys. Rev.* C77 (2008), p. 064601.

- [21] Y. Maghrbi et al. *Coherent photoproduction of π^0 - and η -mesons off ${}^7\text{Li}$* . In: *Eur. Phys. J.* A49 (2013), p. 38.
- [22] S. Schumann et al. *Threshold 0 photoproduction on transverse polarised protons at MAMI*. In: *Phys. Lett.* B750 (2015), pp. 252–258.
- [23] V. Bernard, N. Kaiser, and U.-G. Meissner. *Neutral pion photoproduction off nucleons revisited*. In: *Z. Phys.* C70 (1996), pp. 483–498.
- [24] V. Bernard, N. Kaiser, and U.-G. Meissner. *Chiral dynamics in nucleons and nuclei*. In: *Int. J. Mod. Phys.* E4 (1995), pp. 193–346.
- [25] A. Gasparyan and M. F. M. Lutz. *Photon- and pion-nucleon interactions in a unitary and causal effective field theory based on the chiral Lagrangian*. In: *Nucl. Phys.* A848 (2010), pp. 126–182.
- [26] M. Lenkewitz et al. *Threshold neutral pion photoproduction off the tri-nucleon to $\mathcal{O}(q^4)$* . In: *Eur. Phys. J.* A49 (2013), p. 20.
- [27] V. Bernard, N. Kaiser, and U.-G. Meissner. *Aspects of near threshold neutral pion photoproduction off protons*. In: *Eur. Phys. J.* A11 (2001), pp. 209–216.
- [28] P. Maris et al. ${}^{12}\text{C}$ *properties with evolved chiral three-nucleon interactions*. In: *Phys. Rev.* C90.1 (2014), p. 014314.
- [29] A. Calci and R. Roth. *Sensitivities and correlations of nuclear structure observables emerging from chiral interactions*. In: *Phys. Rev.* C94.1 (2016), p. 014322.
- [30] H. Georgi. *Effective field theory*. In: *Ann. Rev. Nucl. Part. Sci.* 43 (1993), pp. 209–252.
- [31] D. B. Kaplan. *Effective field theories*. In: *Beyond the standard model 5. Proceedings, 5th Conference, Balholm, Norway, April 29-May 4, 1997*. 1995.
- [32] D. R. Phillips. *Building light nuclei from neutrons, protons, and pions*. In: *Czech. J. Phys.* 52 (2002), B49.
- [33] S. Scherer and M. R. Schindler. *A Primer for Chiral Perturbation Theory*. In: *Lect. Notes Phys.* 830 (2012), pp.1–338.
- [34] H.-W. Hammer and S. König. *General aspects of effective field theories and few-body applications*. In: *Lect. Notes Phys.* 936 (2017), pp. 93–153.
- [35] S. Weinberg. *Phenomenological Lagrangians*. In: *Physica* A96.1-2 (1979), pp. 327–340.
- [36] R. Machleidt and D. R. Entem. *Chiral effective field theory and nuclear forces*. In: *Phys. Rept.* 503 (2011), pp. 1–75.
- [37] M. Tanabashi et al. *Review of Particle Physics*. In: *Phys. Rev.* D98.3 (2018), p. 030001.
- [38] J. Gasser, M. E. Sainio, and A. Svarc. *Nucleons with Chiral Loops*. In: *Nucl. Phys.* B307 (1988), pp. 779–853.
- [39] S. Weinberg. *Nuclear forces from chiral Lagrangians*. In: *Phys. Lett.* B251 (1990), pp. 288–292.
- [40] E. Epelbaum. *Nuclear Forces from Chiral Effective Field Theory: A Primer*. In: 2010.
- [41] S. Weinberg. *Effective chiral Lagrangians for nucleon - pion interactions and nuclear forces*. In: *Nucl. Phys.* B363 (1991), pp. 3–18.
- [42] E. E. Jenkins and A. V. Manohar. *Baryon chiral perturbation theory using a heavy fermion Lagrangian*. In: *Phys. Lett.* B255 (1991), pp. 558–562.
- [43] S. Weinberg. *Three body interactions among nucleons and pions*. In: *Phys. Lett.* B295 (1992), pp. 114–121.
- [44] D. R. Entem and R. Machleidt. *Accurate charge dependent nucleon nucleon potential at fourth order of chiral perturbation theory*. In: *Phys. Rev.* C68 (2003), p. 041001.

- [45] P. F. Bedaque and U. van Kolck. *Effective field theory for few nucleon systems*. In: *Ann. Rev. Nucl. Part. Sci.* 52 (2002), pp. 339–396.
- [46] H. A. Bethe. *Theory of the Effective Range in Nuclear Scattering*. In: *Phys. Rev.* 76 (1949), pp. 38–50.
- [47] D. B. Kaplan, M. J. Savage, and M. B. Wise. *A New expansion for nucleon-nucleon interactions*. In: *Phys. Lett.* B424 (1998), pp. 390–396.
- [48] D. B. Kaplan, M. J. Savage, and M. B. Wise. *Two nucleon systems from effective field theory*. In: *Nucl. Phys.* B534 (1998), pp. 329–355.
- [49] J.-W. Chen, G. Rupak, and M. J. Savage. *Nucleon-nucleon effective field theory without pions*. In: *Nucl. Phys.* A653 (1999), pp. 386–412.
- [50] J.-W. Chen, G. Rupak, and M. J. Savage. *Suppressed amplitudes in $n p \rightarrow d \gamma$* . In: *Phys. Lett.* B464 (1999), pp. 1–11.
- [51] M. V. Zhukov et al. *Bound state properties of Borromean Halo nuclei: He-6 and Li-11*. In: *Phys. Rept.* 231 (1993), pp. 151–199.
- [52] P. G. Hansen, A. S. Jensen, and B. Jonson. *Nuclear halos*. In: *Ann. Rev. Nucl. Part. Sci.* 45 (1995), pp. 591–634.
- [53] B. Jonson. *Light dripline nuclei*. In: *Nucl. Phys.* A734 (2004), pp. 263–270.
- [54] K. Riisager. *Halos and related structures*. In: *Phys. Scripta* T152 (2013), p. 014001.
- [55] I. Tanihata. *Nuclear Physics with RIB's: How it all started*. In: *Eur. Phys. J. Plus* 131.4 (2016), p. 90.
- [56] F. Ajzenberg-Selove. *Energy levels of light nuclei $A = 11-12$* . In: *Nucl. Phys.* A506 (1990), pp. 1–158.
- [57] G. Hagen et al. *Ab initio coupled-cluster approach to nuclear structure with modern nucleon-nucleon interactions*. In: *Phys. Rev.* C82 (2010), p. 034330.
- [58] G. Hagen et al. *Coupled-cluster computations of atomic nuclei*. In: *Rept. Prog. Phys.* 77.9 (2014), p. 096302.
- [59] B. R. Barrett, P. Navratil, and J. P. Vary. *Ab initio no core shell model*. In: *Prog. Part. Nucl. Phys.* 69 (2013), pp. 131–181.
- [60] V. N. Efimov. *Weakly-bound states of 3 resonantly-interacting particles*. In: *Sov. J. Nucl. Phys.* 12 (1971), p. 589.
- [61] E. Braaten and H.-W. Hammer. *Universality in few-body systems with large scattering length*. In: *Phys. Rept.* 428 (2006), pp. 259–390.
- [62] H.-W. Hammer and L. Platter. *Efimov States in Nuclear and Particle Physics*. In: *Ann. Rev. Nucl. Part. Sci.* 60 (2010), pp. 207–236.
- [63] G. Hagen et al. *Efimov Physics Around the Neutron-Rich ^{60}Ca Isotope*. In: *Phys. Rev. Lett.* 111.13 (2013), p. 132501.
- [64] H.-W. Hammer and D. R. Phillips. *Electric properties of the Beryllium-11 system in Halo EFT*. In: *Nucl. Phys.* A865 (2011), pp. 17–42.
- [65] G. Rupak and R. Higa. *Model-Independent Calculation of Radiative Neutron Capture on Lithium-7*. In: *Phys. Rev. Lett.* 106 (2011), p. 222501.
- [66] X. Zhang, K. M. Nollett, and D. R. Phillips. *Marrying ab initio calculations and Halo-EFT: the case of $^7\text{Li} + n \rightarrow ^8\text{Li} + \gamma$* . In: *Phys. Rev.* C89.2 (2014), p. 024613.
- [67] X. Zhang, K. M. Nollett, and D. R. Phillips. *Combining ab initio calculations and low-energy effective field theory for halo nuclear systems: The case of $^7\text{Be} + p \rightarrow ^8\text{B} + \gamma$* . In: *Phys. Rev.* C89.5 (2014), p. 051602.

- [68] B. Acharya and D. R. Phillips. *Carbon-19 in Halo EFT: Effective-range parameters from Coulomb-dissociation experiments*. In: *Nucl. Phys.* A913 (2013), pp. 103–115.
- [69] D. L. Canham and H.-W. Hammer. *Universal properties and structure of halo nuclei*. In: *Eur. Phys. J.* A37 (2008), pp. 367–380.
- [70] D. L. Canham and H.-W. Hammer. *Range corrections for two-neutron halo nuclei in effective theory*. In: *Nucl. Phys.* A836 (2010), pp. 275–292.
- [71] J. Rotureau and U. van Kolck. *Effective Field Theory and the Gamow Shell Model: The ${}^6\text{He}$ Halo Nucleus*. In: *Few Body Syst.* 54 (2013), pp. 725–735.
- [72] C. Ji, C. Elster, and D. R. Phillips. *${}^6\text{He}$ nucleus in halo effective field theory*. In: *Phys. Rev.* C90.4 (2014), p. 044004.
- [73] S.-I. Ando. *Hypernuclei in Halo/Cluster Effective Field Theory*. In: *Int. J. Mod. Phys.* E25.05 (2016), p. 1641005.
- [74] G. Rupak. *Radiative reactions in halo effective field theory*. In: *Int. J. Mod. Phys.* E25.05 (2016), p. 1641004.
- [75] J. Braun. *Extrapolation Techniques for Importance-Truncated No-Core and Valence-Space Shell Model*. Master's Thesis. TU Darmstadt, 2015.
- [76] R. Roth. *Importance Truncation for Large-Scale Configuration Interaction Approaches*. In: *Phys. Rev.* C79 (2009), p. 064324.
- [77] H. Hergert et al. *The In-Medium Similarity Renormalization Group: A Novel Ab Initio Method for Nuclei*. In: *Phys. Rept.* 621 (2016), pp. 165–222.
- [78] C. D. Sherrill and H. F. Schaefer. *The configuration interaction method: Advances in highly correlated approaches*. In: *Advances in quantum chemistry* 34 (1999), pp. 143–269.
- [79] S. D. Glazek and K. G. Wilson. *Renormalization of Hamiltonians*. In: *Phys. Rev.* D48 (1993), pp. 5863–5872.
- [80] R. Roth et al. *Similarity-Transformed Chiral $\text{NN}+3\text{N}$ Interactions for the Ab Initio Description of ${}^{12}\text{C}$ and ${}^{16}\text{O}$* . In: *Phys. Rev. Lett.* 107 (2011), p. 072501.
- [81] R. J. Buenker and S. D. Peyerimhoff. *Individualized configuration selection in CI calculations with subsequent energy extrapolation*. In: *Theoretica chimica acta* 35.1 (1974), pp. 33–58.
- [82] G. Rupak, L. Fernando, and A. Vaghani. *Radiative Neutron Capture on Carbon-14 in Effective Field Theory*. In: *Phys. Rev.* C86 (2012), p. 044608.
- [83] F. Ajzenberg-Selove. *Energy levels of light nuclei $A = 13$ –15*. In: *Nucl. Phys.* A449 (1986), pp. 1–155.
- [84] L. Fernando, A. Vaghani, and G. Rupak. *Electromagnetic form factors of one neutron halos with spin $1/2+$ ground state*. In: *arXiv preprint arXiv:1511.04054* (2015).
- [85] F. Ajzenberg-Selove. *Energy levels of light nuclei $A = 16$ –17*. In: *Nucl. Phys.* A460 (1986), pp. 1–110.
- [86] D. Suzuki et al. *Lifetime measurements of excited states in ${}^{17}\text{C}$: Possible interplay between collectivity and halo effects*. In: *Phys. Lett.* B666 (2008), pp. 222–227.
- [87] D. Smalley et al. *Lifetime measurements of ${}^{17}\text{C}$ excited states and three-body and continuum effects*. In: *Phys. Rev.* C92.6 (2015), p. 064314.
- [88] L. S. Brown and G. M. Hale. *Field Theory of the $d + t \rightarrow n + \alpha$ Reaction Dominated by a ${}^5\text{He}^*$ Unstable Particle*. In: *Phys. Rev.* C89.1 (2014), p. 014622.
- [89] S. R. Beane and M. J. Savage. *Rearranging pionless effective field theory*. In: *Nucl. Phys.* A694 (2001), pp. 511–524.

- [90] T. Nakamura et al. *Neutron capture cross section of C-14 of astrophysical interest studied by Coulomb breakup of C-15*. In: *Phys. Rev. C* 79 (2009), p. 035805.
- [91] G. 't Hooft. *Dimensional regularization and the renormalization group*. In: *Nucl. Phys.* B61 (1973), pp. 455–468.
- [92] S. Weinberg. *New approach to the renormalization group*. In: *Phys. Rev.* D8 (1973), pp. 3497–3509.
- [93] A. Buckingham. *Molecular quadrupole moments*. In: *Quarterly Reviews, Chemical Society* 13.3 (1959), pp. 183–214.
- [94] W. Greiner and J. A. Maruhn. *Nuclear Models*. Springer Berlin Heidelberg, 1996.
- [95] S. Typel and G. Baur. *Electromagnetic strength of neutron and proton single-particle halo nuclei*. In: *Nucl. Phys.* A759 (2005), pp. 247–308.
- [96] G. Baur, C. A. Bertulani, and H. Rebel. *Coulomb dissociation as a source of information on radiative capture processes of astrophysical interest*. In: *Nucl. Phys.* A458 (1986), pp. 188–204.
- [97] I. Angeli and K. P. Marinova. *Table of experimental nuclear ground state charge radii: An update*. In: *Atom. Data Nucl. Data Tabl.* 99.1 (2013), pp. 69–95.
- [98] R. Kanungo et al. *Proton Distribution Radii of $^{12-19}\text{C}$ Illuminate Features of Neutron Halos*. In: *Phys. Rev. Lett.* 117.10 (2016), p. 102501.
- [99] P. Mueller et al. *Nuclear charge radius of He-8*. In: *Phys. Rev. Lett.* 99 (2007), p. 252501.
- [100] W. M. Yao et al. *Review of Particle Physics*. In: *J. Phys.* G33 (2006), pp. 1–1232.
- [101] A. C. Phillips. *Consistency of the low-energy three-nucleon observables and the separable interaction model*. In: *Nucl. Phys.* A107 (1968), pp. 209–216.
- [102] J. A. Tjon. *Bound states of 4 He with local interactions*. In: *Phys. Lett.* 56B (1975), pp. 217–220.
- [103] A. Nogga, S. K. Bogner, and A. Schwenk. *Low-momentum interaction in few-nucleon systems*. In: *Phys. Rev.* C70 (2004), p. 061002.
- [104] A. Bohr and B. R. Mottelson. *Nuclear Structure, vol. II: Nuclear deformations*. New York, USA: W. A. Benjamin, 1969.
- [105] P. Navratil. *Local three-nucleon interaction from chiral effective field theory*. In: *Few Body Syst.* 41 (2007), pp. 117–140.
- [106] E. Epelbaum, W. Gloeckle, and U.-G. Meissner. *Improving the convergence of the chiral expansion for nuclear forces. 1. Peripheral phases*. In: *Eur. Phys. J.* A19 (2004), pp. 125–137.
- [107] K. Hebeler and R. J. Furnstahl. *Neutron matter based on consistently evolved chiral three-nucleon interactions*. In: *Phys. Rev.* C87.3 (2013), p. 031302.
- [108] I. Tews et al. *Neutron matter at next-to-next-to-next-to-leading order in chiral effective field theory*. In: *Phys. Rev. Lett.* 110.3 (2013), p. 032504.
- [109] T. Krüger et al. *Neutron matter from chiral effective field theory interactions*. In: *Phys. Rev.* C88 (2013), p. 025802.
- [110] R. Reifarh et al. *The C-14(n, γ) cross section between 10-keV and 1-MeV*. In: *Phys. Rev.* C77 (2008), p. 015804.
- [111] M. Lenkewitz et al. *Neutral pion photoproduction off ^3H and ^3He in chiral perturbation theory*. In: *Phys. Lett.* B700 (2011), pp. 365–368.
- [112] M. Lenkewitz. *Neutral pion electroproduction off light nuclei in chiral perturbation theory*. PhD thesis. 2013.
- [113] S. R. Beane et al. *Neutral pion photoproduction on deuterium in baryon chiral perturbation theory to order q^{*4}* . In: *Nucl. Phys.* A618 (1997), pp. 381–401.

- [114] D. Drechsel and L. Tiator. *Threshold pion photoproduction on nucleons*. In: *J. Phys.* G18 (1992), pp. 449–497.
- [115] G. F. Chew et al. *Relativistic dispersion relation approach to photomeson production*. In: *Phys. Rev.* 106 (1957), pp. 1345–1355.
- [116] L. D. Pearlstein and A. Klein. *Transition Amplitudes for Photoproduction of Mesons from Nucleons and Photodisintegration of the Deuteron*. In: *Phys. Rev.* 107 (1957), pp. 836–842.
- [117] P. Dennery. *Theory of the Electro- and Photoproduction of pi Mesons*. In: *Phys. Rev.* 124 (1961), pp. 2000–2010.
- [118] V. Bernard, N. Kaiser, and U.-G. Meissner. *Threshold neutral pion electroproduction in heavy baryon chiral perturbation theory*. In: *Nucl. Phys.* A607 (1996). [Erratum: *Nucl. Phys.*A633,695(1998)], pp. 379–401.
- [119] H. Arenhovel. *Invariant amplitudes for coherent electromagnetic pseudoscalar production from a spin one target*. In: *Few Body Syst.* 25 (1998), pp. 157–175.
- [120] H. Krebs, V. Bernard, and U.-G. Meissner. *Near threshold neutral pion electroproduction on deuterium in chiral perturbation theory*. In: *Nucl. Phys.* A713 (2003), pp. 405–437.
- [121] N. M. Kroll. *A Theorem on photomeson production near threshold and the suppression of pairs in pseudoscalar meson theory*. In: *Phys. Rev.* 93 (1954), pp. 233–238.
- [122] S. R. Beane, C. Y. Lee, and U. van Kolck. *Neutral pion photoproduction on nuclei in baryon chiral perturbation theory*. In: *Phys. Rev.* C52 (1995), pp. 2914–2924.
- [123] V. Bernard, N. Kaiser, and U.-G. Meissner. *Chiral corrections to the Kroll-Ruderman theorem*. In: *Phys. Lett.* B383 (1996), pp. 116–120.
- [124] J. Suhonen. *From Nucleons to Nucleus*. Theoretical and Mathematical Physics. Berlin, Germany: Springer, 2007.
- [125] W. H. Press et al. *Numerical Recipes in C: The Art of Scientific Computing, Second Edition*. Cambridge University Press, 1992.
- [126] V. Bernard, N. Kaiser, and U.-G. Meissner. *Chiral symmetry and the reaction $\gamma p \rightarrow \pi^0 p$* . In: *Phys. Lett.* B378 (1996), pp. 337–341.
- [127] A. Schmidt et al. *Test of Low-Energy Theorems for $^1H(\rightarrow,^0)^1H$ in the Threshold Region*. In: *Phys. Rev. Lett.* 87 (2001). [Erratum: *Phys. Rev. Lett.*110,039903(2013)], p. 232501.
- [128] V. Bernard, B. Kubis, and U.-G. Meissner. *The Fubini-Furlan-Rosetti sum rule and related aspects in light of covariant baryon chiral perturbation theory*. In: *Eur. Phys. J.* A25 (2005), pp. 419–425.

Jonas Braun

Curriculum vitae

Personal details

Date of birth

[REDACTED]

Email

[REDACTED]

Work experience

2016-present

Institut für Kernphysik der TU Darmstadt (Darmstadt, Germany)
Scientific employee (Jan. - present)

2017

Department of Physics and Astronomy at UTK (Knoxville, USA)
Visiting researcher (Aug. - Nov.)

2015

Institut für Kernphysik der TU Darmstadt (Darmstadt, Germany)
Scholarship holder of Helmholtz Graduate School for Hadron and Ion Research
(May - Dec.)

2008-2009

Diakoniestation Südlicher Odenwald (Fürth, Germany)
Zivildienst (Sept. - May)

Education

2015-present

TU Darmstadt; Ph.D. student (May - present)

2012-2015

TU Darmstadt; M.Sc. in Physics (Oct. - March)

2009-2012

TU Darmstadt; B.Sc. in Physics (Oct. - Aug.)

1999-2008

Martin-Luther-Schule, Rimbach; Abitur (July - June)



Danksagung

Ich möchte mich herzlich für die Unterstützung bedanken, die ich während der letzten Jahre von zahlreichen Seiten erfahren habe.

Herrn Prof. Dr. Hans-Werner Hammer danke ich für das spannende Thema. Während der regelmäßigen Treffen konnte ich mein Verständnis im Bereich der theoretischen Kernphysik deutlich erweitern. Dabei hat mir Prof. Dr. Hans-Werner Hammer mit Anregungen und Denkanstößen wichtige Impulse für diese Doktorarbeit gegeben.

Des Weiteren bedanke ich mich bei Prof. Dr. Robert Roth für seine Unterstützung, insbesondere im Rahmen der Pion-Produktion, für das zur Verfügung stellen der NCSM Wellenfunktionen, und für seine Rolle als Mentor bei den regelmäßigen PhD-Committee Meetings.

Ebenso möchte ich mich bei Prof. Dr. Lucas Platter für die äußerst konstruktive Zusammenarbeit bedanken. Ich habe mich während meines dreimonatigen Aufenthalts in Knoxville, Tennessee, in seiner Arbeitsgruppe außerordentlich wohl gefühlt.

Darüber hinaus gilt mein Dank der gesamten Arbeitsgruppe unter Prof. Dr. Hans-Werner Hammer für die angenehme Arbeitsatmosphäre und die Anregungen für diese Arbeit. Insbesondere die zahlreichen Diskussionen mit Dr. Max Jansen und Wael Elkamhawy habe ich als sehr hilfreich empfunden. Außerdem danke ich Dr. Roland Wirth, der sich immer Zeit für meine Fragen genommen und mir beim Thema Pion-Produktion und dem IT-NCSM Code wichtige Denkanstöße gegeben hat. Von ihrem Feedback habe ich auch über diese Arbeit hinaus profitiert.

Für das gewissenhafte Korrekturlesen meiner Dissertation bedanke ich mich bei Anjuli Franz, Leon Kerber, Rebekka Göttert und Wael Elkamhawy.

Ich danke meinen Freunden und meiner Familie, die mich unentwegt auf meinem Weg unterstützen.
